Microseismicity, tectonic stress, and exhumation rates near the central Alpine Fault, New Zealand

By

Konstantinos Michailos

A thesis

submitted to Victoria University of Wellington

in fulfilment of the requirements for the degree of

Doctor of Philosophy in Geophysics

Victoria University of Wellington

2019

"In all things of nature there is something of the marvelous."

Aristotle

Abstract

This thesis documents a detailed examination of the seismic activity and characteristics of crustal deformation along the central Alpine Fault, a major obliquely convergent plate-boundary fault. Paleoseismic evidence has established that the Alpine Fault produces large to great (M7−8) earthquakes every 250−300 years, in a quasi-periodic manner, with the last surface-rupturing earthquake occurring in 1717. This renders the fault late in its typical earthquake cycle, posing substantial seismic risk to southern and central New Zealand. Understanding the seismic and tectonic character of this fault may yield information of both societal and scientific significance regarding seismic hazard and late-interseismic processes leading up to a large earthquake. However, the central Alpine Fault is currently seismically quiescent when compared to adjacent regions, and therefore requires detailed, long-duration observations to study seismotectonic processes. The work in this thesis addresses the need for a greater understanding of along-strike variations in seismic character of the Alpine Fault ahead of an anticipated large earthquake.

To achieve observations with high spatial and temporal resolution across the length of the central Alpine Fault, I use 8.5 years of continuous seismic data from the Southern Alps Microearthquake Borehole Array (SAMBA), and data from four other temporary seismic networks and five local GeoNet permanent sites. Incorporating all of these temporary and permanent seismic sites provides us with a dense composite network of seismometers. Without such a dense network, homogeneous examination of the characteristics of low-magnitude seismicity near the Alpine Fault would be impossible.

Using this dataset, I have constructed the most extensive microearthquake catalog for the central Alpine Fault region to date, containing 9,111 earthquakes and covering the time between late 2008 and early 2017. To construct this catalog I created an objective workflow to ensure catalog uniformity. Overall, 7,719 earthquakes were successfully relocated with location uncertainties generally $\leq$ 0.5 km in both the horizontal and vertical directions. The majority of the earthquakes were found to occur southeast of the Alpine Fault (i.e. in the hanging-wall). I observed a lack of seismicity beneath Aoraki/Mount Cook that has previously been shown to be associated with locally high uplift rates (6–10 mm/yr) and high geothermal gradients ($\sim$60°C/km). Seismogenic cut-off depths were observed to significantly vary along the strike of the Alpine Fault, ranging from 8 km beneath the highest topography to 20 km in the adjacent areas.

To quantify the scale of the seismic deformation, a new local magnitude scale was also derived, corrected for geometric spreading, attenuation and site terms based on individually calculated GeoNet moment magnitude (M_w) values. Earthquake local magnitudes range between M_L –1.2 and 4.6 and the catalog is complete above M_L 1.1.

To examine the stress regime near the central Alpine Fault, I built a new data set of 845 focal mechanisms from earthquakes in our catalog. This was achieved by manually determining P wave arrival polarity picks from all earthquakes larger than M_L 1.5. In order to determine the orientations and characteristics of the stress parameters, I grouped these focal mechanisms and performed stress inversion calculations that provided an average maximum horizontal compressive stress orientation, S_{Hmax}, of 121±11°, which is uniform within uncertainty along the length of the central Southern Alps. I observed an average angle of 65° between the S_{Hmax} and the strike of the Alpine Fault, which is consistent with results from similar previous studies in the northern and southern sections of the Alpine Fault. This implies that the Alpine Fault is misoriented for reactivation, in the prevailing stress field.

Using a 1-D steady-state thermal structure model constrained by seismicity and thermochronology data, I investigated the crustal thermal structure and vertical kinematics of the central Southern Alps orogen. The short-term seismicity data and longer-term thermochronology data impose complementary constraints on the model. I observed a large variation in exhumation rate estimates (1–8 mm/yr) along the length of the Alpine Fault, with maximum calculated values observed near Aoraki/Mount Cook. I calculated the temperature at the brittle-ductile transition zone, which ranges from 440 to 457°C in the different models considered. This temperature is slightly hotter than expected for crust composed by quartz-rich rocks, but consistent with the presence of feldspar-rich mafic rocks in parts of the crust.

Acknowledgements

Firstly, I would like to express my gratitude to my supervisors John Townend and Martha Savage for the continuous support of my Ph.D. study, their patience, motivation, and immense knowledge. Your guidance helped me throughout the research and writing of this thesis.

Besides my supervisors, I would like to thank Euan Smith, Emily Warren-Smith, and Rupert Sutherland for their insightful comments, encouragement and contribution to my research from various perspectives. Without their precious support it would not have been possible to conduct this research. Thanks to Calum Chamberlain, who has been extremely helpful throughout the past three and a half years. Thanks for sharing your experience and knowledge in coding, field-work and earthquakes.

The present thesis, including field-work and conference travels, was funded by the Marsden Fund of the Royal Society Te Apārangi, the Earthquake Commission of New Zealand (EQC Programme in Seismology and Fault Mechanics at Victoria University of Wellington) and the New Zealand International Doctoral Research Scholarship.

I gratefully acknowledge Carolin Boese for organising the SAMBA network deployment. Thanks to Stephen Barrister and Sandra Bourguignon for kindly making the ALFA–08 data available and Cliff Thurber and Steve Roecker for the WIZARD data. I would also like to thank the landowners in the West Coast and central Otago, New Zealand and the New Zealand Department of Conservation for their kind cooperation. We acknowledge the New Zealand GeoNet project and its sponsors EQC, GNS Science, and LINZ for providing data used in this study.

Field assistance with the SAMBA and COSA network data collection and maintenance by Adrian, Laura-May, Calum, Nicolas, Dominic, Bryant, Chet and Kenny is much appreciated. Thanks for your patience and careful driving in the windy West Coast roads. I am also incredibly grateful to Kenny and Bryant for their help in my last field-trip, during which I had a sore back, or so I claimed, that kept me from lifting or carrying any of the gear.

Special thanks to my past and present office mates: Cécile, Dominic, Emily, Pasan, Bryant and Abhijith. Thank you for always being keen to help me out with never ending, big and small tasks. Thank you to all the past and present SGEES graduate students that helped make this journey more fun. Thanks KJ for proofreading parts

of the text. A warm thanks goes to Io, who, despite the time difference, was always there.

Last but not the least, I would like to thank my family for supporting me throughout writing this thesis and my life in general.

Contents

List of Figures

List of Tables

1 Introduction

1.1 Motivation and objectives

The Alpine Fault is a large plate-boundary strike-slip fault that runs the length of the South Island, posing a major seismic hazard to southern and central New Zealand (*Stirling et al.*, 2012). Its structure and tectonics have similarities with other large strike-slip faults (e.g. San Andreas Fault; *Fuis et al.*, 2007). A striking difference between the Alpine Fault and the San Andreas Fault, however, is that the Alpine Fault has no written record of a major earthquake (M≥7) in the area between Arthur's Pass and the northern Fiordland (*Evison*, 1971; *Anderson and Webb*, 1994), a distance of approximately 300 km along a single fault structure (Fig. 1.1).

In recent decades, a number of paleoseismological studies have shed light on the historic record of the large Alpine Fault earthquakes (*Howarth et al.*, 2018, and references therein). These studies have provided valuable information on the rupture history and earthquake recurrence behaviour of different sections of the Alpine Fault. Large Alpine Fault earthquakes occur quasi-periodically every 250−300 years and the most recent one occurred in 1717 AD (*Sutherland et al.*, 2007; *Berryman et al.*, 2012; *Cochran et al.*, 2017; *Howarth et al.*, 2016, 2018). These results suggest that the Alpine Fault is late in its typical seismic cycle. In light of recent damaging earthquakes in the South Island (i.e. the 2010−2011 Canterbury earthquake sequence and the 2016 Kaikōura earthquake), they have highlighted the importance of improved disaster risk management efforts for a potential large Alpine Fault earthquake (e.g. project AF8; *Orchiston et al.*, 2018).

The large interevent times and resulting infrequency of large earthquakes has turned the scientific focus to the small-scale deformation processes (e.g. tremor and small magnitude earthquakes) that occur more frequently and can provide valuable insights on the processes controlling seismogenesis. Two major projects in the last decade, that this PhD project is related to, have focused on this small-scale tectonic deformation. The initial Marsden Fund project entitled *"Putting a stethoscope on the Alpine Fault"*, provided the funds for the deployment of the SAMBA seismic network (Section 2.1.1) and the enhancement of the network of seismometers near the central Alpine Fault. The second Marsden Fund project named *"Locked and loaded? Effects of deep seismic*

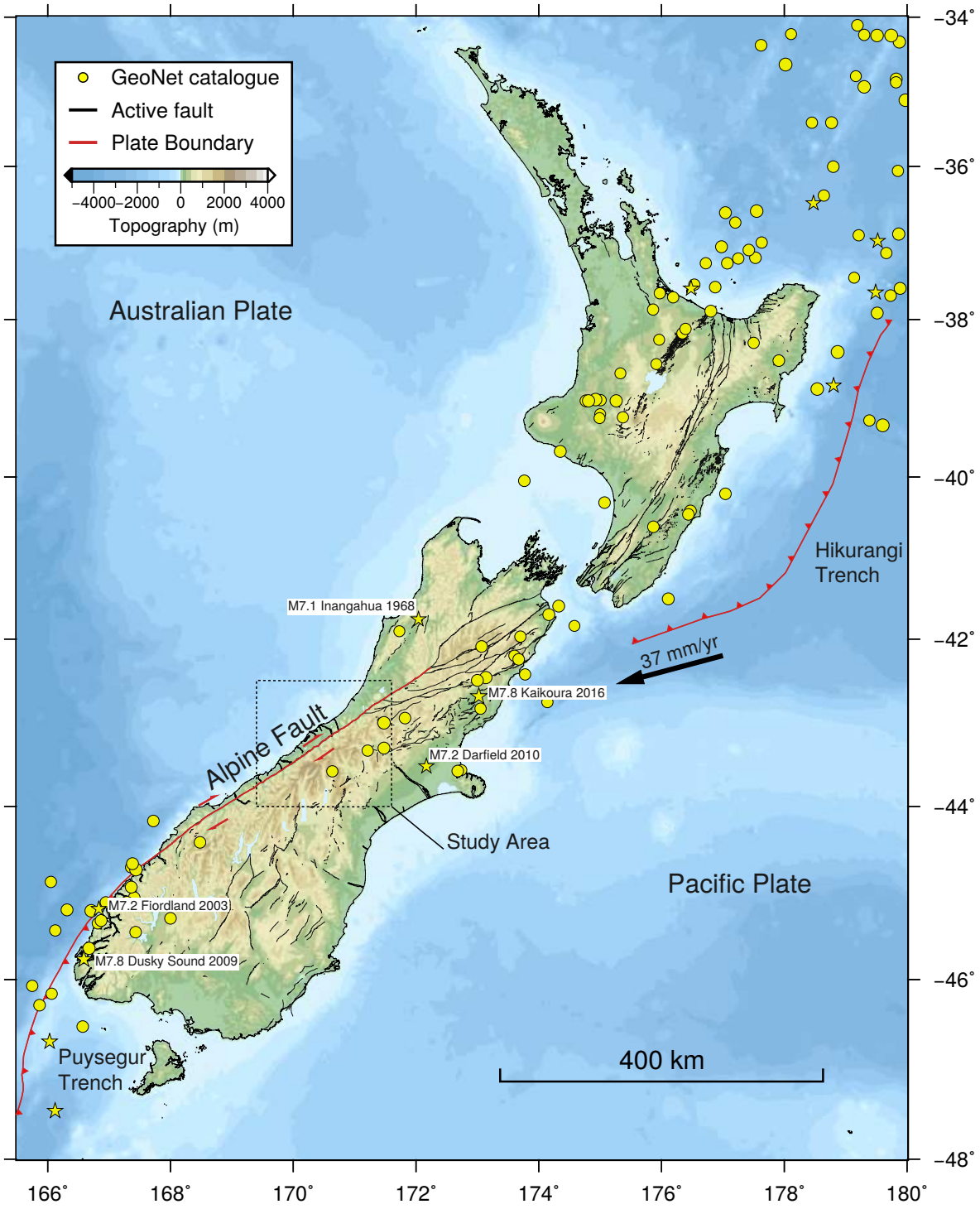

Figure 1.1: Map summarising the main seismotectonic features of New Zealand (namely from South to North; Puysegur Trench, Alpine Fault and Hikurangi Trench). Earthquakes locations with magnitudes M>6.0 from the GeoNet earthquake catalog recorded during instrumental time period (since 1943). Stars depict the major earthquakes with magnitudes M>7.0, since 1943. Dashed square outlines the limits of the study area of this PhD work. Arrow indicates the local velocity of Pacific Plate relative to Australia (∼37 mm/yr; *DeMets et al.*, 2010).

and aseismic deformation on Alpine Fault earthquakes" enabled the continuation of the detection, location and characterisation of the seismic deformation near the central

Alpine Fault, aiming to estimate how deformation is accumulating ahead of a potential future large earthquake.

Accurately detecting and locating the background microseismicity can provide useful information about the structure and mechanics of faults at depth, shed light on their characteristics and yield an estimation for the seismogenic thickness (*Nazareth and Hauksson*, 2004; *Ito*, 1999; *Omuralieva et al.*, 2012; *Yano et al.*, 2017). All of which are key parameters for modelling future damaging earthquakes. The seismogenic thickness can be estimated by the distribution of the hypocentral depths of the background seismicity and their lower cutoff depths (*Sibson*, 1984; *Scholz*, 1988). *Nazareth and Hauksson* (2004) quantitatively defined the seismogenic thickness of the crust in the southern California based on the depth distribution of the seismic moment release and observed highly variable depths ranging from less than 10 km to greater than 25 km depths. The lower cutoff depth of the seismogenic zone adjacent to the central Alpine Fault is estimated to range from 8 to 14 km using earthquake hypocentral depths (*Leitner and Eberhart-Phillips*, 2001; *Boese et al.*, 2012; *Bourguignon et al.*, 2015). This range may reflect a spatial variation in seismogenic thickness.

Magistrale and Zhou (1996) compared the depth extent of the background seismicity with that of aftershock distributions in southern California and suggested that the maximum depth of mainshock earthquake ruptures can be determined from the background seismicity. Most earthquake hazard analyses assume that the seismogenic thickness corresponds to the maximum depth of rupture of moderate and large earthquakes (e.g. *Nazareth and Hauksson*, 2004). Therefore, an improved knowledge of the seismogenic thickness, which corresponds to the width of the faulting major faults (i.e. Alpine Fault), can help towards more accurate potential rupture areas and earthquake hazard analyses and models. Considering this, earthquake hazard models along with other data (e.g. geomorphic consequences, cascading hazards) in the South Island can provide estimations on crucial information that can help local authorities better prepare the efforts for response to a large Alpine Fault earthquake (*Orchiston et al.*, 2018, 2016). More recent studies however, have suggested that large earthquakes sometimes or always also rupture the deeper creeping section of the fault zone (*Jiang and Lapusta*, 2016; *Shaw and Wesnousky*, 2008; *Beeler et al.*, 2018).

As estimations of seismogenic depths have become more detailed and accurate, numerous studies have examined the relationship between the distribution of hypocentral depths and heat flow, rock type, crustal strength, rheology and mechanics (e.g. *Doser and Kanamori*, 1986; *Williams*, 1996; *Bonner et al.*, 2003; *Albaric et al.*, 2009; *Hauksson and Meier*, 2018). The response of crustal rocks to stresses (shear fault strength) varies with depth under different temperature and pressure conditions (*Sibson*, 1984). The shear fault strength increases linearly with depth in the upper brittle (i.e. fracturing and faulting) part of the crust and reaches a peak in the brittle ductile transition

zone (BDT) where both stresses and earthquake magnitudes will be the greatest (*Sibson*, 1984). Below this transition zone in the lower ductile (i.e. plastic flow) part of the crust the shear fault strength decreases exponentially. The depth of the brittle ductile transition zone is controlled by a number of physical factors that include temperature, strain rate, pore fluid pressure, lithology, water content, fault geometry and type of faulting (*Scholz*, 1998; *Sibson*, 1984) and is suggested to roughly correspond to the maximum depths of earthquakes (*Sibson*, 1982).

Dense spatial networks of seismometers, more accurate recording instruments and new techniques for processing seismic data can provide a refined image of the seismicity distribution in the crust. In this project, we use a large number of densely distributed seismometers (i.e. 68) that operated over almost a decade, to examine the microseismicity characteristics and the lateral variations of the seismogenic thickness along the length of the central Alpine Fault.

In light of the recent results from Deep Fault Drilling Project (DFDP-2) in Whataroa, which highlighted a locally extreme near surface geothermal gradient of (125±55°C/km; *Sutherland et al.*, 2017) and in conjunction with inferences from previous thermal model studies (e.g. *Allis and Shi*, 1995; *Shi et al.*, 1996; *Toy et al.*, 2010; *Cross et al.*, 2015; *Kidder et al.*, 2018) that all suggest high temperatures near the Alpine Fault, we investigate the contribution of the crustal thermal structure to the distribution of the seismogenic thickness in the central Southern Alps. To do this, we use the distribution of the hypocentral depths of the microseismicity examined here and thermochronology ages (e.g. *Herman et al.*, 2007, 2009; *Tippet and Kamp*, 1993; *Ring and Bernet*, 2010; *Kamp et al.*, 1989; *Batt and Braun*, 1999; *Batt et al.*, 2000; *Seward*, 1989) as constraints to estimate the crustal thermal structure. An estimation of the distribution of temperatures at depth along the Alpine Fault, which still remains relatively poorly defined, can provide useful insights on better understanding rock strength and kinematics of the crust in the Southern Alps orogen.

Taking advantage of the long duration seismic dataset, we can investigate the spatial and temporal characteristics of the stress regime, using focal mechanism data, in a greater detail than it has been previously afforded. Previous seismicity based tectonic stress studies in the region (e.g. *Balfour et al.*, 2005; *Boese et al.*, 2012; *Warren-Smith et al.*, 2017) have estimated intermediate and high angles of the maximum horizontal compressive stress (σ_1) orientations in relation to the strike of the Alpine Fault, that are not compatible with the Andersonian faulting theory (Byerlee friction and hydrostatic fluid pressure). Similar high angles have been observed along the San Andreas fault (e.g. *Hardebeck and Hauksson*, 1999; *Townend and Zoback*, 2001; *Hardebeck and Michael*, 2004) which led to the suggestion of two end-member fault models (i.e. strong and weak San Andreas Fault). For a strong fault σ_1 should be at an angle of $\sim$30° (*Byerlee*, 1968) and the fault would have large friction coefficients (μ >0.6). While in

the case of a dynamically weak fault σ_1 can be at an angle greater than $\sim$30° and the friction coefficient would be relatively small (μ <0.1). Faulting under conditions described for the weak model would require either high pore fluid pressure or the presence of weak material in the fault zone or a combination of both. A detailed examination of the stress regime in both time and space for the central Southern Alps region will complement and validate the results from previous studies.

This thesis primary objectives can be summarised as below:

1. Construct a spatially and temporally continuous micro-earthquake catalog consisting of accurate phase picks for the central Southern Alps. Using this catalog, examine the spatial seismicity patterns and calculate the seismogenic cutoff depths across and along the strike of the Alpine Fault.

2. Quantify the scale of the active seismicity by deriving a new local magnitude scale for the central Southern Alps, corrected for geometric spreading, attenuation and site terms, which is based on individually calculated GeoNet moment magnitude (M_w) values.

3. Examine the characteristics of the active stress regime by calculating focal mechanisms and seismic moment rates using the newly determined local magnitudes. Investigate the spatial and temporal variations of the stress parameters obtained with stress inversion techniques and focal mechanism data.

4. Model the crustal thermal structure using seismicity and thermochronology data as constraints to obtain exhumation rate estimates in the central Southern Alps.

The outcomes of this research project will provide insight of the seismogenic state of a major fault late in its typical earthquake cycle and will help underpin the hazard evaluation of the Alpine Fault, one of the largest earthquake hazard sources in South Island, New Zealand.

1.2 Alpine Fault

1.2.1 Background

The Alpine Fault is a major continental transform fault that represents the principal tectonic structure outlining the Australian/Pacific plate boundary in the South Island, New Zealand (*Norris and Toy*, 2014). It is clearly observed from satellite images as a distinctive straight line at roughly 055° azimuth that forms the westernmost limit of the Southern Alps orogen. The Southern Alps is a young transpressive orogen that

exhibits high exhumation rates, high erosion rates on its western edge and has no magmatism but high heat flow (Fig. 1.2; *Walcott*, 1998; *Cox and Sutherland*, 2007; *Norris and Toy*, 2014; *Cox and Barrell*, 2007; *Cox et al.*, 2012; *Norris and Cooper*, 2001). Thermochronology age studies in the central Southern Alps yield exhumation rates of up to 8 mm/yr (*Herman et al.*, 2007, 2009; *Little et al.*, 2005; *Tippet and Kamp*, 1993). This region of high exhumation rates is associated with high precipitation and erosion rates (*Koons*, 1990; *Cox et al.*, 2012). These extreme climatic conditions on the western side of the Southern Alps orogen have been suggested to play an important role on the orogen dynamics (*Koons et al.*, 2003). In particular, the extreme erosional conditions erode the upper, stronger part of the crust, making it weaker overall, steepening the isotherms and making the flow of hotter material from the bottom of the crust easier. This continuous interaction between erosion and exhumation increasingly enhances the steepening of the geotherms, increasing heat flow and making the crust weaker (*Zeitler et al.*, 2001; *Koons et al.*, 2003). Thermal models (*Koons*, 1987; *Shi et al.*, 1996; *Cross et al.*, 2015; *Toy et al.*, 2010) infer that high temperatures exist at shallow depths near the Alpine Fault, particularly in a narrow zone of 10−25 km width immediately east of the fault's surface trace. One manifestation of the high heat flow related to these rapidly exhumed rocks is the large number of thermal springs located close to Alpine Fault's surface trace (*Cox et al.*, 2015).

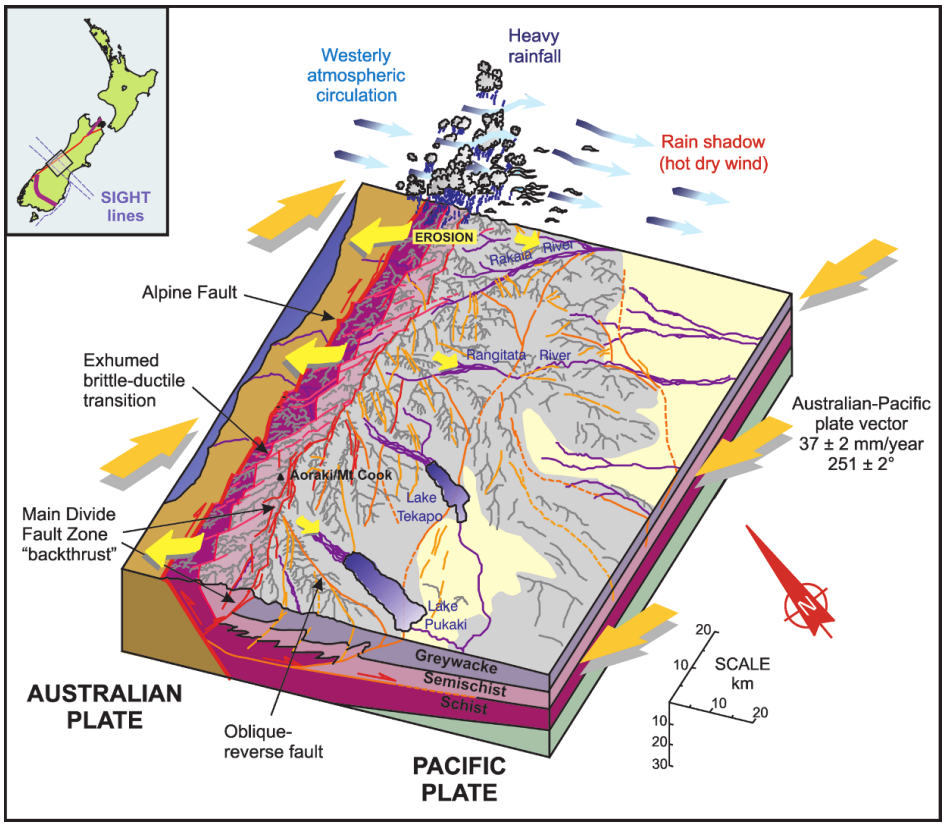

Figure 1.2: Summary of the main features and processes controlling the Southern Alps active orogen. Figure adopted from *Cox and Sutherland* (2007).

The Alpine Fault was first identified by (*Wellman and Willet*, 1942) and comprises, along with the Marlborough faults (MFS), a transition zone that links the west-dipping Hikurangi subduction to the north and the east-dipping Puysegur subduction zone to the south (Fig 1.1). The Alpine Fault is ∼800 km long and, including its continuation to the north, the Wairau fault (*Berryman et al.*, 1992), and thus extends most of the length of the South Island, New Zealand.

Barth et al. (2013) divided the Alpine Fault in five sections with distinctive structural, seismic and geomorphological features (Fig. 1.3). This division of the Alpine Fault is largely after *Berryman et al.* (1992). The northeastern-most section of the Alpine Fault (Wairau; Fig. 1.3), has a length of 200 km, a relatively low strike-slip rate (3−6.7 mm/yr) and close to zero dip-slip rates, (*Zachariasen et al.*, 2006). The Wairau Fault's average strike is 067° and the fault is almost vertical in dip. Background seismicity in this section has been found to be extremely low (*Arabasz and Robinson*, 1976). In the North Westland section (Fig. 1.3) both dextral strike- and dip-slip (SE-side-up) rates increase relative to that in the Wairau section, reaching values of 10−13.6 and 3.4−6 mm/yr, respectively. The average strike and dip of the Alpine Fault here are 055° and 55° to the southeast, respectively. Background seismicity rates are slightly increased relative to the Wairau section but are still generally low in comparison to seismicity rates in the rest of New Zealand (*Bourguignon et al.*, 2015; *Boese et al.*, 2012). The uplifted side is the southeastern part of the fault (hanging wall), which makes up the bulk of the Southern Alps orogen.

In the central section of the Alpine Fault (Central; Fig. 1.3), the average rate of dextral strike-slip is significantly higher than the two aforementioned sections to the north (28 ± 4 mm/yr; *Norris and Cooper*, 2001). The dip-slip rates in this section exhibit the highest values along the length of the Alpine Fault, ranging from 2 to 8 mm/yr (*Norris and Cooper*, 2001). The average strike of the fault is similar to the North Westland section. The Alpine Fault here is inferred to dip eastward at an angle of between 40° and 60° according to surface structural (*Norris and Cooper*, 1997), seismicity (*Guo et al.*, 2017), reflection (*Stern et al.*, 2000) and geodetic data (*Beavan et al.*, 1999). Background seismicity is extremely low and most earthquakes have shallow hypocentral depths (*Boese et al.*, 2012). Around 70% of the current plate boundary deformation is accommodated by a single fault structure, the Alpine Fault (*Norris and Cooper*, 2001). The width of the orogen is less than 80 km (*Little et al.*, 2005; *Cox and Barrell*, 2007).

In the Southern Westland section (Fig. 1.3), strike slip rates stay almost the same as the section in the north (29 ± 3.5 mm/yr), while the dip-slip rates values decrease and approach values close to zero (*Barnes et al.*, 2005). The average strike of the Alpine Fault also remains relatively the same as the two sections in the north. However, the average dip of the fault becomes nearly vertical (82° to the SE). The background seismicity here is relatively high (*Warren-Smith et al.*, 2017b). Another important

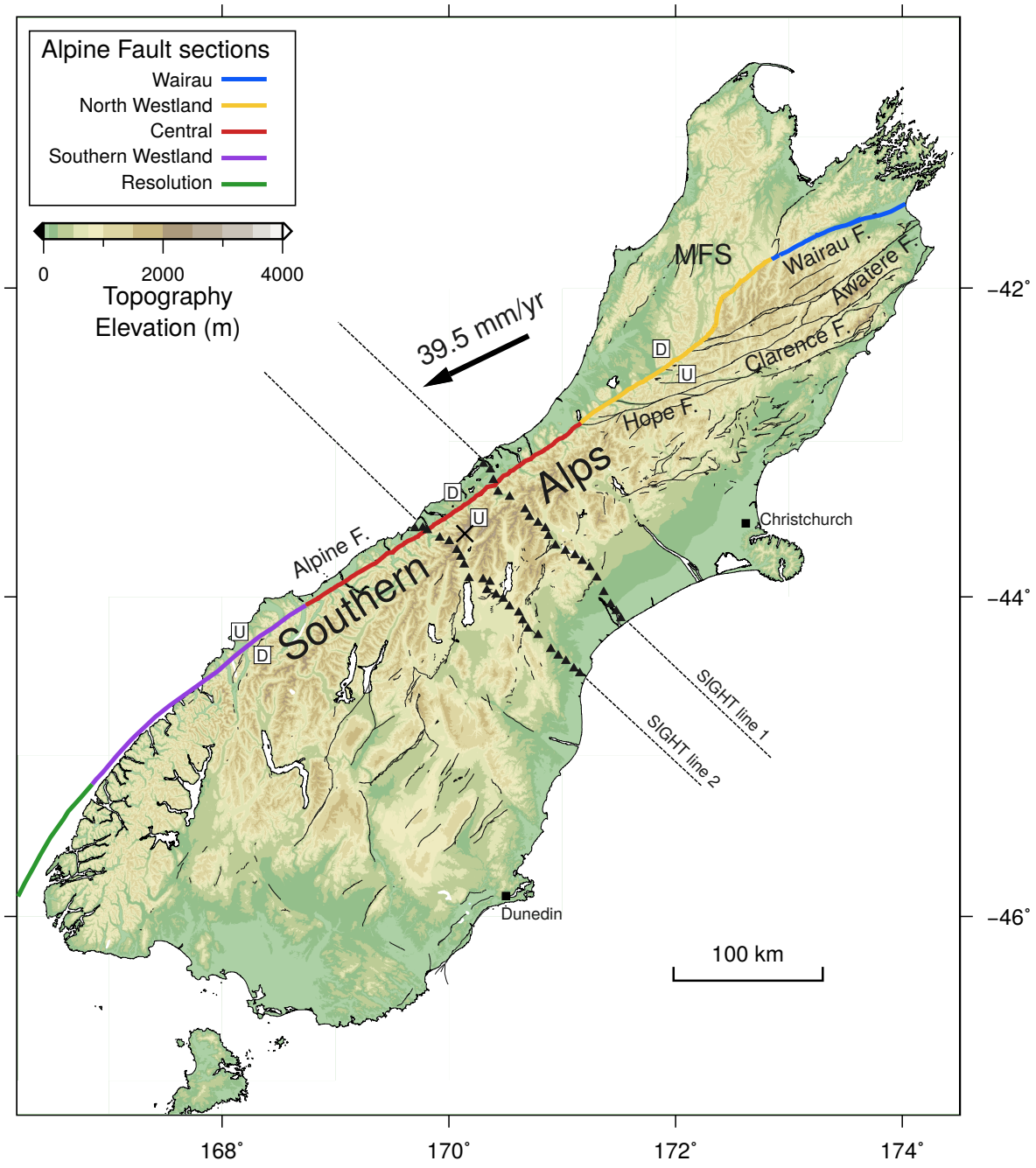

Figure 1.3: Map of the South Island, New Zealand that illustrates the division of the Alpine Fault into five sections according to *Barth et al.* (2013) shown with different colors. Figure adapted from (*Howarth et al.*, 2018). Arrow indicates the local velocity of Pacific Plate relative to Australia (∼39.5 mm/yr in Fox Glacier; *DeMets et al.*, 2010). MFS = Marlborough Fault System. Grey dashed lines depict the two transects of the SIGHT project (*Davey et al.*, 1998; *Okaya et al.*, 2002).

difference compared to the sections to the north is that the uplifted side of the fault is in the northwest side.

In the southwestern-most section (Resolution; Fig. 1.3) the Alpine Fault displays the largest strike-slip rates (31.4 mm/yr) and dip-slip rates are zero within this section. Also, the highest percentage (87%) of the plate boundary motion is concentrated on the

Alpine Fault in this section. The average strike of the fault is rotated approximately 10° counterclockwise relative to the sections to the north (040°). Seismicity here defines a steep Wadati-Benioff zone dipping at around 70° to the southeast extending to depths of at least 150 km (*Warren-Smith et al.*, 2017b).

1.2.2 Regional geology and total displacement

The Alpine Fault separates two different types of basement rocks that were both formed in the Gondwanaland margin, named the Western and Eastern Provinces (Fig. 1.4; *Cox and Sutherland*, 2007). Although both provinces formed in similar tectonic environments, they have undergone very different pre-Cretaceous tectonic processes (*Mortimer*, 2004). The Western Province (Buller Terrane; Fig. 1.4) is located northwest of the surface trace of the Alpine Fault and consists mainly of Paleozoic sedimentary, plutonic and metamorphic rocks. The Eastern Province (Torlesse composite terrane; Fig. 1.4) was southeast of the Alpine Fault and mostly comprises metamorphosed semischists and schists.

In 1949, Wellman argued that the Alpine Fault had accommodated a 480 km, of Cenozoic dextral displacement, based on the offset of Paleozoic-early Mesozoic rocks (Dun Mountain Ophiolite Belt Terrane; *Benson*, 1952). This notion, especially the timing of the displacement, became more generally accepted only after the development of plate tectonic theory. Since then, with the advances in quantifying plate motions, a number of studies have estimated the total displacement that occurred during the Cenozoic (*Sutherland*, 1999; *Lamb et al.*, 2016). *Sutherland* (1999) suggested a total dextral offset of 440−470 km based on the offsets of basement terranes and plate reconstructions. *Lamb et al.* (2016) revised the displacement history of the Alpine Fault and argued for a total Cenozoic strike-slip displacement that is greater than 700 km.

1.2.3 Previous geophysical projects

The Alpine Fault provides a unique opportunity to investigate the lithospheric structure, deformation characteristics, rock properties and geophysical features in a developing orogen (i.e. Southern Alps) before a large potential future earthquake (*Townend et al.*, 2009). Therefore, a number of large multidisciplinary geophysical projects have been undertaken during the last three decades, which we outline below.

The South Island Geophysical Transect (SIGHT) took place in 1996 and 1998 and included two lines (Transect 1 and Transect 2; Fig. 1.3) of active and passive seismic deployments spanned the South Island perpendicular to the strike of the Alpine Fault (*Davey et al.*, 1998; *Okaya et al.*, 2002; *Stern et al.*, 2007). The active seismic explo-

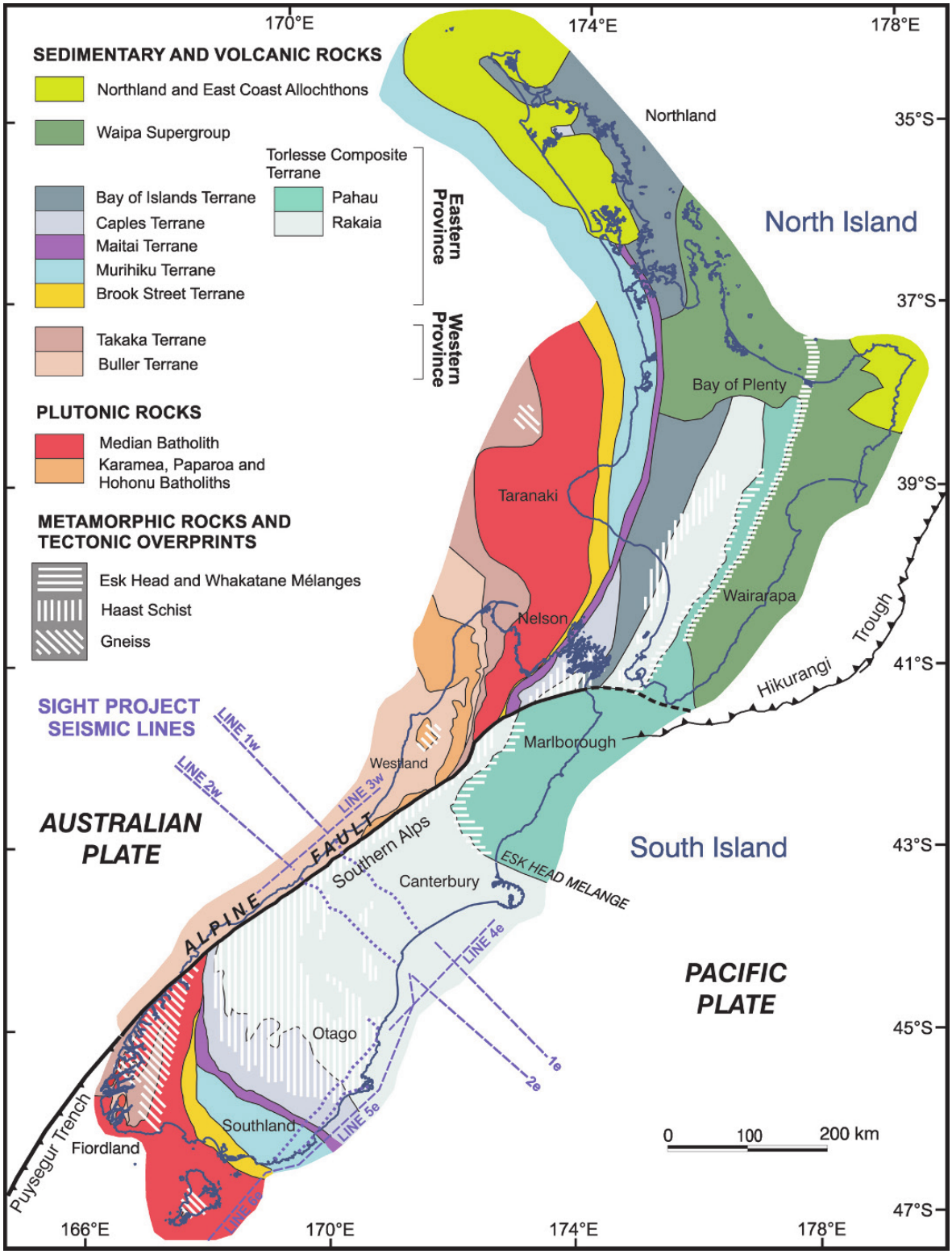

Figure 1.4: Geologic map of New Zealand adopted from *Cox and Sutherland* (2007)

ration provided a detailed overview of the crustal structure in the central Southern Alps. The thickest crust estimated from inversion of reflection-refraction data along Transect 1 is approximately 37 km (*Van Avendonk et al.*, 2004) and approximately 44 km along Transect 2 (*Scherwath et al.*, 2003). *Eberhart-Phillips and Bannister* (2002) compiled a three-dimensional V_p and V_p/V_s velocity model using earthquake and active source

seismic data and imaged the crustal root beneath the Southern Alps. They observed a maximum crustal thickness of 43 km around 80 km south of Aoraki/Mount Cook. The deepest crustal thickness was found east of the area with the highest topography in the central Southern Alps (*Davey et al.*, 1998). Bouguer gravity anomaly measurements suggest the existence of an extensive crustal root of lower-density material (*Bourguignon et al.*, 2007). This material is inferred to have resulted from lithospheric thickening caused by the convergence between the Australian and the Pacific plates and consisting of parts of the middle and lower crust (*Scherwath et al.*, 2003). Seismic reflections beneath the Southern Alps revealed an eastward-dipping Alpine Fault with dip angles varying from 40° to 55°, flattening in the lower crust (*Davey et al.*, 1995). Areas of high conductivity and low velocities were found to coincide with these reflections (*Wannamaker et al.*, 2002; *Stern et al.*, 2007).

The Deep Fault Drilling Project (DFDP) has to date been undertaken in two stages. Its primary goal was to drill a borehole in the plate interface of the central Alpine Fault and examine various geological and geophysical characteristics within the fault structure (*Townend et al.*, 2009) prior to an expected major earthquake (*Sutherland et al.*, 2007; *Howarth et al.*, 2018). DFDP-1 was the first stage and took place at Gaunt Creek, southeast of Whataroa. Two boreholes were drilled (128 and 98 m deep) and fault rocks were sampled from the hanging wall (*Sutherland et al.*, 2012). Various geological and geophysical measurements performed on the borehole cores showed a highly fractured and impermeable fault zone (*Sutherland et al.* (2012); *Townend et al.* (2013) and references therein). Fault zone gouges from DFDP-1 were found to have relatively high coefficients of friction (μ=0.61−0.76) for a range of temperatures and normal stresses (T = 70–350°C, effective normal stresses, $\sigma_n^{'} = 31 - 156\,MPa$; *Boulton et al.*, 2014). A relatively high geothermal gradient of ∼63°C/km was also found (*Sutherland et al.*, 2012).

The second stage of the project, DFDP-2, took place in Whataroa Valley in 2014. The DFDP-2B borehole was drilled to 818 m depth on the hanging wall of the Alpine Fault (*Sutherland et al.*, 2017). This borehole was planned to investigate the temperature, pore fluid pressure and structure of the hanging wall and eventually intersect the Alpine Fault plane at a depth of around 1 km. The borehole did not reach this target depth due to technical difficulties (*Sutherland et al.*, 2015). The borehole measurements and observations revealed an active high-temperature hydrothermal circulation system, high permeability and elevated pore fluid pressure beneath the Whataroa Valley (*Townend et al.*, 2017; *Sutherland et al.*, 2017). In particular, a geothermal gradient of 125±55°C/km and pore fluid pressures 10% above hydrostatic levels were found. Geothermal gradient values exceeding 80°C/km are normally related to volcanic regions, but there is no evidence for any volcanism near Whataroa (*Sutherland et al.*, 2017). This extreme geothermal gradient in Whataroa Valley is interpreted to be

caused by exhumation of hotter rocks from depth and a fluid flow within the fractured rocks that concentrates heat from higher topographic areas into the valleys (*Sutherland et al.*, 2017).

1.2.4 Paleoseismicity

Paleoseismic studies in Westland, South Island, New Zealand have been extremely important in establishing a long record of ruptures and providing crucial information on the earthquake cycle characteristics of the Alpine Fault.

The first paleoseismic study of the Alpine Fault was conducted by *Adams* (1980) who collected radiocarbon dates from landslides and aggradation terranes that coincided in time and were inferred to be related to large earthquakes on the Alpine Fault. *Wells et al.* (1999) combined a number of different techniques (e.g. fault trenches, landslide episodes, radiocarbon dates, tree-ring growth anomalies) and provided evidence for three Alpine Fault paleoearthquakes occurring at approximately 1717, 1630 and 1460 CE. *Sutherland et al.* (2007) compiled evidence on the three most recent large earthquakes and estimated moment magnitudes of M_w 7.8−8.0. They suggested that large earthquakes of $M_w \geq$7.0 will almost certainly occur in the future, including a realistic chance for large, $M_w \geq$8.0 earthquakes on the Alpine Fault (*Sutherland et al.*, 2007).

More recent paleoseismic studies, summarised in *Howarth et al.* (2018), have created a remarkably long and continuous Alpine Fault earthquake record. This record indicates that the Alpine Fault produces large magnitude (M7−8) earthquakes every 291 ±23 years (*Berryman et al.*, 2012; *Cochran et al.*, 2017; *Howarth et al.*, 2016) with the last major earthquake occurring in 1717 CE. The distribution of the paleoearthquakes in time and space is summarised in Fig. 1.5, which highlights the characteristics of the paleoearthquakes in three sections of the Alpine Fault (i.e. South Westland, Central and North Westland sections). The most recent paleoearthquake 1717 A.D. have ruptured all the Alpine Fault sections. However, the preceding ruptures have both single and multi-section ruptures that, in combination with the large data gaps mainly in the North Westland section, make it difficult to suggest any strong temporal pattern of which segments of the Alpine Fault rupture (*Howarth et al.*, 2018).

The periodicity of the paleoearthquake occurrence on the Alpine Fault is remarkable when compared with the seismic records of other major strike slip faults (*Berryman et al.*, 2012). These data suggest that the Alpine Fault has a ∼30% chance in the next 50 years of failing in a large (M7−8) earthquake (*Cochran et al.*, 2017; *Biasi et al.*, 2015; *Howarth et al.*, 2018), posing one of the largest earthquake hazard threats to Southern New Zealand.

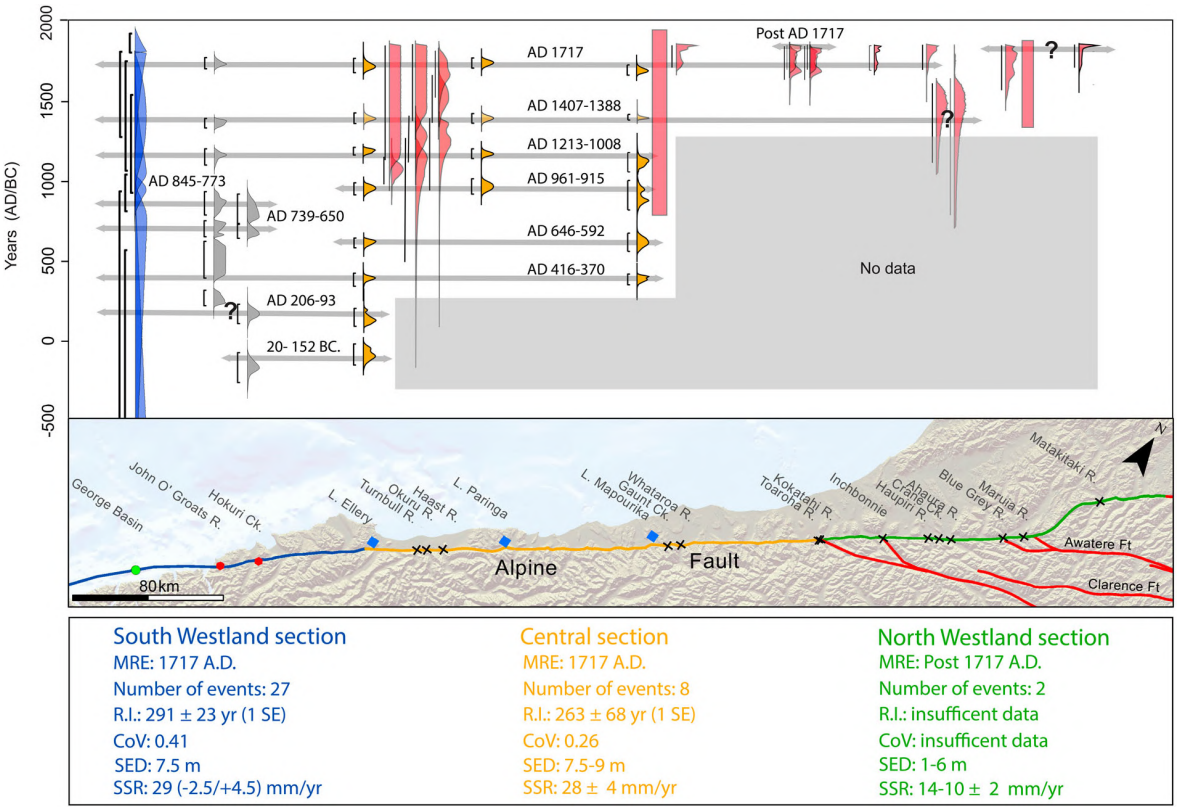

Figure 1.5: Diagram adopted from *Howarth et al.* (2018) that summarises all the available paleoearthquake data of the Alpine Fault in space and time. Probability density functions with time are colored according to the paleoseismic techniques used (e.g. on-fault records with red, lake deposits near the fault with yellow, observations made in wetland records with grey and marine turbidite results with blue). MRE = most recent earthquake; R.I. = recurrence intervals; CoV = coefficient of variation; SED = single event displacements; SSR = strike-slip rates

1.2.5 Seismicity

Seismic activity near the central section of the Alpine Fault mostly occurs within the crust of hypocentral depths of less than 30 km (*Evison*, 1971; *Eiby*, 1971; *Scholz et al.*, 1973; *Boese et al.*, 2012; *Bourguignon et al.*, 2015; *O'Keefe*, 2008; *Feenstra et al.*, 2016; *Guo et al.*, 2017). A relatively small number of deeper earthquakes (subcrustal; 30−120 km hypocentral depths) take place in the upper-mantle (*Reyners*, 1987; *Boese et al.*, 2013, 2018). Apart from the microseismicity studies mentioned above, a number of studies have also examined other seismic phenomena, such as seismic tremor (*Wech et al.*, 2012, 2013) and low-frequency earthquakes (*Chamberlain et al.*, 2014; *Baratin et al.*, 2018). Figure 1.6 shows the variations of depth distribution of the seismic activity across Southern and Central New Zealand. Intermediate depth earthquakes (70−300 km depth) are frequent in the north and south of the South Island and delineate the Hikurangi and Puysegur subduction zones, while they are less frequent in the central South Island.

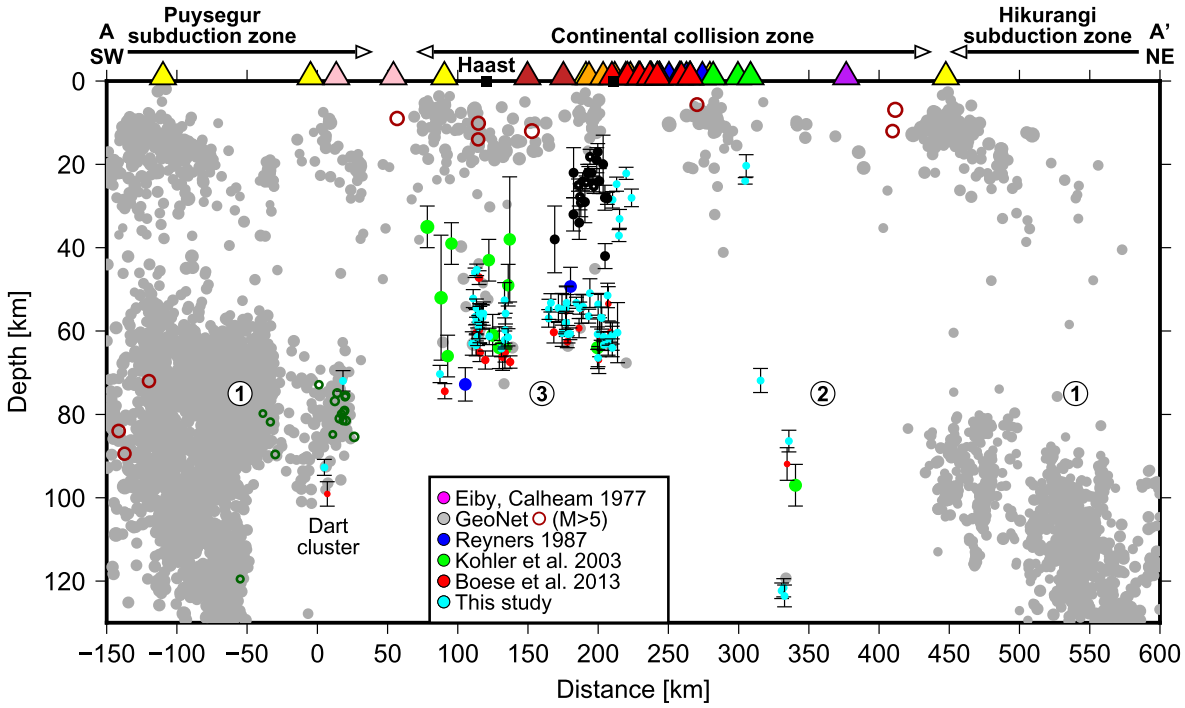

Figure 1.6: Cross-section of the seismicity along the length of the Alpine Fault adapted from (*Boese et al.*, 2018, "This study"). Grey circles depict the M≥5 earthquakes recorded from GeoNet, while the red open circles show the earthquakes for which focal mechanisms were calculated. Blue, green, red and cyan full circles represent the subcrustal earthquakes located by *Reyners* (1987), *Kohler and Eberhart-Phillips* (2003), *Boese et al.* (2013) and *Boese et al.* (2018), respectively. Black circles display the locations of the low frequency earthquakes from *Chamberlain et al.* (2014) and *Baratin et al.* (2018). Triangles on top of the cross-section show the locations of the different seismic networks used by *Boese et al.* (2018).

The initial identification of anomalously low levels of seismic activity in the central South Island relative to the rest of New Zealand was made by (*Eiby*, 1971; *Evison*, 1971). Since then, numerous researchers have examined this seismic gap in the central Southern Alps region further. One of the first microseismicity studies in the area was carried out by *Scholz et al.* (1973) and *Caldwell and Frohlich* (1975) and showed a diffuse distribution of epicenters with no clear association to major faults.

More recent studies (*Reyners*, 1987; *Leitner and Eberhart-Phillips*, 2001; *O'Keefe*, 2008; *Boese et al.*, 2012; *Bourguignon et al.*, 2015; *Warren-Smith et al.*, 2017b) have examined the low seismic activity along the Alpine Fault in great detail (Fig. 1.7). The results from these previous microseismicity studies are presented in Chapter 3 (Section 3.2.2).

1.3 Thesis content and publications

Chapter 1 has outlined the background information related to the seismotectonic properties of the central Southern Alps region.

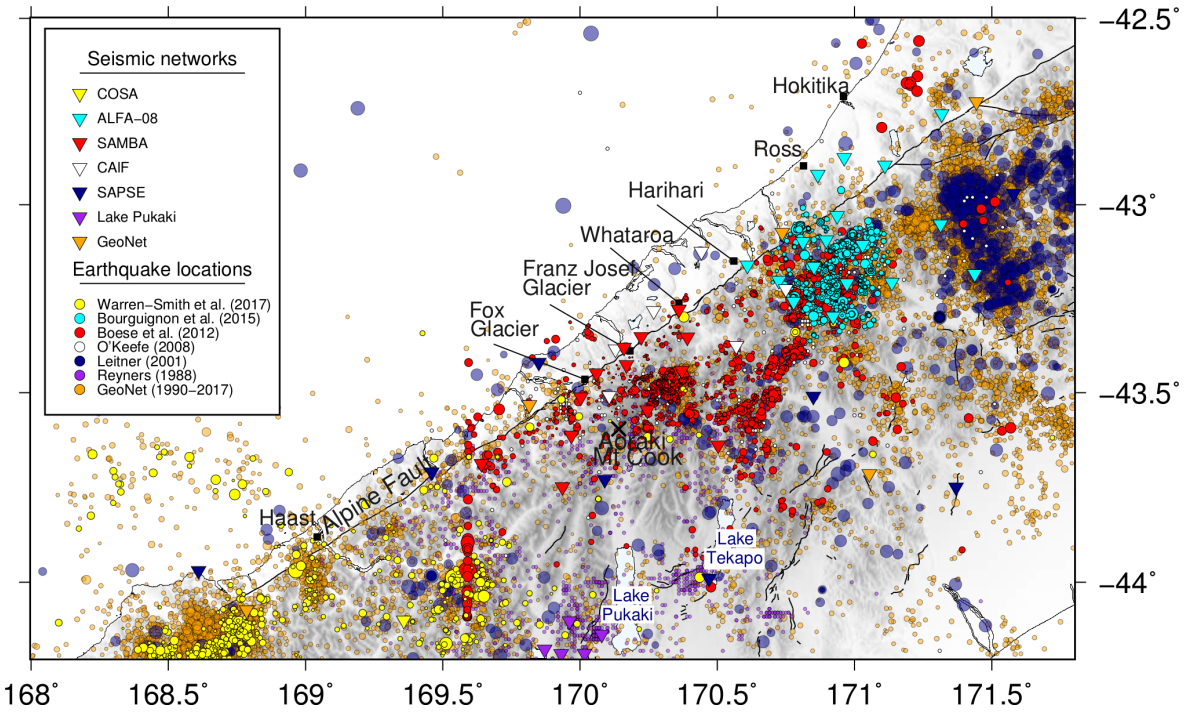

Figure 1.7: Regional and local seismicity near the central Alpine Fault since 1990 recorded by GeoNet is shown in the background (orange circles). Local microseismicity earthquake locations from (*Reyners*, 1987) purple; (*Leitner and Eberhart-Phillips*, 2001) dark blue; (*O'Keefe*, 2008) white; (*Boese et al.*, 2012) red; (*Bourguignon et al.*, 2015) cyan and (*Warren-Smith et al.*, 2017b) yellow; are also shown. Seismic sites are plotted in equivalent colors to the respective earthquake catalogs.

Chapter 2 provides a summary of the SAMBA network and the other seismic networks from which data have been used in the present study. There is also a description of all the processing and methods applied to the data as well as their theoretical background.

Chapter 3 addresses the construction of a new microseismicity earthquake catalog and the characteristics of the seismic activity in the central Southern Alps, New Zealand. These findings have been published in *Geochemistry, Geophysics, Geosystems*; publication (*Michailos et al.*, 2019). Magnitude calculations were carried out with the guidance and MATLAB coding assistance of Euan Smith. Calum Chamberlain contributed significantly within the framework of this chapter. Some of the material from this chapter might be repeated elsewhere to keep the continuity of the thesis structure.

Chapter 4 concerns the tectonic stress regime in the central Southern Alps, calculated using focal mechanism data. It outlines the generation of focal mechanisms and the calculation of stress parameters as well as an examination of their temporal and spatial variations. Emily Warren-Smith provided comments and advice as a coauthor in this manuscript. This chapter has resulted in a manuscript under review to the journal *Tectonophysics*.

Chapter 5 discusses the results on the thermal structure of the crust and exhumation estimates near the central Alpine Fault using seismicity and thermochronology data.

Modeling within this chapter was performed with the help of Rupert Sutherland.

Chapter 6 provides a synthesis of the thesis' key findings and their significance and implications, as well as suggestions for future work.

Chapters 3, 4, and 5 are individual projects and have been written in a form suitable for publications with their own abstracts, introductions, methodologies and conclusions. These chapter are written in the first person plural ("we"), as this constitutes a common practice for publications including more than one author. The work in these projects has been undertaken by the author of this thesis (Konstantinos Michailos), under the supervision of John Townend and Martha Savage, unless stated otherwise.

During the course of my PhD, I also contributed to two more projects that resulted in publications:

- Boese, C.M., Stern, T.A., **Michailos, K.**, Townend, J., and Chamberlain, C.J., 2018. Implications of upper-mantle seismicity for deformation in the continental collision zone beneath the Alpine Fault. *New Zealand Journal of Geology and Geophysics*: 1-26, doi: https://doi.org/10.1080/00288306.2018.1509357.

- Chamberlain, C.J., Hopp, C.J., Boese, C.M., Warren-Smith, E., Chambers, D., Chu, S.X., **Michailos, K.**, and Townend, J., 2017. EQcorrscan: repeating and near-repeating earthquake detection and analysis in Python. *Seismological Research Letters*, doi: 10.1785/0220170151.

2 Data and Research Methods

The Chapter below consists of two main sections. The first presents details of the seismic networks from which data have been used. The second outlines the methods used during each of the processing steps undertaken. In addition, a brief description of the theoretical background behind each of these methods is given.

2.1 Seismic networks and data

The seismic networks used in this thesis are described in this section. The Southern Alps Micro-earthquake Borehole Array (hereafter referred to as the SAMBA network) comprises 10 borehole sites established in late 2008 (red inverted triangles in Fig. 2.1; *Boese et al.*, 2012) and three additional surface sensors from early 2013 (red triangles in Fig. 2.1; *Baratin et al.*, 2018). The SAMBA network remains operational and was deployed in order to augment the three regional GeoNet sites FOZ, WVZ and RPZ (Fig. 2.1) to better detect the microseismicity within a previously identified seismic gap near the central Alpine Fault (*Leitner and Eberhart-Phillips*, 2001; *Boese et al.*, 2012; *O'Keefe*, 2008).

To expand the region of high station density, we also use data from four other temporary seismic networks (WIZARD, DFDP-10, DFDP-13 and ALFA-08) that operated at various times and that overlapped in time with the SAMBA network (Fig. 2.1). The Wisconsin New Zealand Array Regional Deployment (WIZARD) network comprised 10 short period sensors and 10 broadband sensors (*Thurber et al.*, 2012; *Feenstra et al.*, 2016; *Guo et al.*, 2017), and was deployed in the area northeast of the SAMBA network (purple inverted triangles in Fig. 2.1). The Alpine Fault Array (ALFA-08) comprised eight seismometers covering the area between Harihari and Hokitika (cyan inverted triangles in Fig. 2.1; *Bourguignon et al.*, 2015). DFDP-10 was part of the first phase of the Deep Fault Drilling Project (DFDP-1; *Sutherland et al.*, 2012): it consisted of 12 short-period seismometers and was installed to help detect the background seismicity near the central Alpine Fault in anticipation of the drilling efforts in Gaunt Creek (yellow triangles in Fig. 2.1). The DFDP-13 network includes four shallow borehole (28 m) seismometers that were installed near the DFDP-2 (*Sutherland et al.*, 2017) drilling site in the Whataroa Valley (blue inverted triangles in Fig. 2.1). These sites

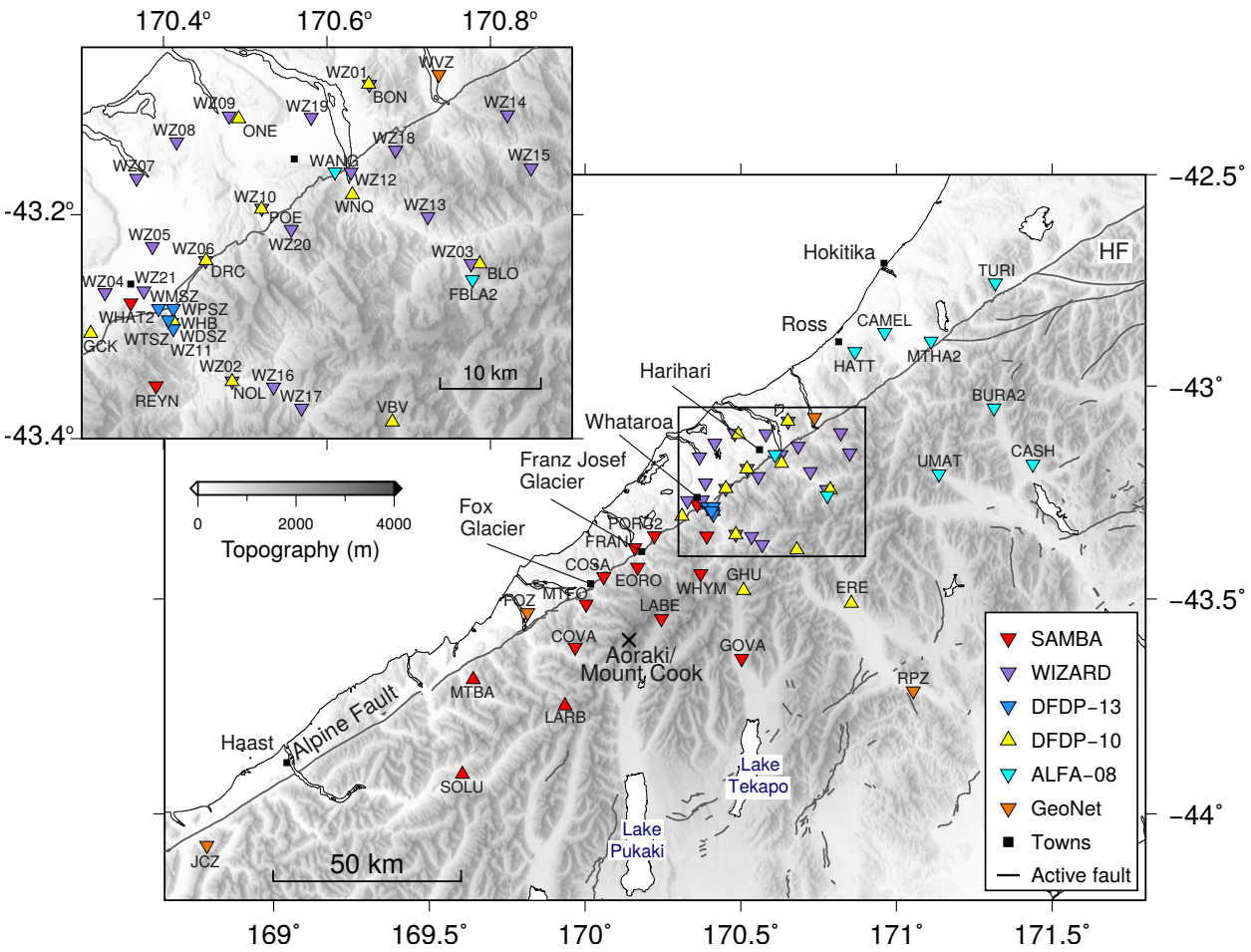

Figure 2.1: Map showing the distribution of the seismic sites, with the site's code names, used in this study. SAMBA seismic sites are marked by red inverted triangles (red triangles represent the three southern sites that were installed in 2013). Cyan, purple, blue and orange inverted triangles depict the ALFA-08, WIZARD, DFDP-13 and GeoNet networks. Yellow triangles indicate the DFDP-10 seismic network. Black squares show the major West Coast townships. Inset shows an expanded view of the region marked by a box. Grey thick lines represent the active faults from the New Zealand Active Faults Database (*http://data.gns.cri.nz/af/*). HF is the Hope Fault.

were deployed to detect seismicity related to the second phase of the DFDP project (*Chamberlain et al.*, 2017a).

The aforementioned temporary seismic networks complemented the five nearby GeoNet seismic sites (FOZ, WVZ, RPZ, LBZ and JCZ) that are part of the New Zealand national network and have been operating continuously since 1990 (orange inverted triangles in Fig. 2.1). Figure 2.1 depicts the distribution of the stations of each seismic network referred in this thesis. Further details of each network are given in Tables A.1–A.6 of Appendix A. The data continuity of each seismic site is shown shown in Appendix B.

2.2 Data acquisition and processing

Raw waveform data from SAMBA and DFDP-13 seismic networks were collected during servicing field trips that took place every six months, typically in May and September. The data were recorded by RefTek RT-130 digitizers, which store the recorded data on compact flash (cf) cards in 15 minute or hour-long files in a proprietary compression format based on miniSEED Steim2. During servicing, the cf cards are swapped and the raw data from the RT-130 cf cards are then backed up. At the same time quality tests are made to the control logs (using the *logpeek* IRIS software) and the waveform data (using the *pql* IRIS software). Next the data are converted to day-long single-channel miniSEED files using the *rt_mseed* Reftek tool. The SAMBA data from early 2015 to late 2018 have been archived at the Incorporated Research Institutions for Seismology Data Management Center (IRIS–DMC) under the network code 9F[1].

The waveform data from the rest of the temporary seismic networks (WIZARD, DFDP-10, ALFA-08, DFDP-13) were downloaded directly in MiniSEED format from the IRIS–DMC using the following network codes: WIZARD, ZT; DFDP-10, XO; DFDP-13, 6F; and ALFA-08, YR. Data from the GeoNet sites were downloaded from GeoNet's web services. All the waveform data were converted into the same format, namely single channel day-long MiniSEED files, using Python routines primarily from the ObsPy package (*Beyreuther et al.*, 2010; *Krischer et al.*, 2015).

For the routine processing of the earthquake data, picking of manual P and S phases, and P wave first motion polarities, the SEISAN earthquake analysis software (*Havskov and Ottemoller*, 2008) was used. SEISAN is a freely available software package that provides the essential tools for basic processing of earthquake data (i.e. earthquake location, magnitude, source parameters and focal mechanisms). Earthquake event information is stored in SEISAN Nordic format files. For detecting seismic signals, we use a standard energy-based detection algorithm, described in the following Section.

2.3 Earthquake detection methods

The detection of seismic signals (e.g. earthquakes, seismic tremor, low frequency earthquakes, etc.) constitutes one of the first steps in most seismological studies. There are many methods for detecting earthquakes (e.g. energy based, the cross-correlation based). Each method has advantages, disadvantages and limitations when used for various seismological tasks.

Traditional energy-based methods (e.g. STA/LTA algorithms; *Allen*, 1978) are based on

[1] `https://doi.org/10.7914/SN/9F_2008`

observing changes in seismic amplitude. Such methods do not require any prior event information and are fast and simple to implement across large volumes of continuous waveform data. However, these energy-based algorithms can produce a large number of false detections, especially if the waveform data are noisy. Methods dependent on amplitude variations are not ideal for detecting small earthquakes occurring in the coda of larger earthquakes, or when events are close in time.

Correlation based detection methods, on the other hand, generally require prior information (e.g. P and S time arrivals) and are more computationally expensive than STA/LTA. These methods use a known signal as a template and look within the continuous seismic data for similar waveforms (e.g. *Gibbons and Ringdal*, 2006). Matched-filter detection is recognised to be very effective in detecting repeating or near-repeating seismicity (e.g. *Schaff and Richards*, 2011; *Gibbons and Ringdal*, 2006; *Chamberlain et al.*, 2017c). This method has been applied to a number of seismological tasks including the detection of repeating seismicity (e.g. *Frank et al.*, 2016; *Beaucé et al.*, 2017), low frequency earthquakes (e.g. *Chamberlain et al.*, 2014; *Baratin et al.*, 2018; *Shelly*, 2017) and aftershock sequences (e.g. *Yao et al.*, 2017; *Warren-Smith et al.*, 2017).

To create a new earthquake catalog for the central Southern Alps that encompasses almost a decade of seismicity, we considered two approaches. The first consisted of using the earthquake locations of the previously constructed earthquake catalogs (*Boese et al.*, 2012; *Bourguignon et al.*, 2015; *O'Keefe*, 2008) as templates and the matched-filter detection method to look for near-repeating seismicity. The second approach consisted of using an energy-based detection method to detect as many new earthquakes as possible.

The main goal of this study is to obtain a complete and representative picture of seismicity spanning over a range of spatial and temporal scales and to robustly examine the characteristics of the seismicity throughout the central Southern Alps region. We therefore followed the latter approach and built a catalog using the standard energy-based detection method. We chose to use this method rather than a cross-correlation method because the matched-filter detection inherently only detects events similar to those previously observed. Moreover, the previous earthquake catalogs, which could have formed a template database, each covered only a year of the almost decade-long dataset available here. For that reason, an earthquake catalog created using the cross-correlation method would most likely not fully represent the temporal variations of seismicity.

The data used in the thesis are derived from five temporary or semi-permanent deployments, including sites with highly variable noise conditions. To cope with this and to efficiently and homogeneously detect earthquakes throughout the eight years of

the dataset, a number of Python function were written and are distributed as part of EQcorrscan; (*Chamberlain et al.*, 2017c). These codes allow different triggering parameters to be applied to each seismic site based on its noise characteristics. In testing, we found that using station specific parameters reduced the likelihood of false triggers.

The energy-based detection method implemented here is derived from the detection algorithm proposed by *Allen* (1978). The routine works in the following way: firstly, it scans the waveforms in two different moving time windows: a short-time average (STA) window, which is designed to be sensitive to energy released by earthquakes, and a long-time average (LTA) window that is set to be dominated by the average seismic noise at the site. The STA/LTA ratio (characteristic function) is calculated for the vertical channels of each seismic site. These values are then compared to thresholds (e.g. trigger-on/-off thresholds) specified for each seismic site individually. The trigger on threshold controls the amount of events that will be recorded. A relatively high or low value will respectively record fewer or more earthquakes. When the characteristic function's value exceeds the threshold set, a single trigger is created. These calculations are repeated for all the available seismic sites and a list of all the single-triggers is compiled. Finally, the single-trigger times from each seismic site are compared to each other and if they overlap at four or more stations within a 60-second window, an event detection is made.

The principal advantage of the detection method created here when compared to commonly used STA/LTA network trigger routines is that it allows the user to set a number of operational parameters (e.g. STA and LTA values, triggering thresholds, band-pass filters) individually for each seismic site. In this way, we are able to adjust and optimise the performance of the routine for each seismic site according to the noise conditions of each site. For example, we observed that for a seismic site in a noisy environment we should have a higher value of trigger-on threshold and a higher value of the LTA parameter compared to a seismic site in a quiet environment. As a consequence of using different threshold values for each station, the triggers are more likely to be earthquake signals, and fewer false triggers are expected to occur. In our case, we took advantage of existing earthquake catalogs by manually adapting our parameters to identify small-magnitude earthquakes already catalogued by *Boese et al.* (2012). Details of the parameters used for the triggering algorithm are provided in Tables B.2 and B.3 of the Appendices. Fig. 2.2 shows an example of an earthquake detected by two SAMBA stations (WHYM and GOVA) on 3 of March 2009 using the STA/LTA network triggering routine.

Despite the advantages of the network triggering routine outlined above, there are also issues related to the creation of a large number of false triggers, caused by noise signals in the continuous waveforms. A frequent noise signal observed during the daytime at specific seismic sites (e.g. POCR2 site from SAMBA network) was found to be caused

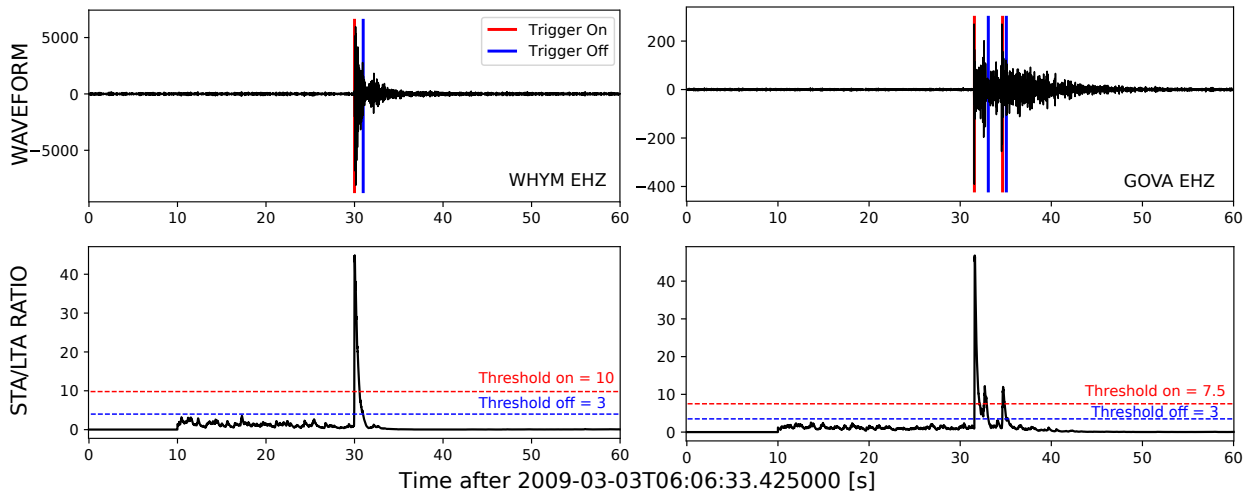

Figure 2.2: Earthquake recorded and detected at two SAMBA seismic sites (WHYM and GOVA) using the STA/LTA network triggering routine. The upper box shows the continuous waveform data of the vertical component bandpassed and sampled at 200 Hz. Red and blue vertical lines indicate the trigger on and off, respectively. The lower box shows the STA/LTA ratio or characteristic function of the seismic signal above. Red horizontal dashed lines show the trigger on threshold, while the blue horizontal dashed lines show the trigger off threshold.

by solar charge controllers used to regulate solar panel and battery power (*Boese*, 2012; *Chamberlain*, 2016). An example of a waveform contaminated by the solar controller-induced spikes is shown in Fig. 2.3. To overcome this, we applied a despiking function (distributed in EQcorrscan) before applying the network triggering routine.

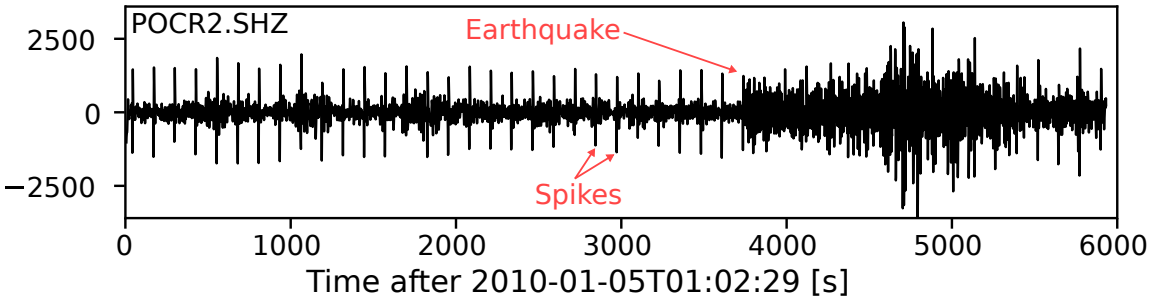

Figure 2.3: Example of seismic data from SAMBA site POCR2 contaminated with solar controller induced noise signals "spikes".

2.4 Identification of P and S wave arrivals

The correct estimation of P and S phase arrival onsets is the backbone of every earthquake catalog and has a significant contribution to the quality of an earthquake catalog (e.g. *Woessner et al.*, 2010). P and S wave arrivals can be determined either by manual

picking or by automatic picking algorithms.

Manual picking can be impractical due to the large volume of seismic data available (a decade of continuous waveform data in our case). In addition, manual picks are subjective and contain human errors due to the different picking behaviours of each analyst (e.g. inconsistent use of filters or misidentification of wave phases), which can lead to inconsistencies in phase picks (*Douglas*, 1997; *Scherbaum*, 2013). Such inconsistencies can be reduced by following some strategies for manual phase picking (e.g. *Scherbaum*, 2013; *Diehl et al.*, 2009).

Automatic phase pickers are fast, consistent and can be applied efficiently to large data-sets (*Vassallo et al.*, 2012). However, the quality of picks obtained by automatic pickers can vary significantly and distinguishing the "bad" picks from the "good" ones can be challenging. Therefore, the choice of which of the two methods for the P and S wave arrivals estimations is determined by the unique needs and goals of each seismic study. Here, the data-set spans almost a decade of continuous data, making manual picking impractical. We have opted to use an automatic picker to determine preliminary P and S wave arrivals that we later inspect and evaluate manually.

During the last several decades many different approaches for automatic picking of wave phase arrivals (i.e. P and S phase wave arrivals) have been developed. *Allen* (1978) published an energy-based autopicker algorithm that defines possible picks by comparing the short (STA) and the long-term (LTA) properties of the seismic signal. *Leonard and Kennett* (1999) developed an autoregressive algorithm that scans the continuous waveform data and calculates the variations of specific statistical properties of the seismic signals, in order to separate these signals from the noise and define possible picks. Other autopicking algorithms use wave polarization analysis (*Cichowicz*, 1993; *Baillard et al.*, 2014; *Ross and Ben-Zion*, 2014) to separate the energy originating from specific phases and thus determine possible picks. There are also hybrid algorithms that use a combination of the aforementioned techniques (*Sleeman and Eck*, 1999; *Diehl et al.*, 2009).

The automatic pickers mentioned above can provide good and robust results. However, most of them are very complex and difficult to generate good results because they have a large number of parameters to set. Taking that into consideration, we chose to use a simpler, but demonstrably accurate, autopicking algorithm developed by *Rawles and Thurber* (2015). This algorithm is based on the method for classifying time series developed by *Nikolov* (2012). The algorithm uses a number of reference waveforms that contain P and S wave phase signals to identify phase onsets in the input waveforms. To do that the routine scans the input waveforms in a defined moving window and calculates a score function of similarity to the sum of the reference picks. Phase picks are declared at the position of the local maximuma of the score function. An example

of automatic P and S wave phase picks made using kpick is shown in Fig. 2.4.

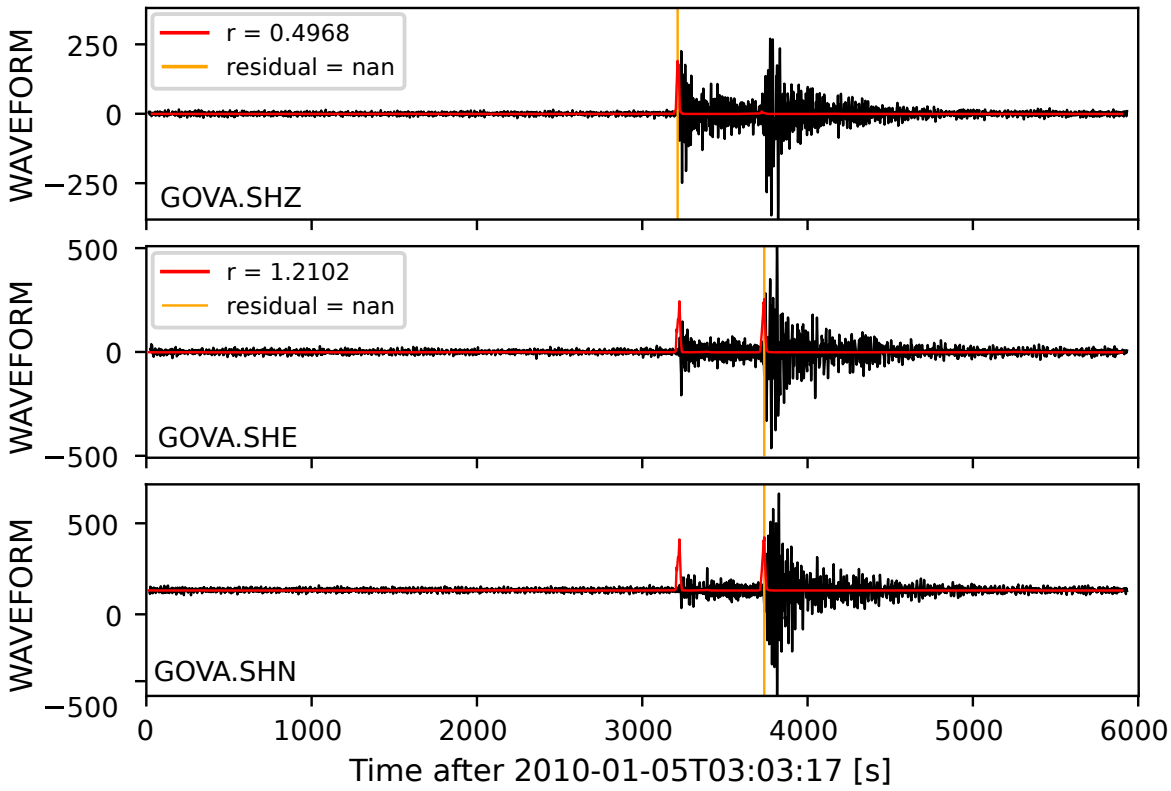

Figure 2.4: Bandpass-filtered waveforms from SAMBA seismic site COSA, that show the seismic signal of an earthquake of magnitude M_L=1.04 that occurred on the 5th of January 2010. Yellow vertical lines indicate the P and S wave phase arrivals determined using the automatic picking algorithm kpick (*Rawles and Thurber*, 2015). Red lines show the quantity of the score function of similarity to the sum of the reference picks.

A check is performed by the kpick algorithm to identify and remove any erroneous automatic picks. This is carried out using a Wadati diagram (Fig. 2.5) that shows the difference between automatic S and P picks versus automatic P pick and a L1-norm fit line. Using this L1-norm fit the outliers (erroneous picks) can be easily identified (Fig. 2.5).

2.5 Automatic preliminary earthquake locations

We calculate preliminary hypocenter locations using the HYPOCENTER location algorithm (*Lienert et al.*, 1986) incorporated in the SEISAN analysis software (*Havskov and Ottemoller*, 2008). This preliminary location process is carried out in an iterative manner whereby we use the output from the kpick algorithm (a number of P and S phase picks associated with each trigger) to obtain an estimate of the earthquake hypocenter. We remove the picks with the highest residuals at each iteration until the following quality criteria are met: 1) minimum number of four P wave picks, 2) mini-

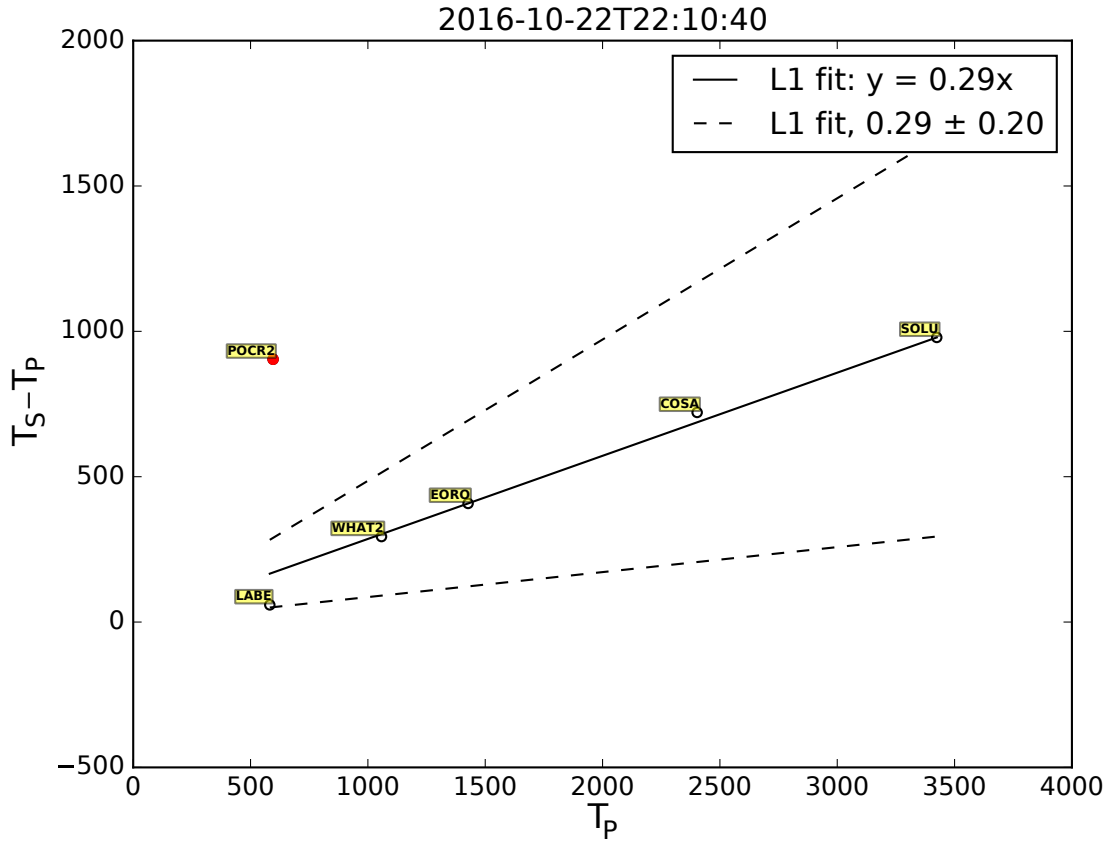

Figure 2.5: Wadati diagram with a L1-norm fit line (solid line) used by the automatic picking algorithm kpick (*Rawles and Thurber*, 2015) to identify erroneous picks and remove them from the analysis. Outliers (red circles) are considered the points that fall outside of the lines with slope ±0.20 (dashed lines). These outliers are not kept by the automatic picker in the final output.

mum number of three S wave picks and 3) a maximum permissible root-mean-square (rms) travel time residual of one second. As part of the final routine processing in the estimation of the P and S wave phase time arrivals, these automatic preliminary earthquake locations were manually inspected and erroneous picks were removed and replaced with manual ones. We do so this because we found it to be more efficient to manually inspect these autolocated potential earthquakes rather than to inspect every single automatic pick.

2.6 Quality assessment of automatic P and S phases

Before applying the triggering and picking processing steps described in the previous sections to the complete dataset, we assessed the accuracy of the automatic picker and the performance of the automatic detection-location method applied here. To achieve this, we ran our automatic detection-location-picking process using the same seismic data as in the previously compiled catalog of *Boese et al.* (2012).

Boese et al. (2012) manually located 2,182 earthquakes that occurred between late 2008 and the end of 2009. Using the automated process described above, not including the final manual inspection of the preliminary earthquake locations, we obtained 828 automatic earthquake locations. The difference in numbers between the two data-sets is attributed to the different approaches applied during the initial data processing (i.e. STA/LTA algorithm, manual inspection of all triggers looking for earthquakes compared to automatic determination of earthquakes and manual versus automatic picks). Manual inspection of all the available triggers would provide us with more earthquakes, however such a process, as described above, would be extremely time-consuming in our case due to the size of the data-set (almost 10 years of continuous waveform data).

From the 828 events located during this test, 653 were the same as the earthquakes in the *Boese et al.* (2012) catalog (allowing up to a five second difference in the origin times and up to three seconds difference in the phase pick arrival times). We first compared the origin times of automatic versus manual for all determined phases of the common events. Figure 2.6 shows the automatic versus manual origin time differences plotted against the magnitudes of the common events *Boese et al.* (Magnitudes from 2012). The mean difference in origin times is equal to −0.062. The distribution of the data is symmetrical with a standard deviation of less than one second, suggesting that automatic origin times are in good agreement with the manual ones (Fig. 2.6). In addition, the earthquake origin time differences behave consistently throughout the entire magnitude range examined, without showing any dependence on magnitude.

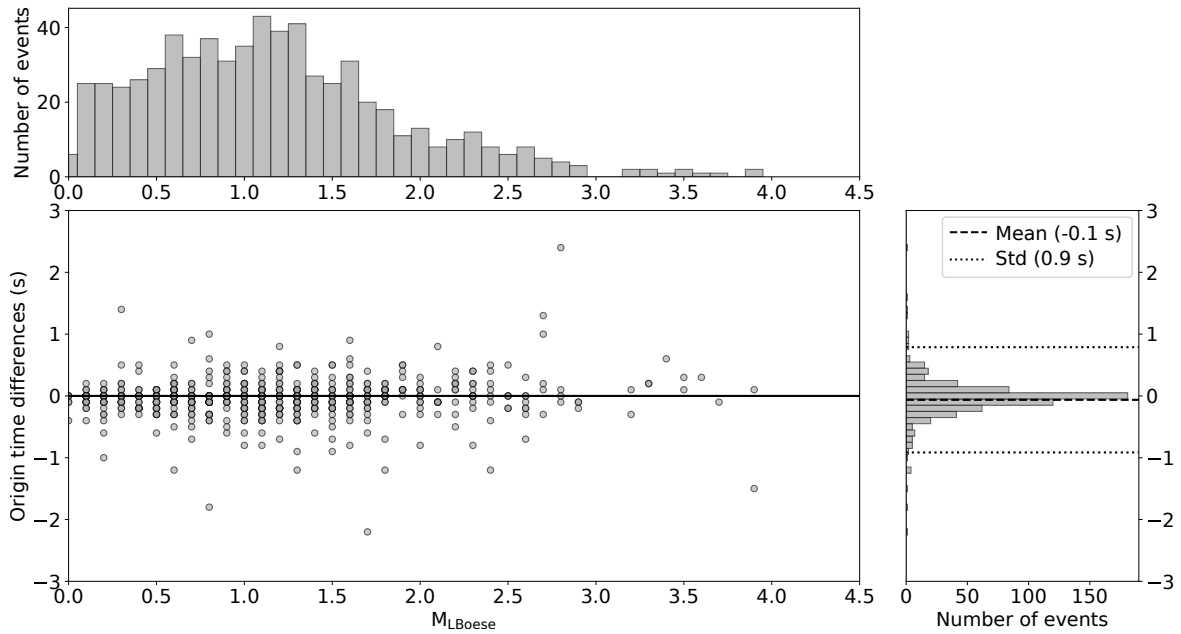

Figure 2.6: Automatic versus manual earthquake origin times for earthquakes recorded by SAMBA and GeoNet stations between November 2008 and December 2009. Histograms are shown at the side edges.

Next, we compared the time differences between automatic and manual P and S phase pick arrivals (Fig. 3.2 in Chapter 3). Overall, the 4,175 P phase picks yield a mean time difference of -0.003 seconds and a median of 0.01 seconds. Overall, 96% of the data show absolute differences of less than 0.2 seconds. The distribution is slightly skewed towards negative values, which indicates a small discrepancy between automatic and manual picks. This means that the automatic P picks (this study) tend to be slightly earlier than the manual ones, especially for smaller magnitudes. In contrast, the 3,139 S phase picks have a mean difference of 0.03 seconds and a median of 0.01 seconds. Almost 90% of the data-set exhibits absolute values of less than 0.2 seconds. The distribution is generally uniform and shows a small trend towards positive values (automatic S phase picks are slightly later than manual picks).

Having estimated the preliminary automatic earthquake locations, we also examine the hypocentral depths between the 653 common events recorded and located by *Boese et al.* (2012) and in this study. Fig. 2.7 shows the map view of the epicenters of the two data-sets connected with yellow lines. The mean differences in latitude, longitude and depth are 0.181, -0.141 and -0.47 km, respectively (Fig. 2.8). In summary, this comparison between manual and automatic picks reveals that the automatic picker used here provides us with high quality data.

2.7 Earthquake location methods

The calculation of earthquake locations (latitude, longitude, depth, origin time) is fundamental for studying seismic activity, mapping active faults, estimating the seismic hazard of a region and for any seismological consideration. The accuracy of the earthquake location is controlled by several factors including the network geometry, the available P and S phase picks, the arrival-time reading accuracy and knowledge of the crustal structure (*Stein and Wysession*, 2009).

In this section, we summarise the theoretical background of the three different earthquake location methods used in this study. These are, a linearised method for the calculation of preliminary earthquake locations, a non-linear method to obtain absolute earthquake locations, and a relative earthquake relocation method that uses double difference techniques to get the final earthquake relocations.

2.7.1 Iterative linearised location

Iterative linearised location methods like HYPOCENTER (*Lienert et al.*, 1986), and HYPO71 (*Lee and Lahr*, 1972), use Taylor series expansions to represent the non-linear inversion location problem. As a first step, a hypocenter coordinates in Cartesian

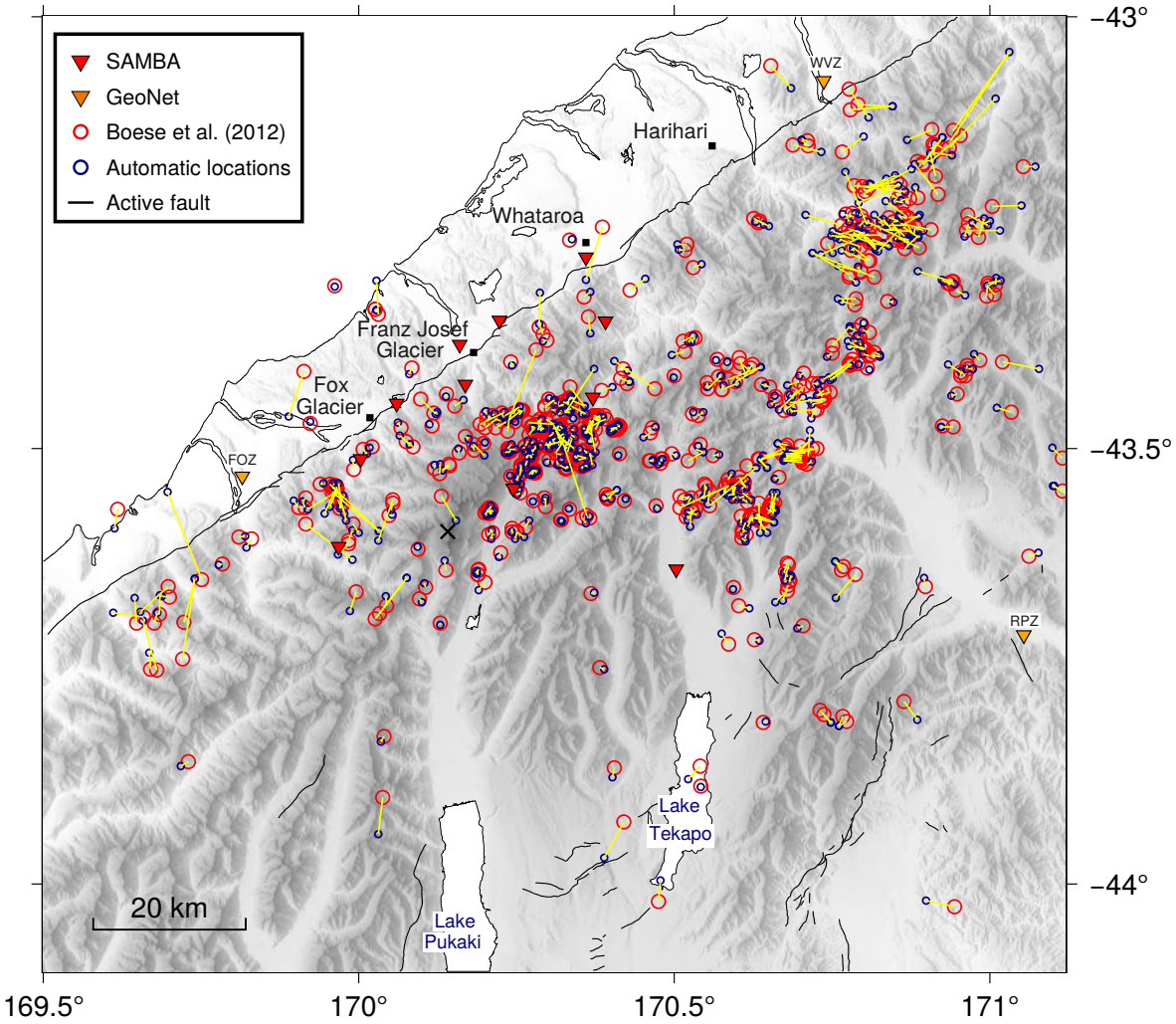

Figure 2.7: Epicenters of the 653 automatic locations (blue) determined in this study and the common events (red) recorded by *Boese et al.* (2012). The automatic locations were obtained using the same seismic sites as used by *Boese et al.* (2012). Black squares show the major West Coast townships. Grey thick lines represent the active faults from the New Zealand Active Faults Database (*http://data.gns.cri.nz/af/*).

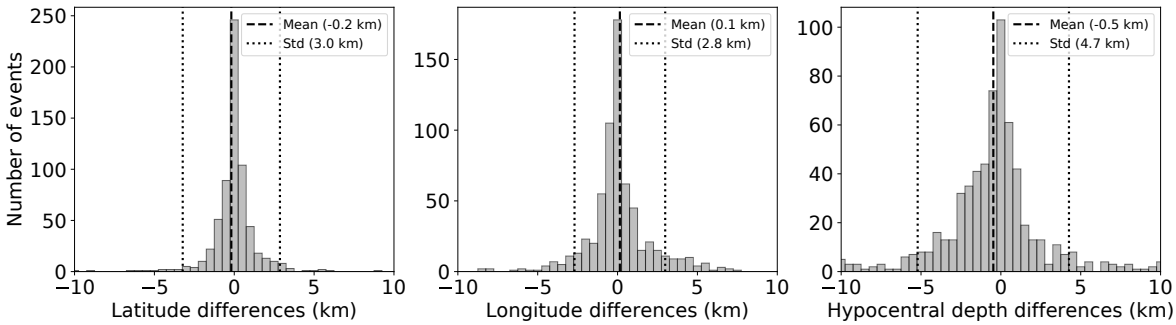

Figure 2.8: Automatic versus manual earthquake location differences for earthquakes recorded by SAMBA and GeoNet stations between November 2008 and December 2009.

coordinates (X, Y, Z) and origin time are set (x_0, y_0, z_0, t_0). The simplest way of doing this is to set the origin time, t_0 to the earliest phase pick time. It is then assumed that the true hypocenter is close to the set one in order to express the travel time residuals

as a linear function of the correction needed to be made in the hypocentral distance. The arrival time at station i is given by the following equation:

$$t_i = T(x_i, y_i, z_i, x_0, y_0, z_0) + t_0 \tag{2.1}$$

T is the travel time as a function of the seismic site (x_i, y_i, z_i) and hypocenter locations. Equation 2.1 contains four unknowns, meaning that at least four arrival-time observations from at least three seismic sites are required to calculate the hypocenter and the origin time. In the case of $n \geq 4$ observations the system becomes over-determined and can be solved by minimizing the residual, r_i at each seismic site. The residual r_i at a particular site represents the difference between the observed and calculated arrival times.

$$r_i = t_i^{obs} - t_i^{calc} \tag{2.2}$$

where t_i^{obs} and t_i^{calc} are, respectively, the observed and calculated arrival times at the i^{th} station. Because the travel-time function T is a non-linear function of the model parameters, it is generally impossible to solve the problem with analytical methods. Δx, Δy, Δz, and Δt are the corrections needed to be applied to the origin times for the residuals to be minimized. When these corrections have relatively small values, the corresponding corrections in travel-times can be calculated by approximating the travel-time function with a Taylor series and using only the first term. The residuals are then equal to:

$$r_i = \frac{\partial T}{\partial x_i}\Delta x + \frac{\partial T}{\partial y_i}\Delta y + \frac{\partial T}{\partial z_i}\Delta z + \Delta t_0 \tag{2.3}$$

Here, all terms are as before and the derivatives represent the adjustments to be made to the hypocenter. The first-order partial derivatives of Equation 2.3 are specified below (*Thurber*, 1985):

$$\frac{\delta t}{\delta X} = \frac{X - x_i}{vS} \tag{2.4}$$

$$\frac{\delta t}{\delta Y} = \frac{Y - y_i}{vS} \tag{2.5}$$

$$\frac{\delta t}{\delta Z} = \frac{Z - z_i}{vS} \tag{2.6}$$

where S is the length of the ray path in km.

The linear Equation 2.3 has four unknowns (i.e. the corrections of the hypocenter and the origin time), and one equation exists for each observed phase time arrival. The original trial location is corrected by solving these equations with least squares techniques. The best solution of Equation 2.3 is then used as a trial location for the next iteration. The iteration process continues until a predetermined criteria is met. These criteria can be a minimum residual, r, value or a total number of iterations. This inversion was originally proposed by *Geiger* (1910).

Iterative linearised earthquake locations return a single best-fit (e.g. maximum likelihood) hypocenter and origin time with linearly estimated uncertainties assumed to have normal distributions centered on the best-fit hypocenter and origin time (*Lomax et al.*, 2009). This type of location can be unstable due to insufficient observations, velocity structure complexities, and other causes (*Lomax et al.*, 2000). Linearised earthquake location errors are commonly represented and quantified using the least squares method that finds the minimum of the sum of the squared residuals e from n observations.

$$e = \sum_{1}^{n} r_i^2 \tag{2.7}$$

The root-mean-squared residual (rms) of the travel time residuals for the final earthquake location is determined as $\sqrt{e/n}$. The rms value only provides an indication of the fit of the data during the linearised inversion process. Therefore, a low rms value does not necessarily mean an accurate hypocenter. For example, if we consider an earthquake location that has only four travel-time measurements available the rms would be underestimated compared to the same location with more travel-time measurements.

In the present work, we have used linear location methods only to obtain preliminary locations, as they are fast and easy to implement. However, due to the limitations mentioned above we did not perform any subsequent analysis with the preliminary earthquake locations.

2.7.2 Non-linear location

Including second order terms of the Taylor series in Equation 2.3 gives more stable earthquake locations for a complex medium or for a shallow source (*Thurber*, 1985). The second derivative for the Z are represented below.

$$\frac{\partial^2 t}{\partial Z^2} = \frac{1}{vS}\left[1 - \frac{(Z - z_i)^2}{S^2}\right] \tag{2.8}$$

$$\frac{\partial^2 t}{\partial Y \partial Z} = -\frac{(Y - y_i)(Z - z_i)}{vS^3} \tag{2.9}$$

$$\frac{\partial^2 t}{\partial X \partial Z} = \frac{(X - x_i)(Z - z_i)}{vS^3} \tag{2.10}$$

similar solutions can be obtained for the terms X and Y.

By comparing the non-linear equation (2.10) to the linear equation (2.6), it is obvious that in the case where $Z = z$, which represents a shallow event at zero depth, the first-order partial derivative vanishes while the second order partial derivative gets its maximum value (*Thurber*, 1985). This feature of the non-linear method gives greater depth sensitivity and accuracy for shallow earthquakes. Non-linear methods yield more stable hypocenters for earthquakes that occur outside the boundaries of the network.

Probabilistic non-linear earthquake location

We use a probabilistic non-linear location method called NonLinLoc (*Lomax et al.*, 2000) to overcome the location accuracy limitations of the preliminary earthquake locations obtained with HYPOCENTER and hence obtain final absolute earthquake locations. We opt to use NonLinLoc for two main reasons. Firstly, it includes robust earthquake location uncertainty information as a posterior density function (PDF). These PDFs can be plotted as a cloud of possible locations surrounding the maximum likelihood hypocenter. Secondly, because NonLinLoc also enables the use of 3-D P and S wave velocity models and includes station elevation information for the creation of the velocity grid and calculation of travel times, which helps to provide more robust earthquake locations. The station elevation information is important to be considered here due to the high topography of the Southern Alps.

NonLinLoc follows the probabilistic formulation of nonlinear inverse problems developed by *Tarantola and Valette* (1982), which uses normalised and unnormalised probability density functions to describe the values of a parameter. For example, considering a generic normalised density function $f(x)$ for the value of the parameter x, the probability that the value of x is between X and $X + \Delta X$ is described by the following equation.

$$P(X \leq x \leq X + \Delta X) = \int_X^{X+\Delta X} f(x)dx \tag{2.11}$$

In the earthquake location problem the objective is to constrain the values of a vector, $\mathbf{p}$, containing the unknown parameters (i.e. earthquake location) using the information from a vector of observed data, $\mathbf{d}$, (i.e. observed travel times, station locations, etc.)

and a theoretical relationship $\theta(\mathbf{d}, \mathbf{p})$ that relates the two vectors. If the density functions of the prior information of the model parameters $\rho_p(\mathbf{p})$ and of the observations $\rho_d(\mathbf{d})$ are independent, the theoretical relationship $\theta(d, p)$ can be described as a conditional density function $\theta(\mathbf{d}|\mathbf{p})\mu_p(\mathbf{p})$. The complete probabilistic solution is then given by a PDF $\sigma_p(\mathbf{p})$ as below (*Tarantola and Valette*, 1982; *Tarantola*, 1987).

$$\sigma_p(\mathbf{p}) = \rho_p(\mathbf{p}) \int \frac{\rho_d(\mathbf{d})\theta(\mathbf{d}|\mathbf{p})}{\mu_d(\mathbf{d})} d\mathbf{d} \tag{2.12}$$

where $\mu_d(\mathbf{d})$ and $\mu_p(\mathbf{p})$ represent the null information density function, for which there is no available prior knowledge. Assuming that both the observed arrival times and theoretical relationship have Gaussian uncertainties and that the prior information is uniform, it is then possible to calculate the spatial location of the PDF by integrating over the observed data $\mathbf{d}$ with Equation 2.12.

Probabilistic non-linear locations are obtained by applying a grid search for all possible locations in a defined velocity grid by minimizing the misfit between observed and calculated arrival times. For the calculation of the PDFs we used the Oct-Tree algorithm incorporated into NonLinLoc (*Lomax et al.*, 2000). This method recursively subdivides and samples the grid in cells in three dimensions, computing the PDF within each cell. Then, the cell with the largest possibility is further subdivided into a number of smaller cells and a PDF for each cell is computed. This process is repeated until a minimum cell size or a maximum iteration number is reached. These cells are more dense in the areas of higher PDF (lower misfit). The final location of the earthquake hypocenter is the cell with the maximum probability value.

2.7.3 Relative earthquake location

The section below is a brief description of the processing performed to obtain the final earthquake hypocenters that underpin the interpretations in the following Chapters.

We calculate relative earthquake locations using the latest version of HypoDD, 2.1b, after *Waldhauser* (2001), which implements the double-difference method of *Waldhauser and Ellsworth* (2000), incorporates seismic site elevations into the travel time calculations, and enables the use of 3-D velocity models. For travel time calculations this method uses either high-precision cross-correlation measurements, or travel time picks, or a combination of both. In this study we use both travel time picks and cross-correlation measurements.

A basic assumption underpinning the double-difference relocation algorithm is that when a number of events are closely located the effect of velocity heterogeneities can be disregarded in the calculation of the source or station corrections. In other words,

when the hypocentral separation between the two events that constitute a pair is much smaller than the source to receiver distance, the ray paths of the two events will be very similar. Using this approach, the double-difference algorithm minimizes errors in the earthquake locations that are related to unmodeled velocity structures (*Waldhauser and Ellsworth*, 2000). The algorithm improves the location accuracy by obtaining travel time differences, dt, between pairs of events moving the location of the pairs relative to each other. This way travel time residuals of the earthquake pairs are minimized.

One of the main differences and major advantages of the double-difference locations over the commonly used linearised and non-linear earthquake locations, is that the double-difference allows the use of P and S cross-correlations that can provide even more precisely calculated travel time differences, reducing the location errors. Relative earthquake location uncertainties can be obtained using statistical resampling methods (e.g. bootstrapping, jackknife methods; *Efron and Gong*, 1983). The relative uncertainties are in general improved by more than an order of magnitude compared to the corresponding uncertainties of the absolute earthquake locations (*Waldhauser and Ellsworth*, 2000).

Having considered the advantages described above, it is also of crucial importance to consider some of the issues that could be encountered while using double-difference location methods. The robustness of these methods are highly related to the correctness of the velocity model and the accuracy of the absolute earthquake locations used (*Michelini and Lomax*, 2004). This can be checked by using different velocity models for a same set of events. In addition, even though double-difference methods can provide a very detailed and accurate pattern for the earthquakes within a cluster, the overall position of the cluster might not always be accurate (*Menke and Schaff*, 2004; *Wolfe*, 2002).

Double-difference algorithm

The double difference algorithm can be applied to either differential travel time data from catalog or cross-correlation measurements, or both. The travel time residuals are given by $r_k^{ij} = (t_k^{obs} - t_k^c)$, where t^o is the observed travel times, and t^c is the theoretical travel times, for earthquakes i and j recorded at a seismic site k.

$$\frac{\partial t_k^i}{\partial m} \Delta m^i = r_k^{ij} \tag{2.13}$$

where $\Delta m^i = (\Delta x^i, \Delta y^i, \Delta z^i, \Delta \tau^i)$ is the difference in hypocenter location and origin time that is related to travel time residuals r of model parameter m. These differential

travel-times provide us with double difference equations:

$$dr_k^{ij} = (t_k^i - t_k^j)^o - (t_k^i - t_k^j)^c \tag{2.14}$$

Here dr_k^{ij} represents the double difference residual between earthquakes i and j for each observation at a seismic site k. Equation 2.14 is highly dependent on the assumption that the velocity structures in the source to receiver ray paths for both events are similar and breaks down when events are not close enough. The change in hypocentral distance between the two events i and j can be obtained by the following equation:

$$\frac{\partial t_k^i}{\partial m}\Delta m^i - \frac{\partial t_k^i}{\partial m}\Delta m^j = dr_k^{ij} \tag{2.15}$$

or

$$\frac{\partial t_k^i}{\partial x}\Delta x^i + \frac{\partial t_k^i}{\partial y}\Delta y^i + \frac{\partial t_k^i}{\partial z}\Delta z^i + \Delta\tau^i - \frac{\partial t_k^j}{\partial x}\Delta x^j - \frac{\partial t_k^j}{\partial y}\Delta y^j - \frac{\partial t_k^j}{\partial z}\Delta z^j - \Delta\tau^j = dr_k^{ij} \tag{2.16}$$

Here, the partial derivatives of the travel times t of events i and j relative to their locations (x, y, z) and origin times (τ) are calculated for the hypocenter and the location of the seismic site k. Δx, Δy, Δz, $\Delta\tau$ are the changes needed to be applied to the model to better fit the data. These changes are calculated using linear techniques for all stations and hypocentral pairs. The HypoDD algorithm solves this problem in a series of iterations during which different weighting schemes are applied. The iteration process stops when the rms residual reaches a threshold defined by the noise level of the data or the predetermined number of iterations is reached (*Waldhauser*, 2001).

Cross-correlation delay times

Cross-correlation techniques are used to calculate the time delays between the signals of two earthquakes. We use the cross-correlation pick correction function available in ObsPy (*Krischer et al.*, 2015), which aligns the waveforms around the P and S wave arrival times of two earthquakes to correct the original pick times. An example of the cross-correlation pick correction is shown on Figure 2.9 in which a parabola is fit to the convex part of the cross correlation function around its maximum, following the approach of *Deichmann and Garcia-Fernandez* (1992). These corrections are used to obtain the cross-correlation differential times for each event pair at a common seismic site to be used in HypoDD algorithm.

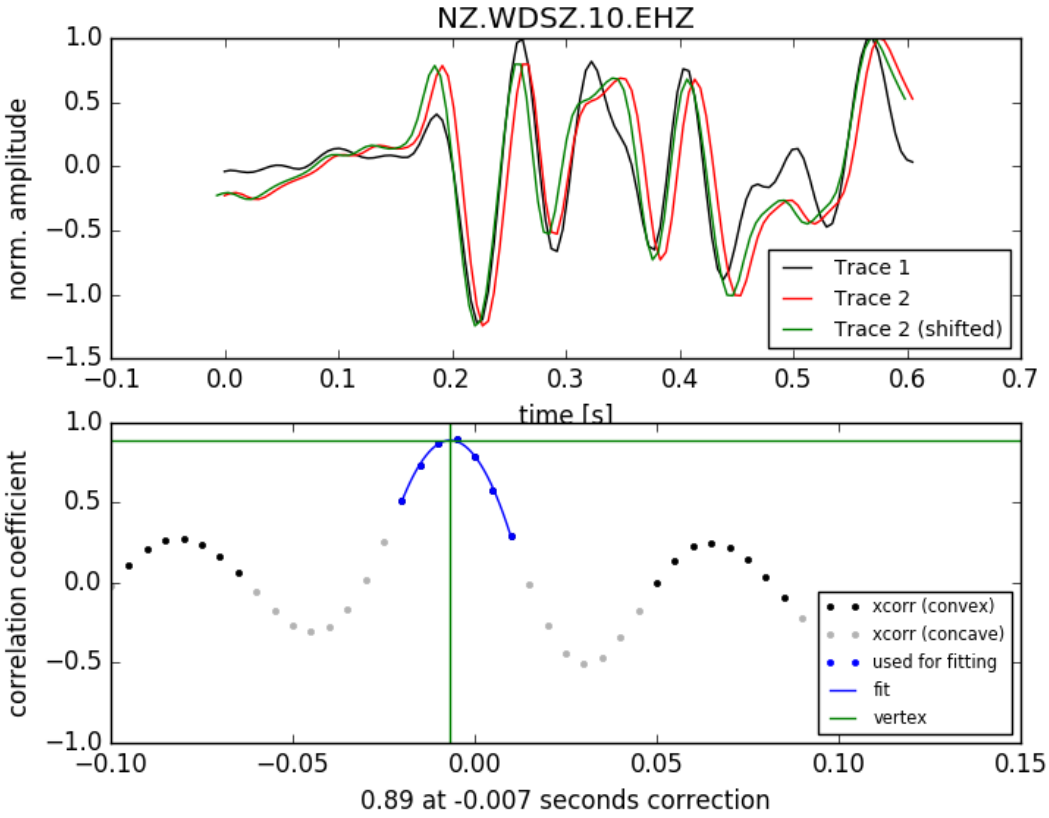

Figure 2.9: Example of a pick correction calculation for the differential pick time determined by cross correlation of the waveforms in narrow windows around a P wave pick at the seismic site WDSZ.

2.8 Earthquake magnitudes

The concept of the earthquake magnitude was introduced by *Richter* (1935), who used seismic wave amplitudes to create the first magnitude scale, M_L. This scale related the earthquake size to observed peak ground motions, for local seismicity recorded by standardized short-period Wood-Anderson seismometers in southern California. This analysis was made using Richter's formula,

$$\mathrm{M_L} = \log_{10}(A/A_0) \tag{2.17}$$

where A is the mean amplitude in microns of the horizontal components of a Wood-Anderson seismograph, with a fundamental period of 0.8 seconds and magnification of 2080, and A_0 is the amplitude expected on the same type of instrument at a distance of 100 km from the earthquake.

When seismic waves propagate through a homogeneous medium their energy density decays in proportion to $1/r^2$, where r is the radius of the wavefront due to geometrical

spreading (*Stein and Wysession*, 2009). Energy density also decays due to attenuation that can either be elastic or anelastic (*Stein and Wysession*, 2009). Anelastic attenuation occurs mostly during shear wave motion associated with lateral movements of the grain boundaries. Elastic attenuation is also known as scattering, which is caused by the heterogeneity of the Earth's crust and mantle. Local magnitude scale calculations can include corrections for geometric spreading, anelastic attenuation and site terms (*O'Keefe*, 2008; *Boese et al.*, 2012; *Warren-Smith et al.*, 2017b). The local magnitude calculation details are explicitly described in Chapter 3 (Sections 3.4.2 and 3.5.1).

2.9 Focal mechanisms

Focal mechanisms provide information on the rupture geometry of earthquakes (*McKenzie*, 1969). Commonly established methods for calculating focal mechanisms include using information such as the first motion polarities of P waves, polarizations and amplitudes of S waves (*Khattri*, 1973), analysis of P/S amplitude ratios (*Kisslinger et al.*, 1981) and moment tensor inversion (e.g. *Aki and Richards*, 2002). All these approaches use the radiation pattern of seismic rays related to the orientation of the fault plane and the direction of the slip of a double couple seismic source (*Stein and Wysession*, 2009).

In this study we use P wave arrival polarities to determine focal mechanisms. First motions of P waves on the vertical component of a seismometer, in relation to the seismic source, have either compressional (up) or dilatational (down) motion (Fig. 2.10). These first motions are projected backwards along ray paths to a conceptualized unit sphere surrounding the seismic source, which is assumed to be a point source at the beginning of the rupture. These ray paths are defined by two parameters azimuth from the source and take-off angles. The take-off angle is related to the distance between the seismic source and the seismometer as well as the velocity model used.

Mapping these ray paths in the lower hemisphere of a stereographic projection, we can distinguish between the areas of compression (up) and dilatation (down), and define the compressional and dilatational quadrants. The compressional and dilatational quadrants are defined by the nodal planes and are bisected by the minimum compressive stress (T) and maximum compressive stress (P) axes, respectively (Fig. 2.10; *Stein and Wysession*, 2009). The intersection of the two nodal planes is the null axis (B). The P, T and B axes are orthogonal and along with the characteristics of the nodal planes this consists the information available from focal mechanisms.

The characteristics of the nodal planes consists of three angles that describe the geometry of the fault plane, namely the strike, dip and rake of the focal mechanism (*Stein*

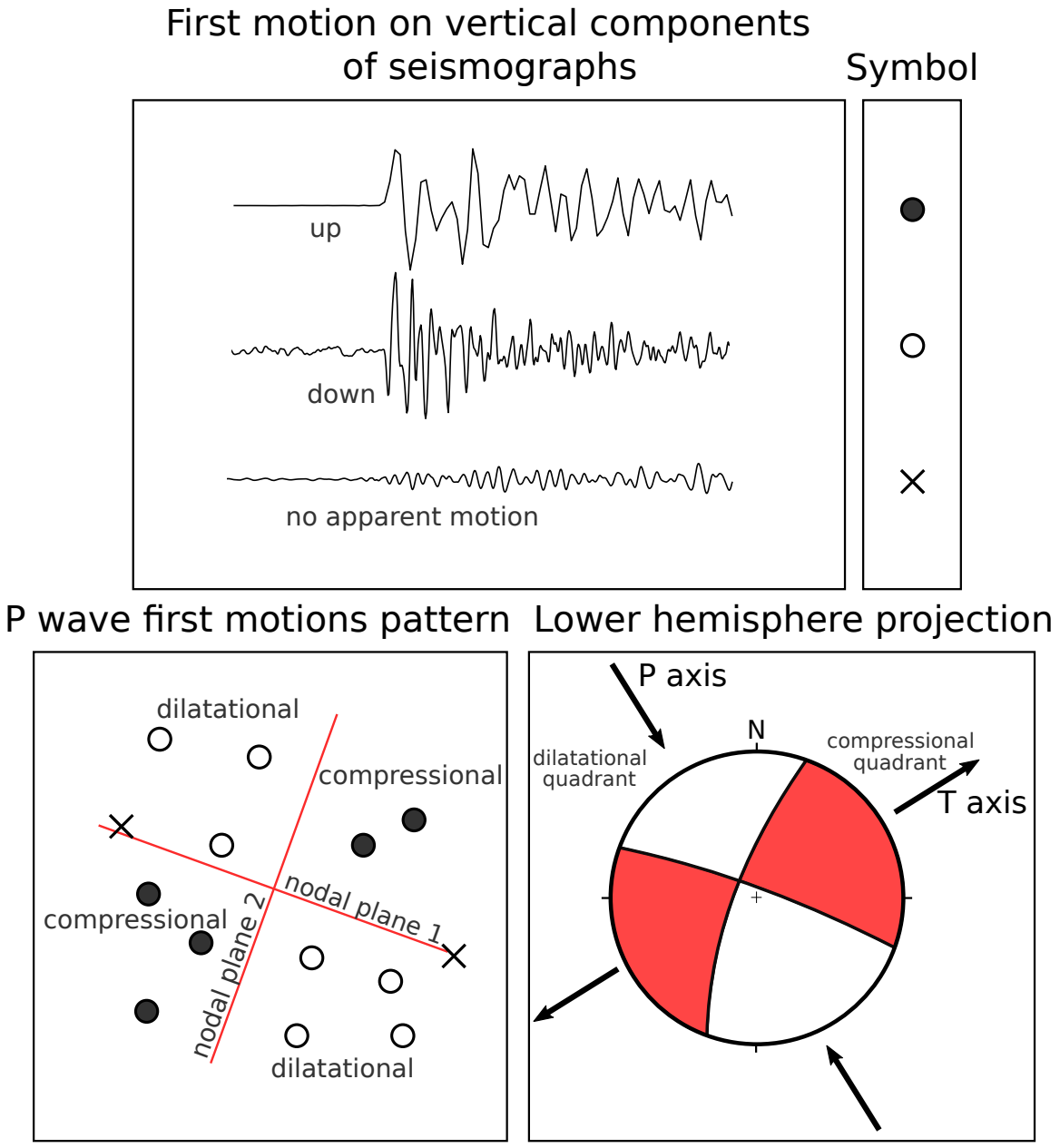

Figure 2.10: Simplistic diagram that outlines the source radiation patterns of strike slip fault and the steps included in calculating a focal mechanism using first motion polarities.

and Wysession, 2009). The strike angle, ϕ, defines the azimuth (measured clockwise from north) of the nodal plane and varies from 0° to 360° (Fig. 2.11a). The dip angle, δ, represents the inclination (measured to the right hand side along the strike) of the nodal plane from the horizontal surface and ranges from 0° to 90° (Fig. 2.11a). The rake angle, λ, specifies the direction of the hanging-wall motion with respect to the footwall (measured anti clockwise in the plane of the fault from the strike direction) and has values that span from −180° to 180° (Fig. 2.11a). Positive rake angles represent upwards motion of the hanging-wall (reverse faulting), while negative rake angles indicate downward motion (normal faulting) (Fig. 2.11b). Focal mechanisms are symmetric and

contain an inherited ambiguity regarding which of the two nodal planes is the actual fault plane that ruptured. To obtain the plane that ruptured additional information is needed (e.g. surface ruptures information or analysis of aftershock distributions if available).

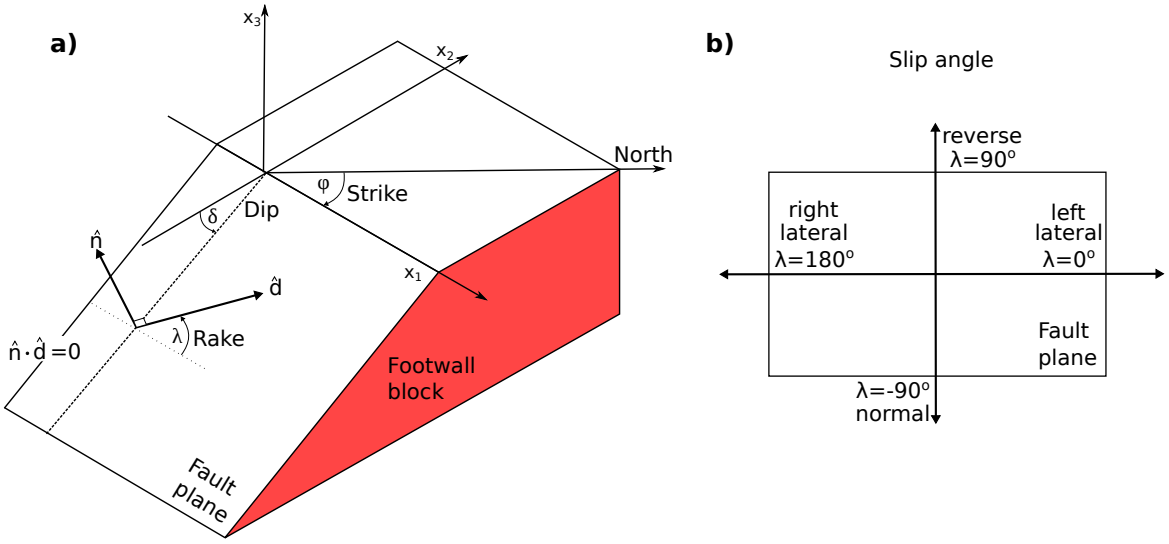

Figure 2.11: Schematic representation of fault geometry. Figure modified from *Stein and Wysession* (2009). $\hat{n}$ and $\hat{d}$ respectively represent the fault plane's normal vector and the motion of the hanging wall block (not shown here) with respect to the footwall block. δ is the dip of the fault plane. The strike, ϕ is the azimuth of the surface trace of the fault plane. Rake, λ, defines the direction of the motion.

First motion P wave polarities are manually determined in SEISAN for all earthquakes with magnitudes larger than M_L=1.5. The picking of the polarities depended on the impulsiveness of the P wave arrivals.

2.10 Stress parameters

Having discussed the characteristics and a way to generate focal mechanisms, this section addresses the methods of using the focal mechanisms to obtain a model of the stress field in the crust.

The state of stress at a point of Earth's crust can be described by the geometric properties of the three principal stress axes the maximum, S_1, intermediate, S_2 and minimum S_3. Principal stress directions are poorly constrained when single focal mechanisms are used as the maximum compressive stress may be anywhere within the dilatational quadrant of the focal mechanism (*McKenzie*, 1969). To overcome this and calculate the geometrical distribution of these parameters combining multiple focal mechanisms a number of stress inversion algorithms have been proposed (*Gephart and Forsyth*, 1984; *Michael*, 1984; *Hardebeck and Michael*, 2006; *Arnold and Townend*, 2007). These in-

version techniques improve the quality of the calculation of the stress parameters compared to using single focal mechanisms for the examination of the stress field. Using the three principal stress axes and a ratio of the relative magnitudes of the principal stresses, the stress ratio R=(S_1–S_2)/(S_1–S_3) is sufficient to calculate the direction, but not the magnitude, of the maximum horizontal compressive stress, S_{Hmax}, (*Lund and Townend*, 2007). Stress inversions are linked to two main assumptions: 1) the focal mechanisms combined lie in a region of uniform stress field that stays the same in time and space (*Townend and Zoback*, 2004); 2) the direction of the earthquake slip occurs in the direction of maximum shear stress (Wallace-Bott hypothesis; *McKenzie*, 1969).

In this thesis we have used two different inversion techniques to estimate the tectonic stresses from seismological observations (i.e. focal mechanisms). We used two different methods to leverage the advantages of each algorithm. The first we used is the probabilistic Bayesian method of *Arnold and Townend* (2007). This approach includes both nodal planes of multiple earthquakes as indistinguishable and the observational errors (e.g. false polarity picks) to the stress inversion calculations. Because of this, the final probabilistic stress inversion results provide realistic constraints on the properties of the stress parameter geometry. In short, we use this technique because it can accurately describe the uncertainties of the stress calculations. The second is the damped inversion method, SATSI, developed by *Hardebeck and Michael* (2006). We also use this method because it resolves the stress field orientation for the data of each subregion (or epoch) taking into account the data from the adjacent subregions to smooth the solution. This way, only large changes in the stress tensor are retained, while variations arising from artifacts like the data subdivision are smoothed. In addition to this, this method has the option to use only one of the nodal planes in the stress inversion calculations.

2.11 Data division methods

To investigate the spatial variations of any given parameter (e.g. seismogenic cut-off depths, stress parameters, etc) the data-set needs to be divided into subregions. To do this, we use two clustering algorithms. We use the quadtree recursive gridding algorithm (*Townend and Zoback*, 2001) and the non-hierarchical clustering algorithm called k-means (*Hartigan*, 1975; *Balfour et al.*, 2005).

The quadtree clustering method begins with a single square bin that contains the whole given area (step 1; Fig. 2.12). This bin is divided in quarters that in their turn are divided in quarters until there are fewer than a predetermined maximum number of earthquake locations in each bin, n_{max} or the bin gets to a minimum dimension of x_{min}. The final grid consists of a mesh of square bins that are smaller and denser where there

are more earthquake locations.

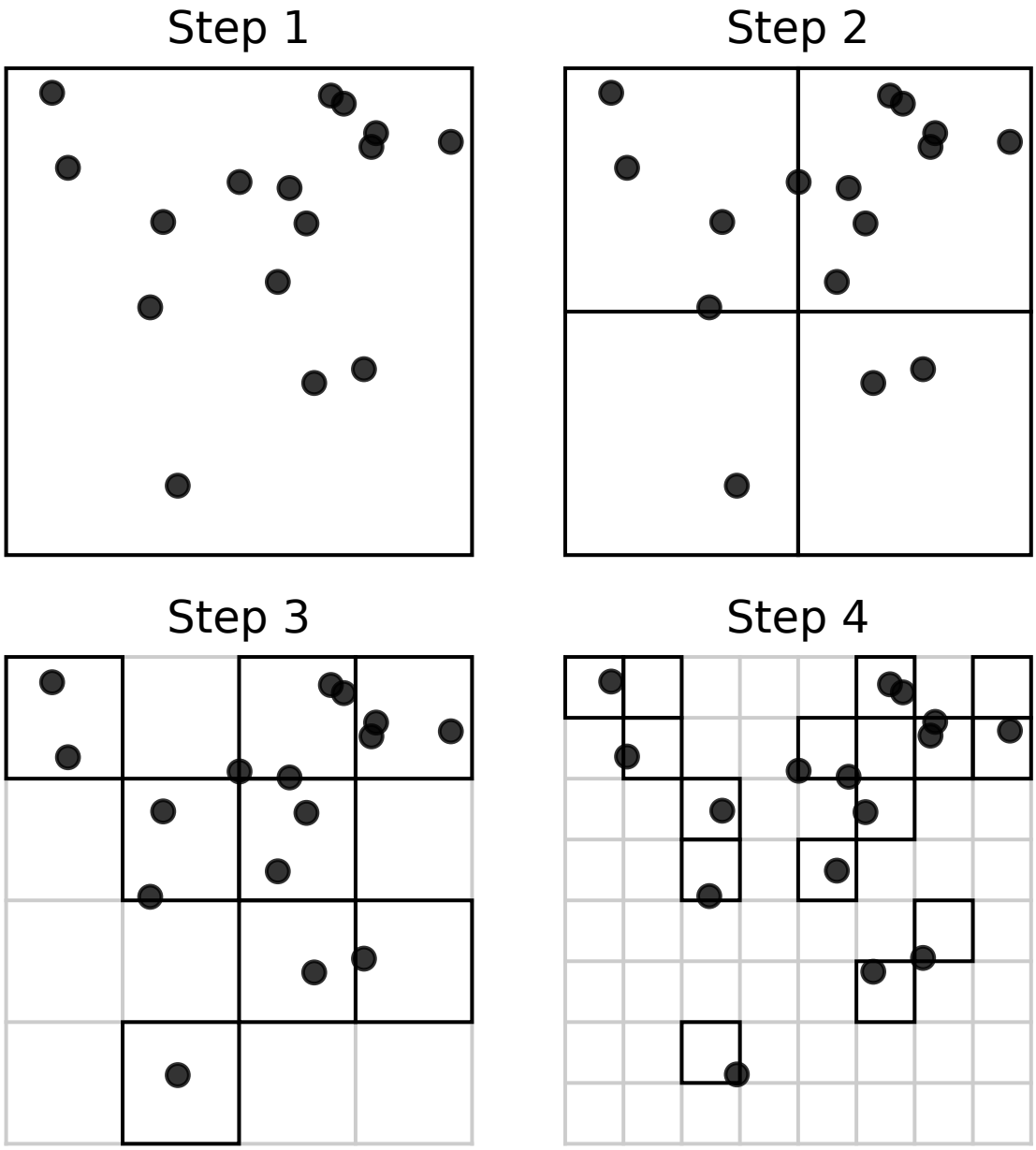

Figure 2.12: Simplified example that shows the processing steps of the quadtree recursive gridding algorithm applied to a randomly generated data set.

The k-means algorithm searches for similarities within a given data set of earthquake locations without using any labels. The only attribute defined beforehand is the number of clusters that the data set will be divided into (Fig. 2.13). At first, the cluster centroids are randomly decided. The algorithm goes through each of the earthquake locations (longitude, latitude and depth) and, depending on the distance from the previously defined centroids, assigns them to one of the clusters. At the same time, the cluster centroids are moved to the mean value of locations of the clusters. This process is repeated until there is no change in the clusters centroids.

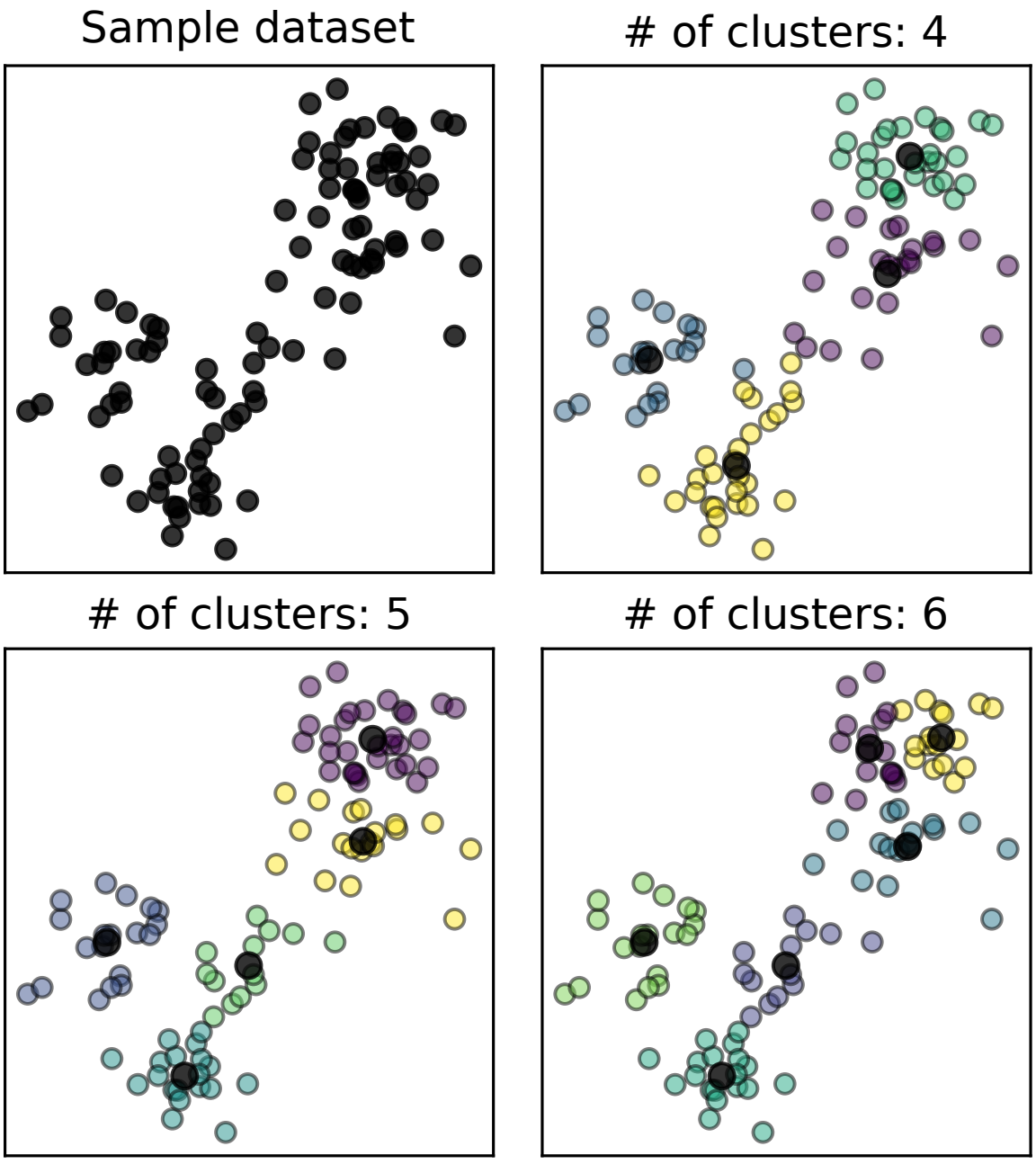

Figure 2.13: Simplified example that shows the results obtained using the k-means clustering algorithm and a number of different number of clusters applied to a randomly generated data set.

3 Variations in seismogenic thickness along the central Alpine Fault, New Zealand, revealed by a decade's relocated microseismicity

In this chapter, I investigate the distribution of the seismic deformation along the length of the central Alpine Fault by creating the longest to date microseismicity earthquake catalog. The chapter is divided into five main sections and begins with an introduction on the topic. The next two sections outline the data and methods used to create the microseismicity earthquake catalog. Finally the last three sections describe the main and supporting findings, their implications and their summary, respectively. This chapter has been published as a peer-reviewed paper in *Geochemistry, Geophysics, Geosystems*[1]. The full earthquake catalog resulting from this publication is available, in QuakeML format, on zenodo open-access repository[2]. The figures and text from this publication have been modified to fit the format of this thesis. The relocated earthquake catalog is included in the electronic appendices (Dataset B1). The citation of the publication is the following:

Michailos, K., Smith, E. G. C., Chamberlain, C. J., Savage, M. K., Townend, J. (2019). Variations in seismogenic thickness along the central Alpine Fault, New Zealand, revealed by a decade's relocated microseismicity. *Geochemistry, Geophysics, Geosystems*, 20, 470–486. https://doi.org/10.1029/2018GC007743

3.1 Abstract

The Alpine Fault is an oblique strike-slip fault that is known to fail in large magnitude (M7–8) earthquakes, yet it is currently seismically quiescent. We examine the low-magnitude earthquake activity occurring along the central portion of the Alpine Fault using seismic data from five temporary seismic networks deployed for various lengths of

[1] https://doi.org/10.1029/2018GC007743
[2] https://doi.org/10.5281/zenodo.3529752

time between late 2008 and early 2017. Starting from continuous seismic data, we detect earthquake arrivals and construct the longest and most extensive microearthquake catalog for the central Alpine Fault region to date, containing 9,111 earthquakes. This enables us to study the distribution and characteristics of the seismicity in unprecedented detail. Earthquake locations are constrained by high quality automatic and manual picks and we perform relocations using waveform cross-correlation to better constrain hypocenters. We have derived a new local magnitude scale, calibrated by M_w values. Magnitudes range between M_L -1.2 to 4.6 and our catalog is complete above M_L 1.1. Earthquakes mainly occur southeast of the Alpine Fault (in the hanging-wall) and exhibit low magnitudes. We observe a lack of seismicity beneath Aoraki/Mount Cook, which we associate with high uplift rates and high heat flow. Seismogenic cut-off depths vary along the strike of the Alpine Fault from 8 km, beneath the highest topography, to 20 km in the adjacent areas.

3.2 Introduction

The central South Island of New Zealand is a region of active plate boundary deformation. Its principal tectonic feature is the Alpine Fault, an 850 km-long dextral reverse fault (*Wellman and Willet*, 1942; *Norris and Cooper*, 2001) that is considered to be the plate boundary between the Australian and Pacific plates. The Alpine Fault is known to fail in large (M7–8) earthquakes based on paleoseismological evidence (*Sutherland et al.*, 2007; *Berryman et al.*, 2012; *Howarth et al.*, 2014, 2016; *Cochran et al.*, 2017; *Howarth et al.*, 2018). The most recent large Alpine Fault earthquake occurred in 1717 CE and the southern section of the fault has a recurrence interval for ground-rupturing earthquakes of 291 ± 23 yrs (*Cochran et al.*, 2017). The central section of the Alpine Fault exhibits high rates of geodetic deformation (*Beavan et al.*, 2010), low levels of contemporary (past 50 years) earthquake activity (*Eiby*, 1971; *Evison*, 1971; *Scholz et al.*, 1973; *Leitner and Eberhart-Phillips*, 2001; *Boese et al.*, 2012; *Bourguignon et al.*, 2015; *Feenstra et al.*, 2016; *Chamberlain et al.*, 2017a; *Warren-Smith et al.*, 2017b), little on-fault seismicity, and no measurable creep (*Evison*, 1971; *Sutherland et al.*, 2007). The oblique motion of the Alpine Fault has exposed a thin zone of metamorphic rocks within the hanging wall (*Norris and Cooper*, 1997). These exhumed rocks originate from the lower crust of the fault zone (*Toy et al.*, 2010). This exhumation is inferred to have enhanced the thermal gradient of the shallow part of the hanging wall (*Koons*, 1987; *Allis and Shi*, 1995; *Shi et al.*, 1996; *Sutherland et al.*, 2012). Manifestations of this thermal enhancement in the area include locally extreme near-surface geothermal gradients (125±55 °C/km; *Sutherland et al.*, 2017), hot springs (*Allis et al.*, 1979; *Cox et al.*, 2015), and young thermochronometric ages (*Little et al.*, 2005; *Herman et al.*,

2009).

The central Alpine Fault has been the subject of numerous geophysical studies. Much of the current knowledge of the properties of the crust and upper mantle surrounding the central Alpine Fault is derived from the South Island Geophysical investigation (SIGHT; (*Davey et al.*, 1998; *Okaya et al.*, 2002)), a multidisciplinary geophysical study that took place in late 1995 and early 1996. Seismic reflections beneath the Southern Alps were interpreted as the eastward-dipping Alpine Fault flattening in the lower crust (*Davey et al.*, 1995). Zones of low velocities (*Stern et al.*, 2007) and high conductivity (*Wannamaker et al.*, 2002) were found to coincide with these reflections. Another large study of the central section of the Alpine Fault has been the Deep Fault Drilling Project (DFDP; *Townend et al.*, 2009; *Sutherland et al.*, 2012; *Townend et al.*, 2013; *Toy et al.*, 2015). DFDP has to date involved two stages, and its main goal was to drill into the Alpine Fault and examine the physics of faulting and seismogenesis inside the fault zone. Borehole measurements and observations revealed an active hydrothermal circulation system of high temperatures, high permeability and elevated pore fluid pressure beneath the Whataroa Valley (*Townend et al.*, 2017; *Sutherland et al.*, 2017). These extreme hydrothermal conditions are inferred to exist due to heat advection from depth and topographically driven fluid flow through fractured rocks that concentrate heat within the valleys (*Sutherland et al.*, 2017).

As described in detail below (Section 1.2), the microseismicity along the central Alpine Fault has been examined in several previous studies (*Leitner and Eberhart-Phillips*, 2001; *O'Keefe*, 2008; *Boese et al.*, 2012; *Bourguignon et al.*, 2015; *Feenstra et al.*, 2016; *Guo et al.*, 2017; *Chamberlain et al.*, 2017b). However, these have been limited in either geographic scope or in duration and tended to examine variations of seismicity perpendicular to the strike of the Alpine Fault rather than along its length. To date, a geographically extensive analysis of the characteristics of the microseismicity has not been made for a duration more than 2-3 years. To fully characterize the seismicity in this region of low seismic activity, we require data that have been recorded over a longer interval to reveal the nuances of spatial seismicity patterns.

In this paper, we analyze the characteristics of the low-magnitude regional seismicity, mostly below the completeness level of the GeoNet national seismic catalog[3] (M=2.6), spanning almost a decade of continuous data from five temporary seismic networks. We present here the longest microearthquake catalog constructed to date for the central Southern Alps, starting with continuous waveform data and using a uniform approach and methodology during the data processing stage. Doing so enables us to robustly examine along-strike and cross-strike variations in seismicity, and to constrain estimates of seismogenic thickness along the central Alpine Fault. We also derive a new local

[3] `https://www.geonet.org.nz/data/types/eq_catalogue`

magnitude scale based on seismic moment magnitude values, corrected for geometric spreading, attenuation and site terms.

3.2.1 Tectonics

New Zealand lies along the plate interface between the Australian and Pacific plates. The relative motion in the central South Island is oblique to the plate boundary (*Walcott*, 1998), creating a transpressive tectonic environment and forming the the Southern Alps. The western margin of the Southern Alps orogen is delineated by a major plate boundary strike-slip reverse fault, the Alpine Fault (*Wellman and Willet*, 1942; *Norris and Cooper*, 2001). During the Cenozoic the strike-slip motion of the Alpine Fault has produced a cumulative offset of at least 450 km (*Sutherland*, 1999) and possibly as much as 700 km (*Lamb et al.*, 2016).

The Alpine Fault is commonly separated into three segments according to its dip, structural style and the width of deformation (*Sutherland et al.*, 2006). Through the northern section, northeast of the junction between the Alpine and the Hope faults (Fig. 3.1), crustal deformation is distributed among a number of strike-slip and reverse faults (Marlborough Fault System). In the southern section, south of Haast (Fig. 3.1), the Alpine Fault becomes becomes pure strike-slip in character (*Norris and Cooper*, 2001; *Barnes et al.*, 2005).

The central section, between Hokitika and Haast (Fig. 3.1), which is our study region, exhibits higher uplift rates (>12 mm/yr), exhumation and narrow orogenic width (∼60 km) than the adjacent Alpine Fault sections (*Little et al.*, 2005; *Norris and Cooper*, 2007). The central Alpine Fault's surface trace average strike is 055°, oblique (on average 18° anticlockwise) by approximately 18° anticlockwise to the relative Pacific-Australia plate motion (39.5 ± 0.7 mm/yr; *DeMets et al.*, 2010). The Alpine Fault accommodates 70–75 % of the inter-plate motion, which results in 27 ± 5 mm/yr of dextral strike-slip motion and 0–10 mm/yr of dip-slip motion (*Norris and Cooper*, 2001). This oblique motion has uplifted a zone of high grade mylonites exhumed in the hanging-wall (*Toy et al.*, 2010). This exhumation has resulted in an uplift of the isotherms and an increase in the thermal gradient in the upper crust of the hanging-wall (*Koons*, 1987; *Sutherland et al.*, 2012, 2017).

3.2.2 Previous seismicity studies

The first systematic analysis of the seismicity in the central South Island were conducted by *Eiby* (1971) and *Evison* (1971), who recognized a seismic gap adjacent to the central Alpine Fault. Subsequent studies focused on this low-seismicity region

(*Scholz et al.*, 1973; *Caldwell and Frohlich*, 1975). The first comprehensive modern analysis of the seismicity in the central South Island along the Alpine Fault was made by *Leitner and Eberhart-Phillips* (2001). They used six months of seismic data from the Southern Alps Passive Seismic Experiment (SAPSE), which operated between 1995 and 1996 and augmented the permanent seismic network of 15 sites with 40 additional sites. *Leitner and Eberhart-Phillips* (2001) calculated absolute locations for 195 earthquakes with magnitudes varying from M_L 2.0 to 4.2 and observed a nearly uniform maximum seismogenic depth for the central South Island of 10–12 km.

O'Keefe (2008) investigated the seismicity of the narrow region between Fox Glacier and HariHari (Fig. 3.1) using a temporary network of five short-period and three broadband instruments deployed between September 2006 and March 2007. *O'Keefe* (2008) located 411 earthquakes, mostly within swarms, and derived a 1D velocity model for the area.

Boese et al. (2012) installed the SAMBA network (Fig. 3.1) and located more than 1700 earthquakes that occurred between November 2008 and December 2009 with magnitudes of M_L -0.3 to 4.2. The distribution of the seismicity observed was diffuse but spatially correlated with resistivity structures recognised by *Wannamaker et al.* (2002). The seismogenic zone depths *Boese et al.* (2012) calculated throughout the area examined were less than 15 $\pm$ 2 km, with mean depths increasing towards the southeast, perpendicular to the strike of the Alpine Fault. The earthquakes exhibiting the shallowest depths (6 $\pm$ 2 km) were located within the SAMBA network and beneath the area of highest topography.

Bourguignon et al. (2015) derived microearthquake locations and P and S wave velocity models using a 2-year data-set (October 2008 to October 2010) covering the region spanned by the ALFA-08 network (Fig. 3.1), along strike to the northeast of the region analyzed by *Boese et al.* (2012). They located more than 1,300 earthquakes within 50 km of the Alpine Fault trace. Hypocentral depth uncertainties within their seismic network were $\leq$ 0.1 km for 50% of the events and $\leq$ 0.6 km for 95% of the events. The seismogenic cut-off depths observed varied between 8 and 20 km and were inferred to be controlled by temperature and permeability structure variations.

Feenstra et al. (2016) investigated the microseismicity and seismic velocity structure around the Whataroa Valley (Fig. 3.1) using data from the Wisconsin New Zealand Array Rensselaer Deployment (WIZARD; *Thurber et al.*, 2012). *Feenstra et al.* (2016) located 680 earthquakes. Phase arrival times and cross-correlation times from these earthquakes were combined with information from 5,822 events recorded by GeoNet and the previous studies of *O'Keefe* (2008), *Boese et al.* (2012) and *Bourguignon et al.* (2015) to undertake seismic tomography. The best-fit seismic velocity structure resulting from this inversion suggests that the central segment of the Alpine Fault is dipping

steeply (50° – 60°) in the upper part of the crust, before becoming listric (25° – 30°) at greater depths (15 – 20 km). *Feenstra et al.* (2016) also calculated seismogenic cut-off depths for the region as ranging from 10 to 15 km. The minimum seismogenic zone thickness was observed beneath the Main Divide of the Southern Alps, which overlies a broad low-velocity zone. This likely results from the presence of fluids and/or elevated temperatures via enhanced exhumation in this central section (*Feenstra et al.*, 2016).

Chamberlain et al. (2017b) implemented matched filter detection techniques in an area around the DFDP-2 site in Whataroa (Fig. 3.1). They obtained 283 earthquake locations of small magnitudes ($M_L \leq 1.8$). The seismicity observed was diffuse and inferred to occur in a highly fractured zone around the Alpine Fault rather rather than on the discrete fault itself.

Guo et al. (2017) developed the latest 3-D P and S wave velocity model for the central Alpine Fault. They used the data compilation described in (*Feenstra et al.*, 2016) augmented with additional manual and automatic phase picks. *Guo et al.* (2017) substantially increased the number of observations used, compared to those of the previous seismic imaging studies in the area (*Eberhart-Phillips and Bannister*, 2002; *Bourguignon et al.*, 2015; *Feenstra et al.*, 2016; *Lay et al.*, 2016). By doing so, they were able to obtain high-resolution velocity models. They also relocated 700 earthquakes that were found to be clustered within or around low-velocity seismic zones.

Apart from the microseismicity studies mentioned above, there have also been studies examining other more recently recognized seismic phenomena. These studies detected seismic tremor (*Wech et al.*, 2012, 2013), low-frequency earthquakes (*Chamberlain et al.*, 2014; *Baratin et al.*, 2018), subcrustal earthquakes (*Boese et al.*, 2013, 2018) and fault zone guided waves (*Eccles et al.*, 2015) along the central portion of the Alpine Fault.

3.3 Data

We use data from the SAMBA network (SAMBA; *Boese et al.*, 2012) and four other temporary seismic networks in conjunction with data from five GeoNet national network sites. SAMBA has been operating since late 2008 and initially consisted of 10 borehole stations with short-period sensors recording at 200 Hz. In March 2013, the array was expanded towards the southwest with the addition of three further surface stations (*Baratin et al.*, 2018).

Since installation of the SAMBA network, several other temporary seismic networks have been deployed nearby. The ALFA-08 network was installed northeast of SAMBA and covered the area between Harihari and Hokitika (Fig. 3.1) (*Bourguignon et al.*,

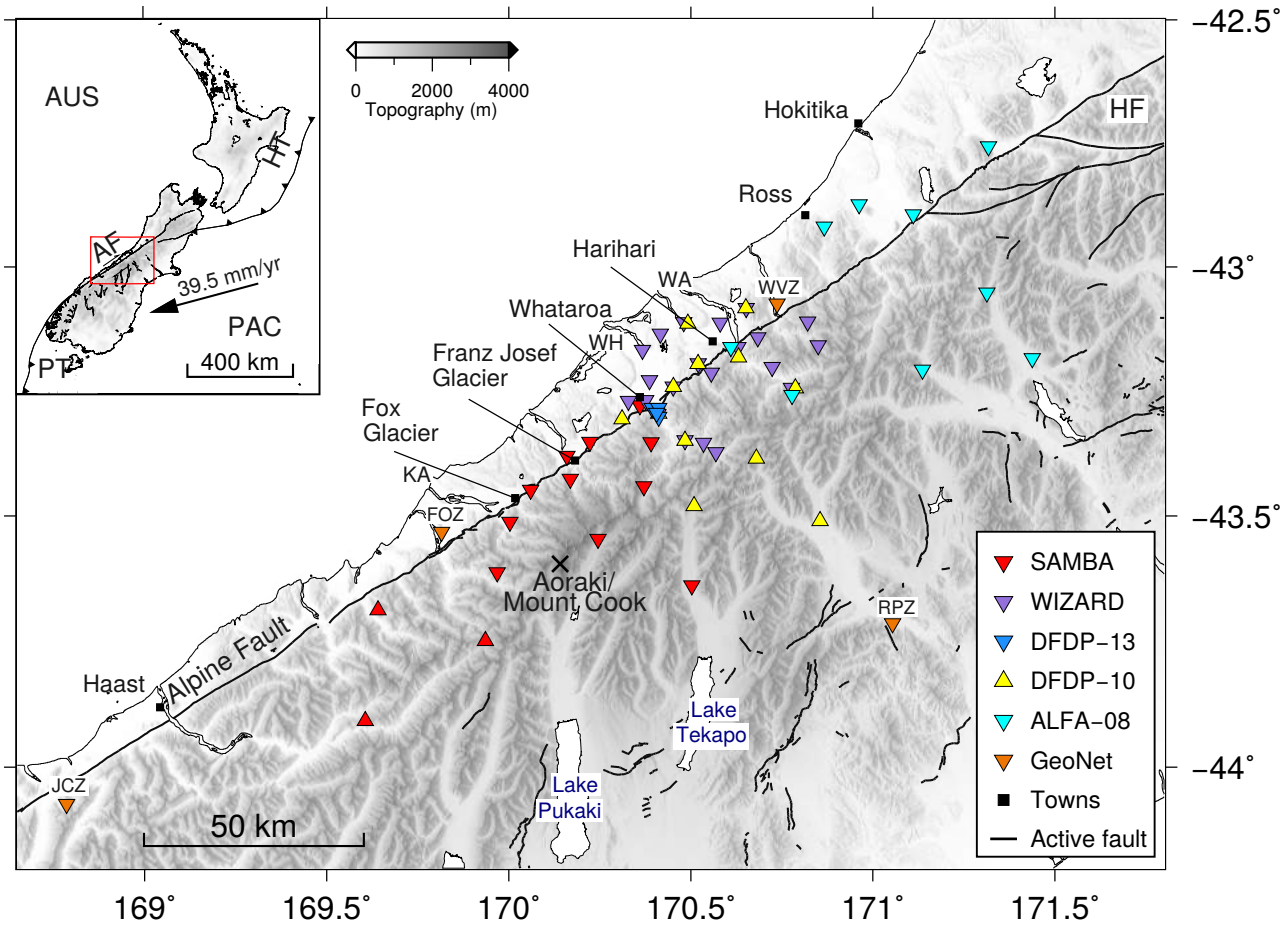

Figure 3.1: Distribution of seismic networks used in this study, consisting of 68 sites in total. These seismic networks operated for various lengths of time between November 2008 and March 2017. Orange, cyan, purple, blue and red inverted triangles depict the permanent GeoNet broadband national network, the ALFA-08, the WIZARD, the DFDP-13 and the SAMBA seismic sites, respectively. Yellow and red triangles show the DFDP-10 network and the three latest SAMBA seismic sites, respectively. Black lines show the active faults from the New Zealand Active Faults Database[4]. HF is the Hope Fault. WA, WH and KA stand for the Wanganui, Whataroa and Karangarua Rivers, respectively. Inset map shows the location of the study area within New Zealand. PAC, Pacific plate; AUS, Australian plate; PT, Puysegur Trench, HT, Hikurangi Trough and AF, Alpine Fault. Arrow indicates the local velocity of Pacific Plate relative to Australia (∼39.5 mm/yr in Fox Glacier; *DeMets et al.*, 2010).

2015). ALFA-08 comprised eight seismometers that operated from October 2008 until October 2009. The Whataroa-Wanganui Passive Seismology Experiment 2010 (DFDP10; *Boese et al.*, 2014) was part of the Deep Fault Drilling Project (*Townend et al.*, 2009) and consisted of 12 short-period seismometers operating from January to April 2010 between the Whataroa and Wanganui Rivers (Fig. 3.1). The WIZARD network was established northeast of SAMBA in January 2012 (*Feenstra et al.*, 2016) and operated until January 2014. WIZARD consisted of 10 short-period sensors 10 ten broadband sensors all recording at 100 Hz. The DFDP-13 network comprises four shallow borehole (28 m deep) short period sensors that were installed in January 2013 (*Chamberlain et al.*, 2017a) around the DFDP2 drill site (*Sutherland et al.*, 2017) in Whataroa Valley (Fig. 3.1). In addition, we use five seismic sites from GeoNet's permanent broadband national network (*Petersen et al.*, 2011).

The continuity and density of the SAMBA network allows us to obtain a nearly homogeneous and continuous earthquake catalog for the central Southern Alps over a longer time period than has ever been done previously. By augmenting the SAMBA network with three new SAMBA sites, four other temporary networks and the five GeoNet seismic sites, we extend the region of high resolution up to 150 km along-strike of the Alpine Fault. The combined seismic network consists of 68 sites in total. Of these 68 sites, between 15 and 42 of them operated at the same time from late 2008 and early 2017 (compared to five permanent GeoNet sites). The average station spacing in the central part of the network varies from 7 to 15 km; in the peripheral part of the composite network the station spacing increases up to 50 km (GeoNet's network spacing is 80 to 100 km). Seismic site coordinates, altitudes, sensor types and data continuity can be found in Appendix A.

3.4 Methods

3.4.1 Automatic detection and location of earthquakes

To obtain a uniform earthquake catalog, we use a semiautomatic processing method to analyze, in a consistent way, the entire data-set in a relatively short amount of time. The automatic processing steps implemented are summarized below. Initial processing of the continuous raw data-set (e.g. data conversion from Reftek format to single channel MiniSEED files) is done using the ObsPy package in Python (*Beyreuther et al.*, 2010; *Krischer et al.*, 2015).

We make preliminary detections using a ratio of short-term average to long-term average (STA/LTA) detection algorithm (*Allen*, 1978) with site-specific trigger values (e.g.short-term average, long-term average values, triggering thresholds) and band-

pass filters. This enables us to optimize the performance of the triggering algorithm, especially at noisy sites. We make detections when four or more sites trigger within 8s. Details of the parameters used for the triggering algorithm are provided in Tables B.2 and B.3 of Appendix B. At this stage, all triggers are still considered as potential earthquakes. Next, we use an automatic phase picker called kpick (*Rawles and Thurber*, 2015) to define the preliminary P and S wave picks, where possible, in a 30-second window cut around the preliminary detections. The kpick algorithm uses a nearest-neighbor approach based on the method for classifying time series developed by *Nikolov* (2012). The algorithm uses a number of reference waveforms known to contain P and S wave phases to identify phase onsets in the input waveforms.

To evaluate kpick's accuracy, we compare its automatic picks with manual picks from the existing catalog of *Boese et al.* (2012). To do this, we re-run our automatic detection process with the same data-set *Boese et al.* (2012) used and make automatic picks using kpick. In total we compare 4,175 P and 3,139 S wave picks. The comparison shows that 96% and 90% of the automatic P and S wave picks, respectively, are within 0.2 s of the manual picks made by *Boese et al.* (2012) (Fig. 3.2).

We determine preliminary hypocenter locations using the HYPOCENTER location algorithm (*Lienert et al.*, 1986) incorporated in the SEISAN analysis software (*Havskov and Ottemoller*, 2008) and a 1-D velocity model developed by *O'Keefe* (2008) and modified by *Boese et al.* (2012). The location process is carried out iteratively whereby we remove picks with the highest residuals at each iteration until quality criteria are met in this case, we set the minimum number of P wave picks to 4, the minimum number of S wave picks to 3 and the maximum permissible root-mean-square (rms) travel time residual to 1s. A final quality check applied to those potential earthquakes meeting the quality criteria was to manually inspect the automatic picks and remove any earthquakes with poorly associated picks. It was found to be more efficient to manually inspect these autolocated potential earthquakes rather than to inspect every single detection. A total of 222,678 automatic P and S wave phase arrivals were inspected: of these, 96,674 were retained, 53,583 were re-picked and the rest were removed as false picks. In terms of earthquakes, 10,827 events were manually inspected ultimately yielding 9,111 revised events.

To reduce the preliminary earthquake location errors obtained from HYPOCENTER, we use the probabilistic non-linear location software package NonLinLoc (*Lomax et al.*, 2000). We choose to use NonLinLoc for the absolute earthquake locations for the following reasons: (1) This method includes second order terms in the calculations, which gives greater depth sensitivity and accuracy for shallow earthquakes. (2) It enables the use of 3-D P and S wave velocity models. (3) The method includes station elevation information for the creation of the velocity grid and the calculation of the travel times. The input parameters used in NonLinLoc (*Lomax et al.*, 2000) are described in

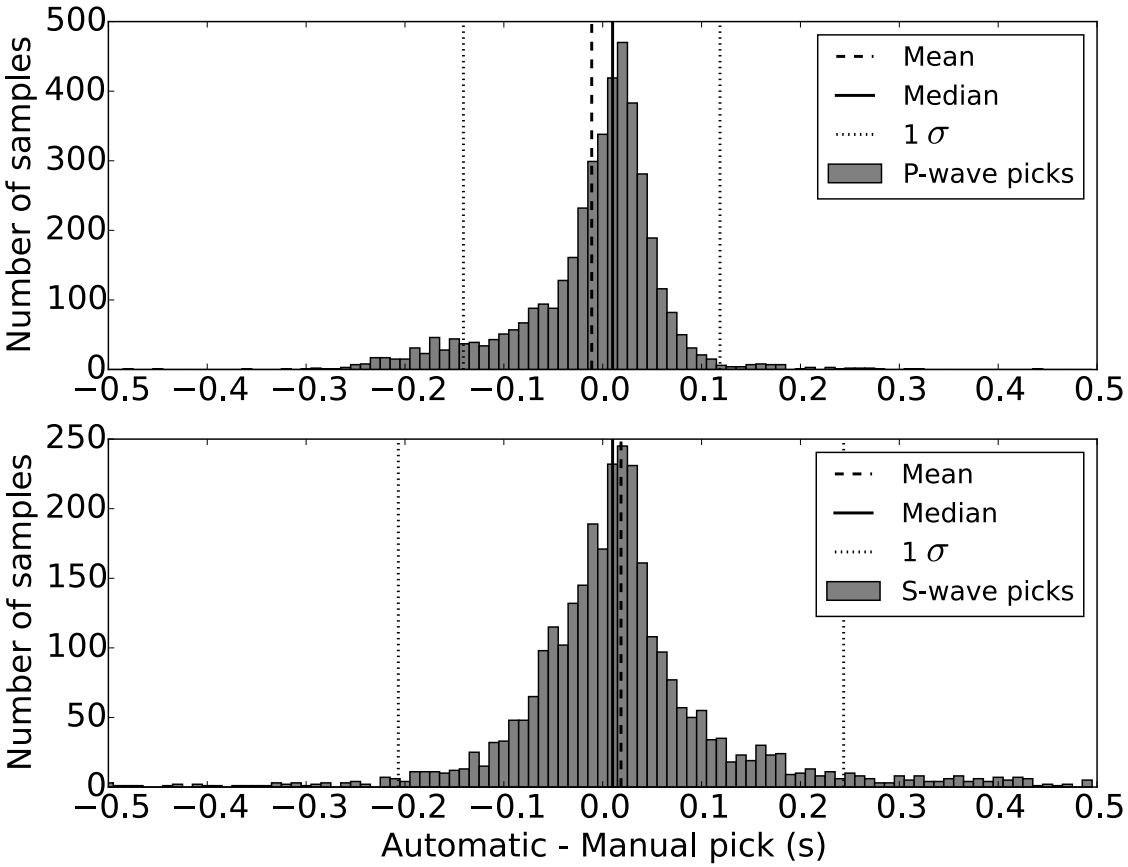

Figure 3.2: Difference between automatic (this study; kpick) and manual (*Boese et al.*, 2012) phase pick times for earthquakes recorded by SAMBA and GeoNet stations between November 2008 and December 2009. The upper box shows the P wave pick time differences, while the lower box shows the S wave pick time differences. Dashed, solid and dotted lines show the mean, median and standard deviation (1σ) of the distribution, respectively.

table B.5 of Appendix B.

3.4.2 Magnitudes

We estimate local magnitudes to quantify the spatial distribution of the earthquakes' moment release following the same approach as *O'Keefe* (2008) and *Boese et al.* (2012). To do that, we use two data-sets of earthquakes. The first data-set consists of 65,709 half peak-to-peak amplitude measurements, from the 9,111 absolute earthquake locations determined here. Amplitudes are automatically picked on the horizontal components of seismograms in a 1-s time window starting after the S wave picks, using a utility function from the EQcorrscan Python package (*Chamberlain et al.*, 2017c). Details on the function used to pick amplitudes are available in Appendix B. The second data-set contains 74 earthquakes recorded in this study for which M_w values have been calculated using moment tensor inversion of GeoNet national network data (*Ristau*,

2013).

We invert amplitude picks and hypocentral distance information to derive a new local magnitude scale for the Southern Alps region tied to M_w values and corrected for geometric spreading and attenuation. The local magnitude scale was originally defined by *Richter* (1958) as :

$$M_L = \log_{10}(A/A_0) \tag{3.1}$$

where A is the mean amplitude in microns of the horizontal components of a Wood-Anderson seismograph with a fundamental period of 0.8 seconds and magnification of 2080 and A_0 is the amplitude expected on the same type of instrument at 100 km from the earthquake. The effects of geometric spreading and anelastic attenuation are estimated in place of the A_0 term in (1) and an adjustment is made for the instrument magnification and frequency response of each seismic site with the addition of a site term. The result is expressed in terms of the observed amplitudes A_j.

$$\log_{10} A_j = M_{Lu} - \alpha \log_{10} r_j - \eta r_j + S_j + \epsilon_j \tag{3.2}$$

where M_{Lu} is the uncalibrated local magnitude, r_j is the slant distance (km) of the hypocentre from seismic station j, S_j is the site term, α is the geometric spreading parameter (here assumed to be 1), η is a constant that corrects for anelastic attenuation and ϵ_j is a random error. The anelastic attenuation parameter η is related to Q by:

$$Q = \frac{\beta}{\pi \eta f} \tag{3.3}$$

in which β is the shear wave velocity (km/s), appropriate for amplitudes measured on the horizontal components and f is the frequency (Hz) of the wave with the maximum amplitude. M_{Lu} values are then calibrated by relating them to the predetermined M_w values:

$$M_{Lu} = M_w + C + \xi \tag{3.4}$$

where ξ is a random error. We estimate C and the standard deviation of ξ from the mean and standard deviation of the difference between M_{Lu} and M_w. Equation 2 is solved by least squares. For N earthquakes recorded M times in total on K seismographs, this results in M equations in N+K+1 unknowns.

$$\mathbf{Y} = \mathbf{Xm} + \mathbf{e} \tag{3.5}$$

$\mathbf{Y}$ includes the known variables: 65,708 automatically picked amplitudes and 74 GeoNet moment magnitudes (M_w). $\mathbf{X}$ is the matrix containing the reference data (events located in this study that match timing and location of GeoNet events). $\mathbf{m}$ is the list of the parameters of interest (new magnitudes, attenuation parameter and station

correction terms) and **e** is the vector of magnitude residuals. We solve the equations, using a subset of 4,000 events recorded between 2008 and 2017; we could not use the whole set of events due to insufficient computing memory. The subset used was carefully selected so each seismic site had enough observations to provide us with reliably estimated site term values S_j. This way, the equations are of rank $N+K$, since the mean uncalibrated magnitude and the mean station term cannot be independently estimated. This problem is overcome by constraining the sum of the site effects S_j to be zero.

We noted that the preliminary results obtained from the two data-sets (4,000 events and the 74 M_w values) gave different values for the attenuation parameters. After trials, it was found that this problem arose from the fact that the majority of the 4,000 events had smaller slant distance values (r_j) than the events with M_w values, which tended to be more distant. Thus, we calculated two attenuation parameters; one for events with r_j up to 60 km and one for the events for the remaining paths (r_j – 60 km). After doing so, there was good agreement between the results obtained from the two different data-sets (the rms of the scatter is less than 0.1; Figure B.4 in Appendix B). The results are not sensitive to the choice of 60 km, but transitions at 40 and 80 km gave inferior results.

3.4.3 Hypocenter relocation

We use double difference techniques (*Waldhauser and Ellsworth*, 2000) to further constrain the earthquake hypocenters. In particular, we use the latest HypoDD version, 2.1b, (*Waldhauser*, 2001) which includes station elevations for the travel time calculations and enables the use of 3D velocity models. We use the 3D P wave velocity model obtained by *Guo et al.* (2017) and a constant V_P/V_S ratio of 1.70 (the value used to construct the velocity models).

For each earthquake, we create differential times with up to 20 neighboring events within 10 km of one another and with a maximum source-receiver distance of 200 km. For each earthquake pair, we calculate differential travel times for both P and S wave phases for up to 50 stations. The minimum number of links required to define a neighbor is 8. In total we compute 3,501,920 catalog differential travel times. We then calculate differential travel times using waveform cross-correlation. We divide the dataset into four subsets according to the operating time periods of the temporary seismic networks used (Figure B.1 of Appendix B). We do this to make the cross-correlation calculations more practical and time efficient. We band pass each seismogram between 2 and 20 Hz and use a window starting 0.1 s before and ending 0.4 s after both P and S phase picks, applying time shifts of up to 0.1 s. We use the cross-correlation approach of *Deichmann and Garcia-Fernandez* (1992) that fits a parabola to the five samples

closest to the sample with the highest cross-correlation coefficient. A cross-correlation coefficient of 0.6 has to be exceeded for the event pair to be listed in the cross-correlation catalog. We obtain 1,058,547 cross-correlation differential travel times.

During the first weighting iterations of HypoDD, we apply full weight to the catalog pick differential times to obtain initial bulk relocations for all earthquakes. In the following iterations, we increase the weights of the cross-correlation differential times and progressively down-weight the catalog pick differential times. In the final iterations, we only use the cross-correlation calculations to further refine the hypocenter locations. Input parameters used in HypoDD (*Waldhauser*, 2001) are shown in table B.6 of Appendix B.

3.5 Results

3.5.1 Magnitude estimations

Using the method described in Section 3.3, we rewrite equation (2) to obtain the following:

$$\mathrm{M_{Lu}} = \log_{10} A_j + \log_{10} r_j + \eta r_j - S_j - C \tag{3.6}$$

where r_j is the slant distance, A is the amplitude observation and C is the mean $\mathrm{M_{Lu}}$ – $\mathrm{M_w}$ difference equal to –3.644 ± 0.50 (95% CI), which includes the Richter magnitude constant. The attenuation parameter η is calculated separately for two different hypocentral distance ranges, η_1 for ≤ 60 km (1.20×10^{-2} km^{-1}) and η_2 for > 60 km (0.01×10^{-2} km^{-1}). η_1 and η_2 values are shown in Table 3.1, along with their corresponding Q values. Our attenuation parameter values are similar to previous estimates by *O'Keefe* (2008) (1.69×10^{-2} km^{-1}) and *Boese et al.* (2012) for hypocentral distances ≤70 km (1.89×10^{-2} km^{-1}). However, for hypocentral distances exceeding 70 km *Boese et al.* (2012) obtained an attenuation parameter of 0.95×10^{-2} km^{-1}, which is larger by a factor of almost 100 from the corresponding attenuation value calculated here. This discrepancy arises from the broader area examined in this study. To calculate the Q values we use nominal wave frequencies of 5 and 10 Hz and shear wave velocities, β, of 3 and 3.5 km/s for the upper and lower crust, respectively. Q values are low (<100) for distances <60 km, and one to two orders of magnitudes higher at larger distances. These values are comparable to the low Q_p values of 100–200 *Eberhart-Phillips et al.* (2008) obtained for the brittle crust from the 3-D attenuation structure. The newly derived attenuation parameters' effect on the magnitude estimates is shown in Figure B.2 of Appendix B. Magnitude residuals calculated with the new magnitude scale display no bias with hypocentral distance, and hence yield an average residual of near zero at all hypocentral distances.

The magnitudes calculated range from –1.2 to 4.6 (events in GeoNet's catalog from the same region have local magnitudes between 1.3 to 4.9). We compare a subset of our magnitude estimates to the corresponding estimates in the catalog of *Boese et al.* (2012). On average, our results are 0.32 ± 0.03 (95% CI) magnitude units smaller (Figure B.4 in Appendix B). This discrepancy likely arises because the magnitudes calculated here are tied to M_w values instead of M_L values and are expected to better represent the moment released. We obtain a magnitude of completeness of M_c=1.1, which is similar to that of *Boese et al.* (2012, M_c=1.4) when the average difference in magnitudes between the two catalogs are taken into account. It should also be noted that *Boese et al.* (2012) used a different detection method and number of stations. In comparison, the GeoNet catalog has a substantially higher M_c of 2.6. A b-value of 0.850 ± 0.003 is calculated by fitting the cumulative density function with a power-law above the magnitude of completeness and is similar to that found in the previous analysis (b-value = 0.86; *Boese et al.*, 2012).

Table 3.1: Attenuation parameters and estimated Q values. CI is the confidence interval.

Earthquake data set	η_1	95% CI	Estimated Q (f=5,10 Hz)	η_2	95% CI	Estimated Q (f=5,10 Hz)
M_w	0.005	±0.0036	20-40	0.0012	±0.0016	100-200
Combined	0.012	±0.00044	10-16	0.00010	±0.0008	1000-2000

3.5.2 Absolute earthquake hypocenter locations and uncertainties

Taking advantage of our dense seismic network, we are able to locate approximately 9,000 events spanning from late 2008 to early 2017 using the NonLinLoc location program *Lomax et al.* (2000). We also locate 41 quarry blasts close to the SAMBA site in Whataroa (Fig. 3.1). For the same time period and area, GeoNet recorded and located 2,151 earthquakes, which commonly have fixed depths, due to the sparser network spacing. Our initial data set consists of 83,138 P and 67,119 S wave high precision phase picks. Of these, 64.3% are automatic phase picks that have been manually revised, while the remainder are manual picks. For further details on the initial earthquake locations, refer to Figure B.6. The distance to the closest station provides us with a good indication of the quality of the hypocenters. In our case, 90% of the earthquakes have distances smaller than 27 km and have a mean of 9.8 km. Hence earthquakes that are deeper than approximately 10 km will have better-constrained depths.

Uncertainties of the absolute earthquake locations are calculated by fitting the 68%

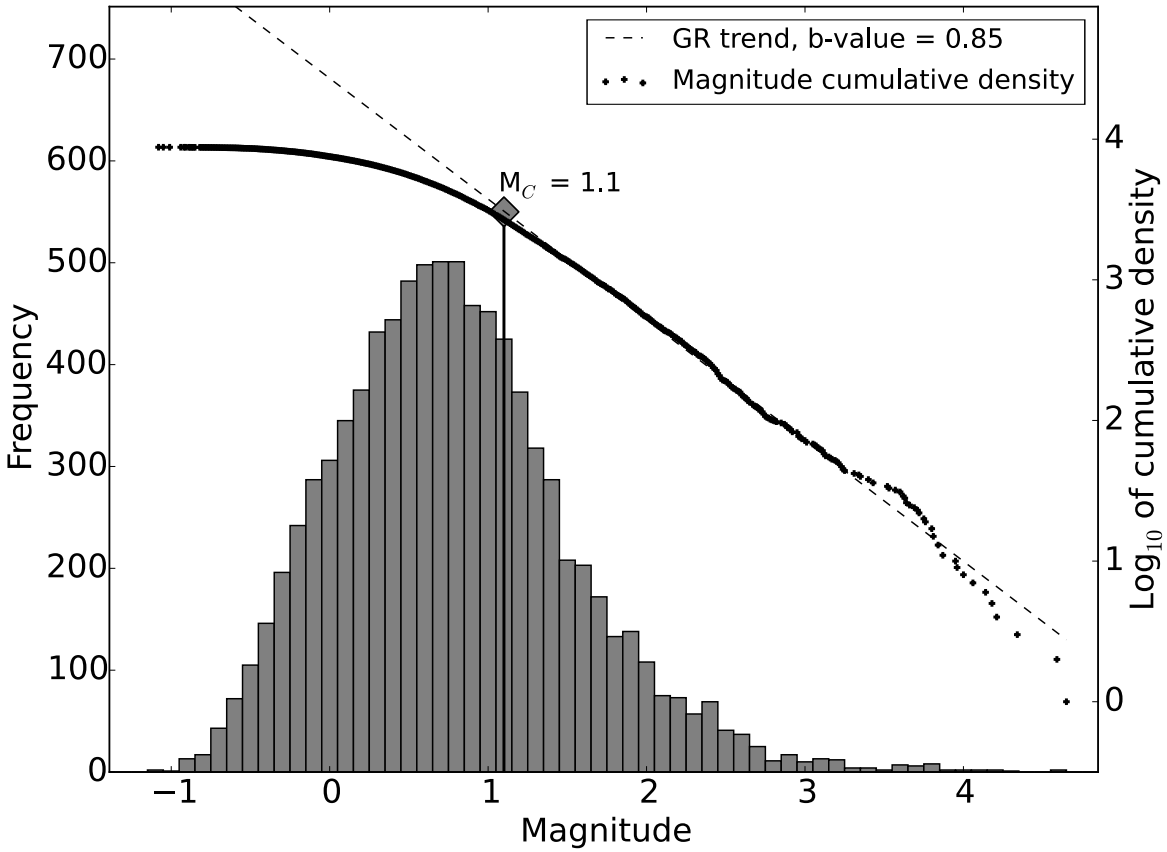

Figure 3.3: Magnitude frequency distribution of earthquakes in the central Southern Alps region from November 2008 to March 2017. Left axis (Frequency) represents the number of earthquakes in each magnitude bin. Right axis (logarithm of cumulative density) shows the cumulative number of earthquakes of magnitude M_L and higher. The magnitude of completeness (M_c = 1.1) is calculated using the goodness of fit test method (*Wiemer and Wyss*, 2000). The b-value is equal to 0.85 and is calculated by fitting the cumulative density function with a power-law above M_c.

confidence ellipsoid of the posterior probability density function (*Lomax et al.*, 2000). Probability density function solutions are nonlinear and depend on the event position relative to the seismic network, the arrival time errors and the theoretical travel time errors (*Lomax et al.*, 2000). Location uncertainties are controlled by the distribution of the seismic network in time and the velocity model used. Overall, 90% of the absolute earthquake hypocenters show average horizontal errors less than 503 m (median 273 m) and depth errors less than 801 m (median 370 m)(Fig. 3.4a,b).

3.5.3 Relative earthquake hypocenter relocations and uncertainties

Of the initial 9,111 earthquakes, we were able to relocate 7,719 events using double-difference techniques. The relocated earthquake catalog is available as supporting information. We calculate relative location uncertainties using 200 bootstrap resamplings (*Efron and Gong*, 1983) and the approach described by *Mesimeri et al.* (2017). We resample the residuals derived from the final double difference inversion, add them to the differential times of each event with unit weights and repeat the relocation for each resample. We then use the covariance matrix of the spatial distribution of the differences between the resamples and the final locations to estimate the relative location uncertainties. In general, 90% of the relative earthquake locations' uncertainties in the horizontal direction are smaller than 314 m (median 86 m), while in depth 90% of the relative errors are smaller than 491 m (median 130 m)(Fig. 3.4c,d).

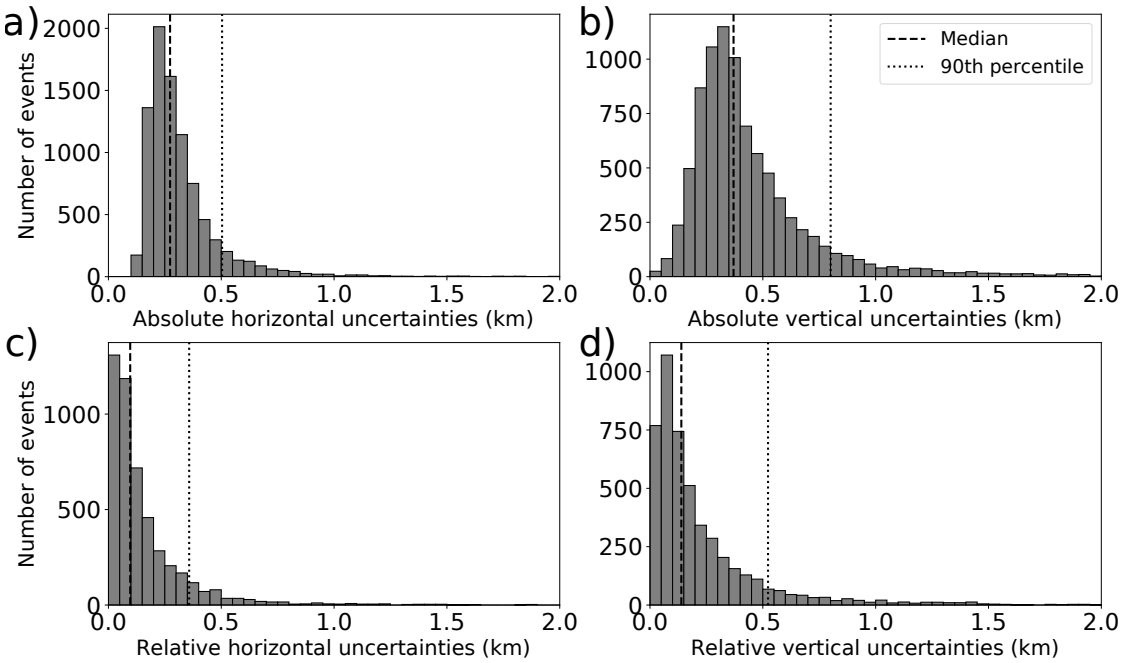

Figure 3.4: Distributions of location uncertainties in the horizontal and vertical directions given by NonLinLoc and HypoDD in the top and bottom row boxes, respectively. (a, b) Absolute earthquake uncertainties are obtained from the dimensions of the the posterior probability density function (PDF) determined by NonLinLoc. (c, d) Relative uncertainties were obtained from bootstrapping tests for 200 resamples for the HypoDD locations. Dashed and dotted lines show the median and the 90th percentile of the distribution, respectively.

Figure 3.5 shows the final relocated seismicity distribution for 7,719 earthquakes from late 2008 to early 2017. Earthquake epicenters delineate the surface trace of the Alpine Fault and otherwise mainly occur on the southeastern side of the Fault (hanging-wall), which is known to be highly fractured (*Cox et al.*, 2015; *Townend et al.*, 2017). We divide hanging-wall seismicity into three clusters according to the earthquakes' spatial

distribution and magnitudes (Fig. 3.5). Cluster 1 occurs in the northeastern edge of our network and has larger magnitudes and deeper hypocenters relative to the adjacent areas (Fig. 3.6, cross-section A–A'). Cluster 2 lies within the previously identified Whataroa seismic gap (*Leitner and Eberhart-Phillips*, 2001; *Boese et al.*, 2012). Seismicity there is sparse and consists of small-magnitude earthquakes at shallow depths (Fig. 3.6, cross-sections B–B' and C–C'). Seismicity at greater depths outlines the Whataroa seismic gap (Fig. 3.7). Cluster 3 lies within the SAMBA network, the area of highest topography and exhibits anomalously shallow and low-magnitude seismicity (Fig. 3.6, cross-sections D–D' and E–E'). The vicinity of cluster 3 is also where low-frequency earthquakes, detected by *Chamberlain et al.* (2014) and *Baratin et al.* (2018), have been observed. We observe some sparse seismicity on the northwest side of the Alpine Fault (footwall). This might be due to the the sparser seismic network coverage in that region. We also observe 42 earthquakes with hypocenter depths of between 25 and 50 km.

The distribution of seismicity with depth is highly variable along the strike of the central Alpine Fault, ranging from less than 9 km beneath the area of highest topography to greater than 20 km at the northeastern edge of our network. Figure 3.7 illustrates two cross-sections parallel to the strike of the Alpine Fault and a cross-section of the $^{40}Ar/^{39}Ar$ hornblende ages contour obtained by *Little et al.* (2005). We observe a change in seismicity cut-off depth of up to 10 km in both cross-sections. The lack of seismicity at larger depths beneath Aoraki/Mount Cook partly coincides with the distribution of the low-frequency earthquakes and the youngest hornblende cooling ages. The youngest cooling ages are associated with deeper exhumation and thus higher uplift rates. Seismicity adjacent to the Alpine Fault's surface trace is diffuse and of low-magnitude (Fig. 3.7, cross-sections F–F'). Moving further southeast (away) from the Alpine Fault's surface trace we observe more earthquakes with larger depths and magnitudes (Fig. 3.7, cross-sections G–G'). To ensure that this variation of the distribution of seismicity with depth is not an artifact, we repeated the location and relocation process using the 1-D velocity model of (*O'Keefe*, 2008). The earthquake hypocenters obtained using different location methods and the 1-D velocity model also exhibit the almost 10 km difference in seismogenic cut-off depths (Appendix B, Figures B.9 – B.11). In addition, we do not observe any major differences in the 3-D velocity structure beneath Aoraki/Mount Cook (Appendix B, Figures B.12 – B.15; *Guo et al.*, 2017) that might account for the observed variation in seismogenic cut-off depths.

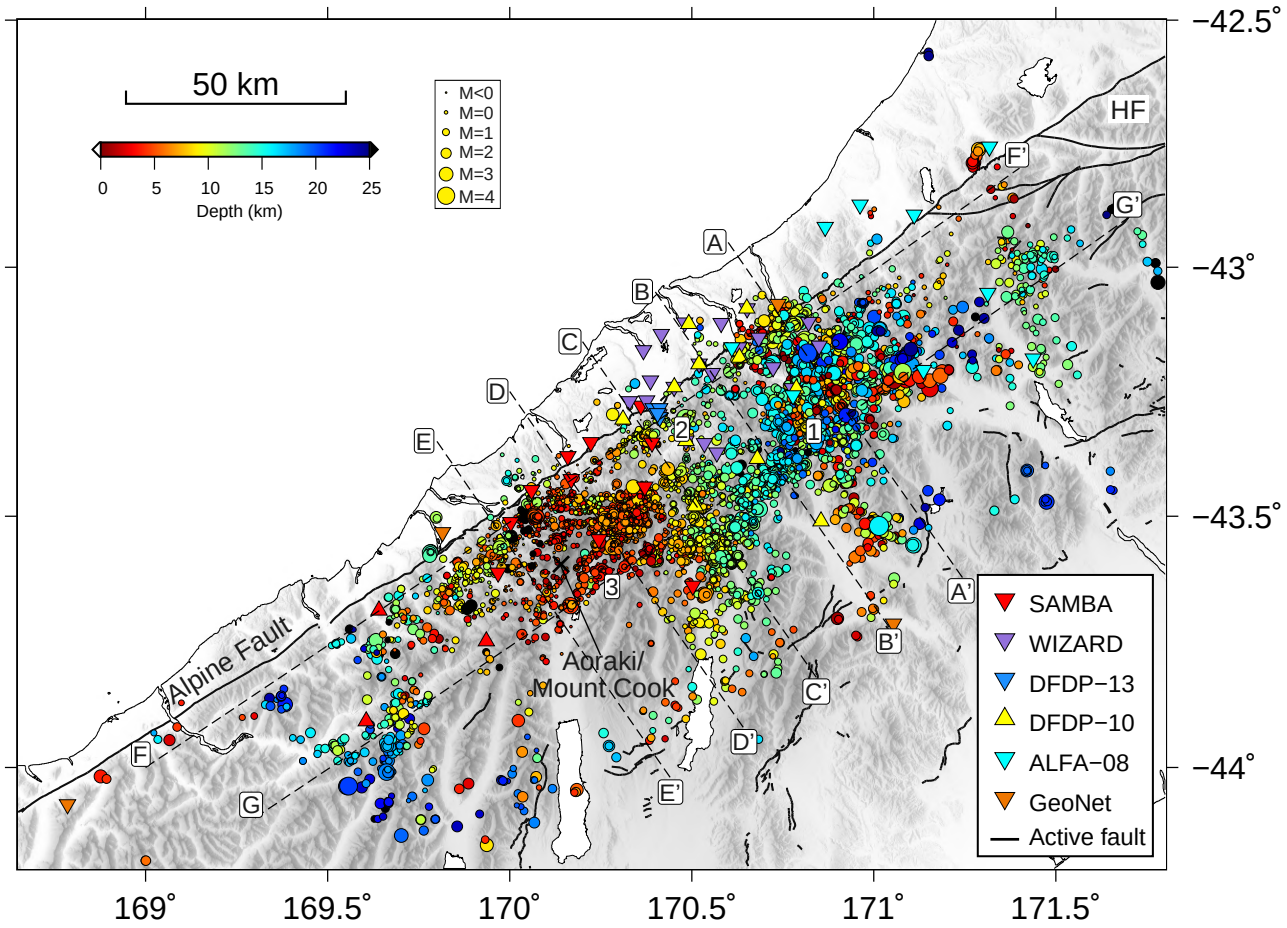

Figure 3.5: Map of 7,719 relocated hypocenter locations, scaled by their respective newly calculated magnitudes for the central Southern Alps region and between November 2008 and March 2017. Earthquake epicenters shown as circles are colored according to their depths (see color scale). Thin black dotted and solid lines with capital letters indicate cross-sections shown in Figures 3.7 and 3.6. 1, 2 and 3 show the seismicity clusters described in the text. Aoraki/Mount Cook is represented by a cross. SAMBA = Southern Alps Microseismicity Borehole Array; WIZARD = Wisconsin New Zealand Array Rensselaer Deployment; DFDP = Deep Fault Drilling Project; ALFA-08 = Alpine Fault Array.

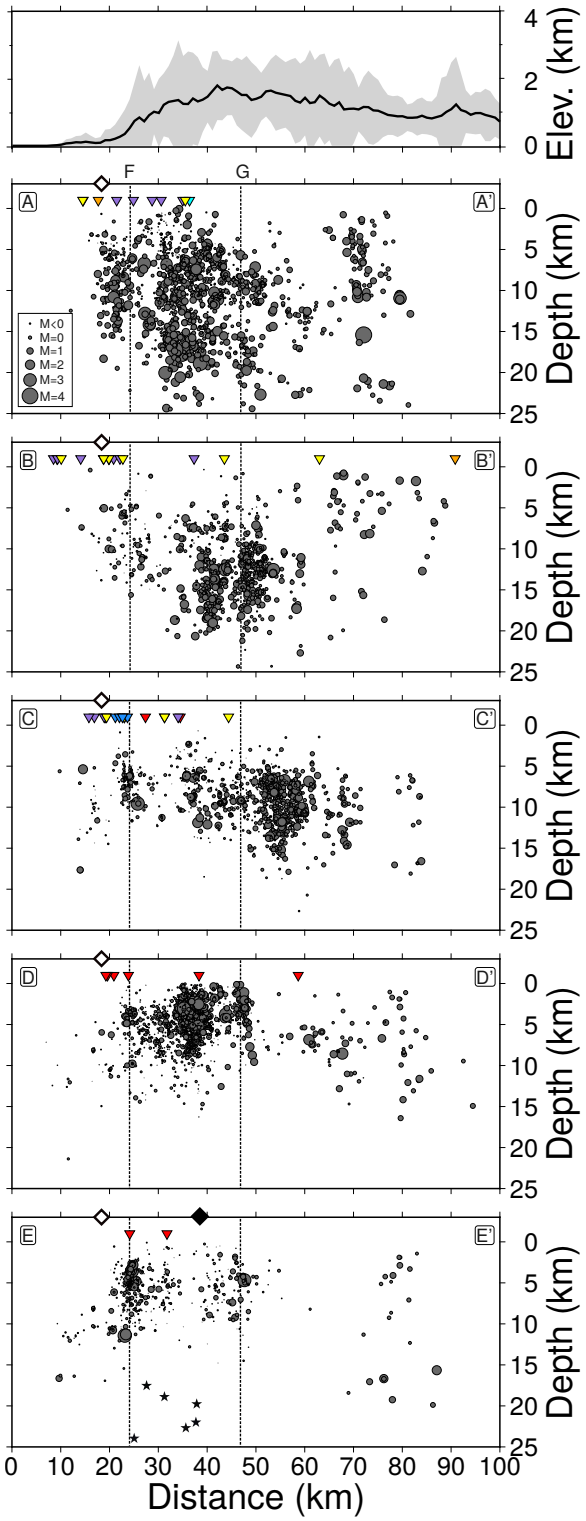

Figure 3.6: Cross-sections of relocated earthquake hypocenters perpendicular to the strike of the Alpine Fault, scaled by magnitude as marked on Fig. 3.5. Earthquakes within 10 km on either side of the cross-section are shown. Stars show locations of low-frequency earthquakes (*Baratin et al.*, 2018). Inverted triangles depict the seismic sites within each cross-section. Black and white diamonds show Aoraki/Mount Cook and the surface trace of the Alpine Fault, respectively. Intersection lines of cross-sections F and G from Fig. 3.7 are also shown. The top panel shows the stacked (median) profile of the elevation in kilometers (black line) and the distribution of topographic profiles within a 10-km swath (gray area). Note that cross-sections are vertically exaggerated.

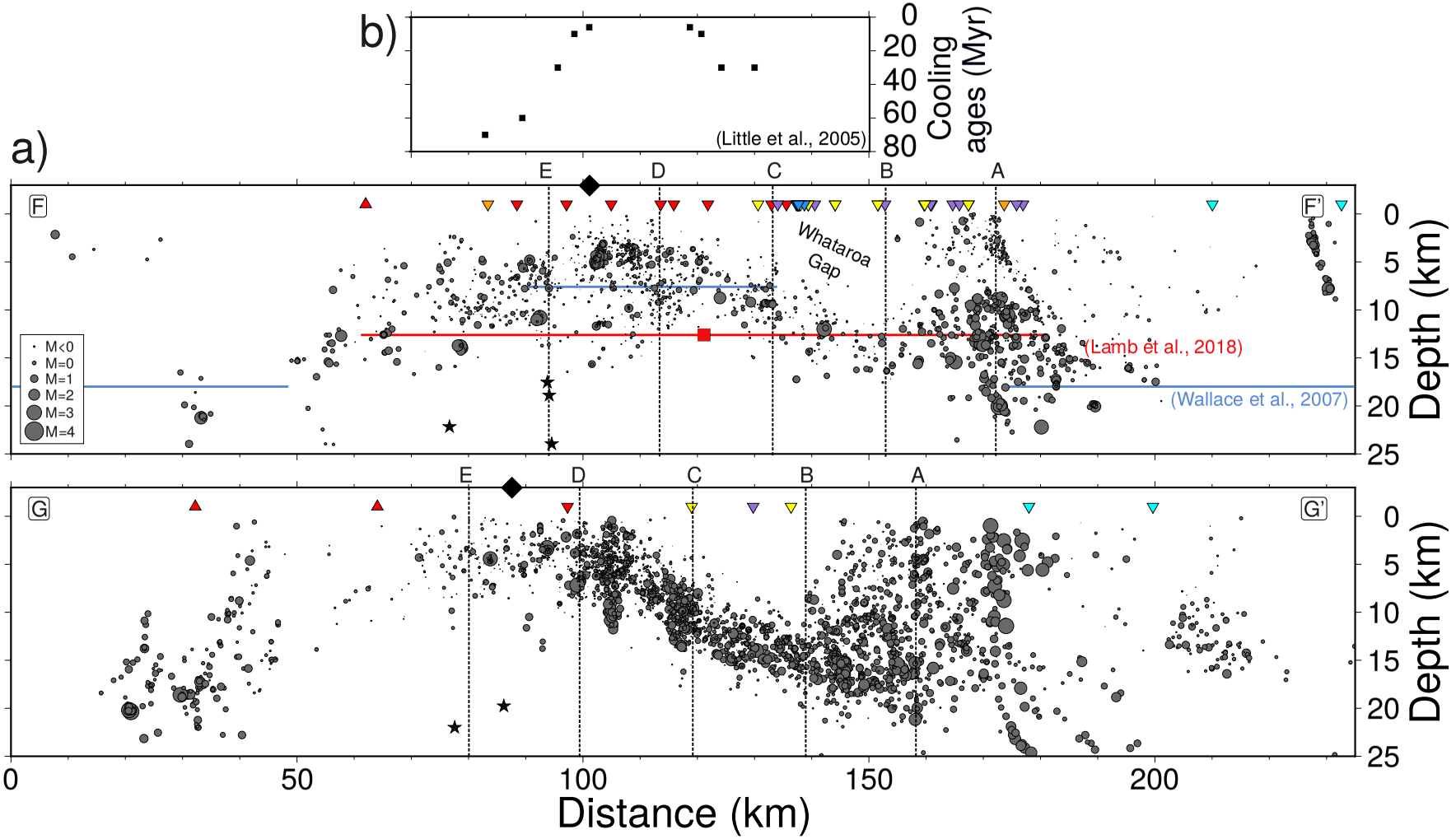

Figure 3.7: (a) Cross-sections of earthquake relocations along the strike of the Alpine Fault with respective magnitudes as shown in Figure 3.5. The locations of the cross-sections are labeled with capital letters in Figure 3.5. Earthquakes within 10 km on either side of the cross-section are shown. Stars show locations of low-frequency earthquakes (*Baratin et al.*, 2018). Inverted triangles depict the seismic sites within each cross-section. Aoraki/Mount Cook is marked by a black diamond. Intersection lines of cross-sections A, B, C, D and E from Fig. 3.6 are also shown. Note that cross-sections are vertically exaggerated. Blue lines indicate the depth where the fault is 75 % coupled (100% = fully locked, 0% = fully slipping) from the block model of *Wallace et al.* (2007). Red line indicates the upper geodetic locking depth from the elastic model of *Lamb et al.* (2018), above which the fault is fully locked and below which the fault is fully slipping. Red square depicts the center of the profile across the Alpine Fault from Figure 6 of *Lamb et al.* (2018). (b) $^{40}Ar/^{39}Ar$ and K–Ar cooling age data for hornblendes from the central Southern Alps, New Zealand (*Little et al.*, 2005).

3.5.4 Spatial distribution of seismogenic cut-off depths

Seismogenic cut-off depths are commonly defined using the spatial distribution of microseismicity and especially the depths above which a specific percentage (e.g., 90, 95 or 99) of the seismicity occurs (*Nazareth and Hauksson*, 2004). These estimates are dependent on the accuracy of the earthquake locations, the clustering of the earthquakes and the choice of the criteria for the cut-off depths. Here we use the 95th percentile of the shallow relocated hypocenters (<25km) and a quadtree griding algorithm (*Townend and Zoback*, 2001) to cluster the earthquakes into square bins with a minimum side length of 2 km that each contain 25 to 100 events. For each bin containing sufficient earthquakes we calculate the 95th percentile of the hypocentral depths.

The seismogenic cut-off depths across the southeast side of the Alpine Fault (hanging-wall) vary from 7 to 22 km (Fig. 3.8). We obtain the thinnest seismogenic layer (<10km) for the area in the vicinity of Aoraki/Mount Cook, within the SAMBA network where the highest uplift rates are observed (*Little et al.*, 2005). Moving towards the southeast, perpendicular to the strike of Alpine Fault and northeast, along the strike of Alpine Fault the seismogenic cut-off depths get progressively deeper, reaching depths of as much as 22 km. The seismogenic cut-off depths in the foot-wall region are deeper by ∼5km than the adjacent boxes in the hanging-wall. The Whataroa seismic gap displays larger bin sizes and its limits are outlined by smaller bins. We observe large bin sizes in the peripheral regions, due to the smaller number of earthquakes detected and relocated, which is mostly due to the sparser network coverage.

3.6 Discussion

The earthquake catalog presented here contains 7,719 high-precision earthquake relocations (9,111 absolute locations), enabled mainly by the long duration and continuity of the SAMBA network (late 2008 to early 2017). By using additional temporary seismic networks, which augmented the area covered by SAMBA, we have been able to highlight the characteristics of seismicity along the central Alpine Fault for the first time and to investigate changes in seismogenic cut-off depths consistently. To generate this earthquake catalog we started with continuous data and applied a systematic processing routine to all the available data (see Sections 2 and 3.1). By doing this, we have avoided inconsistencies that may arise from combining different earthquake catalogs constructed using varying detection, picking and location methods. A brief comparison of the earthquake catalog constructed here with the previous ones can be found in Table B.1 of Appendix B.

Seismicity is clustered in swarms that mainly occur in the highly fractured hanging-

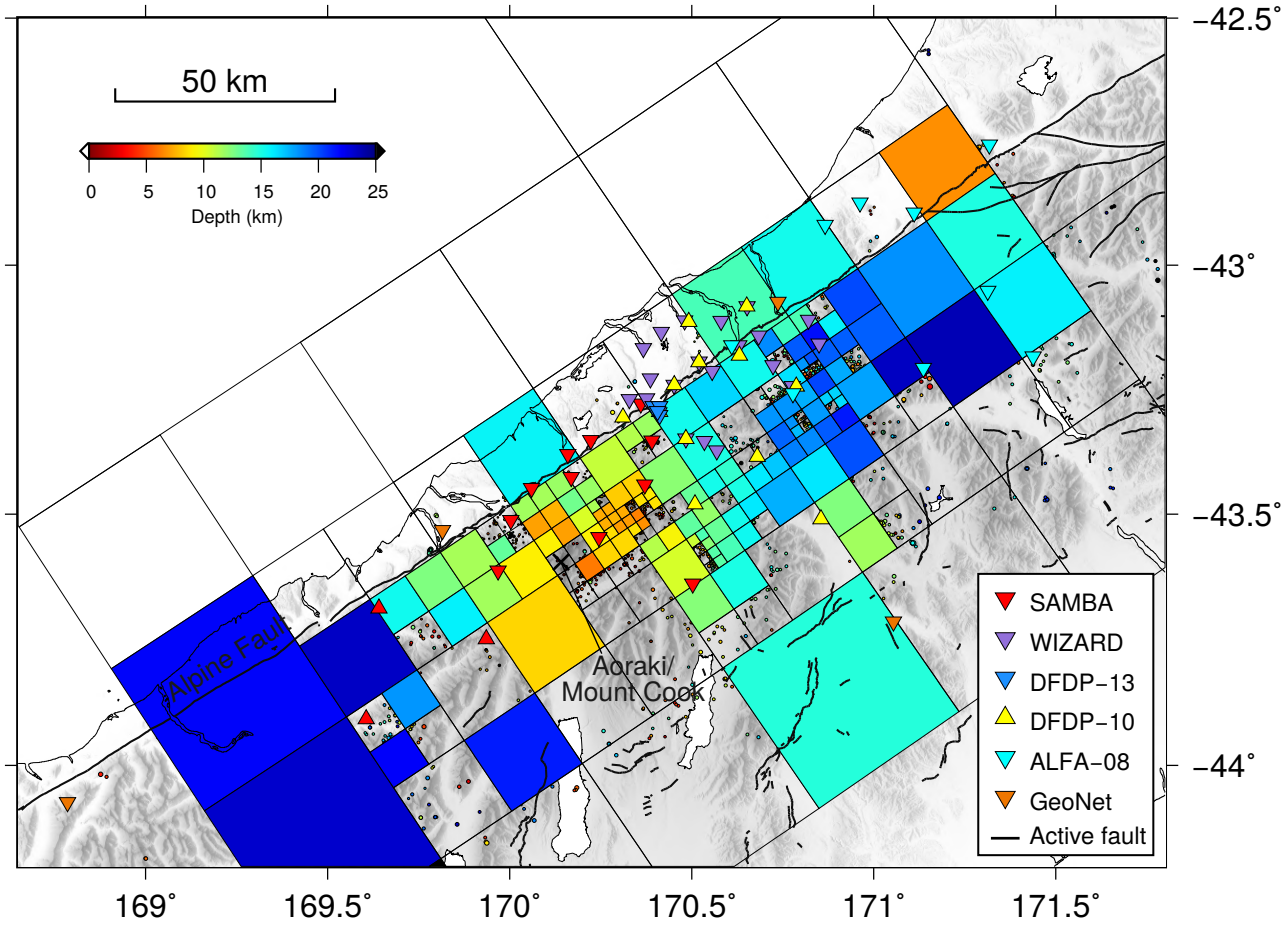

Figure 3.8: Distribution of the 95th percentile of the hypocentral depths in km obtained using a quadtree griding algorithm. Bins containing 25 to 100 earthquakes are colored according to their depths (see color scale) and have a minimum size of 2 km. Bins with fewer than 25 earthquakes are not colored. Earthquake epicenters are also shown as circles of the same size in the background.

wall southeast of the Alpine Fault's surface trace. We observe some sparse earthquake activity northwest of the Alpine Fault surface trace, within the foot-wall. Earthquake epicenters appear to delineate the Alpine Fault's surface trace but do not outline an obvious fault plane at depth. We note that the shallowest seismicity beneath Aoraki/Mount Cook, coincides with the area of the highest topography and uplift rates (*Norris and Cooper*, 2001; *Little et al.*, 2005). In particular, the anomalously shallow seismicity beneath Aoraki/Mount Cook seems to coincide with the lowest $^{40}Ar/^{39}Ar$ hornblende cooling ages (Fig. 3.7, cross-sections F–F'), which are related to exhumation rates of up to a maximum value of ∼6–9 mm/yr in the area (*Little et al.*, 2005). These high uplift rates are inferred to have distorted the isotherms towards the surface, enhancing the thermal gradients within the upper crust and making it weak (*Koons*, 1987; *Sutherland et al.*, 2012). As a result, this thermally weakened crust beneath Aoraki/Mount Cook appears to restrict the vertical distribution of seismicity by moving the brittle-ductile transition to shallower depths compared to the adjacent areas. There is an approximately 10-km difference in the depth of the brittle-ductile transi-

tion between Aoraki/Mount Cook and the adjacent areas where uplift rates are almost equal to zero. Further analysis and modeling of the heat flow beneath Aoraki/Mount Cook is required to examine this interpretation, but is beyond the scope of this paper.

This 10-km difference in the seismicity depths along the Alpine Fault has not been observed in previous seismicity studies due to the limited number of earthquakes they encompassed. (*Boese et al.*, 2012) observed a 5-km depth difference between profiles 1 and 5 in their Figure 4 (cross-section E–E' and A–A' Fig. 3.6 of this study). Profile 1 of (*Boese et al.*, 2012) lies within the SAMBA network and has seismicity shallower than 10 km, which is in agreement with the seismicity we observe. Profile 5 of (*Boese et al.*, 2012) has depths smaller than 15 km, while we observe depths as deep as 23 km. This difference in the seismogenic depths between the two studies arises because *Boese et al's* profile 5 lies in the boundary of their seismic network, which means that seismicity there can not be completely recorded. In addition, *Boese et al.* (2012) were only able to examine a year of seismicity (compared to eight years examined in this study).

Boese et al. (2012) interpreted the vertical distribution of seismicity in terms of a resistivity model derived by *Wannamaker et al.* (2002) along SIGHT transect T1, which coincides with cross-section C–C' (Fig. 3.6). We observe the same correlation of seismicity and high-resistivity areas as reported by *Boese et al.* (2012). A comparison of the lack of seismicity beneath Aoraki/Mount Cook with resistivity would be of great interest, but resistivity measurements have been only acquired along the SIGHT line, perpendicular the Alpine Fault.

Considering similar examples of large changes in the seismogenic depths on other large strike slip faults, we note an alternative explanation provided by *Jiang and Lapusta* (2016) for the absence of concentrated microseismicity at the bottom of the seismogenic zone on a mature segment of the San Andreas fault. *Jiang and Lapusta* (2016) proposed that a deeper penetration, beneath the seismogenic zone, of a previous large earthquake can move the brittle-ductile transition to depths below the seismogenic zone, where stresses building up are unlikely to produce earthquakes. In our case, an indication for a deeper brittle-ductile transition beneath Aoraki/Mount Cook may be obtained from the depth distribution of the low-frequency earthquakes reported by *Baratin et al.* (2018) that range from 17 to 42 km depths. In addition, the Alpine Fault is known to have produced large earthquakes in the past (*Sutherland et al.*, 2007; *Berryman et al.*, 2012), which supports that explanation. The most recent large Alpine Fault earthquake (1717 CE) is inferred to have ruptured at least 300 km of the length of the Alpine Fault including the central section (*Sutherland et al.*, 2007); however there is no available information on the depth of the rupture.

The seismogenic cut-off depths vary systematically along the strike of the Alpine Fault,

extending between less than 9 km at the southwestern edge of our network to more than 20 km at the northeastern edge. The distribution of our seismic network limits the precision of the seismogenic cut-off depths in the peripheral areas where fewer earthquakes were detected and relocated. Geodetic studies (*Wallace et al.*, 2007; *Lamb and Smith*, 2013; *Lamb et al.*, 2018) have yielded locking depths along the Alpine Fault ranging from 7 to 18 km (Fig. 3.7). *Wallace et al.* (2007) obtained partial interseismic coupling depth (coupling coefficient of 75%; 100% = fully locked, 0% = fully slipping) estimations of 18 km representative for the northern and southern segments of the Alpine Fault. For the central segment of the Alpine Fault, near Aoraki/Mount Cook, *Wallace et al.* (2007) calculated a much shallower partial coupling depth (7 km). In the same region, *Lamb and Smith* (2013) and more recently *Lamb et al.* (2018) derived a locking depth at 12.6 km with an additional locked patch at 24.2 km. They suggested that this deeper patch exists in a region of embrittlement at high pore fluid pressure, which results in a return to brittle behavior at higher temperatures and pressures. This deeper locked patch seems to coincide with the distribution of low-frequency earthquakes detected by *Chamberlain et al.* (2014) and *Baratin et al.* (2018). In general there is a reasonable agreement between seismic and geodetic depths for the region in the vicinity of Aoraki/Mount Cook. However, there remains a discrepancy between seismic and geodetic depths on the northeastern part of our examined area where the seismogenic depths exceed 20 km. Similar differences have been observed on various segments of the San Andreas fault (*Smith-Konter et al.* (2011), and references therein), and have been attributed to creeping deformation or to a time-varying stress adjustment at depth during the earthquake cycle following a major event. However, there is no evidence of surface creep in the case of the Alpine Fault and there has not been any major historical event in that area either. This difference may arise due to the sparser GPS network coverage.

Having considered the seismogenic zone depths and their variations from the two independent observations, geodetic and seismic data, we can obtain a rough estimate of the seismic moment release of a potential large Alpine Fault earthquake that ruptures the whole central section (from Haast to the Alpine Fault and Hope Fault junction). We estimate the seismic moment in Newton meters using the equation $M_o = \mu u S$ (*Aki and Richards*, 2002), where μ is the crustal shear modulus, u is the average slip and S is the area of the ruptured fault, the product of the fault's length and width. We assume an average slip of 8 m (observed paleoseismic displacements range from 7.5 to 9 m; *Berryman et al.*, 2012; *Howarth et al.*, 2014), a rupture length of 250 km and a representative shear modulus of $\mu = 30$ GPa. We consider four different potential rupture scenarios for the central section of the Alpine Fault. In the first case we assume a uniform 20 km depth for the seismogenic layer (250 km×20 km). This equates to a moment magnitude of $M_w = 7.98$ using the equation $M_w = 2/3 \log(M_o - 6.07)$ of

Hanks (1979). In the second case, we subtract the area covered by the seismic gap beneath Aoraki/Mount Cook (∼600 km^2) and we obtain a moment magnitude of 7.94. We also examine the case in which the currently aseismic part fails. This case provides us with a M_w 7.37 earthquake. Finally, we examine the case in which the seismic gap beneath Aoraki/Mount Cook works as a barrier preventing the rupture of the whole central segment (length of rupture 125 km). This case gives us an earthquake of 7.74 M_w. These calculations are subject to a substantial number of assumptions (e.g. uniform slip along the fault length and depth, vertical fault plane) but provide us with a rough estimation of a potential large Alpine Fault spanning from 7.3 to 7.9 M_w. These values are comparable with the geologically estimated moment magnitudes calculated by *Sutherland et al.* (2007). These seismic moment estimations do not appear to be greatly affected by the existence of the narrow seismogenic zone beneath Aoraki/Mount Cook, but further work is required to investigate the effects of this feature on rupture processes and radiation patterns.

We have elucidated the geometry of the previously identified seismic gap in Whataroa valley (*Leitner and Eberhart-Phillips*, 2001; *Boese et al.*, 2012). *Leitner and Eberhart-Phillips* (2001) associated this lack of seismicity with changes in geology, while *Boese et al.* (2012) explained its existence as either an effect of a localized yielding and uplift from rapid ice loss from the last glacial period or as a seismic gap of the second kind identified by *Mogi* (1979), that is, quiescent of small earthquakes building up stresses before a large event. We note the recent measurements obtained from the DFDP-2B borehole in Whataroa (*Sutherland et al.*, 2017; *Townend et al.*, 2017), which revealed an extremely high average geothermal gradient (125±55 °C/km) and pore fluid pressures 10% above hydrostatic levels. If we were solely to explain the seismic gap with the high thermal gradient, a shallower seismogenic cut-off depth would be expected. Further calculations and orogen-scale thermal modeling is required to provide an accurate explanation for this lack of seismicity around Whataroa.

We have derived a new local magnitude scale corrected for geometric spreading, attenuation and site terms. This new local magnitude scale is calculated following the same process as used by *Boese et al.* (2012), except it is tied to M_w values instead of M_L. Local magnitudes are based on amplitude measures that are subject to local variations in attenuation and ground motion site amplification. By using M_w instead of M_L to calibrate the magnitudes we ameliorate these inherited issues. M_w values are determined by moment tensor inversions and represent a direct more accurate measure of the moment release that can be related to similar studies elsewhere. Hence, the local magnitudes here are expected to better represent the seismic energy release and to be equivalent to M_w. Magnitudes calculated range between –1.2 and 4.6 and have an estimated magnitude of completeness, M_c=1.1 with a b-value of 0.85 ± 0.003. These values are comparable to those obtained by (*Boese et al.*, 2012) (M_c=1.4 and b-value =

0.86). The magnitude distribution suggests that local strain rates are mainly released through swarms of low-magnitude earthquakes during the last 8 years.

3.7 Conclusions

The earthquake catalog determined here contains 7,719 high-precision locations processed starting from continuous data recorded by five temporary seismic networks (SAMBA, WIZARD, DFDP-10, DFDP-13 and ALFA-08) and five GeoNet sites along the central Southern Alps. This large data-set has enabled us to precisely characterize the seismicity and its variations in depth along the central Alpine Fault in greater detail than afforded by previous studies. In particular, we were able to systematically examine seismogenic cut-off depth variations along the Alpine Fault, for the first time, rather than just perpendicular to the fault. This provides us with reliable seismogenic cut-off depth estimations for almost a 150-km-long portion of the central Alpine Fault, which will assist in refining seismic hazard assessments. We clearly observe the previously identified seismic gap in Whataroa and suggest that seismogenesis there is controlled by the recently documented extreme hydrothermal conditions. The shallow seismicity in the vicinity of Aoraki/Mount Cook is associated with younger cooling ages, deeper exhumation and high uplift rates that are inferred to have pushed up the isotherms and the brittle-ductile transition.

4 Detailed spatiotemporal properties of the tectonic stress regime along the central Alpine Fault

This chapter outlines the results obtained on the crustal stress orientations and parameters in the central section of the Alpine Fault. The chapter is divided into five main sections which deal, respectively, with what is known about the topic, the data set and methodology used, the main and supporting results obtained, a comparison with different studies using different methodologies or data and a final section that concludes summarizing the findings. The focal mechanism catalog is included in the electronic Appendices. The work from this chapter has resulted to an accepted manuscript in *Tectonophysics*.

Michailos, K., Warren-Smith, E., Savage, M. K., and Townend, J. Detailed spatiotemporal analysis of the tectonic stress regime near the central Alpine Fault, New Zealand, *Tectonophysics* (accepted).

4.1 Abstract

We construct a new data set of 845 focal mechanisms derived from microseismicity recorded between late 2008 and early 2017, to investigate the state of stress near the central Alpine Fault, a major oblique convergent plate boundary fault. We obtain an average maximum horizontal compressive stress orientation, S_{Hmax}, of 121±11°, which is uniform to first-order along the length of the central Southern Alps. We also make use of the local magnitudes of the earthquakes with focal mechanisms to examine the spatial patterns of seismic moment release and obtain a relatively uniform cumulative seismic moment release distribution adjacent to the central Alpine Fault, which appears to be independent of both the perpendicular and parallel distances to the fault. We observe an average angle between the S_{Hmax} and the Alpine Fault of 65°, which is consistent with previous observations in the northern and southern sections of the Alpine Fault. This result implies that central Alpine Fault is not optimally oriented for reactivation. Detailed temporal investigations using two different approaches did

not show any change of the stress parameters with time. We examine the distribution of the shear to normal stress ratio on the fault and did not observe any significant variation along the Alpine Fault. This lack of variation combined with the high angle between the fault strike and S_{Hmax} implies that the fault is unfavourably oriented for slip.

4.2 Introduction

The Alpine Fault is a major strike-slip fault that poses the largest seismic hazard to southern New Zealand (*Stirling et al.*, 2012). This fault has not experienced a major earthquake of M≥7 during the last 300 years. However, on the basis of paleoseismological evidence (*Berryman et al.* (2012); *Sutherland et al.* (2007); *Cochran et al.* (2017); *Howarth et al.* (2016, 2018) and references therein), the Alpine Fault is considered to be late in its typical interseismic cycle. Due to this, the broader deformation zone near the Alpine Fault provides a unique opportunity to examine processes such as the tectonic stress orientations and seismic moment release during the late interseismic stage of the earthquake cycle, and their variations in space and time. To do this, we create the longest focal mechanism catalog to date for the central Southern Alps, which contributes towards better understanding of the tectonic processes controlling seismogenesis.

Individual earthquake focal mechanisms place weak constraints on the principal stress axes (*McKenzie*, 1969), but can nevertheless be used together to determine the orientations of the tectonic stresses. To obtain a more accurate estimation of the tectonic stress parameters, sets of focal mechanisms are combined to determine the orientations of the principle stress axes by inversions (*Hardebeck and Michael*, 2006; *Arnold and Townend*, 2007; *Gephart and Forsyth*, 1984; *Michael*, 1984; *Angelier*, 1979; *Lund and Slunga*, 1999). A major advantage of stress analysis over strain rate analysis is that it incorporates information from small-magnitude earthquakes, whereas strain parameter calculations (e.g. Kostrov summations; *Kostrov*, 1974) are mostly affected by the larger-magnitude earthquakes.

The Alpine Fault forms the western margin of the Southern Alps orogen and has a largely straight and continuous surface trace on ∼50−100 km scales (*Norris and Cooper*, 1995, 2001). It has accommodated a cumulative strike-slip offset of as much as 800 km during the Cenozoic (*Lamb et al.*, 2016; *Sutherland*, 1999; *Barth et al.*, 2014). The central section of the Alpine Fault examined here (Inset in Fig. 4.1) consists of a series of oblique-thrust and strike-slip segments of a few hundred meters to a kilometer long (*Norris and Cooper*, 1995). In addition, near the central section of the Alpine Fault the crust exhibits higher uplift rates (∼6-9 mm/yr), deeper exhumation and the

orogenic width is significantly narrower than the adjacent sections (*Little et al.*, 2005). This rapid exhumation of metamorphic rocks from the lower crust of the fault zone (*Toy et al.*, 2010) is caused by the vertical component of the motion of the Alpine Fault (*Norris and Cooper*, 1997), and is inferred to have affected the local crustal thermal structure (*Koons*, 1987; *Allis and Shi*, 1995; *Shi et al.*, 1996; *Sutherland et al.*, 2012, 2017).

Previous studies have examined the tectonic stresses and seismotectonics along the Alpine Fault using focal mechanisms (Inset in Fig. 4.2). *Scholz et al.* (1973) first determined a northwest−southeast compression direction adjacent to the Alpine Fault using composite focal mechanism data. *Leitner and Eberhart-Phillips* (2001) calculated 130 focal mechanisms using first−motion and amplitude ratio methods. The focal mechanisms were found to be mainly dominated by thrust and oblique strike-slip faulting. *Leitner and Eberhart-Phillips* (2001) obtained a maximum horizontal stress direction of 110°–120°. *Boese et al.* (2012) calculated 211 focal mechanisms, using P wave first motion polarities, for earthquakes as small as M_L 0.44. The majority of these focal mechanisms were found to have strike-slip mechanisms. The maximum horizontal compressive stress, S_{Hmax}, orientation was consistent between different spatial clusters and had an average value of 115±10°. *Bourguignon et al.* (2015) computed 148 focal mechanisms using first motion polarities. Focal mechanisms of their more robustly located hypocenter locations lying close to mapped surface faults indicated predominantly strike-slip motion (*Bourguignon et al.*, 2015). Further southwest along the strike of the Alpine Fault, in the Southern Lakes region, *Warren-Smith et al.* (2017a) analyzed a one-year-long microseismicity catalog to examine the local stress field. They calculated 155 focal mechanisms and obtained an average S_{Hmax} orientation of 114±10°. These S_{Hmax} orientations were found to differ by 9−14° clockwise from the mean principal contraction rate axis determined geodetically. *Warren-Smith et al.* (2017a) suggested that different components of the stress field may have been relieved during the latest large Alpine Fault earthquake, which may have resulted in a residual stress varying in orientation (±15°) during the interseismic period of large earthquakes or that there was a bias related to the focal mechanisms' type of faulting variability. On a broader scale, *Townend et al.* (2012) examined the tectonic stress field throughout New Zealand, using observations made during almost a decade of seismic activity. They found that the 115° angle of S_{Hmax} is characteristic of much of the South Island at seismogenic depths.

The angle between the strike of the Alpine Fault and S_{Hmax} has been calculated to be 60° (*Boese et al.*, 2012; *Townend et al.*, 2012), suggesting lower shear to normal stress ratios than implied by standard (Byerlee) coefficients of friction. Similar high angles were found by studies of the northern and southern sections of the Alpine Fault (*Balfour et al.*, 2005; *Warren-Smith et al.*, 2017a). Faulting under these conditions would require

either a low coefficient of friction or high pore fluid pressure or a combination of both. *Boulton et al.* (2014, 2018) measured the friction coefficient of fault gouges recovered from both the central and the southern section of the Alpine Fault and carried out 3−D stress analyses using these values. Fault gouges from the southern Alpine Fault were found to be extremely weak (low friction coefficients; μ ∼0.2) for a range of temperatures and stress conditions (T = 25–210°C, effective normal stresses, $\sigma_n^{'} = 31.2 - 93.6\,MPa$; *Boulton et al.*, 2018). Fault gouges from the central Alpine Fault were also found to be relatively weak (μ ∼0.4) at temperatures < 140°C (*Boulton et al.*, 2014). However these gouges, in contrast to these from the southern section, become stronger with increases in temperature reaching values up to μ ∼0.75 at T≥200°C (*Boulton et al.*, 2014; *Niemeijer et al.*, 2016).

The aim of this study is to thoroughly investigate the tectonic stress field near the central Alpine Fault using almost a decade of continuous seismic data. Previous focal mechanism studies in the area (*Boese et al.*, 2012; *Bourguignon et al.*, 2015) have examined the stress tensor within small time frames that do not necessarily provide the complete picture of the current state of stress. We present the largest focal mechanism data set compiled to date for the central Southern Alps region, allowing a more detailed examination of the stress regime than has previously been possible. We use the focal mechanism data to obtain stress orientations and examine the stress tensor variation in space and time. In addition, we investigate the spatial distribution of the seismic moment energy release.

4.3 Data and methods

We estimate focal mechanisms for the relocated microearthquake catalog constructed by *Michailos et al.* (2019). This catalog contains accurate relative earthquake relocations for 7,719 events obtained using the latest 3-D P and S wave velocity models (*Guo et al.*, 2017) and seismic data from five temporary seismic networks, deployed for various lengths of time between late 2008 and early 2017, and five permanent GeoNet national network seismic sites.

For the focal mechanism calculations, we use manually picked P wave arrival polarities for all earthquakes larger than M_L 1.5. The dataset is later restricted to those earthquakes with at least seven polarity recordings. Changes in the operating network over the study period mean that the number of P wave polarity recordings available for any particular earthquake varies from 7 to as many as 35. To test for station polarity errors or inconsistencies, we manually inspected the first onsets from two teleseismic events and two explosions from a quarry located near Whataroa (Appendix E; *Boese et al.*, 2012).

We calculate focal mechanisms using the Probabilistic Bayesian method of *Walsh et al.* (2009), which uses the output from NonLinLoc (*Lomax et al.*, 2000) or other probabilistic hypocenter location algorithms. The focal mechanism uncertainties are parameterised by a generalised Matrix-Fisher distribution (*Arnold and Townend*, 2007; *Walsh et al.*, 2009). An advantage of this method is that it accounts for the hypocenter uncertainties arising from the seismic velocity model and the P wave polarities. The earthquake locations used here are calculated using double-difference techniques (HypoDD relative earthquake relocations; *Waldhauser*, 2001), which means that these locations do not contain the necessary arrival information for the focal mechanism calculations (i.e. uncertainties in take-off angles and azimuths). To overcome this, we calculate theoretical take-off angles and azimuths for all phase picks based on their hypoDD hypocenters, using the NonLinLoc function "time2EQ" (*Lomax et al.*, 2000) and the 3D velocity model of *Guo et al.* (2017). Finally, we relocate these with NonLinLoc and obtain the posterior density functions (PDFs) of the earthquake hypocenters based on the hypoDD locations used for the focal mechanism calculations.

To examine spatial patterns in the stress field we divide the study area into sub-regions using a recursive quadtree clustering algorithm following the approach described by *Townend and Zoback* (2001, 2004). The quadtree clustering method begins with a single square bin that encompasses the entire area of interest. Next, this bin is divided in quarters that are in turn subdivided in quarters themselves until there are fewer than n_{max} earthquakes in each bin, or the bin reaches a minimum dimension of x_{min}. The final grid consists of a mesh of square bins that are smaller and denser where there are more earthquakes. We calculate the stress parameters using the Bayesian approach of *Arnold and Townend* (2007), which takes into consideration focal mechanism uncertainties, possible false polarity picks, and nodal plane ambiguity in estimating the tectonic stress orientations. We use the algorithm of *Lund and Townend* (2007) to compute the orientation of S_{Hmax}.

4.4 Results

We obtain 845 focal mechanisms for earthquakes larger than M_L 1.5 that cover the time period between late 2008 and early 2017 (Fig. 4.1). In addition, 74 focal mechanisms calculated using moment tensor inversion of GeoNet national network data (*Ristau*, 2013) are also shown in the background of Fig. 4.1 in grey, for the same time period. The majority of the focal mechanisms are strike-slip and lie on the southeastern (hanging-wall) side of the fault with uncertainties ranging from 20 to 38° (Figure C1 in Appendix C) and only a small number of focal mechanisms are located in the footwall (Fig. 4.1). Overall, 62% of the focal mechanisms are strike-slip, 22% reverse and

oblique reverse and 16% normal and oblique normal faulting (Figures C2 and C3, Appendix C). Reverse and oblique reverse focal mechanisms are more common in the vicinity of Aoraki/Mount Cook (26% of all focal mechanisms in cross section B–B'; Fig. 4.1), while strike-slip focal mechanisms are distributed throughout the examined area. Normal and oblique normal faulting is slightly more common in the northeast part of the study area (17% of all focal mechanisms in cross section A–A'; Fig. 4.1). The occurrence of normal focal mechanisms, mainly in the shallower part of the crust, within a collisional orogen (i.e. Southern Alps) is partly related to gravitational topographic collapse (*Upton and Craw*, 2014). This process has produced widespread small-displacement normal faults and extensional quartz filled veins that cut the basement rocks throughout the orogen (*Upton et al.*, 2011; *Upton and Craw*, 2014). The type of focal mechanism does not show any obvious pattern relative to the earthquake's magnitudes or hypocentral depths (Figures C4 and C5 in Appendix C).

We divide the study area into subregions (bins) using the quadtree algorithm and calculate stress parameters with the focal mechanisms with hypocentral depths shallower than 25 km in each bin (Fig. 4.2). With this method, we obtain 46 square bins with a minimum dimension of 10 km, a minimum number of 15 observations and a maximum number of 75 observations. Of these 46 bins, 23 contain enough focal mechanisms (n=15) for stress inversion calculations. We obtain S_{Hmax} orientations, which vary from 99° to 144° with a mean value of 121° and a standard deviation of 11° (represented by bowties and labeled by the number of their bin; Fig. 4.2). Calculations are not performed for bins containing insufficient data (un-shaded bins; Fig. 4.2). We combine bins 4, 5, 13 and 14 (Fig. 4.2) and obtain a composite solution for the footwall (northwest) side of the fault where the data are sparse. The S_{Hmax} orientation in the footwall (136°) lies within the standard deviation of the average S_{Hmax} values in the hanging wall. S_{Hmax} orientations from previous studies (Inset of Fig. 4.2) are consistent throughout the South Island and have values that lie within the uncertainties of the results obtained here. No clustering was performed on the earthquake catalog, so focal mechanisms with similar faulting from swarms might be over-represented in the stress inversions. This analysis was not carried out as it was considered to be beyond the scope of this study.

The bins in Fig. 4.2 are colored according to the cumulative seismic moment release divided by the area of each bin. For the calculation of the seismic moment release, we assume that the local magnitudes are equivalent to moment magnitudes, M_w. This is appropriate because the local magnitudes calculated by *Michailos et al.* (2019) are tied to moment magnitude values that were calculated independently with moment tensor inversions by GeoNet (*Ristau*, 2013). These magnitudes can be converted to seismic

moments M_o using the relationship developed by *Hanks* (1979).

$$M_o = 10^{1.5(M_w+6.03)} \tag{4.1}$$

where M_o is in N·m. This relationship is derived from intermediate to large earthquakes scales, but it has been shown to also apply to microseismicity scales (*Bakun and Lindh*, 1977). The seismic moment release distribution illustrated in Fig. 4.2 is relatively uniform adjacent to the Alpine Fault (varying by 1–2 orders of magnitude). Seismic moment release values range between 0.6×10^{11} and 0.9×10^{14} N·m/km^2. The largest seismic moment release values are observed in the northeast part of the study area (between Harihari and Ross) within the limits of the seismic network (bin 25; Fig. 4.2), while the lowest values are observed mainly in the periphery of the study area (bin 3, 12, 32, 37; Fig. 4.2.

Table 4.1 summarizes the stress parameter details for each bin illustrated in Fig. 4.2. The corresponding stereonets with the probability density contours and orientations of S_{Hmax} are summarised in Fig. 4.3. The intermediate principal stress axis, S_2, is close to vertical and the maximum and minimum axes S_1 and S_3 are horizontal in most cases (∼80%), indicating a predominantly strike-slip stress state. The stereonet from the footwall has the largest plunge value for the principal stress axis S_2 with low uncertainties (see probability density contour distribution labeled as footwall; Fig 4.3), which highlights a possible difference in the stress regime between the footwall and the hanging wall. We also calculate the stress ratio, R=(S_1–S_2)/(S_1–S_3), which provides constraints on the relative magnitudes of the three principal stresses. An R value > 0.5 implies that S_2 is closer in magnitude to S_3 than to S_1, and since in our case S_2 is mostly vertical (S_2=S_v; strike-slip), the overall stress regime is considered as transpressive.

The largest R values (≥0.8) are obtained for bins (6, 9, 12, 27, 28, 32, 33 ,40; Fig. 4.2 and Fig. 4.3), which lie near Aoraki/Mount Cook and the periphery of our combined seismic network, indicating that there is a large number of reverse focal mechanisms within these bins (Fig. 4.2). The smallest R values (≤0.2) calculated are less frequent and are located in bins (3, 16, 24) that lie in the hanging wall near the Alpine Fault close to Whataroa Harihari and further southweast near Haast (R values are close to zero, indicating that S_2 and S_1 are very similar in magnitude). All bins, apart from three near Aoraki/Mount Cook that exhibit reverse faulting (inverted triangles; Fig. 4.2), display strike-slip faulting (squares; Fig. 4.2), while no bins exhibit normal faulting.

To ensure that the results are not dependent on the clustering method used, we repeat the clustering and stress inversion process using a non-hierarchical clustering algorithm called k-means (*Hartigan*, 1975; *Townend and Zoback*, 2006; *Balfour et al.*, 2005, Ap-

pendix C). Using k-means clustering, we examine the variations of the stresses in depth as well as in map-view. The results obtained using k-means are consistent within their 80% posterior credible intervals with those presented here and show no consistent variation of the maximum horizontal compressive stress azimuth relative to the Alpine Fault or the hypocentral depth.

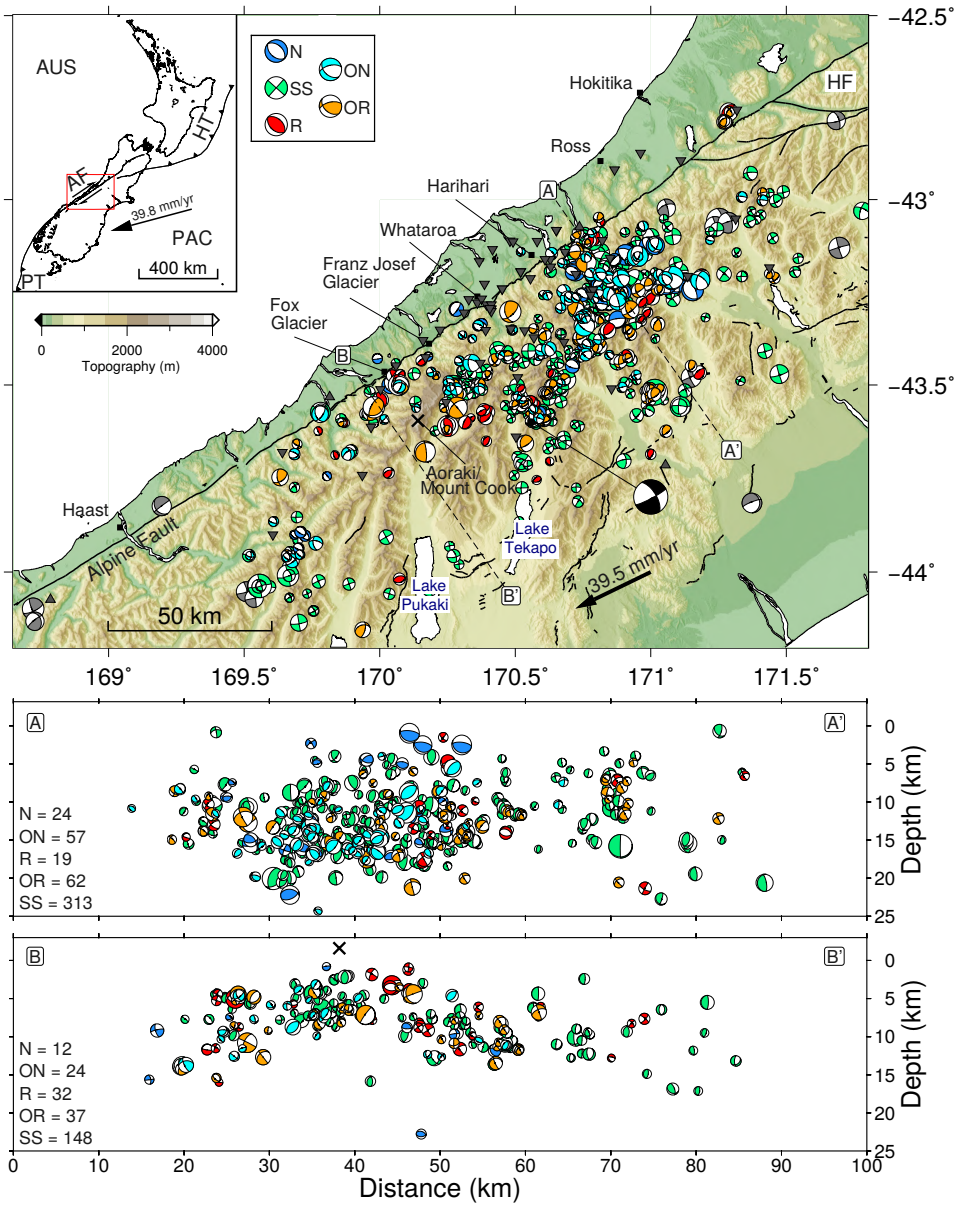

Figure 4.1: Map of the central Southern Alps region showing 845 focal mechanisms with magnitudes greater than 1.5 that occurred between November 2008 and March 2017. Temporary and permanent (GeoNet) seismic sites are shown by grey inverted triangles and grey triangles, respectively. The color of the focal mechanisms represents the type of faulting. Namely; Blue stands for normal (N), green for strike-slip (SS), red for reverse (R), cyan for oblique-normal (ON) and orange for oblique-reverse (OR) faulting. Grey focal mechanisms depict the 74 moment tensor inversions determined by GeoNet for earthquakes with magnitudes larger than M_w4 that happened during the same time period examined here (*https://www.geonet.org.nz/data/types/eq_catalogue*). Black focal mechanism is the 1984 Godley River M 6.1 earthquake (*Anderson et al.*, 1993). Aoraki/Mount Cook is represented by a cross. Black lines show the active faults from the New Zealand Active Faults Database (http://data.gns.cri.nz/af/). HF is the Hope Fault. Arrow indicates the local velocity of Pacific Plate relative to Australia (∼39.5 mm/yr; *DeMets et al.*, 2010). Inset map shows the location of the study area within New Zealand. PAC, Pacific plate; AUS, Australian plate; PT, Puysegur Trench, HT, Hikurangi Trough and AF, Alpine Fault. Focal mechanisms within 40 km on either side of the lines A−A' and B−B' are shown in the cross-sections. The total number of each type of focal mechanisms is shown on the lower left of each cross-section. Focal mechanisms on the cross-sections are projected side-on indicating the motion perpendicular to the cross-section.

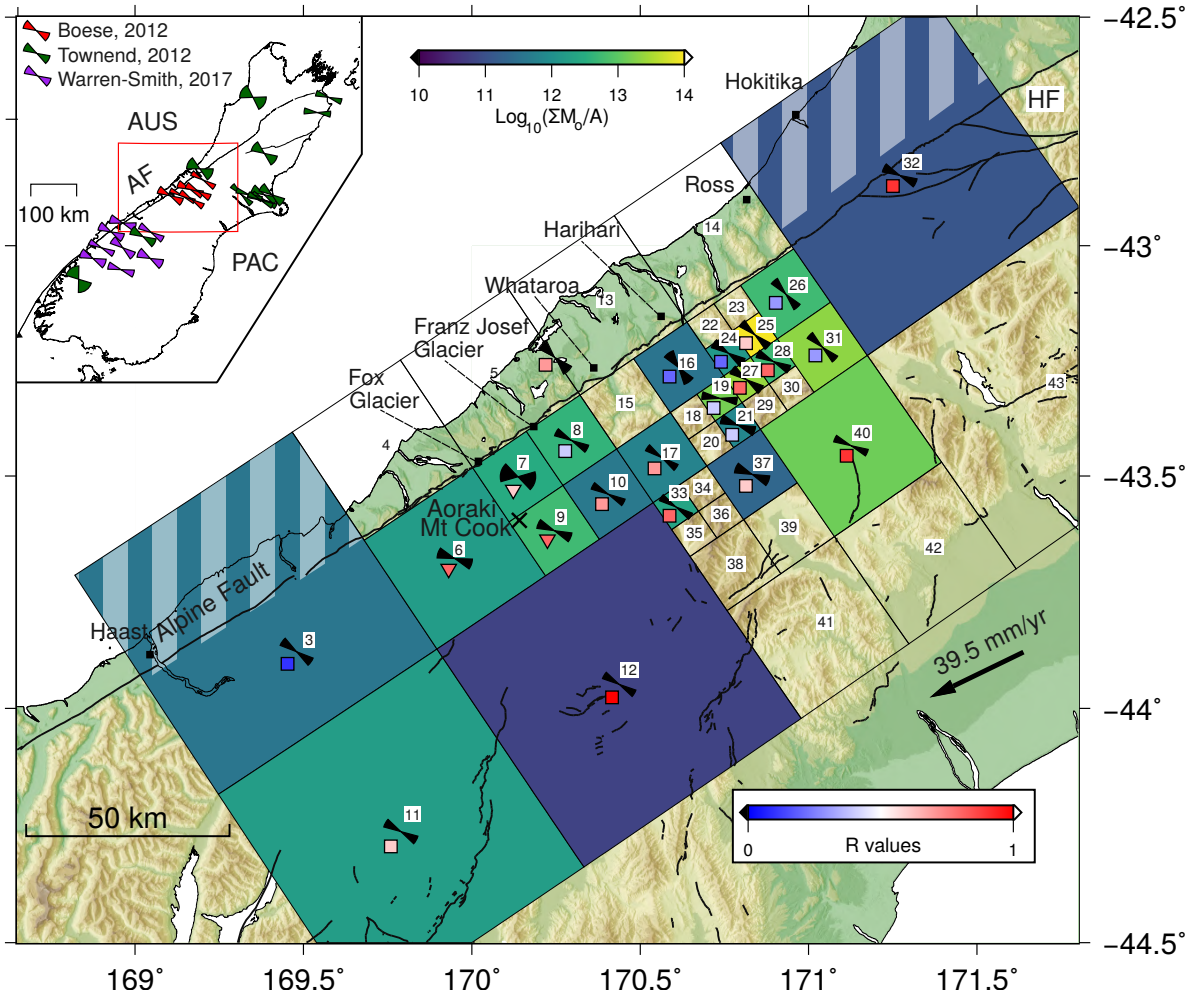

Figure 4.2: Distribution of S_{Hmax} directions along the central Southern Alps region for earthquakes with hypocentral depths shallower than 25 km and magnitudes larger than M_L 1.5. Bins are obtained using the quadtree clustering algorithm and have a minimum size of 10 km. Bins containing 15 to 50 earthquakes are colored according to their cumulative seismic moment release divided by the area of the bin (see color scale). Bins with fewer than 15 earthquakes have no calculations. Bowties indicate the direction and 80 % confidence bound for the direction of the maximum horizontal compressive stress (S_{Hmax}) calculated from focal mechanisms within the bins. Markers indicate the stress regime and are colored according to their R=(S_1–S_2)/(S_1–S_3), values (see color scale). Namely, square markers are strike-slip, and inverted triangle markers are reverse. Numbers indicate the bin's names. Bins numbered 4, 5, 13 and 14 were manually combined and the bowtie lies in the middle of the four bins. Hashed parts of bins 3 and 32 indicate the areas where no focal mechanism data exist. Arrow indicates the local velocity of Pacific Plate relative to Australia (∼39.5 mm/yr; *DeMets et al.*, 2010). Black lines show the active faults from the New Zealand Active Faults Database (http://data.gns.cri.nz/af/). HF shows the location of the Hope Fault. Inset summarises the previous studies S_{Hmax} direction calculations across the South Island (*Boese et al.* (2012) red; *Townend et al.* (2012) green; *Warren-Smith et al.* (2017a) purple bowties). Square highlights the location of the study area. PAC, Pacific plate; AUS, Australian plate; and AF, Alpine Fault.

Table 4.1: S_{Hmax} and principal axes orientations calculated from focal mechanisms within bins defined using the quadtree clustering algorithm and plotted in Fig. 4.2. N is the number of focal mechanisms contained in each bin. Depths represent the median values of the hypocentral depths of the focal mechanisms in each bin. R is the posterior mean stress ratio $(S_1–S_2)/(S_1–S_3)$ for each bin and has values between 0 and 1. Uncertainties for R and S_{Hmax} values are the 80% confidence bound of their posterior probability density functions.

Bin	Lat. (°)	Lon. (°)	Dep. (km)	N	S_1 (Tr./Pl., °)	S_2 (Tr./Pl., °)	S_3 (Tr./Pl., °)	R	S_{Hmax} (°)
3	–43.79	169.36	15.8	25	131/66	099/27	035/77	0.1 (±0.2)	125.9 (–14.8/+14.1)
6	–43.68	169.95	5.9	19	109/90	019/59	019/31	0.8 (–0.3/+0.2)	109.1 (±17.3)
7	–43.5	170.14	5.0	23	102/69	010/87	092/21	0.6 (±0.3)	103.6 (–29.8/+32.9)
8	–43.42	170.30	6.9	31	118/77	138/14	029/85	0.4 (±0.2)	118.7 (–13.2/+12.8)
9	–43.62	170.24	3.6	15	113/88	023/77	031/13	0.8 (–0.2/+0.1)	113.3 (–15.9/+15.5)
10	–43.54	170.40	6.6	44	119/88	043/07	028/83	0.7 (±0.2)	118.8 (–12.2/+11.7)
11	–44.26	169.79	19.1	25	120/82	074/11	029/82	0.6 (±0.4)	119.7 (–14.5/+14.0)
12	–43.95	170.44	9.1	37	121/87	009/07	031/83	1.0 (–0.1/+0.0)	121.2 (±12.2)
16	–43.26	170.61	14.0	15	145/89	060/12	054/78	0.2 (±0.2)	144.6 (–18.3/+17.7)
17	–43.46	170.56	12.2	39	125/80	086/13	034/82	0.7 (±0.2)	124.8 (–11.9/+11.6)
19	–43.33	170.74	15.8	44	099/82	115/08	009/88	0.4 (±0.3)	99.2 (–12.7/+12.3)
21	–43.39	170.79	11.9	17	109/83	165/13	021/79	0.4 (±0.3)	110.2 (–15.6/+15.3)
24	–43.23	170.76	11.9	18	122/74	145/18	034/83	0.2 (–0.2/+0.3)	123.7 (±15.7)
25	–43.19	170.84	15.3	29	132/79	121/11	041/88	0.6 (±0.4)	131.8 (–13.6/+13.1)
26	–43.11	170.93	15.5	33	138/68	147/23	049/87	0.3 (±0.3)	139.2 (–13.6/+13.2)
27	–43.29	170.82	13.8	27	125/71	096/22	032/80	0.8 (–0.3/+0.2)	125.1 (±15.0)
28	–43.25	170.90	15.9	30	117/80	133/11	028/87	0.8 (–0.3/+0.2)	116.7 (–13.7/+13.4)
31	–43.22	171.04	11.3	36	133/86	131/04	043/90	0.3 (±0.2)	133.4 (±13.1)
32	–42.85	171.27	10.7	32	116/72	150/21	030/79	0.9 (–0.2/+0.1)	116.2 (–14.9/+14.3)
33	–43.57	170.61	11.7	47	123/86	020/19	034/71	0.8 (–0.2/+0.1)	122.8 (–12.0/+11.6)
37	–43.50	170.83	10.7	16	114/77	062/21	020/74	0.6 (±0.4)	112.1 (±17.1)
40	–43.43	171.13	10.3	47	114/90	025/24	024/66	0.9 (±0.1)	114.2 (–11.8/+11.4)
footwall	–	–	–	20	131/55	171/43	057/69	0.7 (±0.3)	136.6 (–18.4/+18.2)

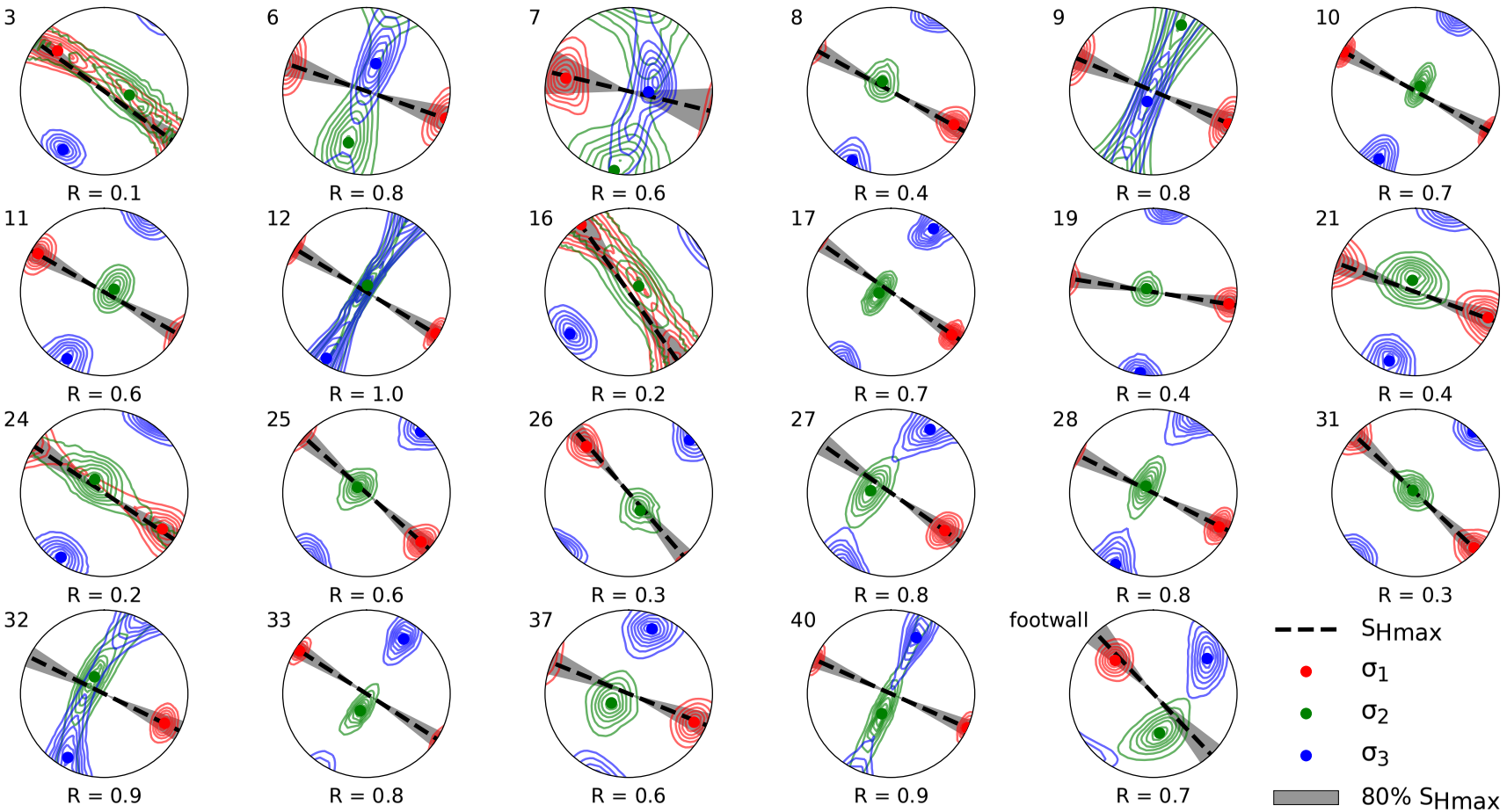

Figure 4.3: Stereonets displaying the probability density contours of the three principal stress axes (S_1 red, S_2 green, S_3 blue) of each bin depicted in Fig. 4.2. Stereonets are lower hemisphere projections at which North is up and East is on the right. The orientation of S_{Hmax} is shown by the black dashed line with 80% confidence bound shaded by light gray. The bin numbers and stress ratio, R values, are respectively on the top left and under each stereonet.

4.5 Discussion

4.5.1 Spatial variation in stress parameters and angle with Alpine Fault

The crustal stress field in the hanging wall of the central Southern Alps is approximately homogeneous with regard to the stress regime (strike-slip, as S_2 is in almost all cases sub-vertical), average S_{Hmax} orientation (121°), and average stress ratio (R=0.6, indicating in this case a transpressive tectonic environment). R values vary along the length of the Alpine Fault (Fig. 4.2), however it should be noted here that the stress ratio values have generally large uncertainties (see Table 1). Near Aoraki/Mount Cook and in most areas further southeast, away from the surface trace of the Alpine Fault, R values are larger than 0.5, representing a transpressive stress field. R values smaller than 0.5 are mainly observed in the northeast and southwest parts of the examined region (Fig. 4.2). The S_{Hmax} orientations, given their uncertainties, are consistent with those of previous studies (*Balfour et al.*, 2005; *Boese et al.*, 2012; *Townend et al.*, 2012; *Warren-Smith et al.*, 2017a).

The average S_{Hmax} orientation in the central Southern Alps forms a high angle (∼66°) with respect to the strike of the Alpine Fault. On the northeast side of the fault (hanging wall; bins 16, 24, 25 and 26; Fig. 4.2) the S_{Hmax} orientations are almost perpendicular to the Alpine Fault trace, forming angles of between 75 and 89°. In the vicinity of Aoraki/Mount Cook (bins 6, 7 and 8; Fig. 4.2) the same angle is substantially smaller (48–63°). Overall, we observe an intermediate to high angle (>60°) between S_{Hmax} and the central Alpine Fault over a ∼150 km distance. Similar stress orientation studies in the central section of the Alpine Fault (*Boese et al.*, 2012; *Townend et al.*, 2012) found angles of up to 60°, suggesting low shear to normal stress ratios. The angles between S_{Hmax} and the Alpine Fault in the two adjacent sections, the section to the north in the greater Marlborough region (*Balfour et al.*, 2005) and the section to the south near the Southern Lakes (*Warren-Smith et al.*, 2017a), have both observed similarly high angles. *Balfour et al.* (2005) suggested that low coefficients of friction or increased pore fluid pressure or a combination of the two cause the Marlborough faults to be weak, while *Boese et al.* (2012) favored increased fluid pressures as the explanation for the fault's reduced strength for the central Alpine Fault. *Warren-Smith et al.* (2017a) proposed that either the fault is weak or that it has undergone significant rotations making it misaligned to the current stress. However even in that case it would be mechanically easier to reactivate these existing structures rather than creating new ones.

Boulton et al. (2018) suggested that earthquake nucleation on a frictionally strong

central Alpine Fault ($\mu \geq$0.6; *Boulton et al.* (2014) based on hydrothermal friction experiments) is only favoured by values of the stress shape ratio, Φ=1–R, less than or equal to 0.2 (equivalent to $R \geq$0.8). For more details on the relationship between R values and the misorientation of the Alpine Fault refer to Fig. C6 of Appendix C adopted from (*Boulton et al.*, 2018). The stress parameters near Aoraki/Mount Cook (bins 6 and 9; bin 32 is not included as it contains some focal mechanisms in the footwall side), exhibit large R values, which means that this section of the fault might be favourably oriented for reactivation. Further south and north along the central Alpine Fault (bins 3, 8, 16 and 26) R values are generally small ($\Phi \geq$0.6) suggesting that, the fault there becomes severely misoriented for reactivation in the absence of pore fluid overpressures (*Boulton et al.*, 2018).

4.5.2 Temporal stress variations

The focal mechanism data used here cover almost a decade of microseismicity near the central Alpine Fault. This continuity of the data set presents us with the opportunity to investigate temporal changes in stress orientations near a major strike-slip fault estimated to have a ∼29% chance of rupturing in the next 50 years in a large magnitude (M7−8) earthquake (*Howarth et al.* (2018) and references therein). In the last decade, there has not been an earthquake nearby large enough to produce obvious changes in the stress parameters. However, there have been several large regional earthquakes in the South Island (e.g. M7.8 Dusky Sound, M7.2 Darfield, M7.8 Kaikōura), that might have affected the local stress field. We calculate the seismic energy density, e, of the large regional earthquakes that occurred during the examined time period of this study. Table 4.2 summarises the details of these large regional earthquakes. Seismic energy density, e, measured in J/m^3 can be approximated by an empirical relation of magnitude-distance of the earthquake and can provide a useful indication of the seismic shaking intensity imposed on a specific site (*Wang*, 2007; *O'Brien et al.*, 2016). Moreover, because the Alpine Fault has a high probability of producing a large earthquake in coming decades, it is crucial to examine whether there are any discernible and systematic changes in stress.

To examine temporal variations of the stress tensor we use all the focal mechanism data and do not perform any spatial clustering, because we did not observe any major spatial variations in the stress parameters apart from slight variations in R values. We divide the data set into 57 epochs of 20 observations with five focal mechanisms overlapping in each epoch and calculate the stress parameters using the same Bayesian approach as before (*Arnold and Townend*, 2007).

Fig. 4.4 summarises the results of the temporal analysis and reveals several key patterns: 1) S_{Hmax} orientation values are consistent with time apart from a anticlockwise

Table 4.2: Details of large regional earthquakes that occurred in the South Island from late 2008 to early 2017. Numbers within the parenthesis correspond to the regional earthquakes plotted on Figs. 4.4, 4.5 and 4.6. Δ is the epicentral distance measured in km from the earthquake hypocenter to the center of our seismic network. e represents the seismic energy density of these earthquakes measured in J/m^3.

Earthquake	Origin time (UTC)	Latitude (°)	Longitude (°)	Depth (km)	M_w	Δ (km)	e (J/m^3)
Dusky Sound (1)	2009-07-15T09:22:29.3	-45.8	166.6	12.0	7.8	437.5	0.38
Fiordland (2)	2009-08-05T08:31:37.4	-45.4	166.1	12.0	6.1	444.2	0.0
Darfield (3)	2010-09-03T16:35:41.8	-43.5	172.2	11.0	7.2	129.4	1.84
Christchurch (4)	2011-02-21T23:51:42.3	-43.6	172.7	5.4	6.2	170.1	0.03
Cook Strait (5)	2013-07-21T05:09:30.5	-41.6	174.3	15.6	6.5	345.4	0.01
Lake Grassmere (6)	2013-08-16T02:31:05.9	-41.7	174.2	7.5	6.5	327.7	0.01
Fiordland (7)	2013-12-16T12:07:24.9	-46.2	166.1	5.0	6.1	496.5	0.0
St. Arnaud (8)	2015-04-24T03:36:42.4	-42.1	173.1	51.5	6.2	233.5	0.02
Kaikōura (9)	2016-11-13T11:02:56.3	-42.7	173.0	15.1	7.8	198.2	4.36

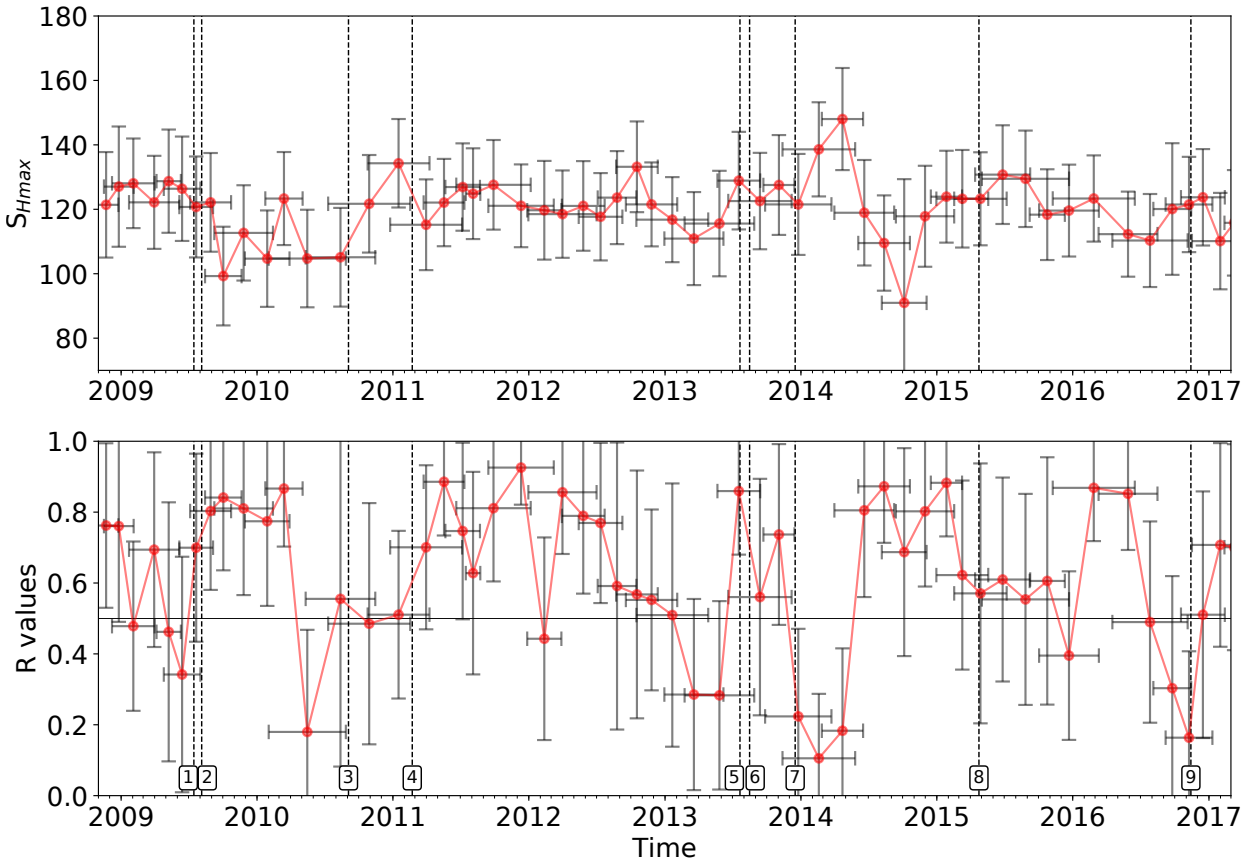

Figure 4.4: Graph showing the distribution of S_{Hmax} orientations and stress ratio values, R=(S_1–S_2)/(S_1–S_3), of each epoch with their uncertainties calculated using the Bayesian approach of (*Arnold and Townend*, 2007). Each epoch contains 20 focal mechanisms, five of which are overlapping. Vertical grey bars depict the calculation's uncertainties (80% confidence bound), while horizontal grey bars show the time period covered by each epoch. Vertical dashed lines indicate the time of occurrence of a number of large regional earthquakes in the South Island (numbers indicate the regional earthquake details in Table 4.2: 1– M7.8 Dusky Sound 2009, 2– M6.1 Fiordland 2009, 3– M7.2 Darfield 2010, 4– M6.2 Christchurch 2011, 5– M6.5 Cook Strait 2013, 6– M6.5 Lake Grassmere 2013, 7– M6.1 Fiordland 2013, 8– M6.2 St. Arnaud 2015, 9– M7.8 Kaikōura 2016).

rotation during late 2009 and late 2014 (the minimum value in late 2014 has a large uncertainty). These two rotations in S_{Hmax} appear to be anti-correlated with the corresponding R values; 2) S_{Hmax} orientations and R values do not show any clear response to any of the large regional earthquakes other than the Dusky Sound earthquake; 3) The R values are mostly larger than 0.5, but fluctuate with large uncertainties; 4) Variability in the S_{Hmax} and R values mostly lie within the uncertainties of the calculations, which impedes many interpretations.

In an attempt to resolve any temporal changes more clearly we have also computed stress parameters a second way. As recommended by *Martínez-Garzón et al.* (2013) and *Warren-Smith et al.* (2019), we first use a joint iterative inversion (*Vavryčuk*, 2014) to identify the preferred nodal plane (fault plane) of each focal mechanism. By doing so, we eliminate the nodal plane ambiguity. We next use a different algorithm that can be set to take into account a single nodal plane. In particular, we use the MSATSI algorithm (*Martinez-Garzon et al.*, 2014) based on SATSI (*Hardebeck and Michael*, 2006; *Michael*, 1984) to compute stress tensors by applying a damped inversion to resolve the stress field orientation for the data of each subregion (or epoch in our case) taking into account the data from the adjacent subregions to smooth the solution. By doing so, only strong changes in the stress tensor are retained, while variations arising from artefacts like the data subdivision are smoothed.

The results from the damped approach described above are summarized in Fig. 4.5, which shows the variations of the plunges and trends of the three principal axes and R values with time. Epochs depicted by circles include 20 observations from which five are overlapping with the previous and subsequent epoch (same epochs as in Fig. 4.4). A striking feature of this figure is that σ_1 and σ_3 trends show remarkably small variations and uncertainties with time. The σ_2 axis is not shown as its trends are not well constrained due to the axis being almost always close to vertical. R values are better constrained and have a different distribution relative to the ones obtained with the Bayesian method (Fig. 4.4). R values are remarkably uniform with time and all have values larger than 0.5 for all the examined time periods, indicating a constant and uniform transpressive tectonic environment.

As with the results obtained with the Bayesian method (Fig. 4.4) we don't in general observe any clear response to the stress parameters after the major regional large earthquakes. However, we observe a significant reduction in the plunge of σ_2 and an increase in the plunge of σ_3 following the Dusky Sound earthquake (late 2009; Fig. 4.5), which implies a transition from strike-slip to reverse or an oblique reverse stress regime, although the uncertainties here are large. We observe a similar reduction in σ_2 plunges during 2015, but this change appears to be associated with the large uncertainties in the probability density contours defining the stress axes (stereonet on top right of Fig. 4.5).

Boese et al. (2014) observed remotely triggered seismicity after the Dusky Sound and Darfield earthquakes but not after the Christchurch earthquake, and suggested a triggering threshold associated with the dynamic stresses imposed by the surface waves in the central Southern Alps. *Boese et al.* (2014) also suggested that the triggered swarms' focal mechanisms are consistent with the favorably oriented faults and stress regime (*Boese et al.*, 2012, 2014). Our results imply that even though the seismicity rates can be influenced by regional large earthquakes, the same does not necessarily apply for the stress parameters.

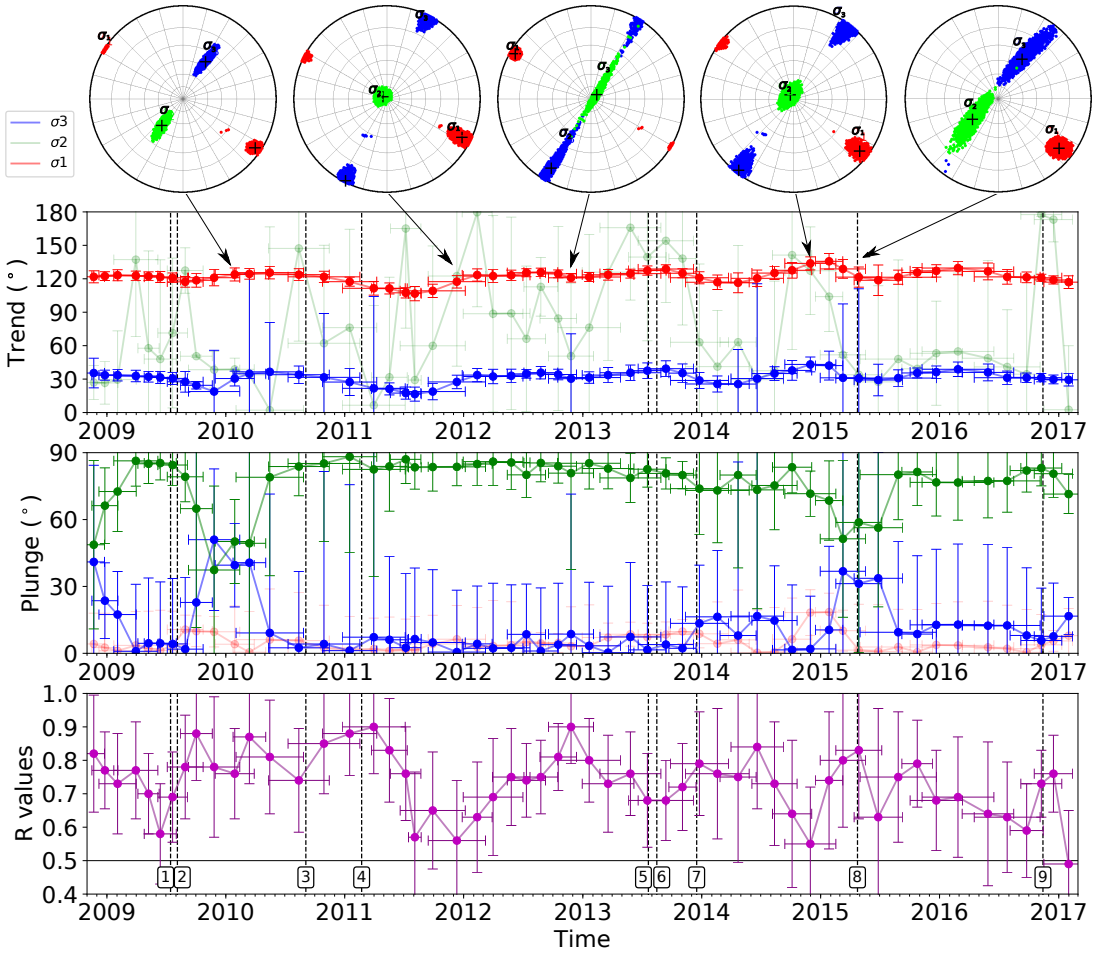

Figure 4.5: Variations of the trends and plunges of the three principal stress axes (S_1 red; S_2 green and S_3 blue) versus time with their respective uncertainties and time period overlaps (upper two panels) calculated using MSATSI (*Martinez-Garzon et al.*, 2014). Stress ratio value, R=(S_1–S_2)/(S_1–S_3), of each epoch is shown versus time (lower panel). Stereonets show representative principal stress geometries for specific time periods. Vertical dashed lines indicate the time of occurrence of a number of large regional earthquakes in the South Island (numbers indicate the regional earthquake details in Table 4.2: 1– M7.8 Dusky Sound 2009, 2– M6.1 Fiordland 2009, 3– M7.2 Darfield 2010, 4– M6.2 Christchurch 2011, 5– M6.5 Cook Strait 2013, 6– M6.5 Lake Grassmere 2013, 7– M6.1 Fiordland 2013, 8– M6.2 St. Arnaud 2015, 9– M7.8 Kaikōura 2016).

A limitation of the temporal analysis described above is that spatial variation in stress can be interpreted as temporal variation because the focal mechanisms analysed occur

in different locations or different times (e.g. *Townend and Zoback* (2001, 2006)). To ensure that strictly time-dependent changes at fixed points in space are analysed, we focus on four geographic clusters. In order to make sure whether there is any clear effect in the stress parameters that might be related to the large regional earthquakes, we define the epochs of each cluster before and after their origin times. We divide the epochs around the five regional earthquakes with the largest seismic energy density values (Table 4.2).

The spatio-temporal variations of the stress parameters are summarised in Fig. 4.6. Overall the stress parameters are uniform, not showing any major changes in either time or space. Two observations that can be made from Fig. 4.6 are: 1) an increase in R values after the Dusky Sound earthquake in the two central subregions (clusters B and C; Fig. 4.6); 2) a decrease in the S_{Hmax} angle after the Kaikōura earthquake and a concomitant increase in R value for the southern central cluster (cluster C; Fig. 4.6). However, the limited number of focal mechanisms after the Kaikōura earthquake limit further interpretations. Another pattern observed from Fig. 4.6 highlights the importance of the dense seismic network of seismometers in providing enough observations (e.g. the northeastern cluster, A, has only enough data after the deployment of the ALFA-08 temporary seismic in that region, and the southwestern cluster, D, has systematically more observations after the southern expansion of the SAMBA network in 2014).

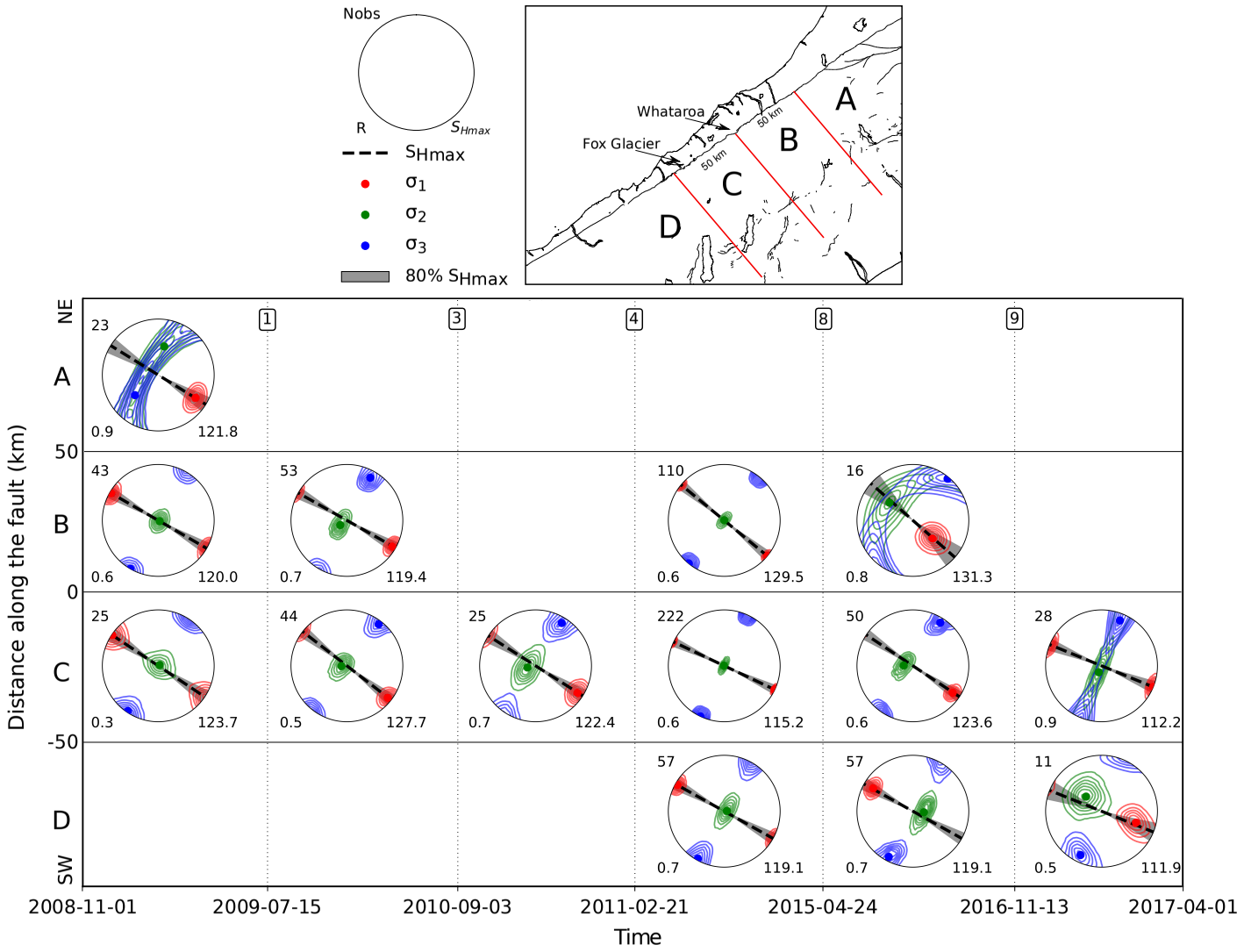

Figure 4.6: Diagram showing the temporal variation of the stress parameters in four different clusters. The clusters are divided according to the focal mechanism's distance along fault (intervals of 50 km along the length of the Alpine Fault; Inset shows the location of the spatial clusters). Stereonets show the geometry of the stress parameters for the epochs between the five largest regional earthquakes in the South Island from late 2008 to early 2017 (labeled as 1, 3, 4, 8 and 9 according to Table 4.2: 1– M7.8 Dusky Sound 2009, 3– M7.2 Darfield 2010, 4– M6.2 Christchurch 2011, 8– M6.2 St. Arnaud 2015, 9– M7.8 Kaikōura 2016). Empty boxes have insufficient number of focal mechanisms for the stress inversion calculations. Number of observations, R values and S_{Hmax} are shown respectively, on the top left, bottom left and bottom right of each stereonet.

4.5.3 Shear and normal stress components along the Alpine Fault

To further examine the stresses acting on the Alpine Fault specifically, we calculate the shear and normal stress components on the fault assuming a representative fault plane geometry with a strike of 055° and dip of 50°. This average fault structure is inferred from results obtained by seismic tomography (*Guo et al.*, 2017), surface structural (*Norris and Cooper*, 1997), reflection (*Stern et al.*, 2000) and geodesy (*Beavan et al.*, 1999). A number of tests were performed with different dip angles between 50 and 60° and the results were consistent with each other. To estimate the stress components on the fault plane, we cluster all the focal mechanisms determined in this study and calculate the stress orientations using the same Bayesian approach as above (*Arnold and Townend*, 2007). Details of the calculation of the shear to normal stresses with the assumed Alpine Fault plane are described in Appendix C. The normal stress component, σ_n, is given by the following relation:

$$\sigma_n = T \cdot \hat{n} \tag{4.2}$$

where T is the traction vector on the normal unit vector $\hat{n}$ of the inferred Alpine Fault plane. The shear stress component is then given by:

$$\tau_n = T - \sigma_n \hat{n} \tag{4.3}$$

The distribution of the shear to normal stress ratio, τ_n/σ_n, along the length of the Alpine fault is shown in Fig. 4.7. Tests with different fault plane dip angles were performed dip angles larger than 70° and smaller than 50° all gave results where all the measurement values had larger normal than shear stress components. We do not observe any dominant pattern of the distribution of the shear to normal stress ratio along the length of the central Alpine Fault. Considering the relative small number of observations (i.e. 19 stress inversions) used here and the assumptions used to estimate the structure of the Alpine Fault in depth (e.g. inferred dip angle, uniform fault geometry) the following interpretations can be made. Relative magnitudes of the shear to normal stress ratios appear to be $\tau_n/\sigma_n > 1$ near Aoraki/Mount Cook (Fox Glacier; Fig. 4.7) while $\tau_n/\sigma_n < 1$ is observed further to the northeast (Whataroa; Fig. 4.7). These relatively high shear to normal stress ratio values near Aoraki/Mount Cook imply that the current stress orientation there might be more favourable for fault reactivation.

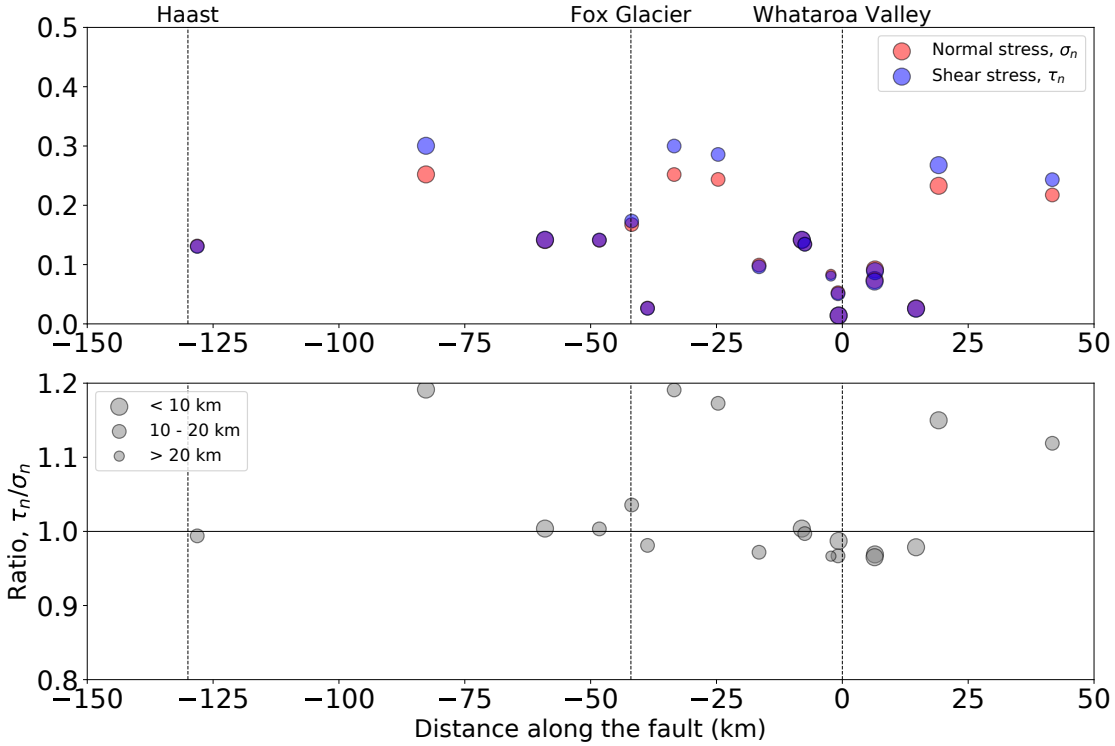

Figure 4.7: Distribution of the normal, σ_n (red), shear stress, τ_n (blue), component and their ratio τ_n/σ_n values projected along the length of the inferred Alpine Fault plane (θ=55°, δ=50°). Circle sizes represent the perpendicular distances from the inferred fault plane (see legend in lower graph).

4.6 Conclusions

We present the longest focal mechanism data set constructed for the central Alpine Fault to date, which encompasses almost a decade of microseismicity. We calculate 845 focal mechanisms, the majority of which occur within the southeastern side of the Alpine Fault (hanging-wall) and correspond to strike-slip faulting. Maximum horizontal compressive stress orientations vary from 99° to 144° with a mean value of 121±11° at the 80% confidence level and are relatively uniform and consistent in space. This results in a high angle of ~65° between the average S_{Hmax} and the strike of the Alpine Fault, which suggests that the central section of the Alpine Fault is unfavorably oriented for failure. Temporal variations in the stress parameters are minor and show no trend to the occurrence of large regional earthquakes. Variations of shear to normal stress ratio along an inferred Alpine Fault structure at depth do not show any clear pattern. Cumulative seismic moment release is relatively uniform near the Alpine Fault, and does not show any trend that could be related to fault-perpendicular or fault-parallel distances.

5 Crustal thermal structure and exhumation rates near the central Alpine Fault

This chapter discusses some implications of the microseismicity catalog constructed in Chapter 3 for the crustal thermal structure of the crust near the central Alpine Fault and for exhumation rates. The chapter is subdivided into eight main sections. The first is the abstract followed by a general introduction to the work. The following three sections provide a description of the seismicity data set and the analysis performed on it, a description of the crustal thermal structure calculated, and the exhumation estimates based on seismicity observations alone. The final, three sections introduce the thermochronology data, outline the optimization process used, and show and discuss the modelling results.

5.1 Abstract

The hypocenters of 7,719 earthquakes that occurred in the central Southern Alps between late 2008 and early 2017 and published thermochronology data from near the central Alpine Fault are used to investigate exhumation rates and the thermal structure of the crust, in the hanging wall of the fault. We obtain an initial estimation of the distribution of orogenic uplift rates and crustal thermal structure by fitting the seismicity observations to a 1-D thermal model. We then combine both the seismicity and the independent thermochronological ages with a simple model of thermal structure beneath the central Southern Alps to estimate local exhumation rates. As calculated, exhumation rate estimates vary from 1 to 8 mm/yr, with maximum values observed in the close vicinity of Aoraki/Mount Cook, which are consistent with geologic and geodetic observations. We calculate a temperature for the brittle-ductile transition in the range 440–457 °C, which is consistent with the temperatures expected for feldspar-rich crustal lithologies.

5.2 Introduction

We use the distribution of hypocentral depths of crustal seismicity and thermochronology data as constraints with which to examine the thermal structure of the crust of a young transpressive active orogen, the central section of the Southern Alps, South Island, New Zealand. The Southern Alps orogen is formed by the interaction between the Australian and Pacific plates (*Walcott*, 1998) and is bounded to the west by the Alpine Fault, a major active plate boundary oblique strike-slip fault of ∼800 km length (*Wellman and Willet*, 1942). The orogen is structurally and kinematically highly asymmetric, exhibiting high rates of uplift, exhumation, rainfall and erosion within a thin layer between the Alpine Fault and the Main Divide (*Koons et al.*, 2003).

Rapid exhumation rates have previously been computed for the Southern Alps from geological (*Norris and Cooper*, 2001; *Little et al.*, 2005; *Herman et al.*, 2007, 2009; *Wellman*, 1979; *Kamp et al.*, 1989) and geodetic data (*Beavan et al.*, 2010, 2004). *Wellman* (1979) derived vertical rates in the central Southern Alps of as much as 10 mm/yr using Quaternary faulting measurements. Fission track dating studies (*Kamp et al.*, 1989; *Tippet and Kamp*, 1993) highlighted the relation between zonations of cooling ages and exhumation rates in the Southern Alps. *Little et al.* (2005) mapped contours of fission-track, Ar/Ar, and K-Ar ages in several different minerals to estimate uplift rates near the central Alpine Fault and found a maximum vertical exhumation rates of ∼6–9 mm/yr near Fox and Franz Josef Glaciers. *Beavan et al.* (2010) calculated the relative vertical component of velocity across the Southern Alps using 10 years of continuous and semi-continuous GPS data, and determined a peak uplift rate of ∼5 mm/yr near the Main Divide on a transect across the Southern Alps (*Beavan et al.*, 2004).

One of the first thermal structure models of the Southern Alps was suggested by *Koons* (1987) that considered the Alpine Fault as a vertical discontinuity, uplift rates of around 10 mm/yr east of the fault, a 4 Myr age for exhumation of the Southern Alps and heat transfer taking place by conduction. *Koons'* (1987) model suggested a ∼5 km zone of rapid uplift adjacent to the Alpine Fault. The crust there has reduced strength due to thermal weakening that produces a high-strain zone. More recent thermal models (e.g. *Allis and Shi*, 1995; *Shi et al.*, 1996; *Toy et al.*, 2010; *Cross et al.*, 2015; *Sutherland et al.*, 2017) all indicate high temperatures at shallow depths near the Alpine Fault, particularly in a narrow zone of 10−25 km width immediately southeast of the fault's surface trace. A manifestation of theses enhanced temperatures is the existence of hot springs in the area (e.g. *Allis et al.*, 1979; *Cox et al.*, 2015).

Temperature, along with other parameters (e.g. strain rate, fluid pressure, and rock composition), play an important role in controlling the distribution of seismicity with

depth (*Chen and Molnar*, 1983; *Sibson*, 1984; *Scholz*, 1990). Temperature increases with depth, which means that at a certain depth, or a range of depths, in the crust rocks transition from brittle to ductile rheological behaviour (brittle ductile transition zone; BDT) and are unable to withhold brittle deformation (i.e. earthquakes; *Chen and Molnar*, 1983). This depth roughly corresponds to the lower limit of the seismogenic layer, hereafter referred to as the seismicity "cut-off depth" (*Sibson*, 1982, 1984; *Jackson*, 2002; *Scholz*, 1988). Therefore the distribution of the hypocentral depths can provide direct observational constraints on the strength and temperature of the crust.

Here we investigate the thermal structure of the crust in the Southern Alps using seismicity (Chapter 3; *Michailos et al.*, 2019) and thermochronology observations as constraints. This is the first study to combine short-term (late-interseismic) seismicity data with the longer-term thermochronology data that is expected to further constrain the crustal thermal model and the vertical kinematics of the orogen.

5.3 Earthquake hypocenters analysis

We analyze the distribution of the 7,719 hypocentral depths from the relocated microseismicity catalog of Chapter 3 (*Michailos et al.*, 2019) that covers the central section of the Alpine Fault for the time period between late 2008 and early 2017. As described in Chapter 3, this earthquake catalog was created by combining raw seismic waveform data from five different temporary deployments and five permanent GeoNet seismic sites. It includes the largest number of high precision earthquake locations to date for the central Southern Alps region (location uncertainties are generally smaller than 0.5 km in both horizontal and vertical directions). The GeoNet catalog in the same area and for the same time period contains around 2,151 locations of mostly fixed depths (Fig. 5.1). Therefore, this large and highly accurate seismicity dataset provides us with a unique opportunity to examine the crustal thermal structure near the central Alpine Fault in a unprecedented detail. We include all the relocated earthquake locations and do not perform any declustering as we have not observed any major aftershock sequences, and seismicity mainly consists of swarms of low-magnitude earthquakes during the last eight years (*Boese et al.*, 2012; *Michailos et al.*, 2019; *Boese et al.*, 2014).

Upper and lower seismicity cut-off depths

To investigate the seismicity in space, we divide the study area into sub-regions using a recursive quadtree clustering algorithm following the method described by *Townend and Zoback* (2001, 2004). The sub-regions obtained with this method consist of a mesh of square bins that are smaller and denser where there are more earthquakes (Fig. 5.3).

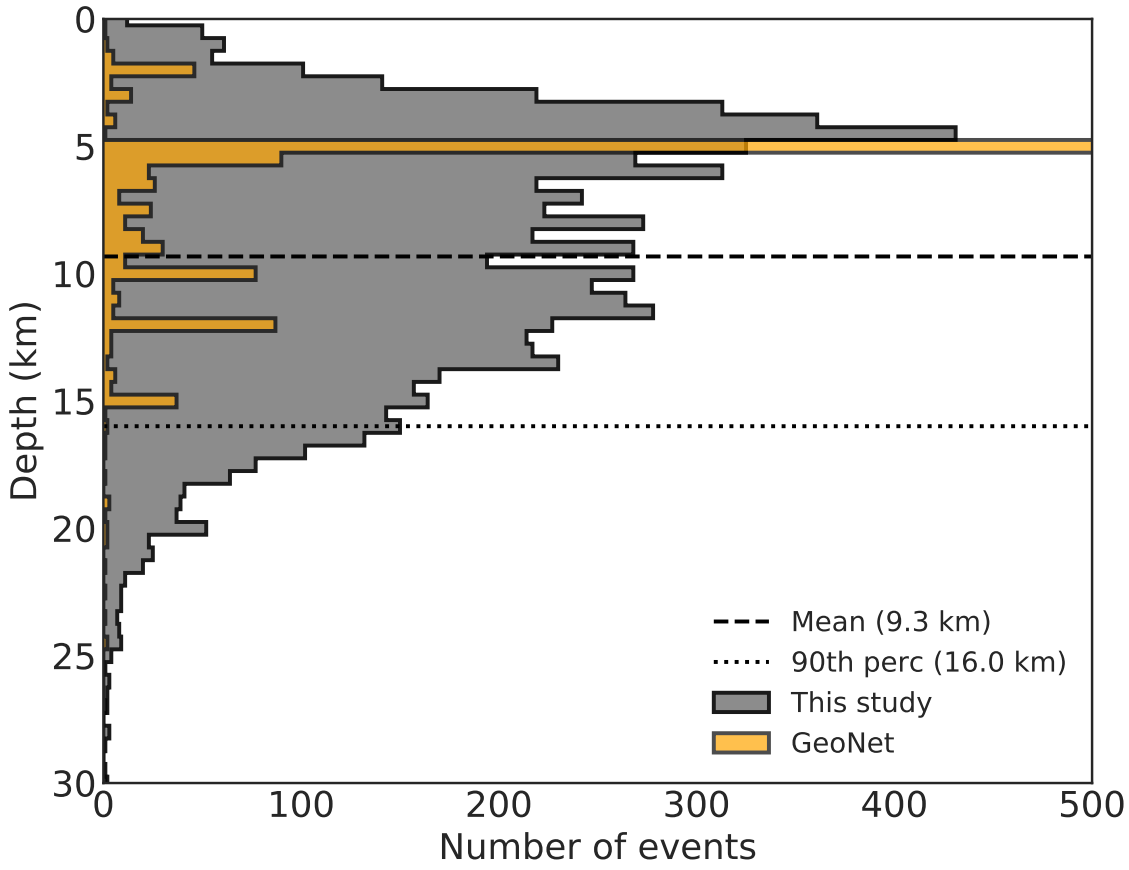

Figure 5.1: Histogram of earthquake hypocentral depths for the relocated central Southern Alps microseismicity (2008−2017) earthquake catalog used in this work (grey). Along with the earthquake depth distribution histogram for the GeoNet catalog (for comparison purposes) for the same area and time period (orange).

By doing so, we take into consideration the lateral variations of hypocentral depths. We examine the distribution of seismicity in depth (Figures D1 and D2 of Appendix D) and parameterize the cumulative distribution of hypocentral depths, including location uncertainties, that lie within each bin.

We use cumulative distribution functions of hypocentral depths for earthquakes in each bin to calculate the upper (z_{100}) and lower (z_0) limits of seismicity in each bin. Specifically, we fit a linear regression line to the cumulative distribution functions bounded from 10 to 90 % of the cumulative distributions (Fig. 5.2). We exclude the upper and lower subsets of the cumulative distributions for the following reasons: 1) the top limits of these distributions are expected to be poorly located as earthquake locations tend to be less accurate at shallow depth ($\leq$5km); and 2) the bottom limit of these distributions is likely related to different tectonic processes below the brittle-ductile transition (i.e. in the deeper ductile part of the crust that is not of interest here; Fig. 5.2a and c).

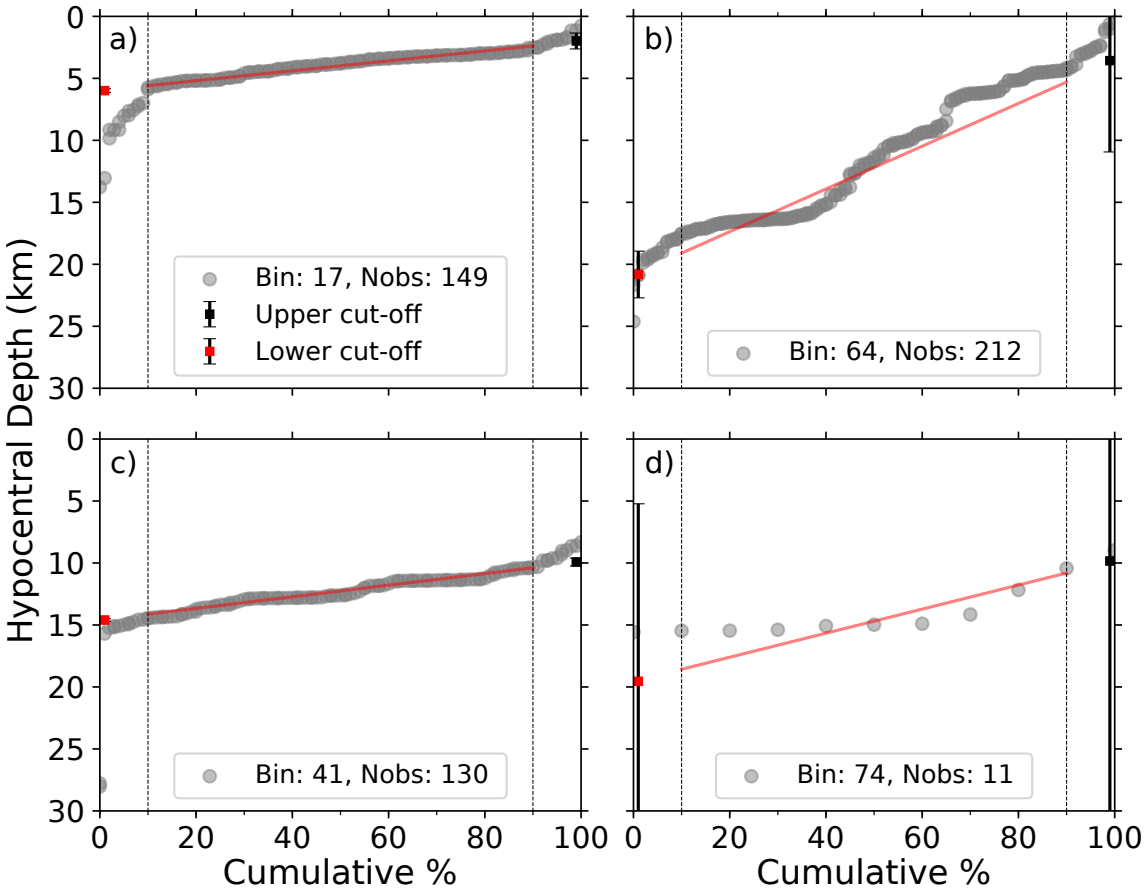

Figure 5.2: Cumulative distribution function of hypocentral depths within bins 17, 41, 64 and 74 (spatial distribution of the bins is shown on Fig. 5.3). Red lines depict linear regression that fits the 10–90 % interval of the observations. The 10–90 % interval is bounded by the black dashed lines. Red and black squares show the lower seismicity cut-off depth (0%) and the upper seismicity cut-off depth (100%) calculated by the predicted values from the linear regression, respectively.

Using these fitted linear regression lines we estimate values for the lower seismicity cut-off depth (0%) and the upper seismicity cut-off depth (100%), as well as the standard errors. Figure 5.2 shows four distinct hypocentral distributions with their fitted linear regression lines and the upper and lower seismicity cut-off depth estimates. We exclude bins that have <30 observations, which are mainly located at the periphery of the seismic network, because their cut-off depth estimates have large uncertainties (e.g. bin 74; Fig. 5.3d). Details for the rest of the bins can be found in Figures D3 and D4 of Appendix D.

Seismicity cut-off depths

The results obtained from analysis of hypocentral depths along the central Southern Alps are summarised in Fig. 5.3. Three sections of the region exhibit distinctly different distributions of hypocentral depths.

In the northeastern section of the central Southern Alps (near Harihari and Ross, Fig. 5.3), lower seismicity cut-off depths are >15 km, reaching in some of the bins up to 23 km depths, which is slightly deeper than typical crustal seismicity depths (e.g. 5-20 km; *Bourguignon et al.*, 2015). Upper cut-off seismicity depths are all <10 km (Fig. 5.3) resulting in seismogenic crustal thickness generally greater than 15 km. In contrast, in the southwestern part of the central Southern Alps (near Fox Glacier and Franz Josef Glacier, Fig. 5.3) the lower cut-off seismicity depths are generally shallow (≤12 km) in the vicinity of Aoraki/Mount Cook. Upper cut-off seismicity depths near Aoraki/Mount Cook are mostly <5 km, which outlines a relatively thin seismogenic layer in the upper part of the crust. In the middle of the examined region (close to Whataroa, Fig. 5.3; bins 25, 41, 42, 43 and 44) lower cut-off seismicity depths vary from 15 to 17 km, and the upper cut-off depths are 10–12 km. This highlights a particularly thin seismogenic layer, but located deeper in the crust (≥10 km), with an absence of seismicity in the shallow part of the crust (≤10 km). This region of deeper seismicity corresponds to the previously identified Whataroa seismic gap (*Leitner and Eberhart-Phillips*, 2001; *Boese et al.*, 2012; *Michailos et al.*, 2019). In general, seismogenic layer thickness in the central Southern Alps is <12 km (Fig. D5 of Appendix D). The maximum and minimum seismogenic layer thickness values are observed northeastern of Harihari (≥20 km) and around Aoraki/Mount Cook (≤5 km), respectively.

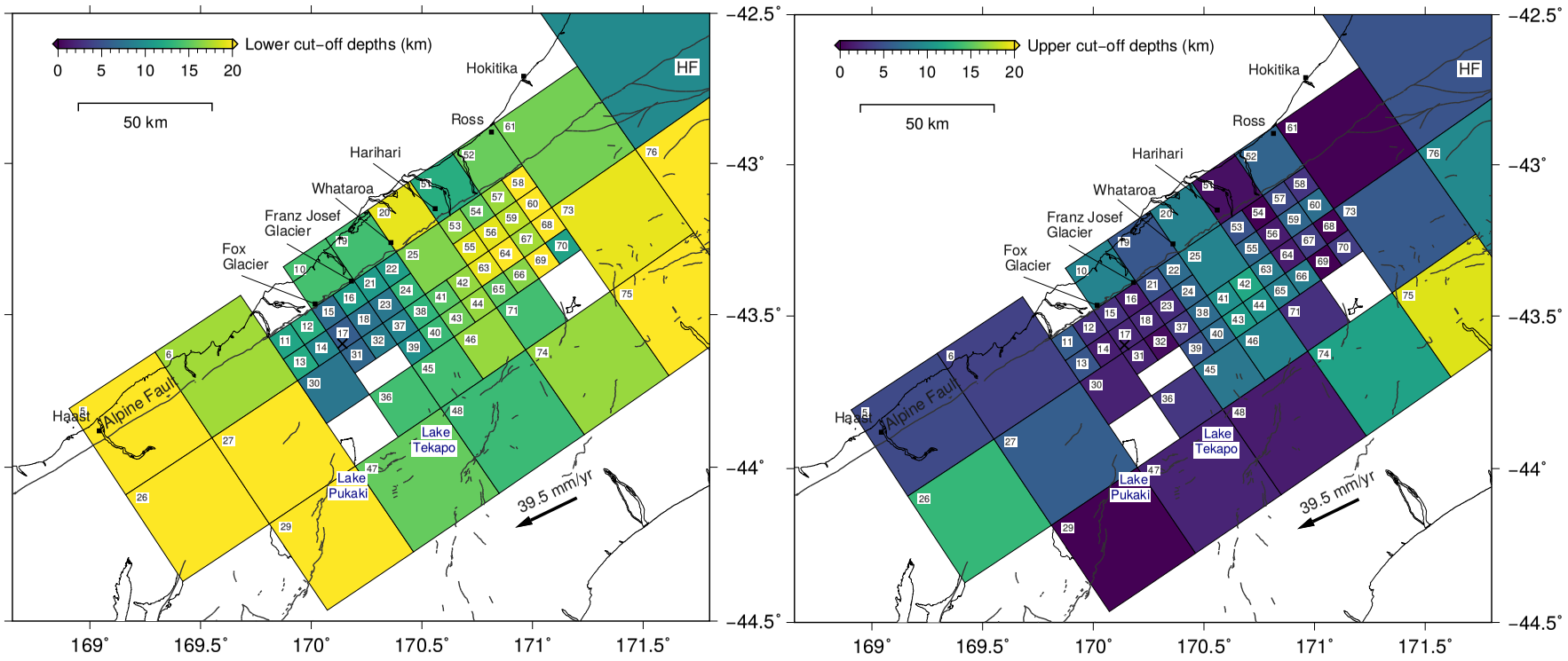

Figure 5.3: Maps showing the spatial distribution of the lower (a) and upper (b) cut-off depths of the shallow seismicity with hypocentral depths smaller than 25 km. Bins are obtained using the quadtree clustering algorithm and have a minimum size of 10 km and contain a minimum of 20 earthquakes. Bins with fewer than 20 earthquakes have no calculations and are not plotted. Numbers indicate each bin's name. Arrow indicates the local velocity of Pacific Plate relative to Australia (∼39.5 mm/yr in Fox Glacier; *DeMets et al.*, 2010). Black lines show the active faults from the New Zealand Active Faults Database[a]. HF shows the location of the Hope Fault.

[a] `http://data.gns.cri.nz/af/`

5.4 1-D thermal modeling

To calculate the crustal thermal structure we assume 1-D steady state exhumation. The depth to the base of the block is constant (Z_{BASE}). Material moves through the block at a constant rate such that the flux in equals the flux out. The base and top of the block have constant temperatures of T_{BASE} and T_0, respectively. We assume a constant temperature of 13°C at the upper boundary (Z_0; sea level) and do not include considerations related to variations of temperatures caused by thermal diffusion with the circulation of meteoric fluids (*Cox et al.*, 2015; *Sutherland et al.*, 2017). This assumption was applied farther south in the Southern Alps by *Upton and Sutherland* (2014) and *Sutherland et al.* (2009). Effects of lateral strain rate variations are neglected in our model. We also infer a topographic steady state, where rock uplift rates are equal to exhumation rate, which is applicable for uplifting regions with high erosion rates (*Adams*, 1981; *Herman et al.*, 2007, 2009).

The 1-D temperature-depth profile is given by the following second-order differential Equation:

$$\kappa \frac{d^2T}{dz^2} + Cv\frac{dT}{dz} + H = C\frac{dT}{dt} \tag{5.1}$$

where z is the depth in (km), κ is the thermal conductivity, C is the volumetric heat capacity, H is the volumetric heat productivity, v is the exhumation rate, T is the temperature, and t is the time. At steady state, trying a solution of the form $T = Ae^{rz}$ yields the general solution:

$$T(z, v) = A_1 + A_2 \exp\left(\frac{Cv}{\kappa}z\right) + \frac{H}{Cv}z \tag{5.2}$$

where A_2, A_1 are the solutions of the second order differential Equation when applying two boundary conditions ($z = Z_0$, $T = T_0$ and $z = Z_{BASE}$, $T = T_{BASE}$):

$$A_2 = \frac{(T_{BASE} - T_0) - \frac{H}{Cv}(Z_{BASE} - Z_0)}{\exp\left(\frac{Cv}{\kappa}Z_{BASE}\right) - \exp\left(\frac{Cv}{\kappa}Z_0\right)} \tag{5.3}$$

$$A_1 = T_0 - A_2 \exp\left(\frac{Cv}{\kappa}Z_0\right) - \frac{H}{Cv}Z_0 \tag{5.4}$$

The analytical solution of the 1-D thermal structure depth profile can be found in the Appendix D. We use the following boundary conditions and assumptions:

1. A thermal conductivity of 3.2 $Wm^{-1}K^{-1}$, a volumetric heat productivity of 3.0×10^{-6} $Wm^{-}3$ and a thermal diffusivity of 2.0×10^{-6} m^2s^{-1}, respectively, mea-

sured on rock samples from typical lithologies of the Alpine Fault hanging-wall (*Janku-Čápová*, 2018).

2. A temperature of T_0=13°C at sea level, which is close to the mean annual temperature and imposed as the upper boundary condition (*Sutherland et al.*, 2009; *Upton and Sutherland*, 2014).

3. A temperature of T_{BDT}=450°C, at the brittle ductile transition zone (*Scholz*, 1988; *Sibson*, 1984), though we later allow this to vary.

4. A decollement depth of Z_{BASE}=35 km, imaged with geophysical techniques during the SIGHT experiment (*Stern et al.*, 2007; *Davey et al.*, 2007).

5. A temperature of T_{BASE}=550°C for the depth of the decollement, based on thermobarometric estimates from high-grade mylonites exhumed in the hanging-wall from the lower part of the crust due to the convergent component of slip (*Toy et al.*, 2010; *Vry et al.*, 2004; *Norris and Toy*, 2014; *Upton et al.*, 1995; *Toy et al.*, 2008).

Solutions are shown in Fig. 5.4. The general shape of the temperature profiles with depth, derived here (Fig. 5.4), are in general agreement with those previously suggested by (*Toy et al.*, 2010; *Cross et al.*, 2015; *Koons*, 1987). They exhibit a high upper-crustal geothermal gradient and a lower geothermal gradient in the deeper parts of the crust. Temperature profiles corresponding to rapid uplift rates exhibit an inverted shape in deeper parts of the model (Fig. 5.4). This is because heat production occurs during advection, as the tectonic processes occur much more rapidly than the loss of heat by conduction *Koons* (1987). This thermal feature of the model is consistent with a prograde metamorphism during advection (e.g. fluid inclusions and peak temperature of ductile deformation; *Upton et al.*, 1995; *Toy et al.*, 2008).

5.5 Thermochronology data

Thermochronology data provide measurements of the timing and rates at which rocks cool as they move towards the surface during exhumation (*Dodson*, 1973). The age estimates are based on the natural occurring radioactive decay or spontaneous fission of a parent nuclide and the accumulation of a corresponding daughter product such as new nuclei (e.g. (U-Th)/He dating) or crystal damage (e.g. fission-track) (*Peyton and Carrapa*, 2013).

At high temperatures and/or depths, the system is reset and daughter products do not accumulate in the system. For example, He atoms are not retained (U-Th/He

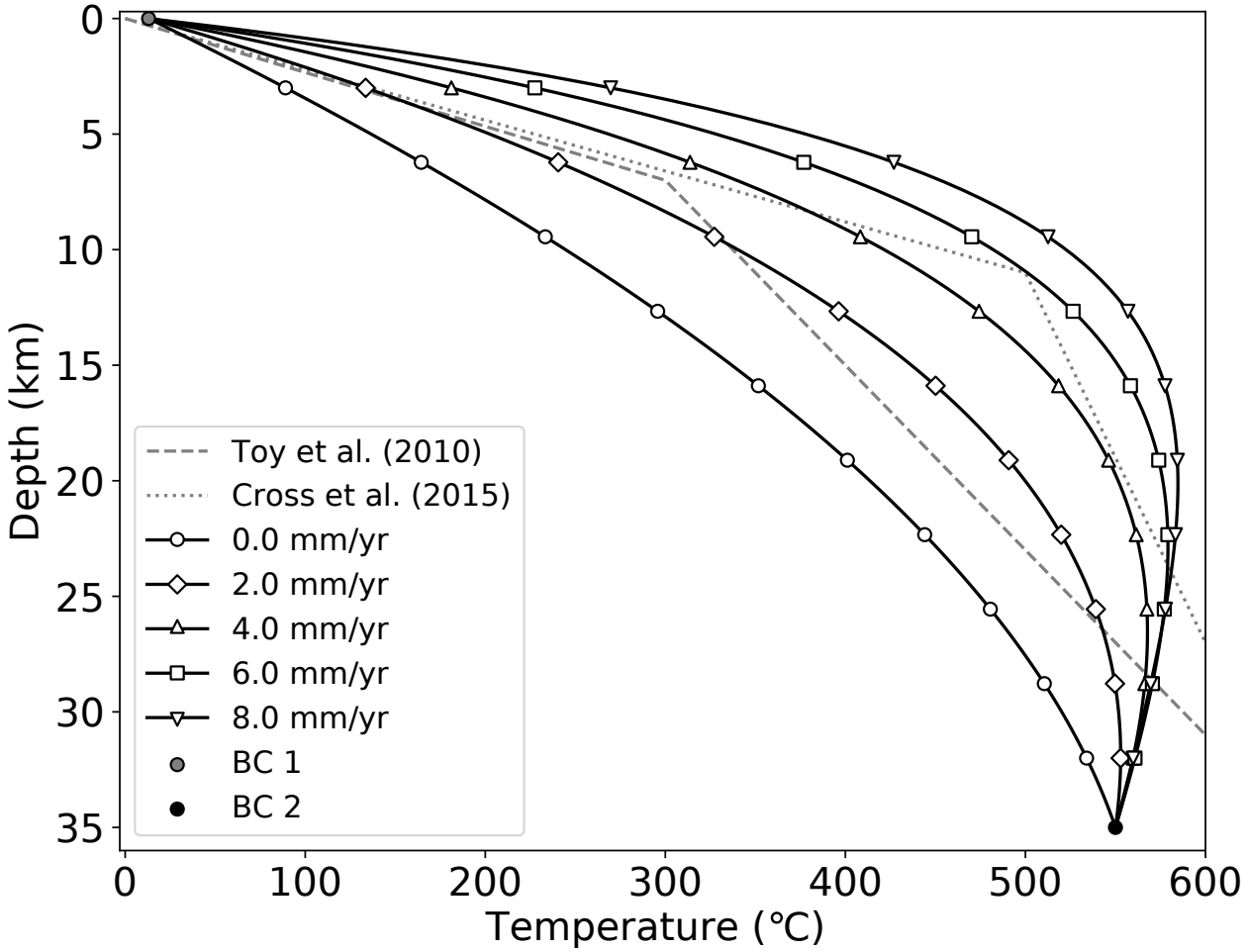

Figure 5.4: Temperature and depth profiles for an exhuming block in the central Southern Alps region with varying exhumation rate values (0, 2, 4, 6 and 8 mm/yr). Grey and black dots represent the two boundary conditions used for the surface and the depth of the decollement, respectively. Previous temperature profiles from *Cross et al.* (2015) and *Toy et al.* (2010) are also shown in grey dotted and dashed lines, respectively.

dating) or fission tracks are healed (annealed). With decreasing temperatures and/or depth, a temperature or depth range exists over which daughter products start to be retained in the system (*Reiners and Brandon*, 2006). These temperature ranges are called the partial retention zones (PRZ; (U-Th)/He) and partial annealing zones (PAZ; fission-track). The annealing process for crystal damage occurs over a range of temperatures for different thermochronometers (e.g. Apatite fission-track, AFT, 80–110°C; Zircon fission-track, ZFT, 190–230°C and Zircon (U-Th)/He, ZHe, 140–180°C; *Reiners et al.*, 2004; *Tagami*, 2005; *Gleadow and Duddy*, 1981). Using the cooling age information a single temperature on the cooling path can be defined; this is known as the effective closure temperature, T_c (*Dodson*, 1973; *Reiners and Brandon*, 2006). Thus, by considering multiple thermochronometric systems with contrasting closure temperatures in coalition, detailed time-temperature paths can be constructed for samples and converted into exhumation rates. Table 5.1 summarises the closure temperatures as a function of cooling rate for different thermochronometers (*Reiners and Brandon*,

2006).

Table 5.1: Effective closure temperatures (T_c) as a function of cooling rates for ZHe, ZFT, and AFT thermochronometers adopted from (*Reiners and Brandon*, 2006).

Cooling rates (°C/Myr)	AFT (°C)	ZFT (°C)	ZHe (°C)
0.1	80	190	140
1.0	100	210	160
10.0	120	230	180
100.0	145	255	205

There are a total of 194 thermochronological AFT, ZFT and ZHe age estimates available across the central Southern Alps conducted by previous studies (Fig. 5.6; *Herman et al.*, 2007, 2009; *Tippet and Kamp*, 1993; *Ring and Bernet*, 2010; *Kamp et al.*, 1989; *Batt and Braun*, 1999; *Batt et al.*, 2000; *Seward*, 1989).

Including the thermochronology data in our model, which cover a long-term period of the kinematics of the orogen, makes the assumption of a steady state in our models problematic. This is because the geothermal structure is changing with time and it was less likely to be in steady state in the past, due to an acceleration in exhumation rates and plate convergence with time. To cope with this issue, we only consider ages less than 10 Ma (132 out of the total of 194; Fig. 5.5).

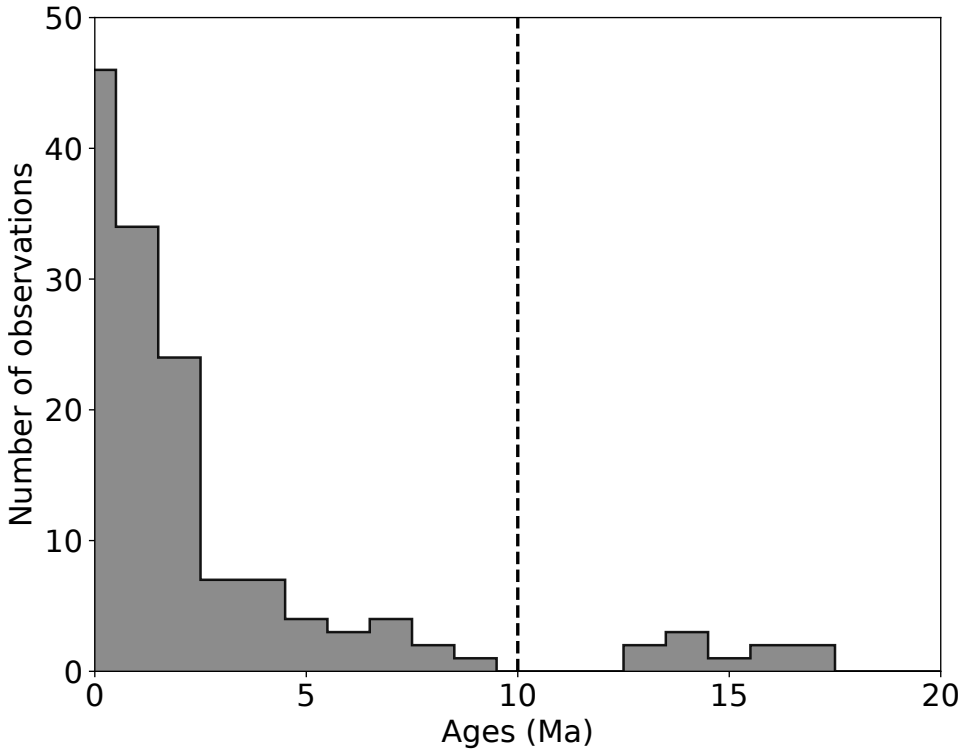

Figure 5.5: Histogram of apatite fission track (AFT), zircon fission track (ZFT), and zircon U-Th/He (ZHe) thermochronological ages (Ma) near the central Alpine Fault, same data as in Fig. 5.6.

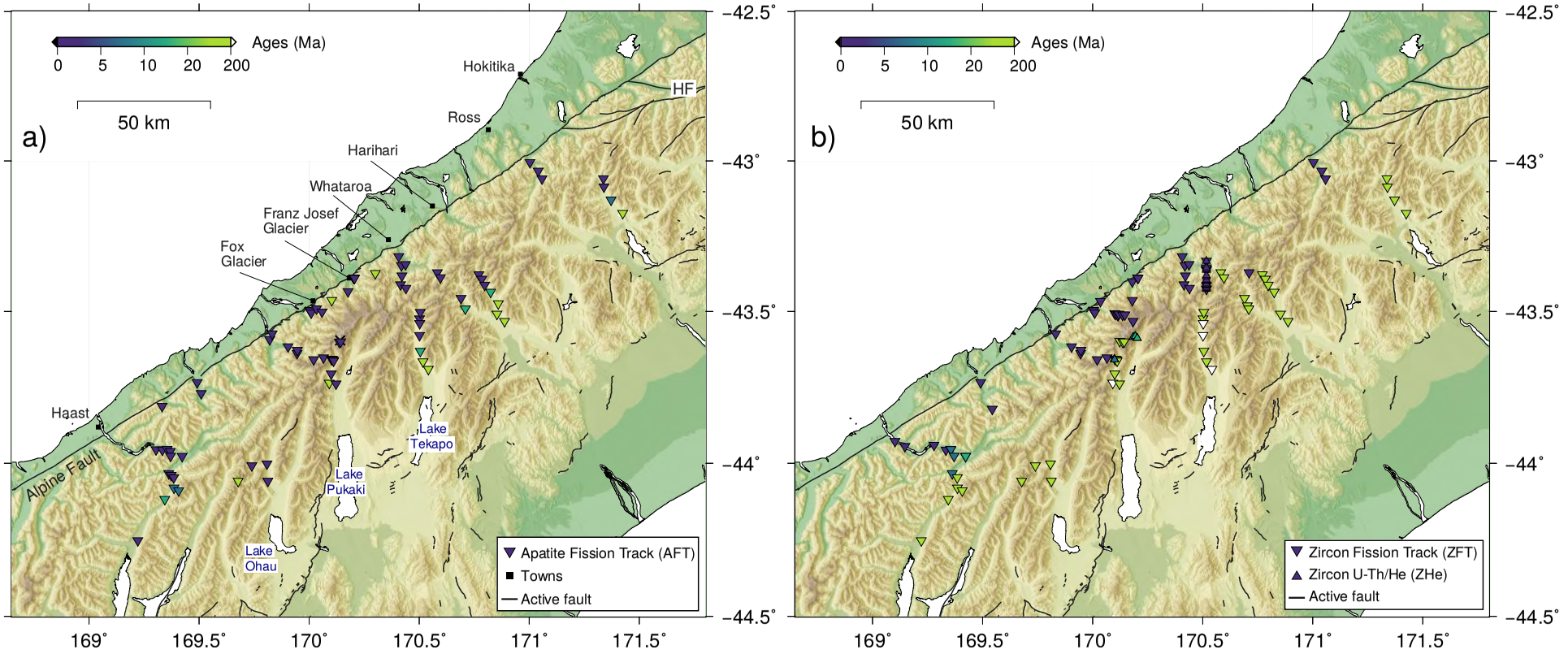

Figure 5.6: Maps showing the spatial distribution of thermochronological ages near the central Alpine Fault (*Herman et al.*, 2007, 2009; *Tippet and Kamp*, 1993; *Ring and Bernet*, 2010; *Kamp et al.*, 1989; *Batt and Braun*, 1999; *Batt et al.*, 2000; *Seward*, 1989), coloured according to their estimated ages (see color scales). (a) AFT is apatite fission track. (b) ZFT is zircon fission track, and ZHe is zircon U-Th/He. HF is the Hope Fault.

5.6 Regional exhumation rate

We calculate a model of the crustal thermal structure using 45 seismicity and 132 thermochronology observations. A major advantage of incorporating the thermochronology observations is that the models will better constrain the longer-term vertical kinematics of the orogen. In addition, because the thermochronometers are independently estimated based on their corresponding closure temperatures, we can solve for the T_{BDT} temperature as well as for the exhumation rates.

We define a grid of 55 points: five lines of 11 points parallel to the Alpine Fault, with a spacing of ∼20 km. We use a relatively coarse grid for simplicity. The 22 points at the northwestern-most and southeastern-most lines are assigned fixed exhumation rates of 0.1 mm/yr, while the 34 points in the interior have adjustable exhumation rate parameters (including a T_{BDT} temperature parameter throughout the model). The model has two fixed parameters that are based on independent geological and geophysical studies (e.g. Z_{BASE}=35 km, T_{BASE}=550°C; *Vry et al.*, 2004; *Toy et al.*, 2010; *Stern et al.*, 2007; *Davey et al.*, 2007).

We create an interpolated 2-D surface of the exhumation rate values within the limits of the grid to define exhumation rate, v^{pred} at the location of each thermochronological or seismicity observation. In the case of thermochronology observations, we use exhumation rate to estimate the temperature profile with depth at the location of the datum using Equation 5.2. Having estimated the temperature profile and knowing the effective closure temperature of each thermochronometer, we obtain the total amount of exhumation, Z_c, that has occurred since the cooling age. We calculate the predicted age, A^{pred} using the following Equation:

$$A^{pred} = \frac{Z_c + \Upsilon}{v^{pred}} \tag{5.5}$$

where Υ is the elevation at which the thermochronology sample was collected. The thermochronology observations misfit, Q_T, is then calculated:

$$Q_T = \sum_{j=1}^{m} \frac{(A_j^{obs} - A_j^{pred})^2}{\sigma_j^2} \tag{5.6}$$

Here m is the number of thermochronology observations and σ_j is the error measurement of each observation.

In the case of the seismicity observations, we again estimate the temperature profile, using Equation 5.2 and obtain the predicted depth of the brittle-ductile transition, Z^{pred} according to the value of T_{BDT} (that is adjustable during the optimization iterations).

The effects of lateral strain rate variations are not considered when calculating Z^{pred}. We calculate the misfit between observed and predicted brittle-ductile depths as:

$$Q_S = \sum_{i=1}^{n} \frac{(Z_i^{obs} - Z_i^{pred})^2}{\sigma_i^2} \tag{5.7}$$

where n is the number of seismicity observations and σ_i is the standard error of Z_{100}=Z_i^{obs} (the line fitting the cumulative distribution of the hypocentral depths; Section 5.3).

To compute the total misfit of each iteration of the optimization process we need to combine two different types of uncertainties. On the one hand, seismicity uncertainties are estimated taking into account the lateral variability of seismicity depths within bins (i.e. real spatial variability; Section 5.3). On the other hand, thermochronology uncertainties represent analytical measurement errors.

In order to cope with this discrepancy between the nature of the uncertainties of the two different datasets, we introduce a regularization parameter α that controls the weight attached to the two types of misfits when minimizing the total misfit. The total misfit is calculated as below.

$$Q = \alpha Q_T + Q_S \tag{5.8}$$

We calculate four different models with varying α values (three for steady state and one with an initial state for the thermochronology data). The first model has α=1.0, meaning that both datasets have equal weight; the second has an $\alpha = n/m$ and removes the weight from the different number of observations; and the third model has an α value that normalises the different type of uncertainties and the different size of the two datasets (i.e. seismicity and thermochronology) so that $\alpha\ Q_T = Q_S$ (α=0.70). Finally, the fourth model assumes an initial geotherm established before the exhumation process in the Southern Alps orogen started. Therefore, in this model when calculating the temperature-depth profile, using Equation 5.2, the exhumation rate is set equal to a small value (i.e. v^{pred}=0.0001 mm/yr).

5.7 Model results

5.7.1 Exhumation rates based on seismicity

As an initial model, we only use seismicity observations to obtain estimates of exhumation rates. Since seismicity observations span a short time scale, compared to

thermochronology data, the steady state assumption is likely to be valid. We use the lower seismicity cut-off depth values (z_0) and assume that they correspond to the brittle-ductile transition at T_{BDT}.

Rearranging Equation 5.2 and setting T=T_{BDT} and Z=z_0 we solve for the exhumation rate, v. For the assumed T_{BDT} temperature of 450°C, we obtain an exhumation rate estimate for each bin containing >30 earthquakes that lies in the hanging wall of the Alpine Fault. We exclude bins on the periphery of the seismic network (bins 5, 6, 26, 29, 62, 76; Fig. 5.3). Details of these estimates are summarised in Table D.1 of Appendix D. However, even in the case in which a bin contains a large number of earthquakes that does not necessarily accurately constrain the seismicity cut-off depths. This issue is dealt by following the analysis described in Section 5.3.

Exhumation rates calculated as outlined above, using the temperature depth profiles vary from 1 to 11 mm/yr (Fig. 5.7). We observe the highest exhumation rates (>6 mm/yr) near the vicinity of Aoraki/Mount Cook. These exhumation rates are in close agreement with the lowest hornblende cooling ages related to exhumation rates of up to a maximum value of ∼6–9 mm/yr by *Little et al.* (2005). The most striking aspect of Fig. 5.7 is the large difference in exhumation rate (∼8mm/yr) over a relatively short along-strike swath (<100 km) of the Alpine Fault.

5.7.2 Exhumation rates on base of seismicity and thermochronology

Figures 5.8–5.11 summarise the results obtained from the four different models considered. All models, including the fourth which is based upon a different assumption, provide very similar patterns of exhumation rate variation in the Southern Alps. In particular, exhumation rates vary from 1–8 mm/yr along the length of the central Alpine Fault, with the highest values (6–8 mm/yr) observed close to Aoraki/Mount Cook. The lowest exhumation rates (<2 mm/yr) are consistently observed in the northeastern part of the examined region (near Harihari and Hokitika; Fig. 5.8a) for all the models. In the southwestern part of the examined region (near Haast; Fig. 5.8a), exhumation rates are generally >1 mm/yr for the first three models (i.e. steady state models with varying α values) and significantly larger (2–3 mm/yr) in the last model that considers an initial geotherm (exhumation rate = 0.0 mm/yr; Fig. 5.4) prior to the exhumation initiation. The distribution of the residuals for the all the models (Fig. 5.8b, 5.9b, 5.10b, 5.11b) exhibits a detailed local variability in the central part of the examined region (more observations) indicating a good fit between the models and the observations. Long-wavelength signals are mostly observed in the periphery of the examined region. The residuals of the third model (Fig. 5.10b) has the lowest values.

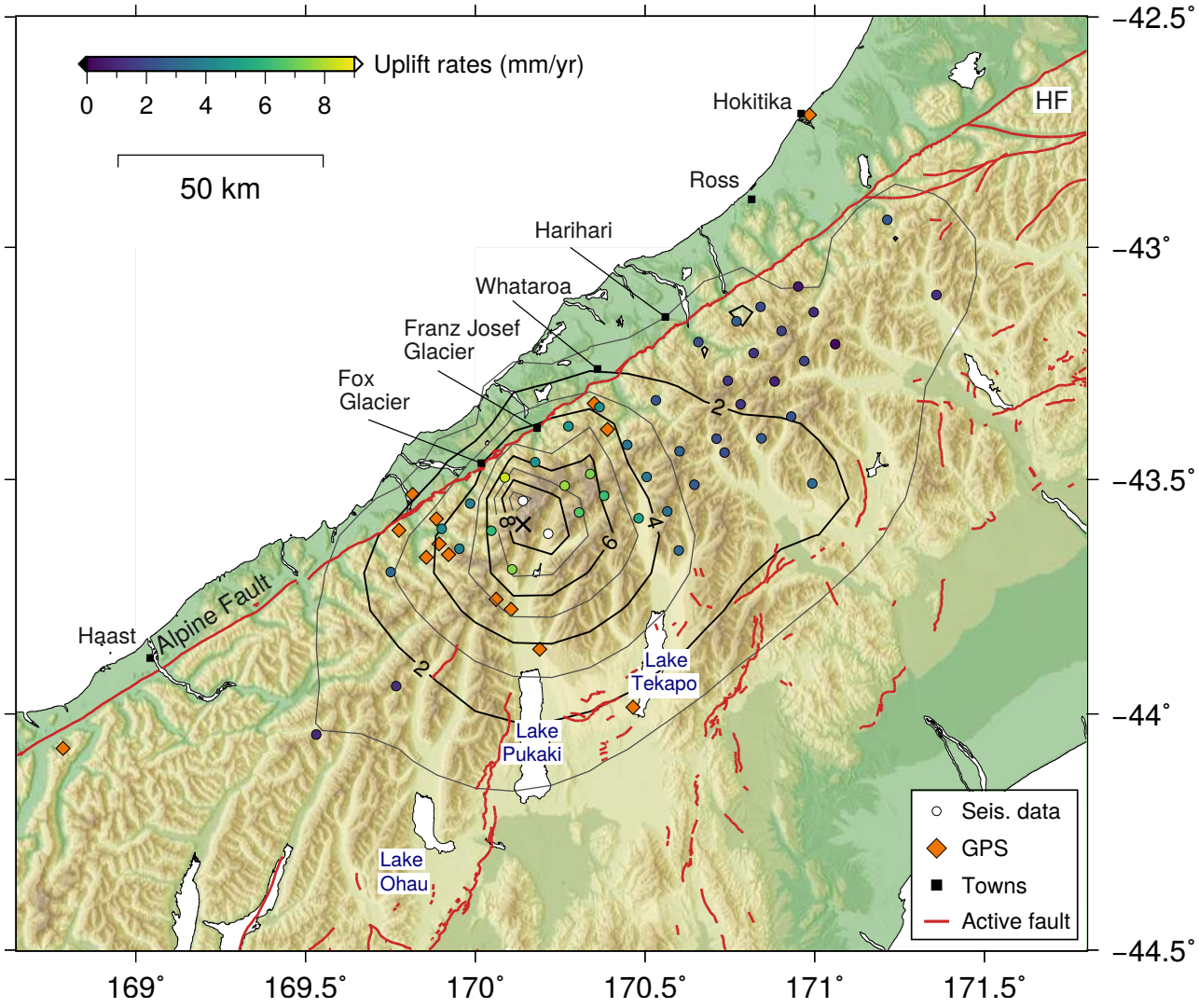

Figure 5.7: Contoured distribution of the exhumation rates along the central Southern Alps based on seismicity and assuming that the base of the seismicity corresponds to a temperature of T_{BDT}=450°C. Circles represent the exhumation rate calculations obtained from the bins defined in Fig. 5.3 that contain >30 observations and their colors denote the exhumation rate values (see color scale). Orange diamonds depict the distribution of the GPS sites.

Our exhumation rate findings are consistent with those suggested by *Wellman* (1979); *Tippet and Kamp* (1993); *Little et al.* (2005), who each inferred rapid uplift and exhumation rates in the central part of the Southern Alps using geological data (e.g. Quaternary faulting, fission track ages). In particular, *Little et al.* (2005) suggested maximum uplift rates of ∼6–9mm/yr in a small region near Franz-Josef and Fox glaciers that is in close agreement with our modeled results here. Moreover, our final results, from model 3, are very similar to the geodetically estimated uplift rates of ∼5mm/yr obtained by *Beavan et al.* (2010) along the GPS transect across the Southern Alps (Fig. 5.12). Exhumation rate estimates calculated here (Model 3) follow the same pattern as the geodetic observations and have slightly larger values (∼1.3 mm/yr; within the geodetic observations confidence limits).

The earthquake hypocenter temperatures obtained from the three steady state models (Fig. 5.8c, 5.9c, 5.10c) based on both seismicity and thermochronology data are very similar to each other. Their $T_{90^{th}}$, T_{median} and T_{BDT} values are 491–509°C, 387–393°C and 442–444°C, respectively. Earthquake hypocenter temperatures from the fourth model (Fig. 5.11), incorporating the initial geotherm before the initiation of the exhumation in the Southern Alps, exhibit slightly hotter temperatures (T_{median}= 396°C, $T_{90^{th}}$= 496°C and T_{BDT}=457°C; Fig. 5.11c) compared to the results from the first three steady state models. These earthquake hypocenter temperatures and the T_{BDT} are slightly hotter than expected for crust composed mainly of quartz-rich rocks (i.e. 300–350°; *Sibson*, 1984). However, these temperature ranges are similar to those expected for a crust consisting of feldspar-rich rocks (i.e. ∼450°; *Sibson*, 1984; *Bonner et al.*, 2003). This is consistent with the presence of feldspar-rich mafic rock composition in some parts of the crust (e.g. Pounamu Ultramafic Belt; *Norris and Cooper*, 2007). Another explanation for these relatively hot earthquake hypocenter temperatures is the existence of locally increased strain rates (*Bourguignon et al.*, 2015; *Lamb and Smith*, 2013). An increase in strain rate results in an increase of the T_{BDT} value (*Sibson*, 1984).

Fig. 5.13 shows a cross-section of the seismicity hypocenters and the 100, 200, 300, 400 and 500 °C isotherms along cross section A–A' marked in Figure 5.10. The distribution of the isotherms depends upon the temperature at the brittle-ductile transition defined by the models. We use the value of T_{BDT}=440°C that we obtained from the three steady-state models. We observe a dense distribution of the isotherms beneath Aoraki/Mount Cook that correlates with the shallow seismicity there.

Having established the thermal structure, we can obtain an approximation for the geothermal gradients at the locations of the seismicity observations (where Z_{BASE} is known). The geothermal gradient estimates range from 16 to 74°C/km, with the highest values coinciding with the areas of high uplift and shallow seismicity cut-off depths. The range of these estimates lies within those obtained by *Sutherland et al.* (2012) in the DFDP-1B borehole at Gaunt Creek (62.6±2.1°C/km). However, our geothermal gradient estimates do not agree with the extreme geothermal gradient of 125±55°C/km observed in the DFDP-2B borehole at Whataroa Valley (*Sutherland et al.*, 2017). This difference in the geothermal gradient near Whataroa is due to the local topographically driven fluid movement that accumulates the heat into the valleys (*Townend et al.*, 2017; *Sutherland et al.*, 2017), a feature that we have not included in our modeling as it was considered to be beyond the scope of this study.

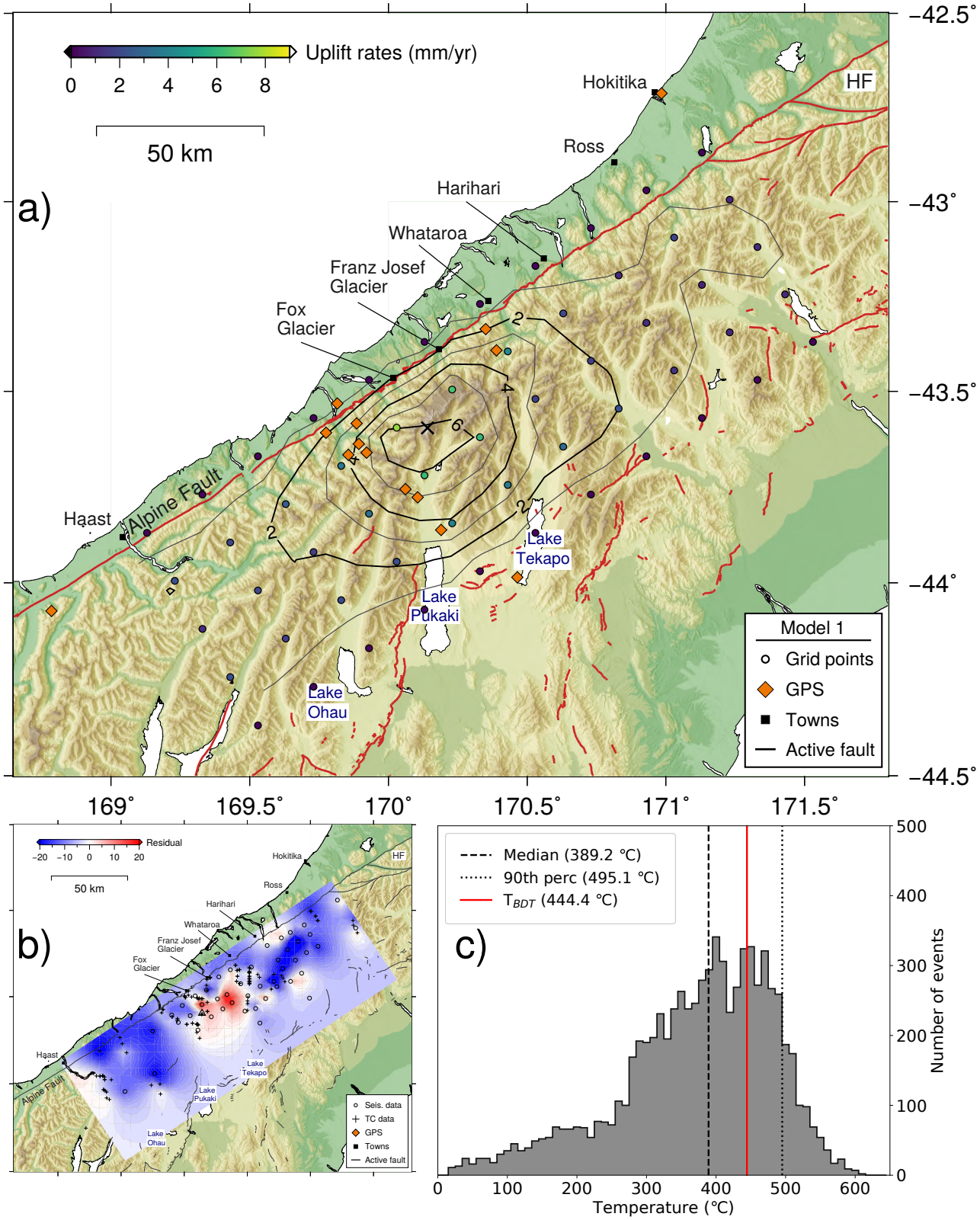

Figure 5.8: Summary of results from the first model that includes both the seismicity and thermochronology observations equally weighted in the optimization process (Model1; α=1.0). a) Contoured distribution of the exhumation rates along the central Southern Alps based on seismicity and thermochronology data. Circles represent the models grid points and their colors denote the uplift rate values (see color scale). Orange diamonds depict the distribution of the GPS sites. b) Spatial distribution of the standard residuals of both seismicity and thermochronology observations. c) Temperature distribution of individual earthquakes.

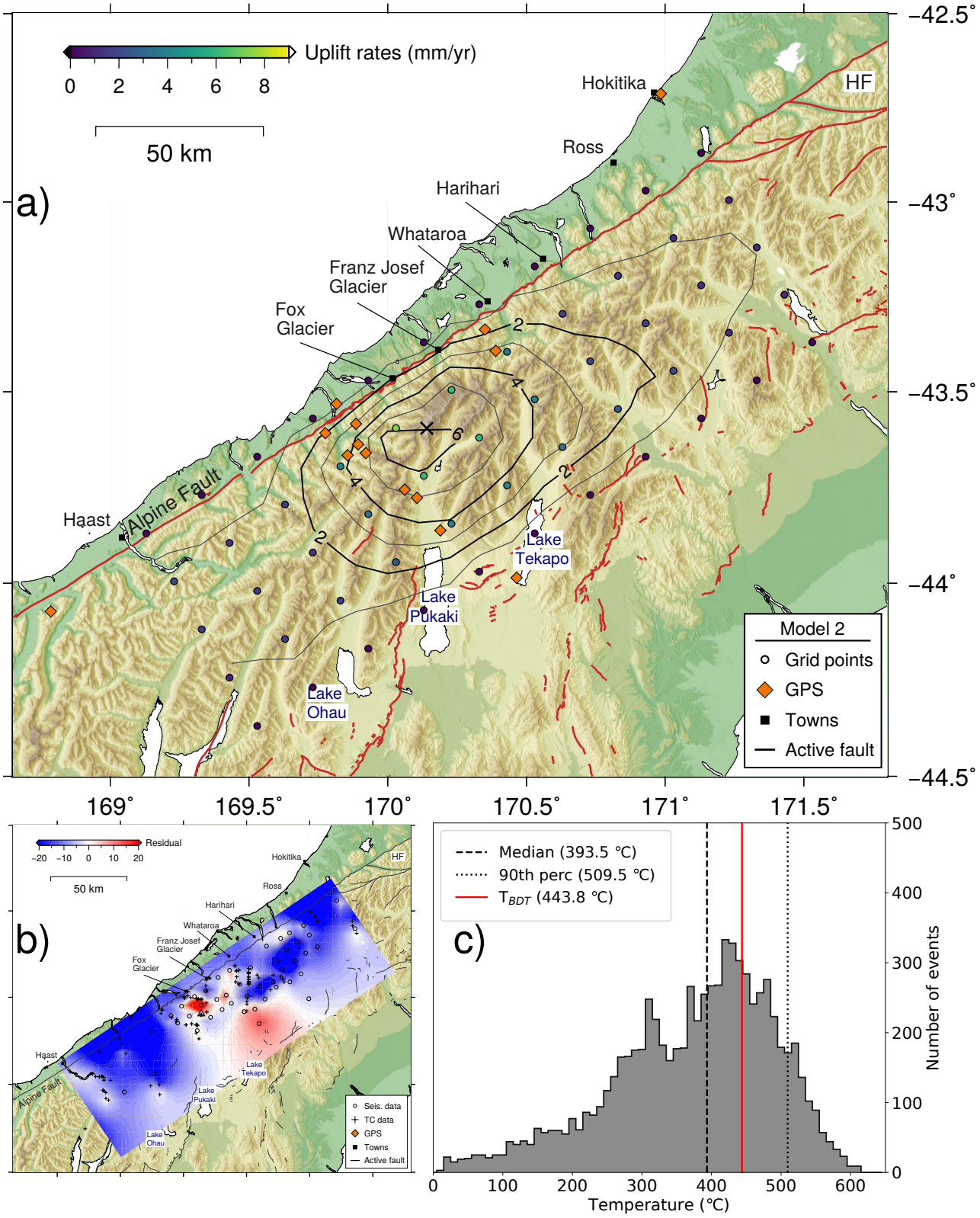

Figure 5.9: Summary of results from the second model that includes both the seismicity and thermochronology observations using an α value of n/m (Model 2; α=0.34), where n and m are the size of the seismicity and the thermochronology data, respectively. Refer to Figure 5.8 caption for more details.

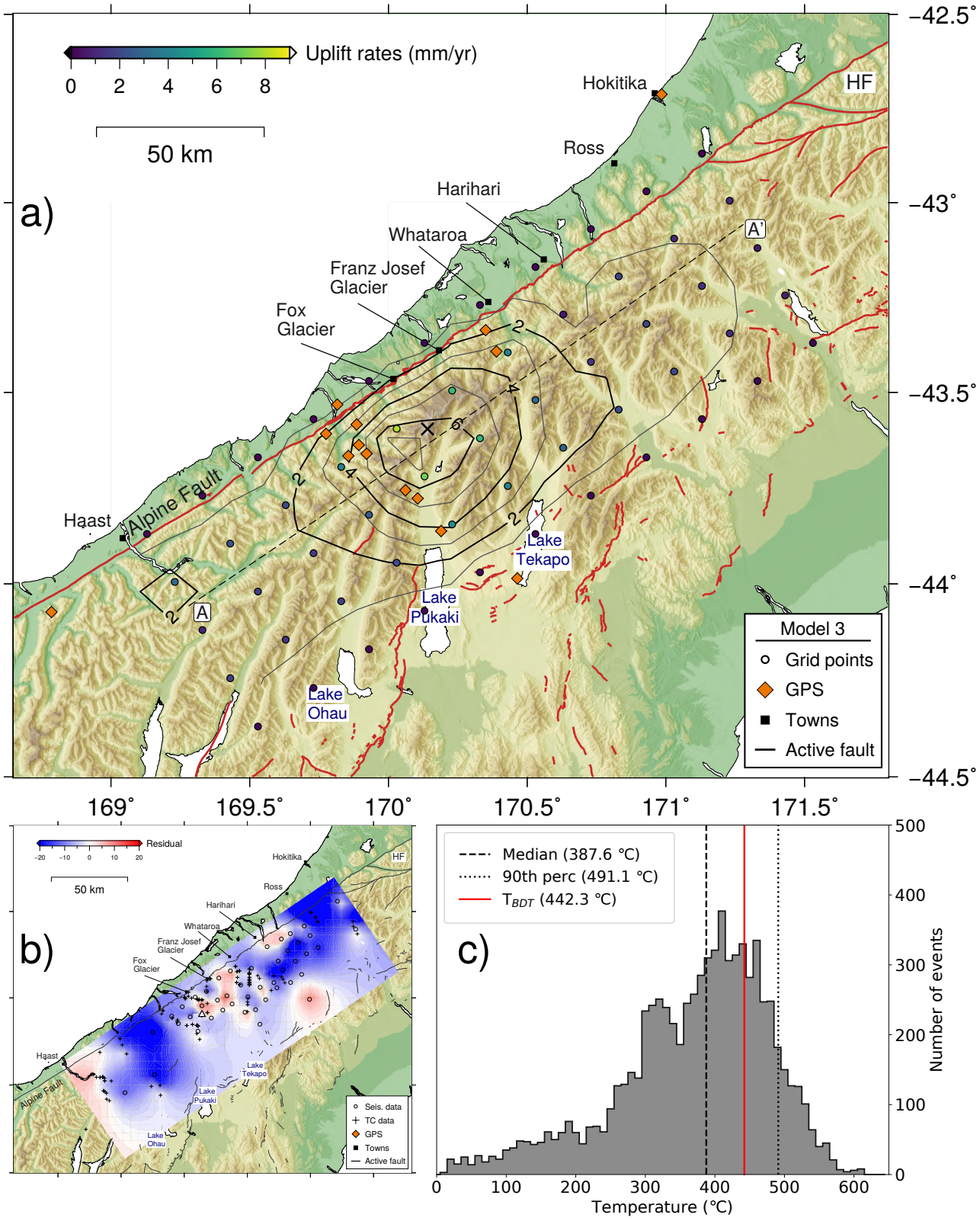

Figure 5.10: Summary of results from the third model using an α value that normalises the different type of uncertainties and the different number of observations so that $\alpha\ Q_T = Q_S$ (Model 3; α=0.70). Refer to Figure 5.8 caption for more details.

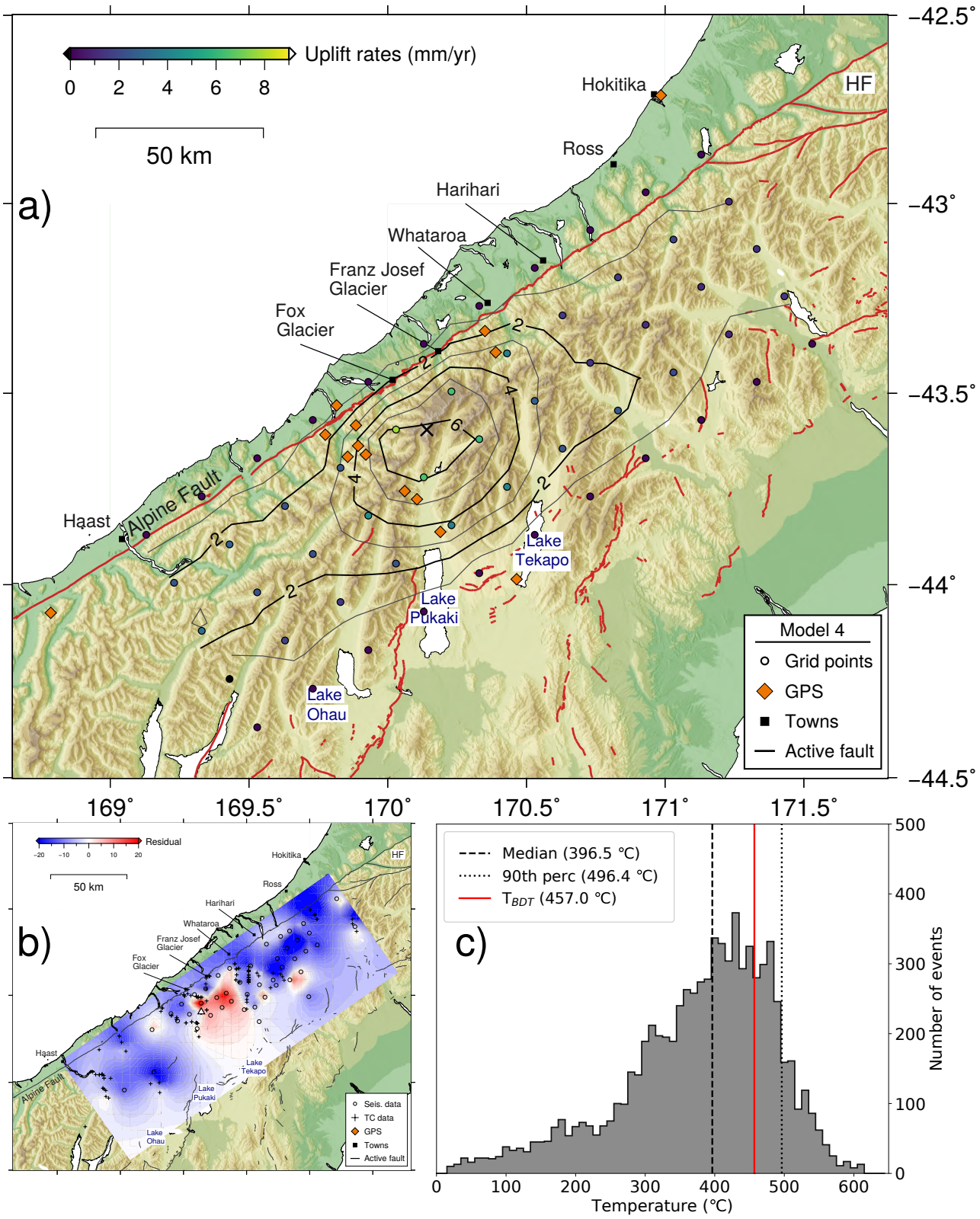

Figure 5.11: Summary of results from the fourth model that assumes an initial geotherm established before the initiation of the exhumation process (Model 4). Refer to Figure 5.8 caption for more details.

In general, well performing models have misfit values (Q) that are approximately equal to the size of the dataset used. However, this is not the case here, where the values range from 32,000 to 48,000 corresponding to relative large residuals >2. This occurs for two main reasons. First, the models presented here are simplified and coarse and therefore cannot depict the real local variation in exhumation rates (i.e. small-scale faulting is impossible to be captured by our models). Second, due to limitations in the seismicity data used here. The time interval covered by the earthquake data is too short to establish the real variability of the exhumation rates. In addition, assuming steady state for the whole of the examined region in the central Southern Alps might also be problematic. Steady-state is suggested to apply only locally in the region of rapid exhumation (*Koons*, 1987; *Allis and Shi*, 1995). However, the simple crustal thermal structure constructed here can provide a good estimation the broader picture of the distribution of exhumation rates, which matches the goals of the present work.

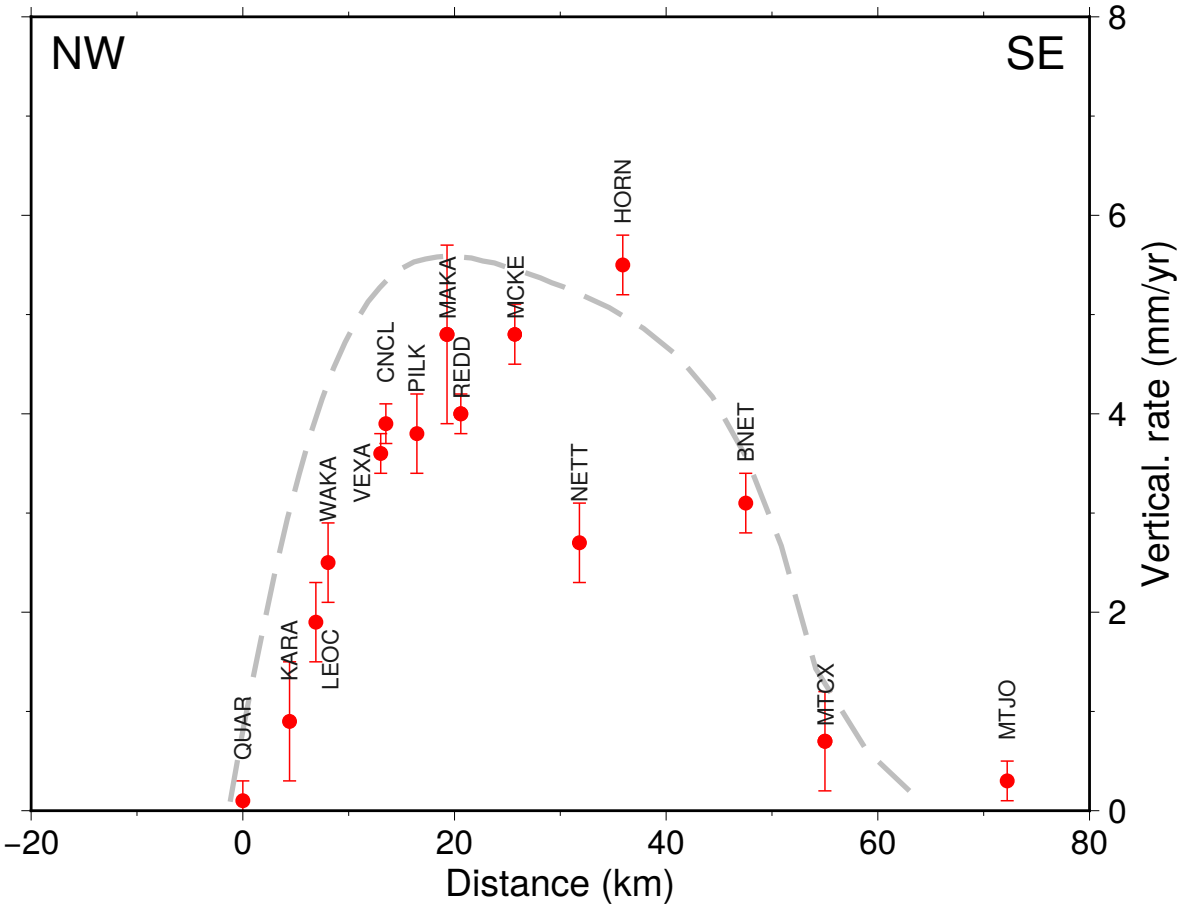

Figure 5.12: Cross-section of interpolated exhumation rate (dashed grey line) estimates from model 3 along the GPS transect across the Southern Alps (*Beavan et al.*, 2004). Vertical rate GPS estimates (red dots with 95% confidence limits) are obtained from Table 1 of *Beavan et al.* (2010). The locations of the permanent GPS sites are shown in Figures 5.8–5.11.

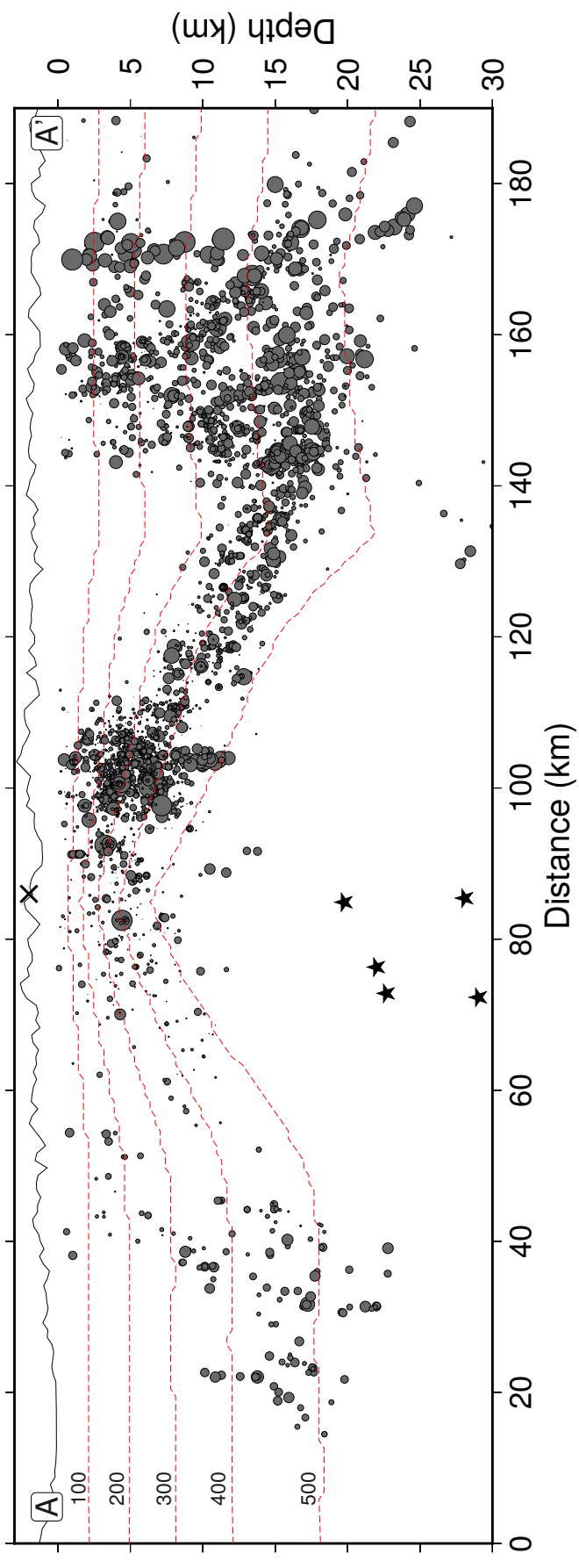

Figure 5.13: Cross-section of earthquake hypocenters and temperature in degrees centigrade (100, 200, 300, 400, and 500 °C isotherms) along line A–A' shown in Figure 5.10. Earthquakes within 10 km on either side of the cross-section are displayed and scaled by magnitude. Stars show locations of low-frequency earthquakes (*Baratin et al.*, 2018). Aoraki/Mount Cook is marked by a cross. Light grey line depicts the topography.

5.8 Conclusions

This study marks the first attempt to combine two different types of data (i.e. seismicity and thermochronological) in order to calculate a crustal thermal model and estimate the exhumation rates in the central Southern Alps region. Our approach enabled us to also estimate the temperature at the lower cutoff depth of the seismicity (T_{BDT}=440–457°C). The most significant finding to emerge from the modeling performed in this study is the exhumation rate estimates and their variation (1–8 mm/yr) along the length of the Alpine Fault. These results are in good agreement with existing geologically (*Little et al.*, 2005) and geodetically (*Beavan et al.*, 2010) determined rates. The highest uplift rates are observed near Aoraki/Mount Cook.

Further analysis of the distribution of the hypocentral depths in the central Southern Alps region, highlights the previously observed seismicity patterns (*Boese et al.*, 2012; *Bourguignon et al.*, 2015; *Michailos et al.*, 2019). These can be summarised as follows: 1) a lack of seismicity in the lower part of the crust ($\geq$ 10 km) near Aoraki/Mount Cook; 2) a lack of seismicity in the upper part of the crust ($\leq$10 km) near the Whataroa valley; and 3) a relatively thick seismogenic layer ($\geq$ 20 km) near Harihari and Ross.

6 Synthesis

The following is a summary and synthesis of the main results. The chapter begins with a description of the main research findings along with their implications, significance, and limitations. Finally, some future work suggestions are provided. These results have either been published or are being prepared for publication in international peer-reviewed journals.

6.1 Summary of key results

Chapter 3: Variations in seismogenic thickness along the central Alpine Fault, New Zealand, revealed by a decade's relocated microseismicity

This study has highlighted a major variation in the seismicity characteristics along the length of the Alpine Fault by constructing the largest and most complete, to date, microseismicity earthquake catalog. Overall, 9,111 absolute earthquake hypocenters were located, of which 7,719 were relocated with double-difference techniques (*Waldhauser and Ellsworth*, 2000). Uncertainties of the relocated hypocenters are in general, less than 500 m on both vertical and horizontal directions.

- Seismicity near Aoraki/Mount Cook exhibits extremely shallow hypocentral depths (<10 km) and low−magnitudes (M_L <1) (black cross; Fig. 6.1). Approximately 70 km to the northeast (between Harihari and Ross; Fig. 6.1) the seismic characteristics are notably different. Earthquake magnitudes are generally larger (M_L >2) and hypocentral depths extend to deeper parts of the crust as much as 22 km.

- These two distinct seismic zones, described above, occur on either side of the previously identified Whataroa seismic gap (*Leitner and Eberhart-Phillips*, 2001; *Boese et al.*, 2012), a seismically quiescent region. Seismic activity there is almost absent down to hypocentral depths of around 7−10 km (WG; Fig. 6.1).

- Seismogenic cut-off depths range from less than 10 km near Aoraki/Mount Cook to more than 20 km in the northeast (Fig. 6.1).

- A rough estimate of a seismic moment release of 7.3 to 7.9 M_w was estimated for a potential earthquake rupturing the whole length of the central section of the Alpine Fault.

Local magnitude scale

Another important result from Chapter 3 was the establishment of a new updated local magnitude scale for the central Southern Alps region that is corrected for geometric spreading, attenuation and site terms.

- This new local magnitude scale provides a more accurate attenuation parameter (η = 0.01 – 1.20 × 10^{-2} km^{-1}) for the central Southern Alps region and is calibrated using independently calculated M_w magnitudes obtained by GeoNet.
- Earthquake magnitudes range from –1.2 to 4.6 with a magnitude of completeness, M_c=1.1 and a b-value of 0.85 ± 0.003.

Chapter 4: Detailed spatiotemporal properties of the tectonic stress regime along the central Alpine Fault

The stress regime within the crust near the central Alpine Fault was investigated in the present thesis by creating the largest focal mechanism dataset to date in this region. This consists of 845 focal mechanism solutions for earthquakes with magnitudes larger than M_L ≥1.5 and representative errors varying from 20 to 38°.

- The majority of these focal mechanisms (62%) exhibit strike-slip faulting that is in accordance with the general transpressive tectonic regime of the central Southern Alps.
- Using a Bayesian stress inversion technique (*Arnold and Townend*, 2007) an average maximum horizontal compressive stress, S_{Hmax}, orientation of 121±11° and stress ratio, R, values generally larger than 0.5 were obtained.
- Detailed spatiotemporal examinations of the variation of the stress parameters showed little to no change (variability in the S_{Hmax} values mostly lies within the uncertainties of the calculations) and no trend related to major regional earthquakes (e.g. M7.8 Dusky Sound, M7.2 Darfield, M7.8 Kaikōura). This suggests a remarkably uniform stress regime along the central section of the Alpine Fault in both time and space.
- This remarkably consistent S_{Hmax} orientations form a high angle of ∼65° with the Alpine Fault, implying a misoriented fault.

- Shear to normal stress ratio values calculated along a representation of Alpine Fault structure at depth do not show any clear pattern.

Chapter 5: Crustal thermal structure and exhumation rates near the central Alpine Fault

Using the prior knowledge that there is a region of rapid uplift rates in the central Southern Alps, suggested by a number of previous studies (e.g., *Wellman*, 1979; *Tippet and Kamp*, 1993; *Little et al.*, 2005; *Beavan et al.*, 2010), we use the distribution of the hypocentral depths of the seismicity and thermochronology ages as constraints to calculate a 1–D temperature model and obtain exhumation rate estimates.

- The highest exhumation rates are observed near Aoraki/Mount Cook (7–11 mm/yr) and coincide with the regions exhibiting shallow seismicity cutoff depths (Fig. 6.1).
- We observe a significant variation of exhumation rate estimates of up to 7 mm/yr on the Southern Alps along the length of the Alpine Fault (Fig. 6.1).
- We provide an estimate of the temperature at the brittle-ductile transition zone, T_{BDT}, ranging from 440 to 457°C within the different models created.
- Individual earthquake hypocenter temperatures reach values of up to 491–509°C, suggesting a more feldspathic rock composition in the crust.

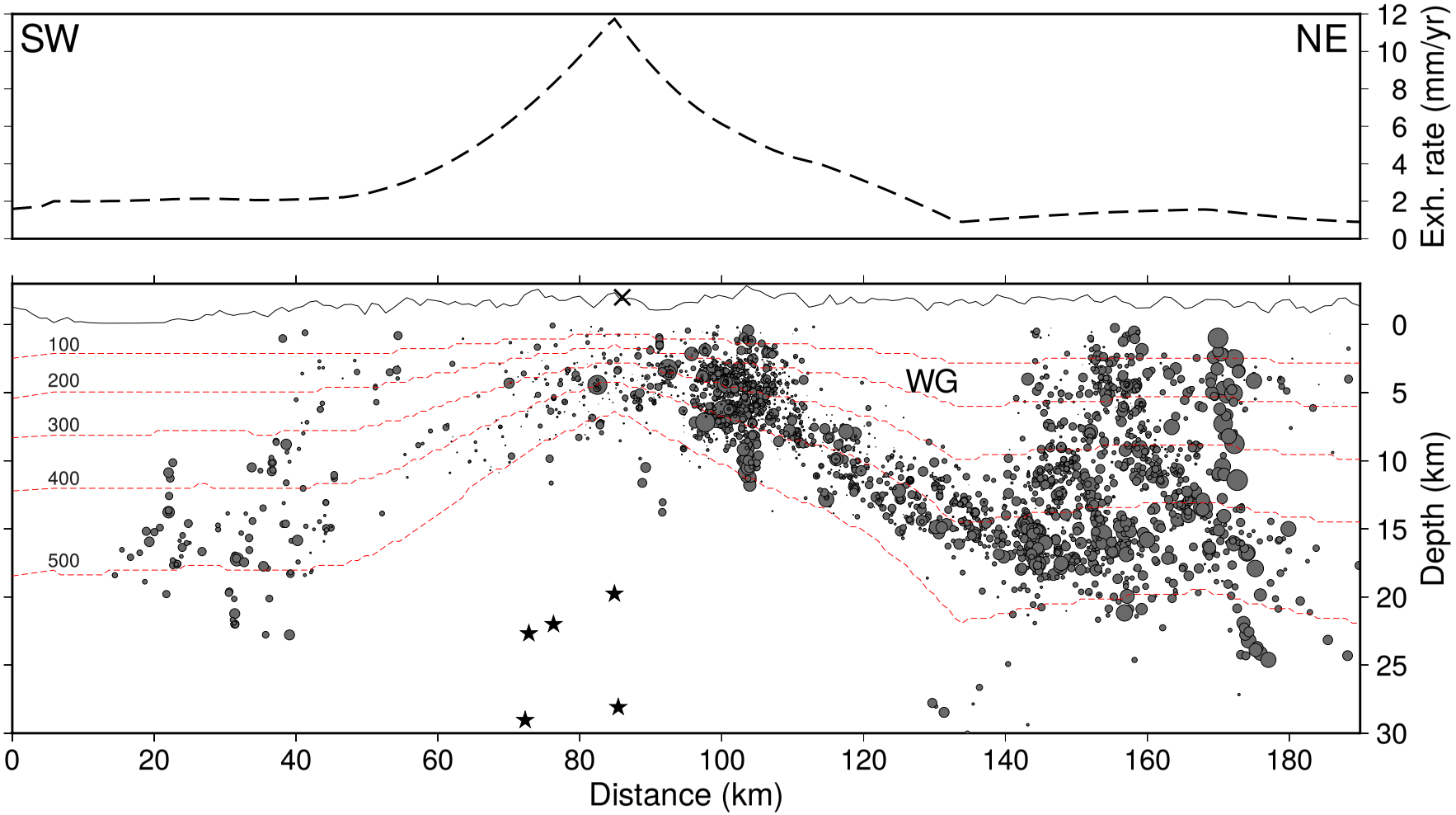

Figure 6.1: Cross-section of temperature in degrees centigrade (100, 200, 300, 400, and 500 °C isotherms; red dashed lines) and interpolated exhumation rate estimates (black dashed line) along line A–A' shown in Figure 5.10 that summarises the results of Model 3 in Chapter 4. Relocated earthquake hypocenters within 10 km on either side of the cross-section are also displayed and scaled by magnitude. Stars show locations of low-frequency earthquakes (*Baratin et al.*, 2018). Aoraki/Mount Cook is marked by a cross. WG = Whataroa gap. Light grey line depicts the topography.

6.2 Implications and contribution of results

Comparison to previous microseismicity catalogs

The earthquake catalog presented here is the most comprehensive to date in the central Southern Alps, which is enabled mainly by the long duration and continuity of the SAMBA network. Fig. 6.2 and Table B.1 highlight the difference in the number of earthquake locations and magnitude distributions with respect to the previous studies of *Boese et al.* (2012) and *Bourguignon et al.* (2015) and GeoNet catalog. The catalog here has the lowest magnitude of completeness (M_c=1.1) and more earthquake locations than all of the previous seismicity studies combined. Our catalog complements the findings of previous studies (e.g. *Leitner and Eberhart-Phillips*, 2001; *Boese et al.*, 2012; *Bourguignon et al.*, 2015; *Feenstra et al.*, 2016) by providing a broader picture of the seismic deformation distribution, particularly, on the along-strike seismicity characteristics (Fig. 6.1).

Even though the earthquake catalog constructed here is the longest to date in the region it still only provides a snapshot of the active seismic deformation with respect to the typical seismic cycle of the large Alpine Fault earthquakes (i.e. 250–300 years; *Howarth et al.*, 2018).

New local magnitude scale

The attenuation parameter, η, calculated here is relatively larger than the one used by GeoNet ($\eta_{GeoNet} = 6.7 \times 10^{-3}$ km^{-1}). This discrepancy in the attenuation parameters is due to the fact that the attenuation parameter used from GeoNet was estimated by *Robinson* (1987) for the Wellington region. This implies that GeoNet magnitudes in the central Southern Alps region are underestimated. For this reason we established a new magnitude scale here that provides an objective and systematic way to quantify the size of earthquakes in the central Southern Alps. A more accurate attenuation parameter can contribute towards better rupture simulations (*Bradley et al.*, 2017) and hazard planning in the region (*Orchiston et al.*, 2018).

Earthquake distribution

A major feature of the distribution of the seismic deformation is the lack of seismicity in beneath Aoraki/Mount Cook (Fig. 6.1). This feature raises questions about the nature of the tectonic processes that control the distribution of the seismic deformation and cause this discrepancy along the length of the Alpine Fault. The distribution of seismic deformation at depth is known to depend on a number of factors that include

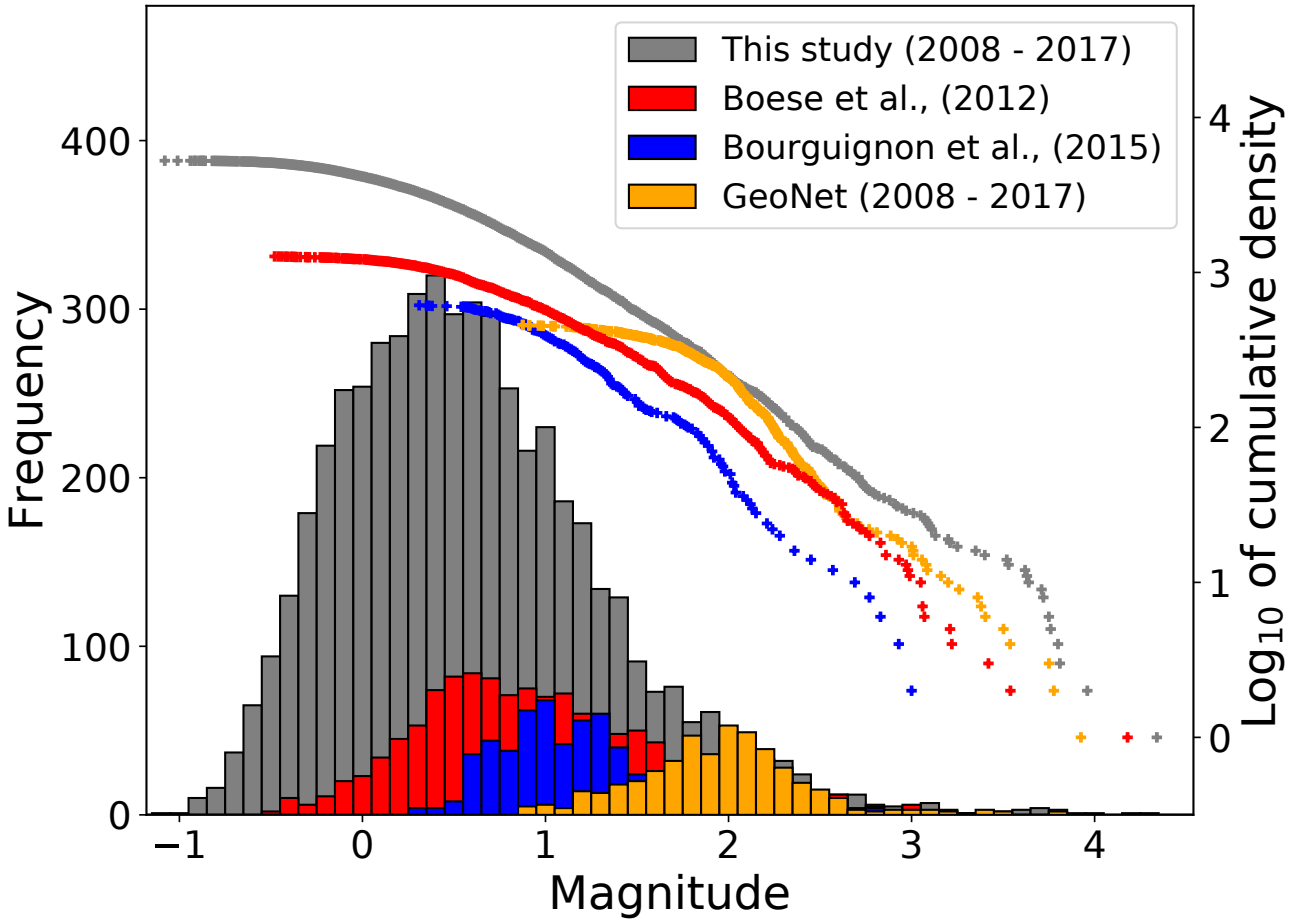

Figure 6.2: Comparison of magnitude frequency distribution of earthquakes located within the limits seismic network, between this study (grey) to the ones located by *Boese et al.* (2012, red), by *Bourguignon et al.* (2015, blue) and by GeoNet for the same time period. GeoNet earthquake local magnitudes M_L are shifted by –0.54 to be equated to M_w (*Ristau*, 2013) as magnitude scale derived here is based on M_w values. Refer to Figure 3.3 caption for more details.

the type of faulting, the petrology, the water composition, the fault geometry, the fluid pressure, the strain rate and the temperature (*Sibson*, 1984; *Scholz*, 1998). As it has been described in Chapter 3, we have attributed the lateral variations of >10 km in the seismogenic cut-off to changes arising from variations in temperature and exhumation rates.

To check this interpretation, we performed modelling of the crustal thermal structure (Chapter 5), where temperature and uplift rates are adjustable parameters. The thermal structure model constructed here consists of the first attempt in the region to combine two different types of data (i.e. seismicity and thermochronology). Thus it incorporates the longer-scale geological observation to obtain a broader and more accurate picture on the tectonic processes taking place. The exhumation rates obtained were in good agreement with existing geologically (*Little et al.*, 2005) and geodetically (*Beavan et al.*, 2010) determined rates. Earthquake hypocenter temperatures of up to 491–509°C were obtained, which appear to be slightly hotter than what is expected

for crust composed by quartz-rich rocks (i.e. 300–350°; *Sibson*, 1984), suggesting for a more feldspar-rich mafic rock composition in some parts of the crust (i.e. ∼450°; *Sibson*, 1984; *Bonner et al.*, 2003). The elevated temperatures, along with the anomalously shallow seismicity near Aoraki/Mount Cook, however, most are most likely due to a combination of more parameters such as the existence of locally increased strain rates and/or high pore fluid pressures as suggested by *Stern et al.* (2001) for the low-velocity zone observed beneath Aoraki/Mount Cook during the SIGHT project (*Davey et al.*, 1998; *Okaya et al.*, 2002).

Implications for rupture simulations

Paleoseismological evidence suggests that past Alpine Fault earthquakes (*Howarth et al.*, 2018) and references therein, have had both single and multi-segment ruptures. This observation along with the anomalously shallow seismogenic crust beneath Aoraki/Mount Cook highlighted here, raises the question whether this narrow patch of seismogenic crust beneath Aoraki/Mount Cook has the potential to operate as a barrier and thus, stop a propagating rupture. Preliminary seismic moment release estimates calculated here showed small differences in the M_w values when including or excluding the area covered by the gap of seismicity. These rough estimates are based on a number of assumptions such as the rupture being constrained within the limits of the seismogenic layer. However, whether large earthquakes sometimes or always rupture the deep creeping section of the Alpine Fault is unresolved (*Jiang and Lapusta*, 2016; *Shaw and Wesnousky*, 2008; *Beeler et al.*, 2018). To examine this question in more detail, further work is required including a number of different rupture simulation models including and excluding this gap of seismicity and its affects on the radiation patterns and local ground shaking.

Relation to low-frequency earthquakes

The central Alpine Fault is locked above a range of depths (10–20 km) determined by the seismicity cut-off depths and geodetic locking depths (*Wallace et al.*, 2007; *Lamb et al.*, 2018). Beneath those depths the deformation is accommodated by steady creep and phenomena such as tremor (*Wech et al.*, 2012, 2013) and low-frequency earthquakes, LFEs, (*Chamberlain et al.*, 2014; *Baratin et al.*, 2018). LFEs occur at depths between 17 and 42 km beneath Aoraki/Mount Cook (Fig. 6.1). At the same area, the seismogenic cutoff depths are generally less than 10–12 km. This results in a gap of 5–7 km between the deepest earthquakes and the shallowest LFEs. This gap between the two types of observations might exist due to incomplete data or due to the detection and location methods used. To provide another explanation for this gap between the hypocentral depths of the earthquakes and the LFEs, we consider a similar

example from the San Andreas fault (*Harrington et al.*, 2016). *Harrington et al.* (2016) suggested that if the gap was real, the strain in this zone might be accommodated by a mechanism controlled by the period of the earthquake cycle (*Rolandone et al.*, 2004) (i.e. earthquake hypocentral depths tend to be deeper during the coseismic and the postseismic periods). In the case of the Alpine Fault, being in a state of late interseismic period, established by a remarkably consistent paleoearthquakes record (*Howarth et al.*, 2018), the observation of the gap between the deeper seismicity and the LFEs is in agreement with the suggestion of *Harrington et al.* (2016).

Sub-crustal earthquakes

A distinct seismicity feature in the central Alpine Fault, that is relatively less frequent, is the occurrence sub-crustal earthquakes. We located at least 30 deep crustal/upper mantle earthquakes, with hypocentral depths ranging from 40 to 80 km. These deep crustal/upper mantle earthquake locations contributed to a recent publication by *Boese et al.* (2018) that reviews current knowledge on the lower−crustal and upper−mantle deformation in the Alpine Fault in the central South Island, adding this new sub-crustal earthquakes to an already existing sub-crustal earthquake catalog created by *Boese et al.* (2013).

6.3 Future work suggestions

The present study has expanded our understanding of the distribution of seismic deformation near the central Alpine Fault significantly, by providing a large amount of observations. This large dataset can form the basis to further research a number of the deformation characteristics, including the occurrence of any repeating seismicity, the calculation of an updated tomography model and more. These suggestions are summarised below:

Matched-filter techniques and repeating seismicity

A natural progression of this work is to further expand the earthquake catalog, using matched-filter detection methods. The use of the matched-filter techniques has been proven to be effective in detecting near-repeating seismic signals (e.g. *Chamberlain et al.*, 2017c; *Shelly et al.*, 2016a; *Shelly*, 2017; *Yao et al.*, 2017; *Schaff and Richards*, 2011). Events located here can be used as templates to detect similar seismic signals in the area and obtain an even more complete picture of the seismic activity and its characteristics. An even longer earthquake catalog could provide more definitive evidence for the seismicity characteristics observed near the central Alpine Fault.

Further to this, research can be carried out to look for any repeating highly similar seismic signals (repeating earthquakes) within the earthquake catalog constructed here. Looking for repeating earthquakes can provide a means of discriminating between the locked and creeping section of the faults and possibly quantify the total amount of creep taking place (*Bohnhoff et al.*, 2017; *Nadeau and Johnson*, 1998; *Schaff and Richards*, 2011).

Focal mechanisms for smaller magnitude events

Whilst this study provided the longest focal mechanism catalog to date (i.e. 845 solutions), it only partially revealed any temporal variations in the stress regime. Currently only around 10% of the earthquake catalog has focal mechanisms solutions associated with them. Using cross-correlation methods (*Shelly et al.*, 2016b), focal mechanisms of smaller-magnitude earthquakes can be determined which would help to examine the stress regime in a more detailed manner.

Earthquake catalog extension

Seismic data from SAMBA seismic network between early 2017 and late 2018, that are archived on IRIS, have not been analysed for earthquake detection and location. Following the workflow described in Chapter 2 can form a basis for extending the earthquake catalog for an additional of almost two years.

Imaging of the Alpine Fault structure at depth

Precise seismic tomography can provide important information about the fault's structures beneath the central Southern Alps. The latest 3−D P and S wave velocity model in the region was calculated by double-difference body wave tomography (*Guo et al.*, 2017), and used 29,417 and 5,145 P and S arrival times, respectively. The catalog created here contains a total of 83,138 P and 67,119 S wave time arrivals and covers a more extended region. Using this larger number of arrival times, body wave tomography can provide an updated more detailed 3−D velocity model for the region.

In addition to seismic tomography, the identification of Fault Zone Head Waves (FZHW) has been proven to provide useful insights on velocity contrasts at large strike-slip faults (e.g. Andreas fault, San Jacinto fault zone; *Ross and Ben-Zion*, 2014). FZHW are the P wave phases refracting on strike-slip fault interfaces in a similar way as the P_n phases refract along the Moho. Earthquakes located close to the Alpine Fault within the catalog created here, along with a recent (9 June 2019) $M5.5$ earthquake[1], which

[1] `https://www.geonet.org.nz/earthquake/2019p428761`

is inferred to have occurred on the Alpine Fault, 40 km northeast of Milford Sound provide a unique opportunity to examine the velocity contrasts of the two interfaces and provide a more detailed structure of the fault at depth.

6.4 Concluding statement

The results from this thesis have contributed the longest and most complete microseismicity earthquake catalog, to date, for the region near the central Alpine Fault. The distribution of the earthquake hypocenters within this catalog have updated the current knowledge of the along-strike variations in the active seismic deformation on a major continental plate boundary. The longest focal mechanism record is also provided here, which outlines a remarkably consistent stress regime in both time and space. This study has also examined the crustal thermal structure by modelling two different types of data (i.e. seismicity and thermochronology) in order to constrain the vertical kinematics of the central Southern Alps orogen. Finally, these results provide the framework for additional research on the state of the crustal seismic deformation near the central Alpine Fault.

Appendices

A Seismic site details

Table A.1: Southern Alps Microseismicity Borehole Array (SAMBA) details

Name	**Location**	**Latitude (°)**	**Longitude (°)**	**Altitude (m)**	**Sensor**	**Period of operation**
COSA	Cook Saddle	-43.448	170.060	377 (*1.4)	GeoSpace Tech HS-1-LT	06/11/2008 - present
COVA	Copland Valley	-43.613	169.968	1477 (*1)	Mark products L-4C3D	22/01/2010 - present
EORO	End of Road	-43.426	170.169	233 (*1.35)	GeoSpace Tech HS-1-LT	22/01/2010 - present
FRAN	Caravan's Knob	-43.380	170.160	124 (*98)	GeoSpace Tech HS-1-LT	07/02/2009 - present
GOVA	Godley Valley	-43.639	170.503	814 (*1.95)	GeoSpace Tech HS-1-LT	17/02/2009 - present
LABE	De la Beche	-43.546	170.245	1590 (*2.15)	GeoSpace Tech HS-1-LT	09/12/2008 - present
LARB	Lansborough	-43.749	169.936	1184	Mark products L-4C3D	13/06/2014 - present
MTBA	Mount Baird	-43.688	169.641	1232	Mark products L-4C3D	27/03/2013 - present
MTFO	Mount Fox	-43.512	170.003	1216 (*2)	GeoSpace Tech HS-1-LT	07/11/2008 - present
POCR2	Potter's Creek	-43.352	170.223	185 (*46)	GeoSpace Tech HS-1-LT	24/03/2009 - present
SOLU	Solution Ranges	-43.908	169.606	1146	Mark products L-4C3D	27/03/2013 - present
WHAT2	Whataroa Quarry	-43.279	170.360	95 (*61)	GeoSpace Tech HS-1-LT	22/03/2009 - present
WHYM	Whymper Hut	-43.441	170.371	906 (*1.3)	GeoSpace Tech HS-1-LT	12/11/2008 - present
MARI	Macaulay River	-43.727	170.575	771	GeoSpace Tech HS-1-LT	01/12/2008 - 01/02/2009
POCR	Potter's Creek	-43.348	170.177	95	Mark products L-4C3D	01/12/2008 - 01/03/2009
REYN	Reynold's Creek	-43.353	170.391	1310 (*1.3)	GeoSpace Tech HS-1-LT	17/06/2009 - 01/02/2010
WHAT	Whataroa Quarry	-43.279	170.361	106	Mark products L-4C3D	01/12/2008 - 01/03/2009

*Borehole depth.

Table A.2: DFDP-10 seismic network site details

Name	Location	Latitude (°)	Longitude (°)	Altitude (m)	Sensor	Period of operation
BLO	Blue Lookout	-43.244	170.787	1607	Mark Products L-22D	3D01/01/2010-06/05/2010
BON	Mt. Bonar	-43.083	170.651	1031	Mark Products L-22D	3D01/01/2010-06/05/2010
DRC	Dry Creek	-43.241	170.452	128	Mark Products L-22D	3D01/01/2010-06/05/2010
ERE	Erewhon Station	-43.510	170.855	600	Mark Products L-22D	3D01/01/2010-06/05/2010
GCK	Gaunt Creek	-43.306	170.311	114	Mark Products L-22D	3D01/01/2010-06/05/2010
GHU	Godley Hut NZAC	-43.480	170.509	1108	Mark Products L-22D	3D01/01/2010-06/05/2010
NOL	Nolans Hut	-43.349	170.484	181	Mark Products L-22D	3D01/01/2010-06/05/2010
ONE	One One Road	-43.114	170.492	62	Mark Products L-22D	3D01/01/2010-06/05/2010
POE	Poerua Valley	-43.195	170.520	103	Mark Products L-22D	3D01/01/2010-06/05/2010
VBV	Veil Bivouac	-43.385	170.520	1019	Mark Products L-22D	3D01/01/2010-06/05/2010
WHB	Whataroa Bridge	-43.295	170.412	97	Mark Products L-22D	3D01/01/2010-06/05/2010
WNQ	Wanganui Quarry	-43.182	170.631	180	Mark Products L-22D	3D01/01/2010-06/05/2010

Table A.3: GeoNet seismic sites used in this study

Name	Location	Latitude (°)	Longitude (°)	Altitude (m)	Sensor	Period of operation
WVZ	Waitaha Valley	-43.076	170.736	75	Guralp CMG-3ESP	06/09/2003 - present
RPZ	Rata Peaks	-43.719	171.054	412	Guralp CMG-3TB	06/06/2001 - present
FOZ	Fox Glacier	-43.566	169.689	10	Guralp CMG-3ESP	13/13/2004 - present
JCZ	Jackson Bay	-44.073	168.785	1062	Guralp CMG-3ESP	15/10/2004 - present
LBZ	Lake Benmore	-44.385	170.184	438	Guralp CMG-3ESP	04/06/2004 - present
GCSZ	Gaunt Creek	-43.316	170.3267	210 (*81)	IESE HS-2	01/04/2012 - present

*Borehole depth.

Table A.4: ALFA-08 seismic network site details

Name	Location	Latitude (°)	Longitude (°)	Altitude (m)	Sensor	Period of operation
BURA2	Wilberforce	-43.052	171.313	735	CMG-40T Taurus	26/10/2008-27/10/2009
CAMEL	Camelback	-42.874	170.962	60	CMG-40T Taurus	26/10/2008-27/10/2009
CASH	Castle Hill	-43.14	171.437	657	LE-3Dlite MkII Taurus	26/10/2008-27/10/2009
FBLA2	Lord Range	-43.258	170.778	1233	LE-3Dlite MkII Taurus	30/10/2008-24/03/2009
HATT	Hatters Creek	-42.919	170.866	178	CMG-40T Taurus	26/10/2008-27/10/2009
MTHA2	Mt. Harry	-42.894	171.110	70	LE-3Dlite MkII Taurus	26/10/2008-27/10/2009
TURI	Turiwhate quarry	-42.756	171.317	154	CMG-40T Taurus	26/10/2008-27/10/2009
UMAT	Upper Mathias	-43.207	171.136	735	LE-3Dlite MkII Taurus	03/11/2008-26/10/2009

Table A.5: DFDP-13 seismic network site details

Name	Location	Latitude (°)	Longitude (°)	Altitude (m)	Sensor	Period of operation
WDSZ	Whataroa	-43.293	170.412	91 (*29)	IESE HS-1-LT	02/02/2013 - present
WMSZ	Mint Creek, Whataroa	-43.280	170.395	78 (*29)	IESE HS-1-LT	02/02/2013 - present
WPSZ	Parker Creek, Whataroa	-43.283	170.413	77 (*29)	IESE HS-1-LT	02/02/2013 - present
WTSZ	Tommys Creek, Whataroa	-43.302	170.412	100 (*29)	IESE HS-1-LT	02/02/2013 - present

*Borehole depth.

Table A.6: WIZARD seismic network site details

Name	Location	Latitude (°)	Longitude (°)	Altitude (m)	Sensor	Period of operation
WZ01	Mt. Bonar	-43.0833	170.6518	1032	Mark Products L22	18/01/2012-31/01/2014
WZ02	Nolans Hut	-43.3487	170.484	194	Mark Products L22	17/01/2012-31/01/2014
WZ03	Blue Lookout	-43.2438	170.7764	1260	Mark Products L22	20/01/2012-31/01/2014
WZ04	Julian	-43.2698	170.3285	73	CMG3-ESP	17/01/2012-31/01/2014
WZ05	Dymock	-43.2285	170.3865	38	CMG3-ESP	16/01/2012-31/01/2014
WZ06	Maisey/Dry Creek	-43.2411	170.4515	123	CMG3-ESP	17/01/2012-31/01/2014
WZ07	Bowater	-43.1674	170.3672	26	CMG3-ESP	18/01/2012-31/01/2014
WZ08	Rotokino	-43.1349	170.4161	73	CMG3-ESP	15/01/2012-31/01/2014
WZ09	White/Oneone	-43.1117	170.4803	34	CMG3-ESP	20/01/2012-31/01/2014
WZ10	MacKenzie/Poerua	-43.1943	170.5203	89	CMG3-ESP	16/01/2012-31/01/2014
WZ11	Friend/Whataroa	-43.2965	170.4098	96	CMG3-ESP	15/01/2012-31/01/2014
WZ12	Black/Wanganui	-43.1619	170.6294	93	CMG3-ESP	21/01/2012-31/01/2014
WZ13	Griffen Spur	-43.2018	170.7234	1181	Mark Products L22	20/01/2012-31/01/2014
WZ14	Isobel Flat	-43.1106	170.8207	1499	Mark Products L22	19/01/2012-31/01/2014
WZ15	Country Hut	-43.1583	170.8497	958	Mark Products L22	18/01/2012-31/01/2014
WZ16	Perth	-43.354	170.5346	267	Mark Products L22	17/01/2012-31/01/2014
WZ17	Scone Hut	-43.3729	170.569	402	Mark Products L22	17/01/2012-31/01/2014
WZ18	Mt. Ashford	-43.1423	170.6838	1354	Mark Products L22	19/01/2012-31/01/2014
WZ19	Curniffe	-43.1129	170.5806	49	CMG3-ESP	17/01/2012-31/012014
WZ20	Mt. Ferguson	-43.2132	170.5563	1194	Mark Products L22	20/01/2012-16/01/2014
WZ21	Whataroa	-43.2682	170.376007	51	Guralp CMG3ESP	22/01/2012-31/01/2014

B Supporting Information for Chapter 3: "Variations in seismogenic thickness along the central Alpine Fault, New Zealand, revealed by a decade's relocated microseismicity"

Introduction

This section contains four tables and accompanying text and seven figures. Table B.1 shows the details of previously created earthquake catalogs compared to the one constructed here. Tables B.2 and B.3 show the values of the parameters used in the triggering algorithm. Tables B.4 outlines the values used in the amplitude picking algorithm. Tables B.5 and B.6 summarize the parameters used for the NonLinLoc location analysis and for the weighting scheme in hypoDD, respectively.

Figure B.1 shows the data continuity of the seismic sites used in this study. Three figures (B.2, B.3 and B.4) show details of the magnitude estimations: Figure B.2 displays the residuals versus the hypocentral distances, Figure B.3 shows the station correction values and Figure B.4 is a scatter plot of the magnitude calculations using the two different datasets described in the Methods section. Figure B.5 depicts a comparison of the local magnitudes obtained by *Boese et al.* (2012) and the magnitudes calculated in this study.

Figure B.6 highlights the details of the absolute earthquake locations obtained using NonLinLoc and a 3-D velocity model (e.g. distance to closest station, azimuthal gap, RMS, number of P– and S–wave picks). Figures B.7 to B.8 are complementary maps to Figure B.6. Figures B.9 to B.11 are cross sections of the seismicity along the Alpine Fault obtained using different velocity models and location methods. Figures B.12 to B.15 are cross sections of the seismicity along and across the Alpine Fault near Aoraki/Mount Cook overlaying the 3-D P– and S–velocity model of *Guo et al.* (2017).

We also include the caption and description of the relocated earthquake catalog constructed as described in the main article; this dataset is uploaded as a separate file in

the electronic appendices (Dataset B1).

Text B1: Comparison of earthquake catalog to previously created

Table B.1 summarizes some of the details of the previously compiled earthquake catalogs in the central Southern Alps in comparison with the catalog created here. The main sources of discrepancies when comparing earthquake catalogs derive from inconsistent earthquake locations due to different picking methods, velocity models, location methods and seismic network edges. Another source of discrepancy arises from inconsistent magnitude of completeness, M_c, values due to different detection methods and seismic network distributions.

The magnitude of completeness differs between the catalogs (maximum M_c in GeoNet's catalog; $M = 2.6$), and implies that the majority of the events from the microseismicity catalogs of (*Boese et al.*, 2012; *Bourguignon et al.*, 2015) would be missing if this completeness was used for the whole duration of a merged catalog. However, even if all the earthquake locations are retained regardless of the M_c and is also assumed that all events in the composite catalogue are unique the maximum number of locations would still be significantly smaller than the number of earthquakes located in this study (∼5,800 compared to ∼9,000 of this study).

Table B1.

Table B.1: Comparison of Southern Alps earthquake catalog details

	Time period spanning	Number of earthquakes	Number of total seismic sites	Magnitudes	M_c
Boese et al. (2012)	Nov. 2008 – Dec. 2009	1700	13	-0.3 – 4.2	1.4
Bourguignon et al. (2015)	Oct. 2008 – Oct. 2010	1300	10	-0.05 – 3.5	1.5
Feenstra et al. (2016)	Jan. 2012 – Jan. 2014	645	21	–	–
GeoNet	Oct. 2008 – Mar. 2017	2151	5	1.03 – 5.95	2.6
All previous studies	**Oct. 2008 – Mar. 2017**	**5796**	**(5 - 25*)**	–	**2.6**
This study	Oct. 2008 – Mar. 2017	9111	71 (15–42*)	-1.2 – 4.6	1.1

*Number of stations operating at the same time.

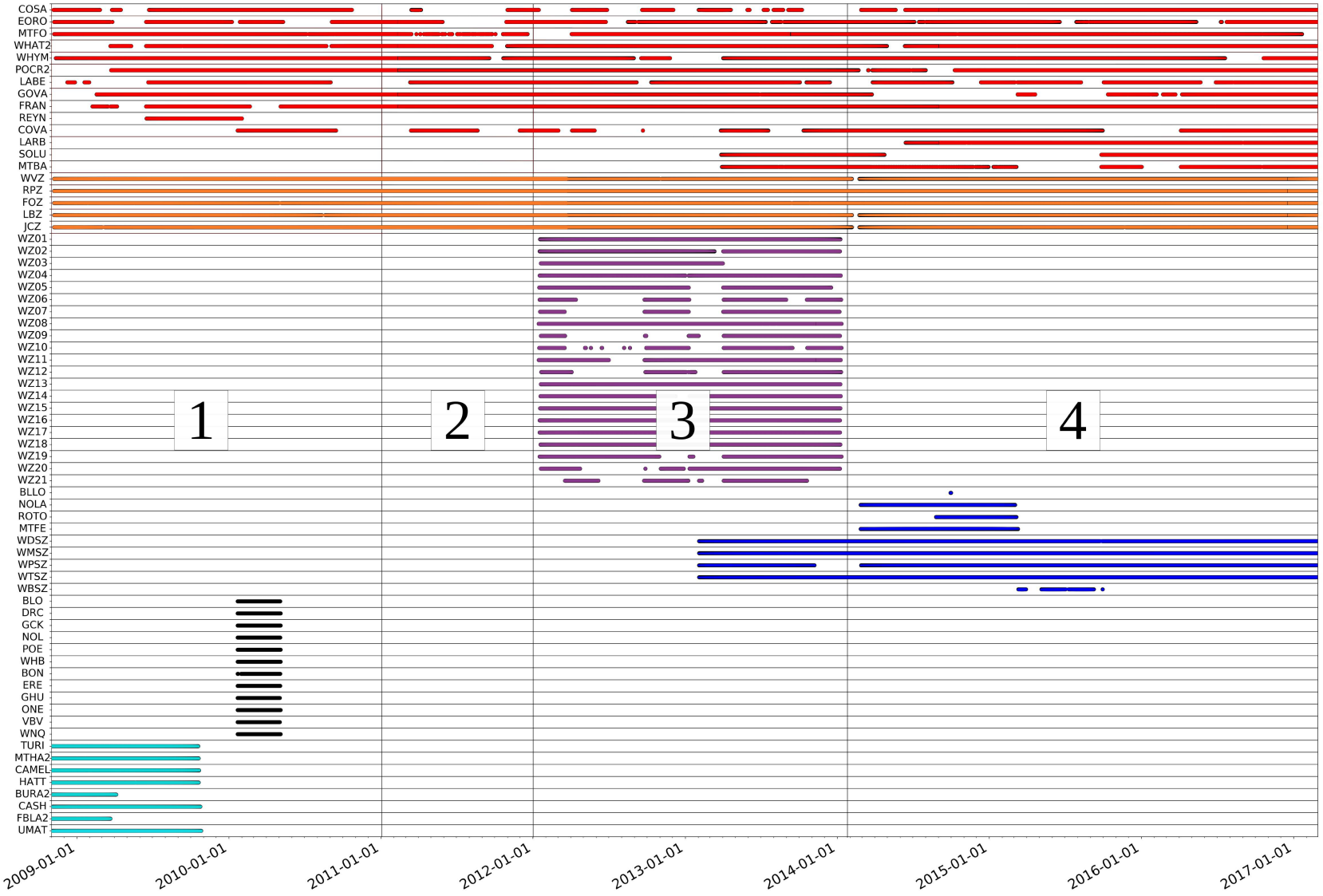

Figure B.1: Continuity of the SAMBA (red), GeoNet (orange), WIZARD (purple), DFDP-10 (black), DFDP-13 (blue) and ALFA-08 (cyan) seismic sites from November 2008 to March 2017. The black lines show the operating (up) times of each station. Many of the stations have intervals of data loss due to several problems (e.g. lightning strikes, power failures, extremely low temperatures) caused by the extreme conditions in the Southern Alps. Vertical lines divide the dataset into four subsets for the cross-correlation calculations.

Text B2: STA/LTA triggering method

The network trigger function used here is designed to allow the user to set parameters like the STA and LTA values, triggering thresholds, bandpass filters individually for each station. This function is available on the open repository Python package EQcorrscan (*Chamberlain et al.*, 2017c). Parameter names in tables B2 and B3 are the same as in the EQcorrscan documentation [1].

Table B2.

Table B.2: Parameters used in the short-term average to long-term average (STA/LTA) network trigger function in EQcorrscan.

Parameter	Description	Value
thr_coincidence_sum	Minimum number of seismic stations required to keep a trigger	4
moveout	Time window in seconds to look for triggers in the detection stage	8
max_trigger_length	Maximum trigger length in seconds	5

Table B3.

Table B.3: Site-specific parameters for short-term average to long-term average (STA/LTA) used in EQcorrscan's network trigger function. Parameter station is the name of the seismic site. sta_len and lta_len are the lengths in samples of the short and long time average windows, respectively. thr_on and thr_off are the values that switch a single station trigger on and off, respectively. lowcut and highcut define the low and high values for the bandpass filter applied. The network trigger was applied to the vertical components of the seismometers.

station	sta_len	lta_len	thr_on	thr_off	lowcut	highcut
COSA	0.3	10	8	3	6	25
EORO	0.2	10	9	3	7	35
FRAN	0.3	10	7	3	4	20
GOVA	0.2	10	7.5	3	8	25
LABE	0.3	10	6.5	2.5	3	30
MTFO	0.3	10	10	3	3	20
POCR2	0.2	10	10	3	7	22
WHAT2	0.2	15	8	3	2.5	25
WHYM	0.2	10	9	3	6	25
REYN	0.2	15	10	3.5	3.5	10
COVA	0.2	10	7	3	7	25

[1] `https://eqcorrscan.readthedocs.io/en/latest/submodules/utils.trigger.html`

SOLU	0.2	10	7	3	8	25
MTBA	0.3	10	7	3	3	30
LARB	0.2	10	7	3	3	35
WVZ	0.5	20	7	3	3	25
RPZ	0.4	15	7	3	3	25
FOZ	0.3	15	8	3	3	25
JCZ	0.5	20	8	3	3	25
LBZ	0.4	20	8	3	3	25
WTSZ	0.3	10	8	3.5	8	25
WMSZ	0.2	6.5	10	3.5	8	25
WPSZ	0.2	10	10	5	8	25
WDSZ	0.3	9	8	3	5	25
MTFE	0.3	10	15	3	5	25
NOLA	0.3	10	8	3	5	25
ROTO	0.3	10	15	3	5	25
WZ01	0.4	10	12	3	3	25
WZ02	0.3	10	7	2.5	5	25
WZ03	0.3	10	9.5	2.5	5	25
WZ04	0.4	10	10	3	3	25
WZ05	0.4	10	12	3	5	25
WZ06	0.4	10	8	2.5	5	25
WZ07	0.3	10	10	3	5	23
WZ08	0.3	10	7	2.5	5	25
WZ09	0.3	10	12	3	8	20
WZ10	0.3	10	12	3	8	25
WZ11	0.3	10	8	2.5	6	25
WZ12	0.4	10	8	3	8	25
WZ13	0.3	10	13	3	4	25
WZ14	0.4	10	10	3	5	25
WZ15	0.4	10	6.5	2.5	5	25
WZ16	0.5	10	8	3	5	25
WZ17	0.3	10	9	2.5	5	25
WZ18	0.3	10	12.5	3	5	25
WZ19	0.4	10	9	3	5	25
WZ20	0.3	10	8	2.5	5	25
WZ21	0.4	10	16	4	4	20
BURA2	0.3	11	10	3	5	25
CAMEL	0.3	10	10	4	5	25
CASH	0.4	10	12	2.5	8	25
FBLA2	0.3	10	8	3	5	25
HATT	0.3	10	10	2.5	4	25
MTHA2	0.3	10	9	2.5	5	25

TURI	0.4	7	14	4	3	15
UMAT	0.3	10	10	2.5	5	25
BLO	0.2	10	7	2.7	5	25
BON	0.3	12	7	2.5	8	25
DRC	0.3	10	10	3	5	25
GCK	0.3	10	13	4	5	25
NOL	0.3	12	7	3	5	25
POE	0.3	10	15	4	5	25
WHB	0.3	10	15	4	8	25
ERE	0.3	10	15	4	7	25
ONE	0.3	10	8	3	5	25
VBV	0.3	10	7	3	5	25
GHU	0.3	12	7	3	5	25
WNQ	0.3	10	8	3	5	20

Text B3: Amplitude picks for local magnitudes

We obtain the amplitude picks for magnitude calculation automatically using a function available on the open repository Python package EQcorrscan (*Chamberlain et al.*, 2017c). This function works in the following way. First, a filter is applied to the waveforms, which is important for small-magnitude earthquakes. The poles and zeros of this filter are tracked and removed from the picked amplitude. Then a Wood-Anderson filter is applied to pick the amplitudes. Parameter names in tables B4 are the same as in the EQcorrscan documentation [2].

Table B4.

Table B.4: Parameters used in the automatic amplitude picking function in EQcorrscan.

Parameter	Description	Value
winlen	Length of time window in seconds to make the pick	1
pre_pick	Time before the S-wave pick to start the cut window in seconds	0.1
pre_filt	Option to apply a pre-filter or not	True
lowcut	Lowcut in Hz for the pre-filter	1
highcut	Highcut in Hz for the pre-filter	20
corners	Number of corners to use in the pre-filter	4
velocity	Option to make the pick in velocity space or not (Wood-Anderson is in displacement)	False

[2] `https://eqcorrscan.readthedocs.io/en/latest/submodules/utils.mag_calc.html`

Figure B2.

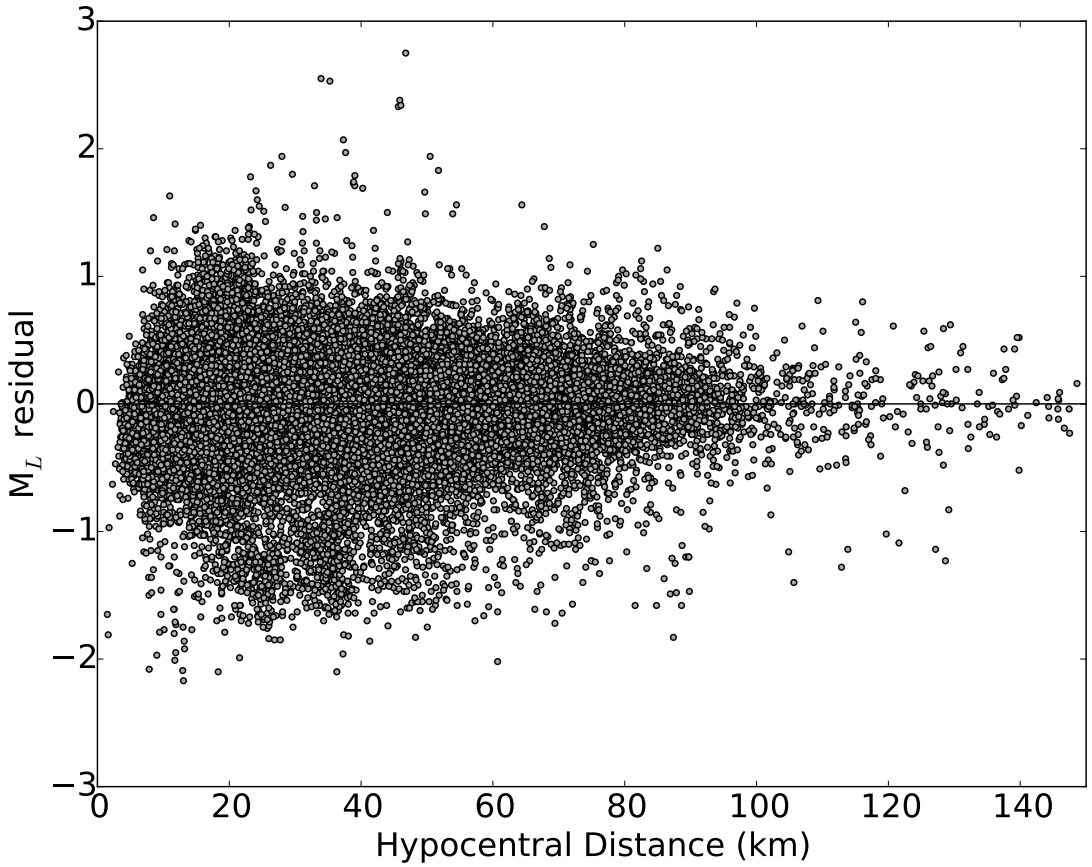

Figure B.2: Magnitude residuals versus hypocentral distances for all available events calculated using the new local magnitude scale for the central Southern Alps region.

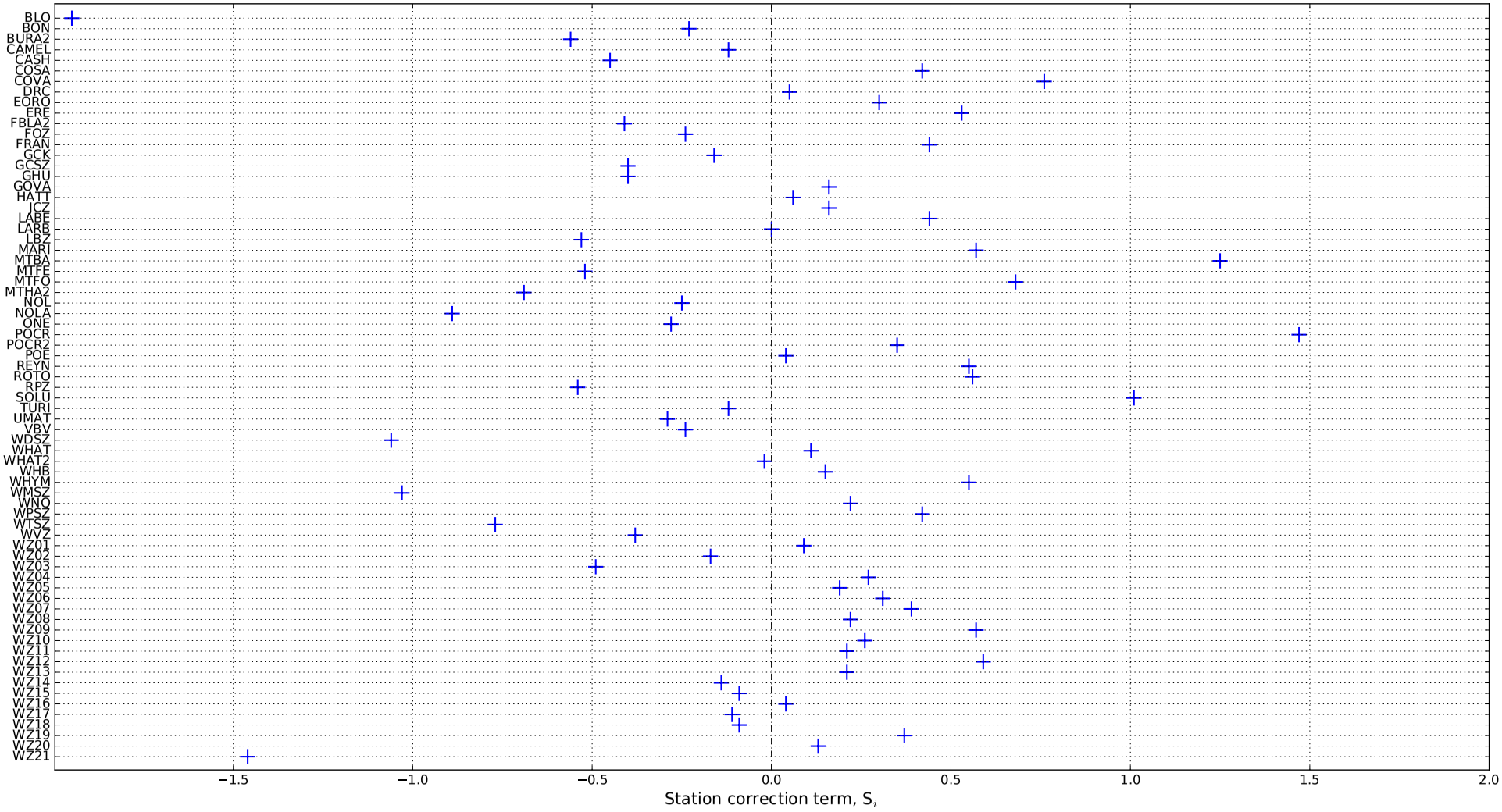

Figure B.3: Station correction terms for the seismic sites used during the magnitude calculation.

Figure B4.

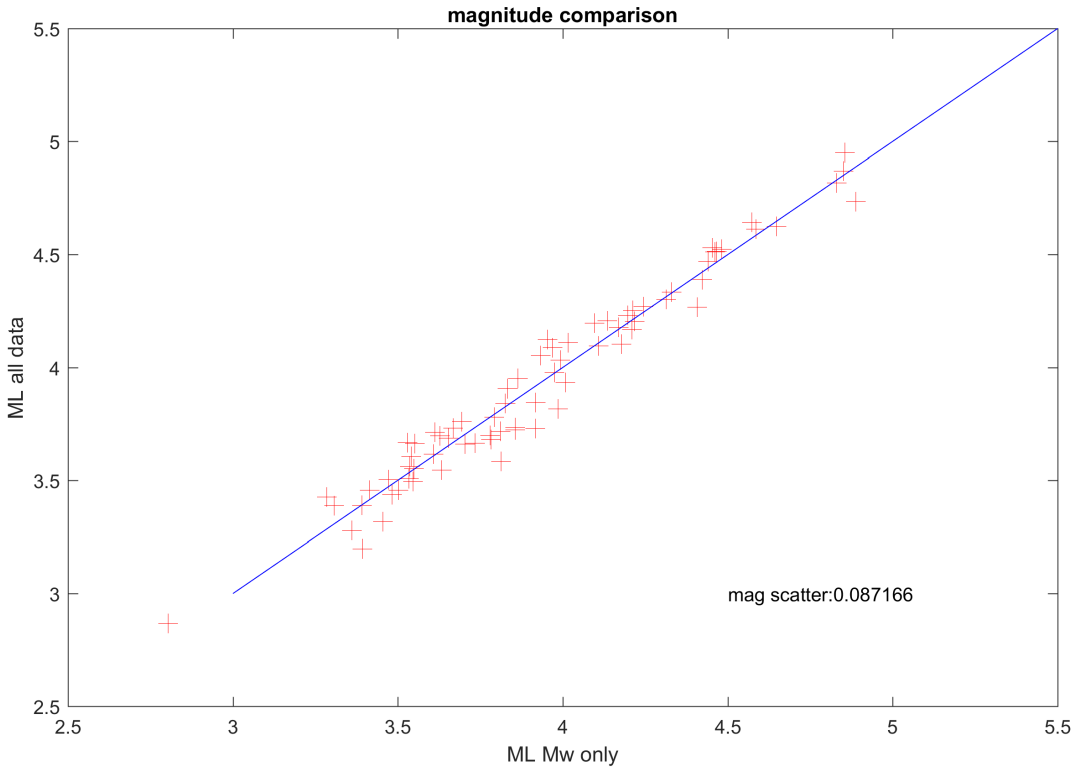

Figure B.4: Comparison of M_L estimates from the 74 event M_w dataset and the 4000 plus 74 combined dataset. The RMS scatter is less than 0.1.

Figure B5.

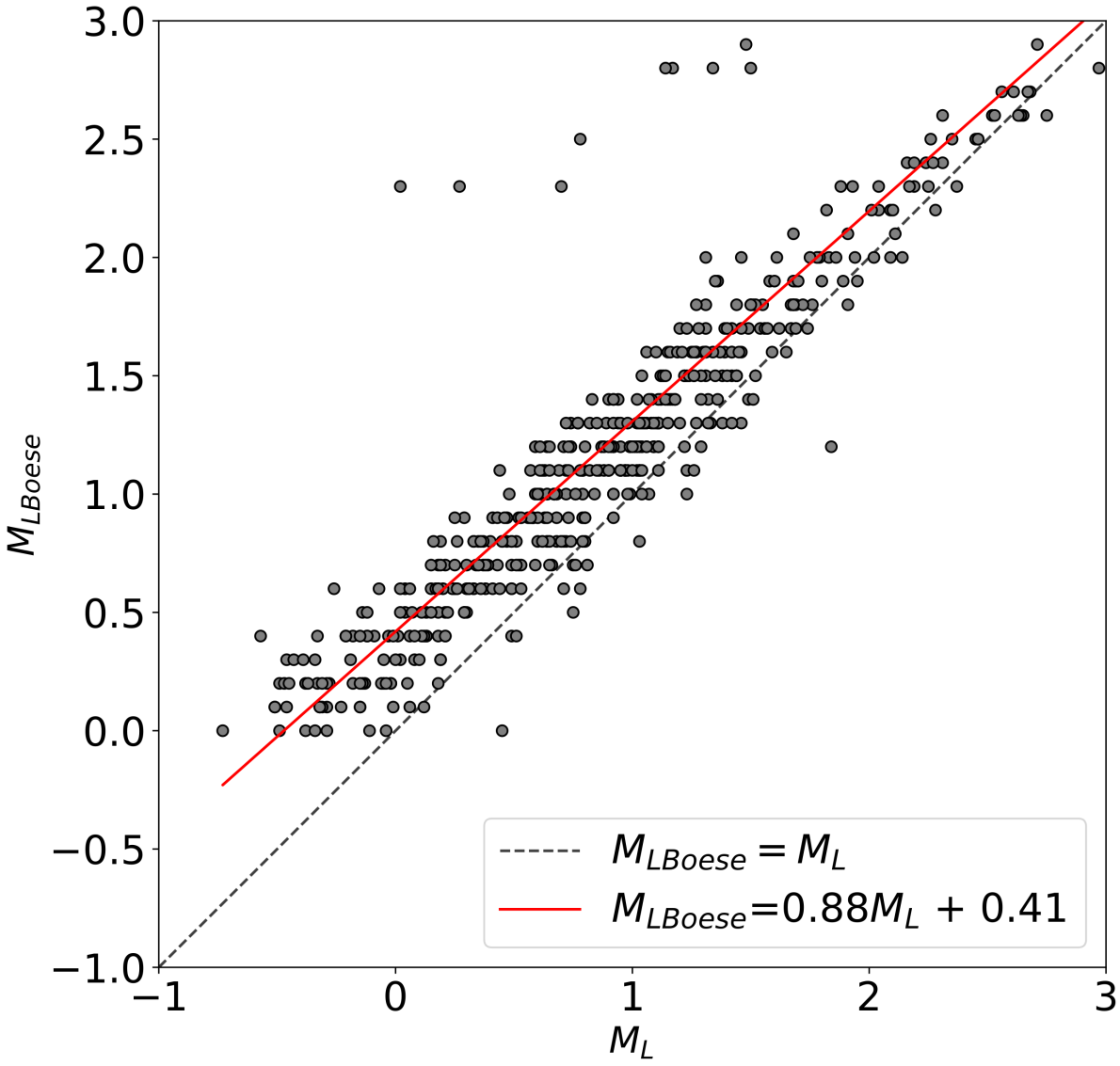

Figure B.5: Comparison of M_{LBoese} calculated by *Boese et al.* (2012) with M_L calculated in this study for 484 common events is shown. The dotted gray line represents $M_{LBoese} = M_L$ and the red solid line is the regression line as indicated in the legend.

Figure B6.

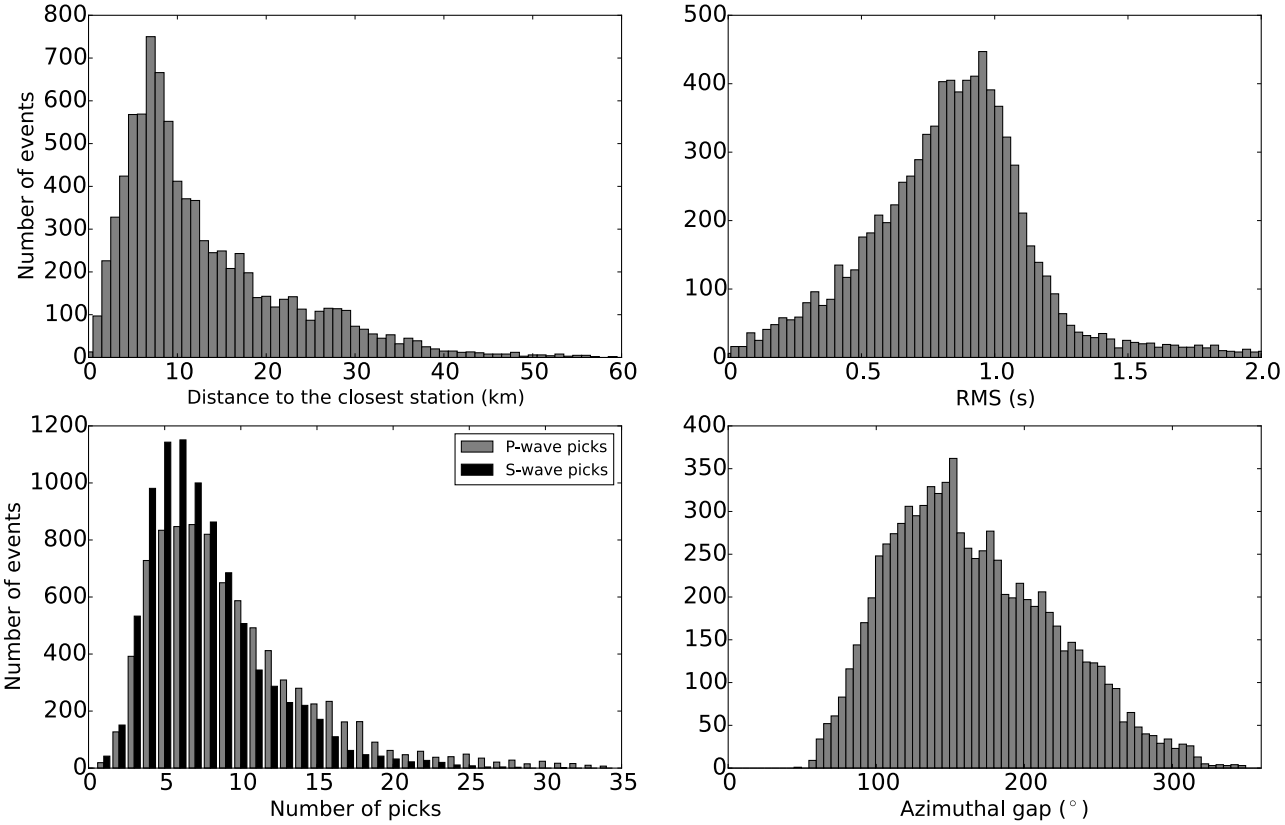

Figure B.6: Location uncertainties in the horizontal direction and depth, distribution of the hypocentral distances to the closest station, azimuthal gap, RMS values and number of P and S wave picks per earthquake given by NonLinLoc.

Figure B7.

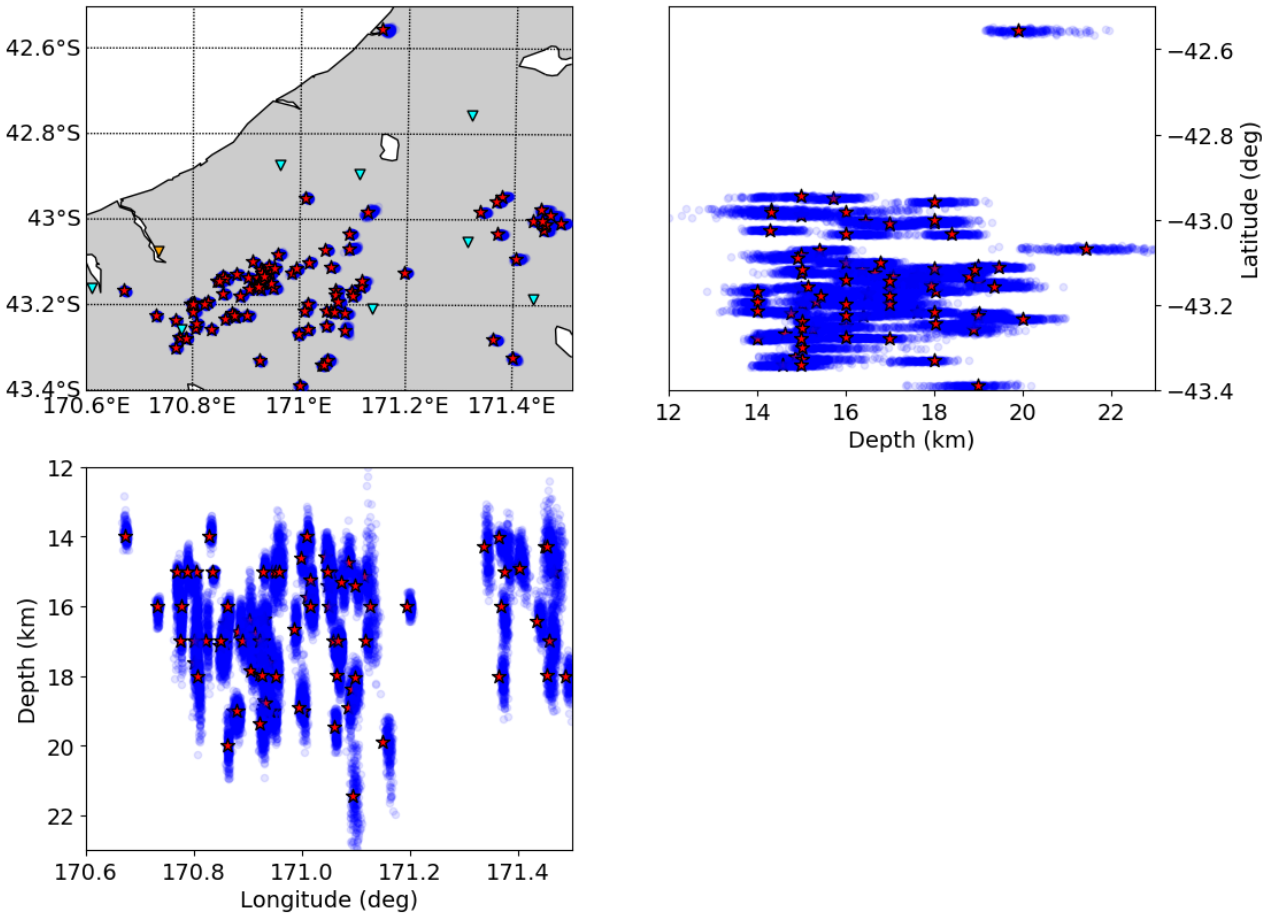

Figure B.7: NonLinLoc earthquake hypocenters (red stars) of a selection of deep events, with their probability density functions (68% confidence level; blue dots) in the northeast side of the composite seismic network used here. (Top left) Map view of epicenters. Inverted triangles depict the position of the seismic sites. (Top right) Cross-section of the events in map-view in the north-south direction. (Bottom left) Cross-section of the events in map-view in the west-east direction.

Figure B8.

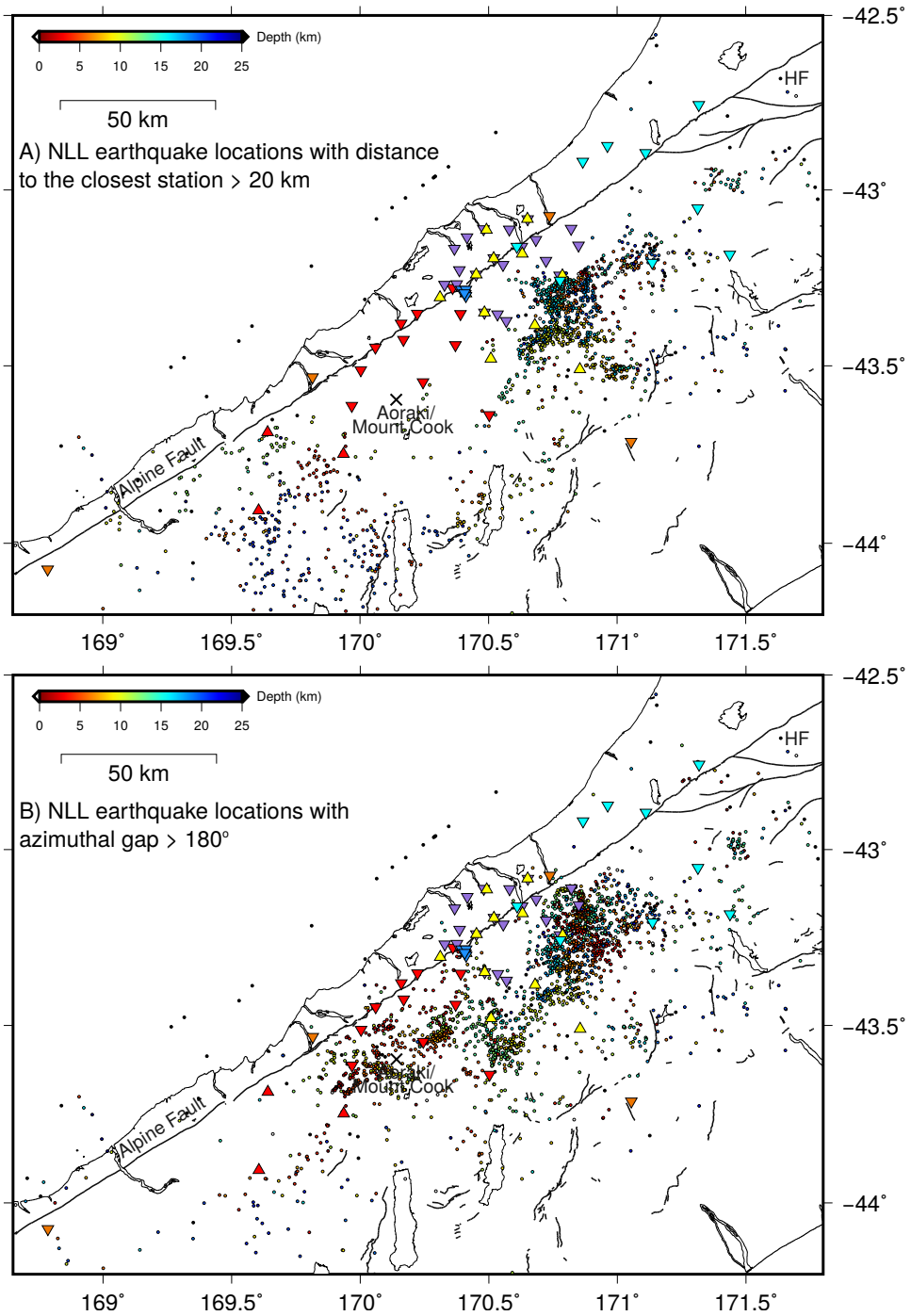

Figure B.8: Distribution of NonLinLoc earthquake locations for comparison to Fig. B.6 showing (A) events with large station-event distances (>20km) and (B) events with large azimuthal gaps (>180°).

Table B5

Table B.5: Basic control options and values used for locating earthquakes with NonLinLoc (*Lomax et al.*, 2000). LOCSEARCH has three possible search types (i.e. $GRID$, grid search; MET, Metropolis; OCT, Octtree) and it defines the type of search applied. Parameter *initNumCells* represent the initial number of Octtree cells in the x, y, and z directions. Parameter *minNodeSize* defines the smallest node side length to be calculated, octtree search is terminated after a node with a side smaller than this length is generated. *maxNumNodes* is the total number of nodes to be processed. *numScatter* determines the number of scatter points generated by the Octtree search. LOCMETH defines the location algorithm used (options: GAU ANALYTIC; EDT, Equal Differential Time). *maxDistStaGrid* is the maximum station to center of the initial grid search distance (very large value for no maximum). Parameters *minNumberPhases* and *maxNumberPhases* are the minimum and maximum number of P phases used for the location, respectively (-1 for no maximum). *minNumberSphases* defines the minimum number of S phases used (-1 for no minimum). *VpVsRatio* is the V_P/V_S ratio value to be used (<0.0 to use the S-travel times). LOCGRID determines the size and attributes of the initial 3-D search grid to be performed. *xNum*, *yNum* and *zNum* stand for the number of nodes along x, y and z axes, respectively. *xOrig*, *yOrig* and *zOrig* determines the grid origin relative to the geographic origin relative to East, North and Down directions, respectively. *dx*, *dy* and *dz* are representing the grid spacing along x, y and z axes. All distances are in km. Further details for the NonLinLoc programs can be found in the NonLinLoc Software Package Control File website: `http://alomax.free.fr/nlloc/soft6.00/control.html`.

NonLinLoc program	Choice	Parameters and values
LOCSEARCH - Search Type	*OCT*	*initNumCells* x = 50 *initNumCells* y = 50 *initNumCells* z = 30 *minNodeSize* = 0.001 *maxNumNodes* = 200000 *numScatter* = 1000
LOCMETH - Location Method	GAU ANALYTIC	*maxDistStaGrid* = 9999.0 *minNumberPhases* = 4 *maxNumberPhases* = -1 *minNumberSphases* = -1 *VpVsRatio* = -1
LOCGRID - Search grid description	PROB DENSITY	*xNum* = 130 *yNum* = 330 *zNum* = 53 *xOrig* = -60 *yOrig* = -120 *zOrig* = -3 *dx* = 1. *dy* = 1. *dz* = 1.

Table B6

Table B.6: Input parameters for the weighting scheme in HypoDD (*Waldhauser*, 2001). NITER is the number of iterations for each set of weights. WTCCP and WTCCS are the weights applied to the cross-correlation P–wave and S–wave data, respectively. WTCTP and WTCTS are the weights applied to the catalog P–wave and S–wave data, respectively. WRCC and WRCT are the cutoff thresholds for outliers of the cross-correlation and catalog data. WDCC and WDCT are the maximum event separation distance (km) for the correlation and catalog data. DAMP is the damping factor that damps the hypocentral adjustments if the adjustment vector becomes large or unstable. Damping values here were chosen after some initial test checking on the condition number (CND). CND values are expected to be between 40 and 80.

	Cross data				Catalog data				
NITER	WTCCP	WTCCS	WRCC	WDCC	WTCTP	WTCTS	WRCT	WDCT	DAMP
5	0.01	0.005	10	-999	1	0.5	10	10	100
5	0.01	0.005	8	-999	1	0.5	6	8	100
5	0.01	0.005	6	7	1	0.5	6	6	100
5	1.0	0.5	5	5	0.01	0.005	6	6	100
5	1.0	0.5	4	3	0.01	0.005	6	6	100

Text B4: Comparison between different velocity models and location methods

To check if the seismogenic zone beneath Aoraki/Mount Cook depends on the velocity model we repeated the location process in two separate ways:

1. We used the same initial earthquake locations from HYPOCENTER. We then obtained the absolute earthquake locations with NonLinLoc and a 1-D velocity model. Finally, we obtained the relative earthquake locations using hypoDD the same 1-D velocity model.

2. We also relocated the earthquake locations obtained from HYPOCENTER, omitting the NonLinLoc step, using HypoDD and a 1-D velocity model.

The relative earthquake locations obtained in both cases show the same almost 10 km difference in the seismogenic cut-off depth beneath Aoraki/Mount Cook. We note that the 1-D relocations have a similar structure for deeper seismicity, however the shallow seismicity distribution is different (the Whataroa gap is not clearly depicted in these two cases). For case 1, this happens because the 3-D velocity model used contains more information about the velocity structure at depth and for case 2 because the linearized inversions have limited constraints for shallow seismicity.

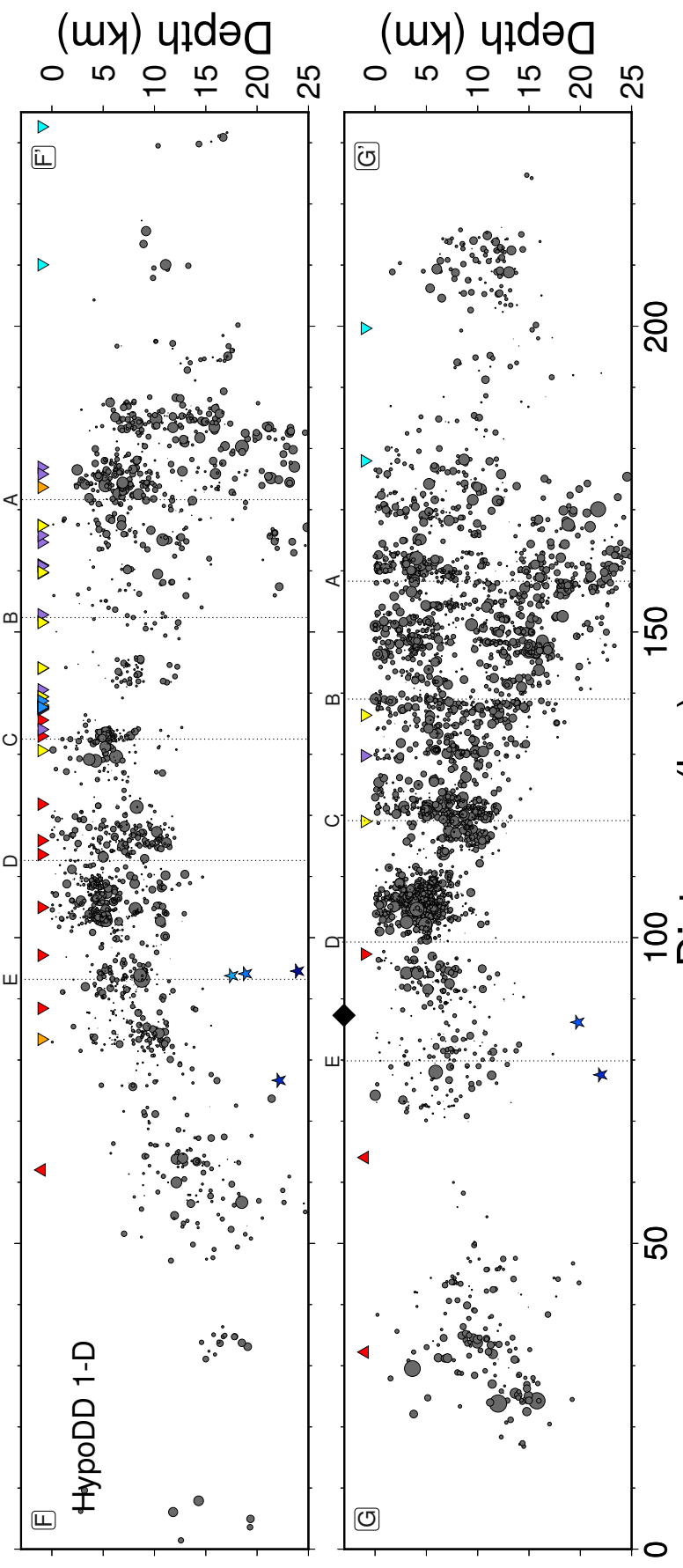

Figure B.9: Cross sections of relocated earthquake locations along the Alpine Fault obtained using HypoDD (*Waldhauser*, 2001) and a 1-D velocity model of (*O'Keefe*, 2008) and modified by (*Boese et al.*, 2012). The locations of the cross sections are labeled with capital letters in Figure 3.5. Earthquakes within 10 km on either side of the cross section are shown. Stars show the locations of low-frequency earthquakes (*Baratin et al.*, 2018). Inverted triangles depict the seismic sites within each cross section. Aoraki/Mount Cook is marked by a black diamond.

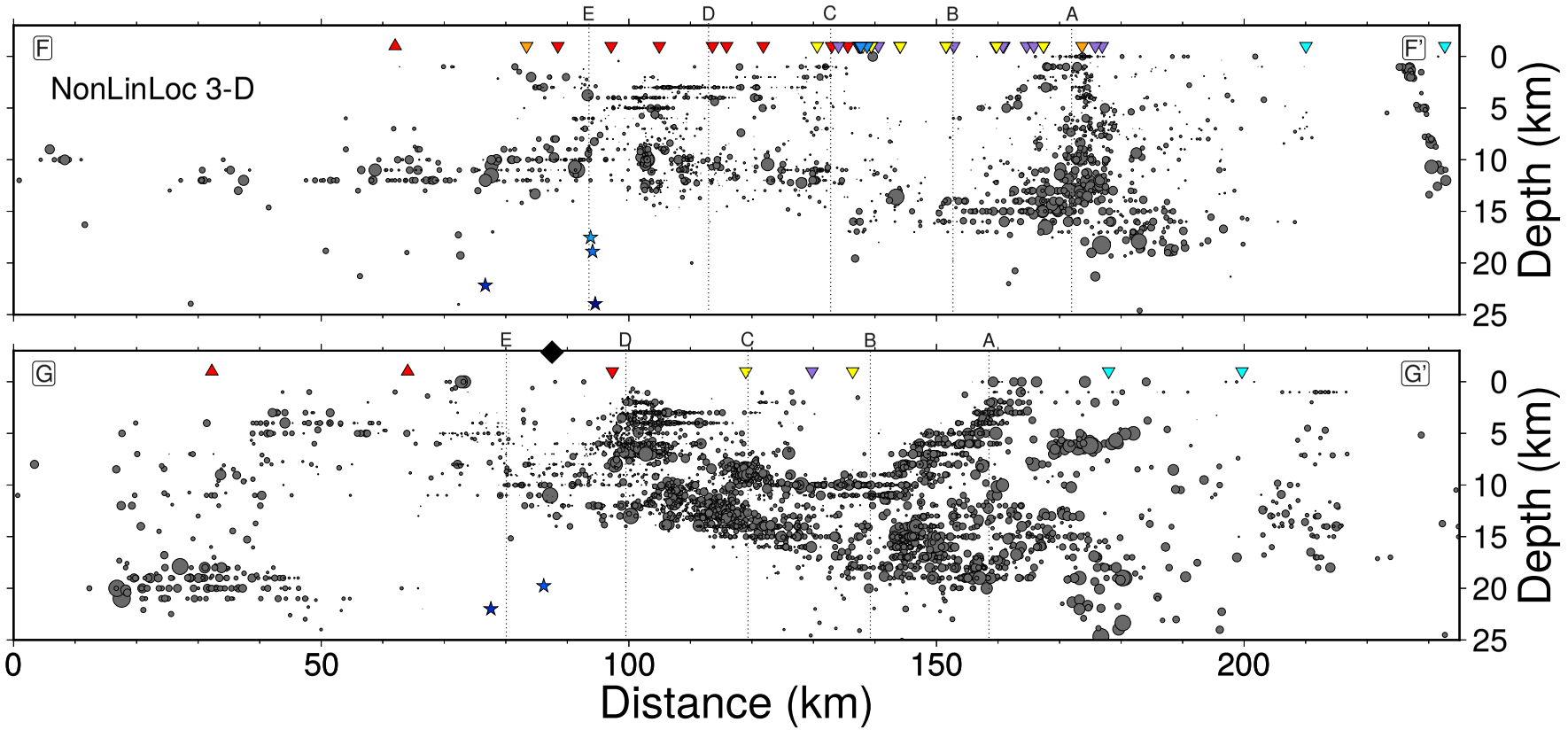

Figure B.10: Cross sections of absolute earthquake locations along the Alpine Fault obtained using NonLinLoc (*Lomax et al.*, 2000) and the 3-D velocity model of (*Guo et al.*, 2017) with respective magnitudes. The locations of the cross sections are labeled with capital letters in Figure 3.5. Earthquakes within 10 km on either side of the cross section are shown. Stars show the locations of low-frequency earthquakes (*Baratin et al.*, 2018). Inverted triangles depict the seismic sites within each cross section. Aoraki/Mount Cook is marked by a black diamond.

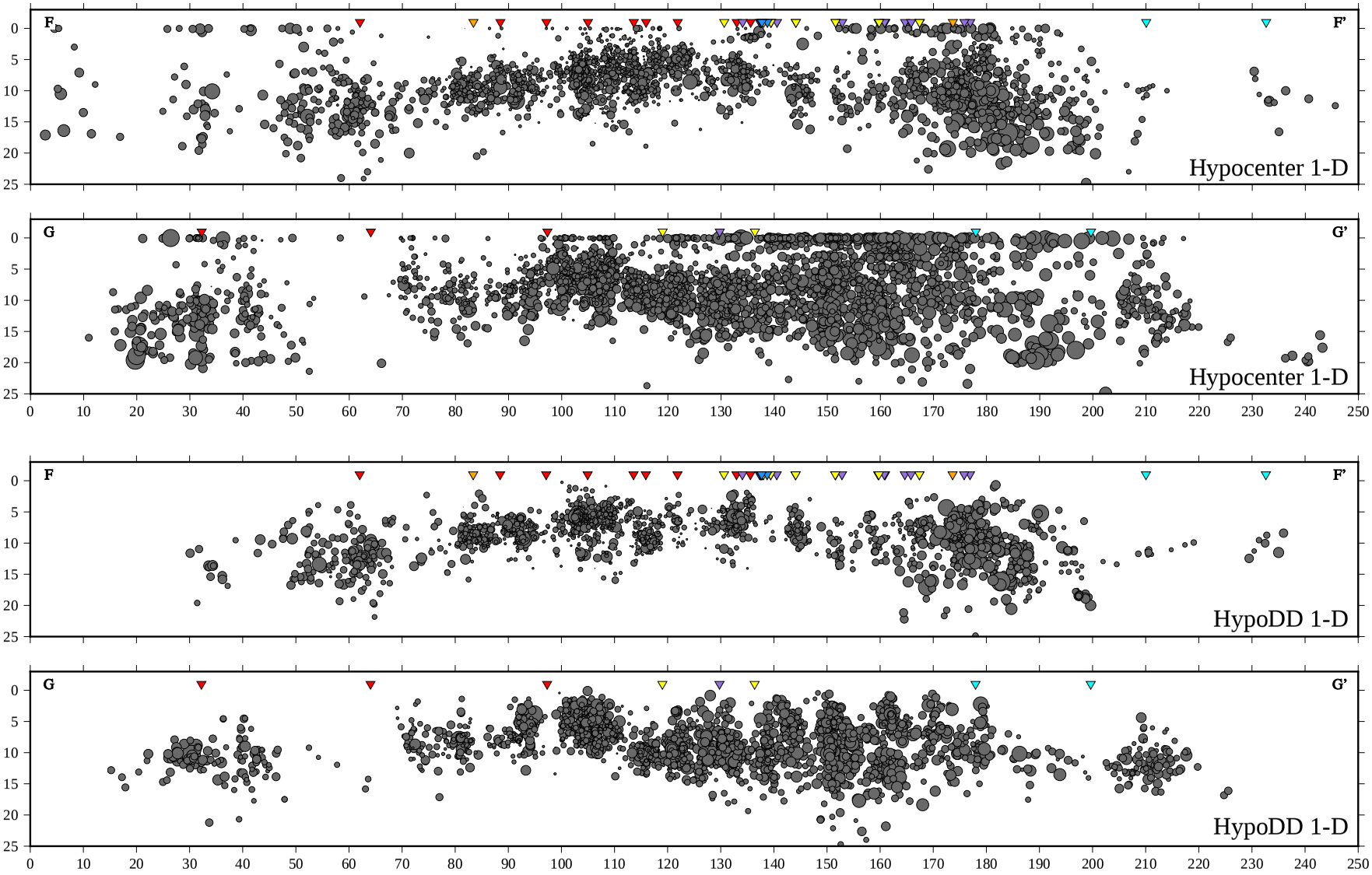

Figure B.11: Cross sections of absolute earthquake locations obtained using HYPOCENTER (*Lienert et al.*, 1986) and the 1–D velocity model of (*O'Keefe*, 2008) modified by (*Boese et al.*, 2012)(top two). Relative earthquake locations using hypoDD (*Waldhauser*, 2001) and the 1–D velocity model of (*O'Keefe*, 2008) modified by (*Boese et al.*, 2012), with respective magnitudes (bottom two). The locations of the cross sections are labeled with capital letters in Figure 3.5. Earthquakes within 10 km on either side of the cross section are shown. Inverted triangles depict the seismic sites within each cross section.

Figure B12.

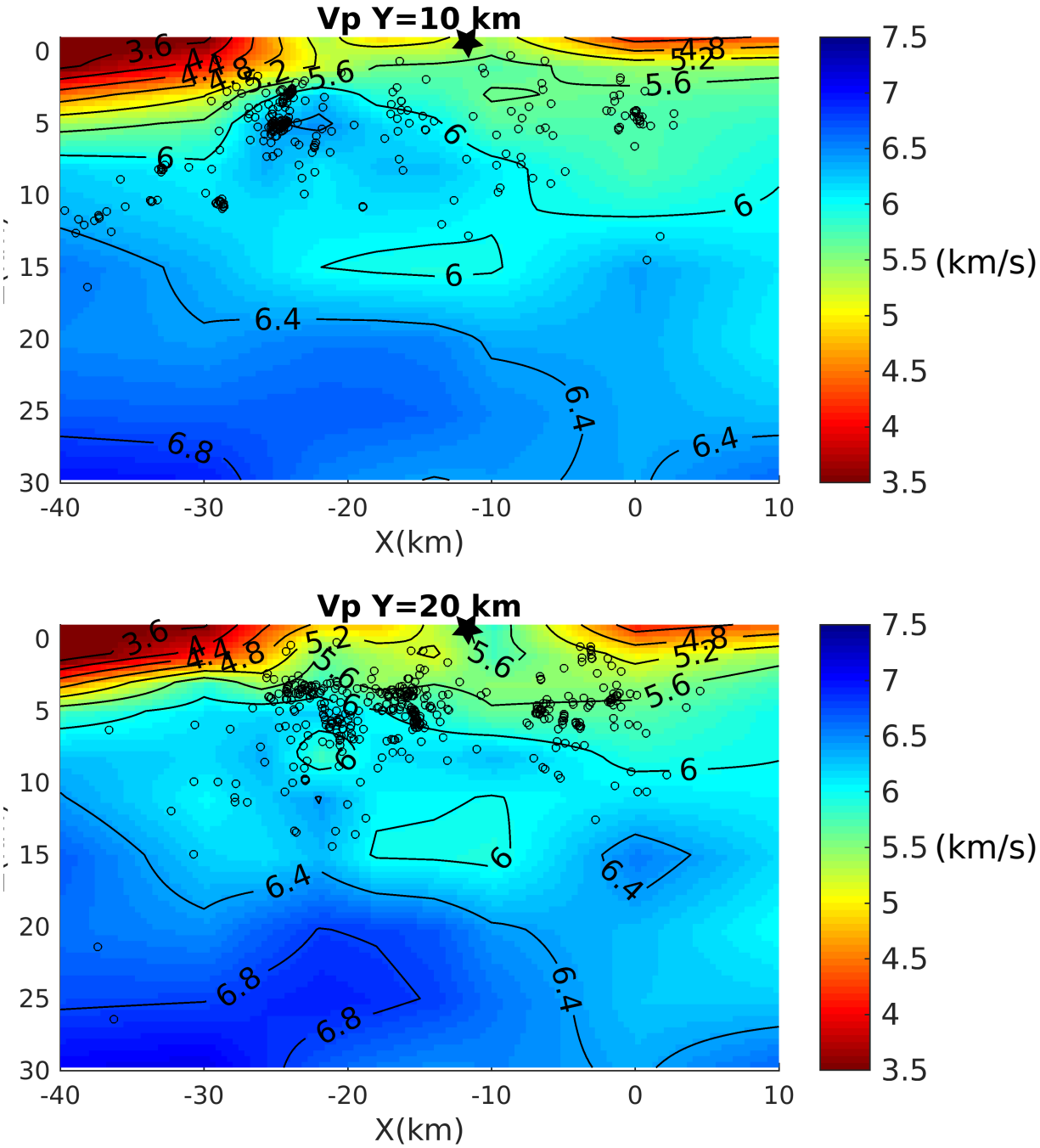

Figure B.12: Cross sections of 3-D P wave velocity model of (*Guo et al.*, 2017) at Y = 10 km and Y = 20 km with the earthquake hypocenters obtained using hypoDD (white circles). The cross-sections are made using the same gridding as used for the 3-D velocity model by *Guo et al.* (2017) and their Figure 1. The black star indicates the position of Aoraki/Mount Cook.

Figure B13.

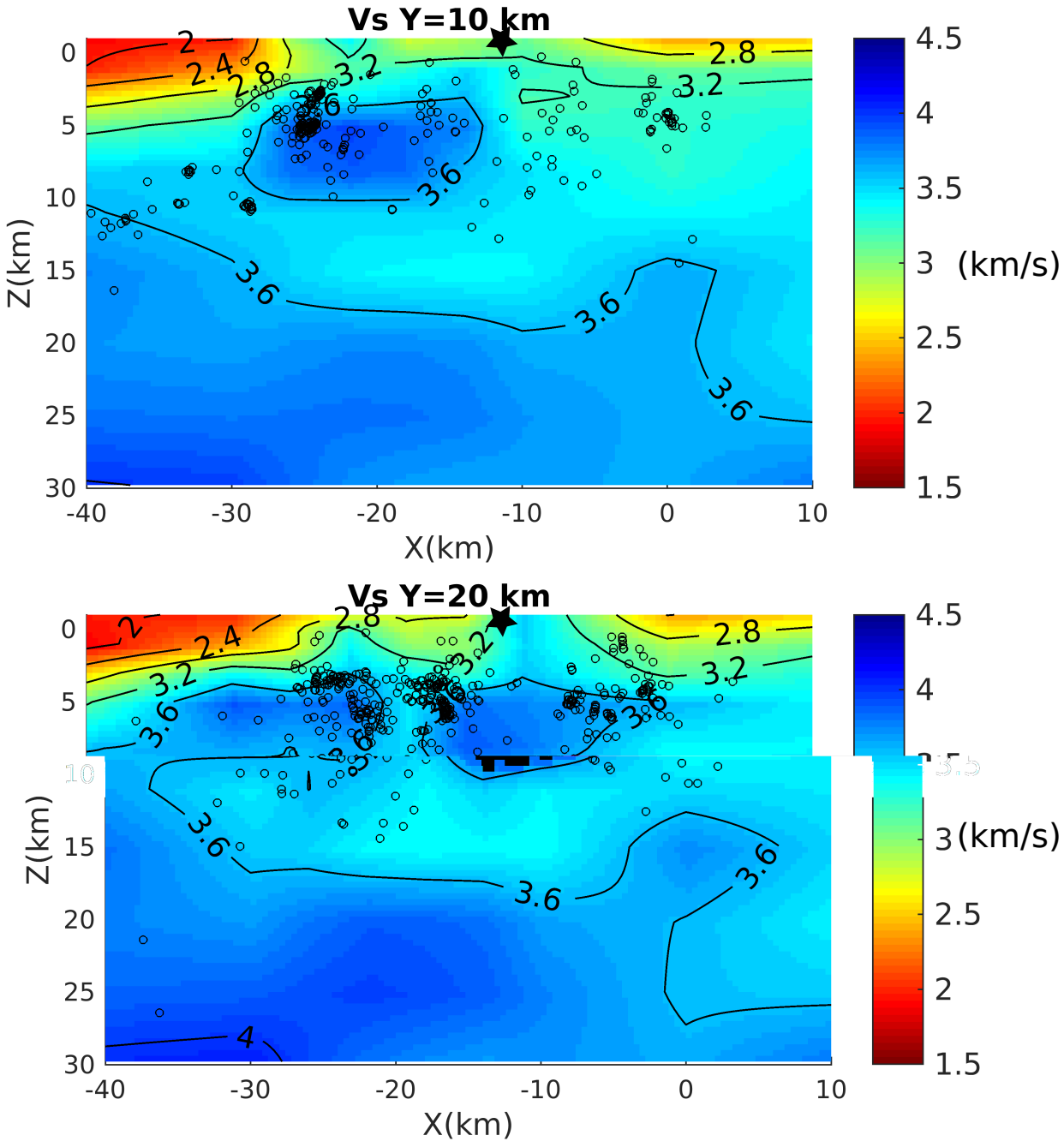

Figure B.13: Cross sections of 3-D S-wave velocity model of (*Guo et al.*, 2017) at Y = 10 km and Y = 20 km with the earthquake hypocenters obtained using hypoDD (white circles). The cross-sections are made using the same gridding as used for the 3-D velocity model by *Guo et al.* (2017) and their Figure 1. The black star indicates the position of Aoraki/Mount Cook.

Figure B14.

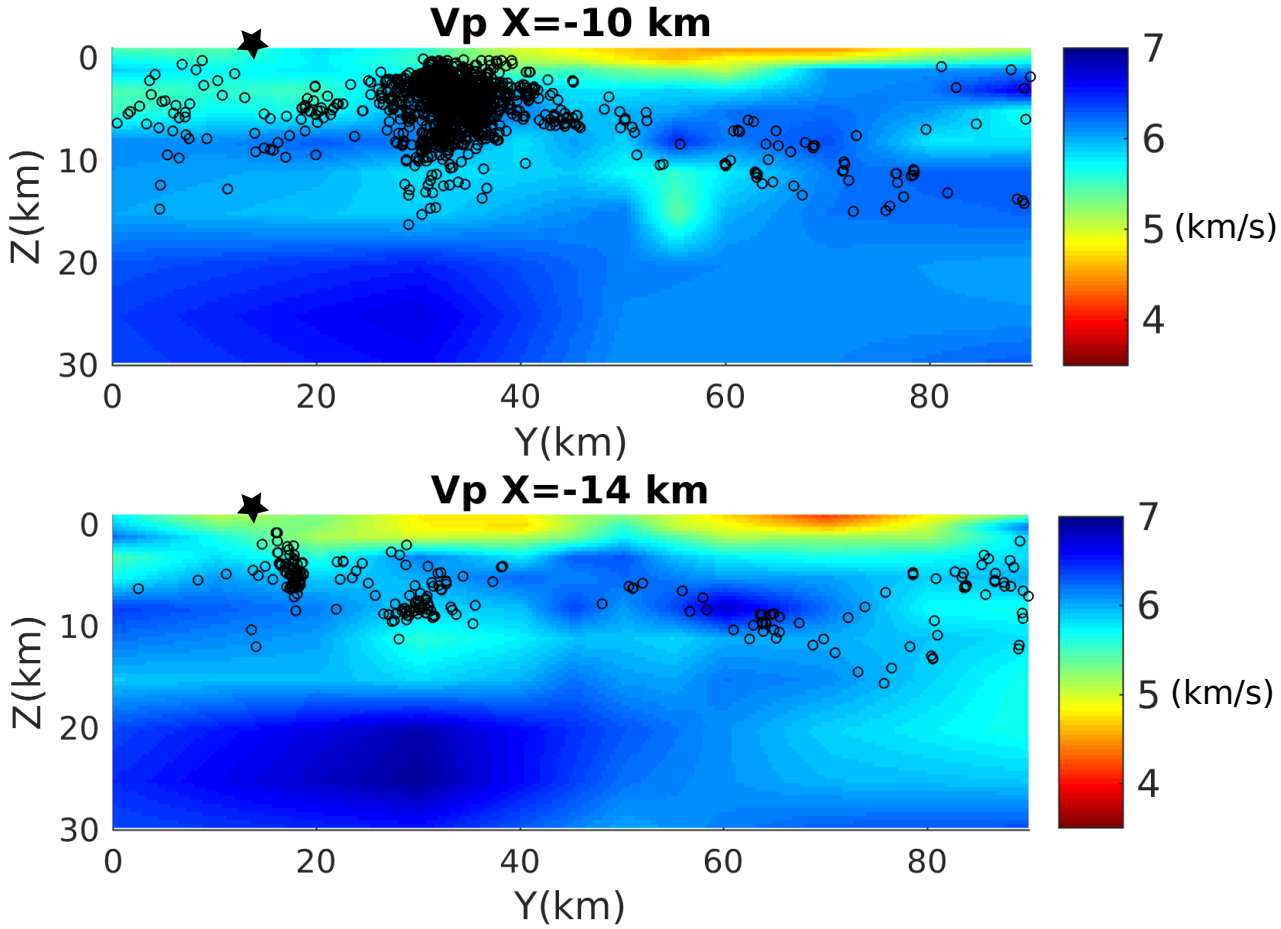

Figure B.14: Cross sections of 3-D P-wave velocity model of (*Guo et al.*, 2017) at X = -10 km and X = -14 km with the earthquake hypocenters obtained using hypoDD (black circles). The cross-sections are made using the same gridding as used for the 3-D velocity model by *Guo et al.* (2017) and their Figure 1. The black star indicates the position of Aoraki/Mount Cook.

Figure B15.

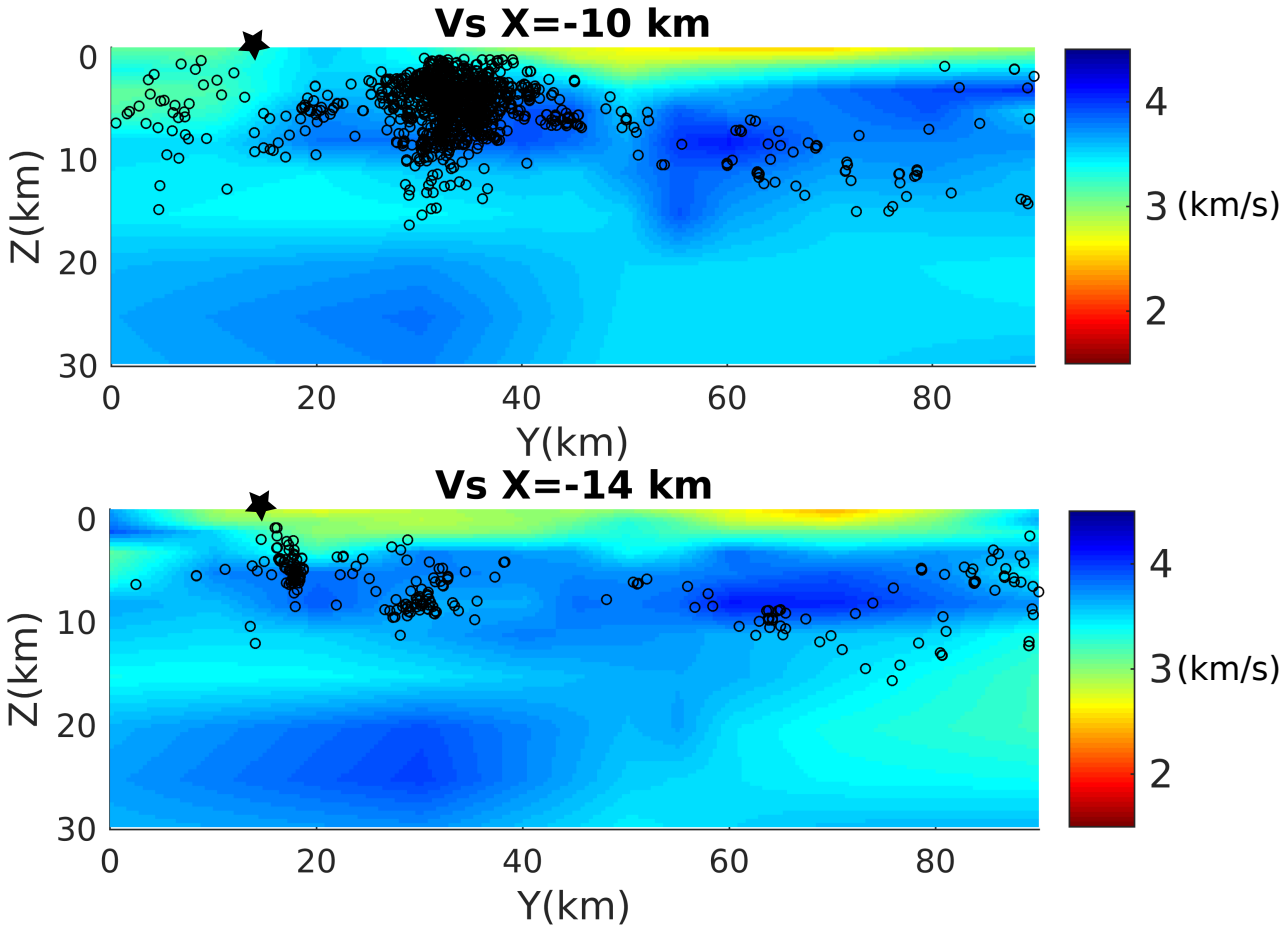

Figure B.15: Cross sections of 3-D S-wave velocity model of (*Guo et al.*, 2017) at X = -10 km and X = -14 km with the earthquake hypocenters obtained using hypoDD (black circles). The cross-sections are made using the same gridding as used for the 3-D velocity model by *Guo et al.* (2017) and their Figure 1. The black star indicates the position of Aoraki/Mount Cook.

Additional Supporting Information (Files uploaded separately)

1. Captions for Dataset B1

Data Set B1.

Dataset B1. Dataset B1 of the electronic appendices contains the relocated earthquake catalogue (hypoDD), constructed using the methods described in the main article. Uncertainties were not obtained for all of the relocations. The earthquakes with no uncertainty values have a dash ('-'). Column descriptions are the following:

1. YYYY – Year
2. MM – Month
3. DD – Day
4. HH – Hours (UTC time)
5. MM – Minutes (UTC time)
6. SS – Seconds (UTC time)
7. Lat – Latitude in degrees
8. Lon – Longitude in degrees
9. Depth – Hypocentral depth in kilometers
10. Mag – Local magnitude calculated
11. Hor unc – Horizontal uncertainty obtained by 200 bootstraps
12. Ver unc – Vertical uncertainty obtained by 200 bootstraps

C Supporting Information for Chapter 4: "Detailed spatiotemporal properties of the tectonic stress regime along the central Alpine Fault"

Introduction

This supplementary material contains one table, three text sections and seven figures. Table C1 presents the stress parameter details each cluster of focal mechanisms obtained with k-means.

Figure C1 summarises the focal mechanism solution uncertainties. Two figures (C2 and C3) classify the type of faulting according to the rake values and the distribution of the B, T and P principal axes, respectively. Figures C4 and C5 outline the focal mechanism details. Figure C6 is adopted from (*Boulton et al.*, 2018) and shows the three dimensional stress analysis calculations for the central Alpine Fault. Figure C7 shows the variation of the type of faulting and magnitudes with time. Figure C8 depicts the S_{Hmax} orientations for clusters defined using the k-means method.

We also include the caption and description of the focal mechanism earthquake catalog constructed as described in the main article; this dataset is uploaded as a separate file in the electronic appendices (Dataset C1).

Figure C1.

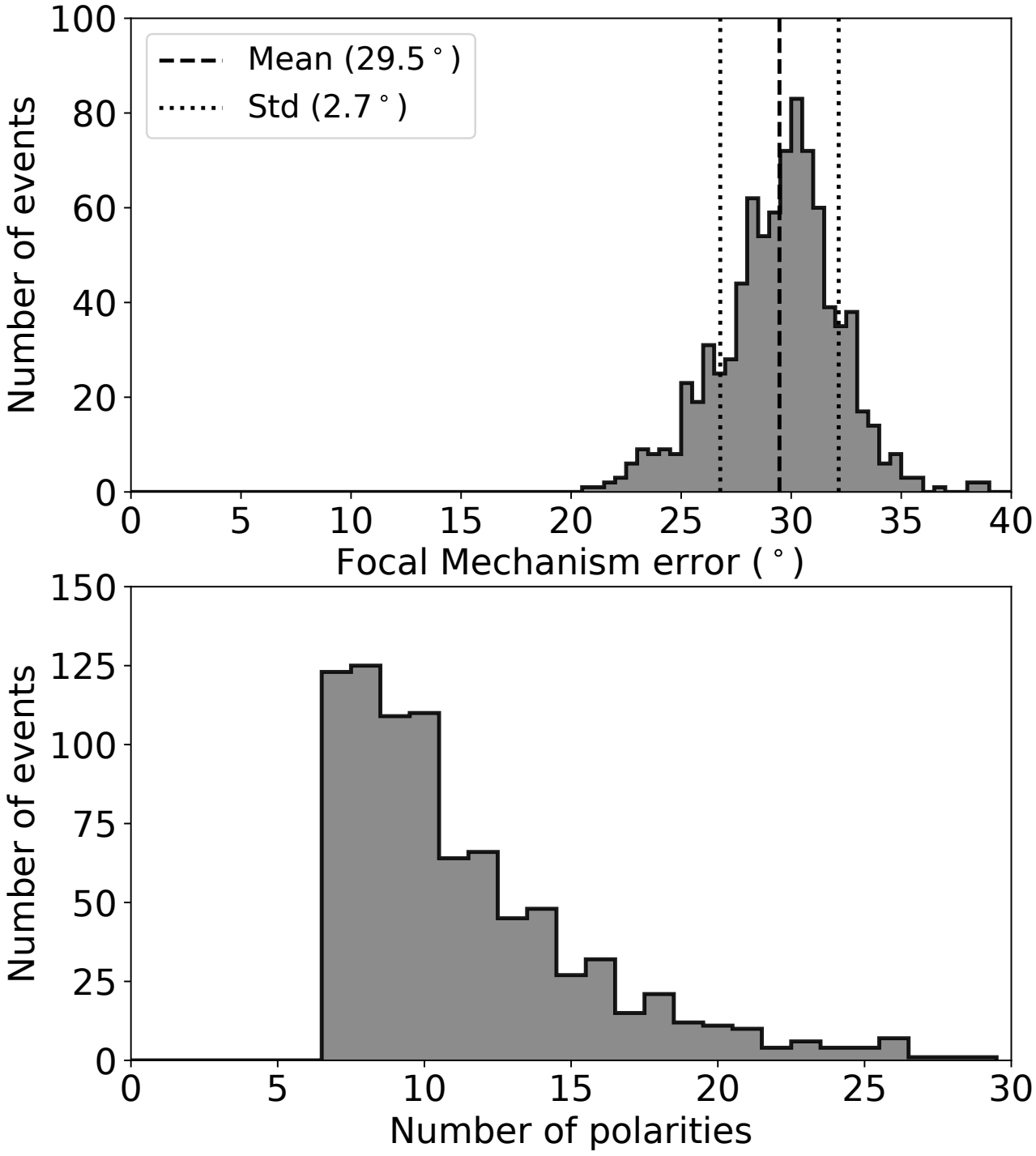

Figure C1: Histograms of the distribution of the uncertainties (top) and number of polarities (bottom) of the focal mechanism solutions calculated using the Bayesian approach of *Walsh et al.* (2009).

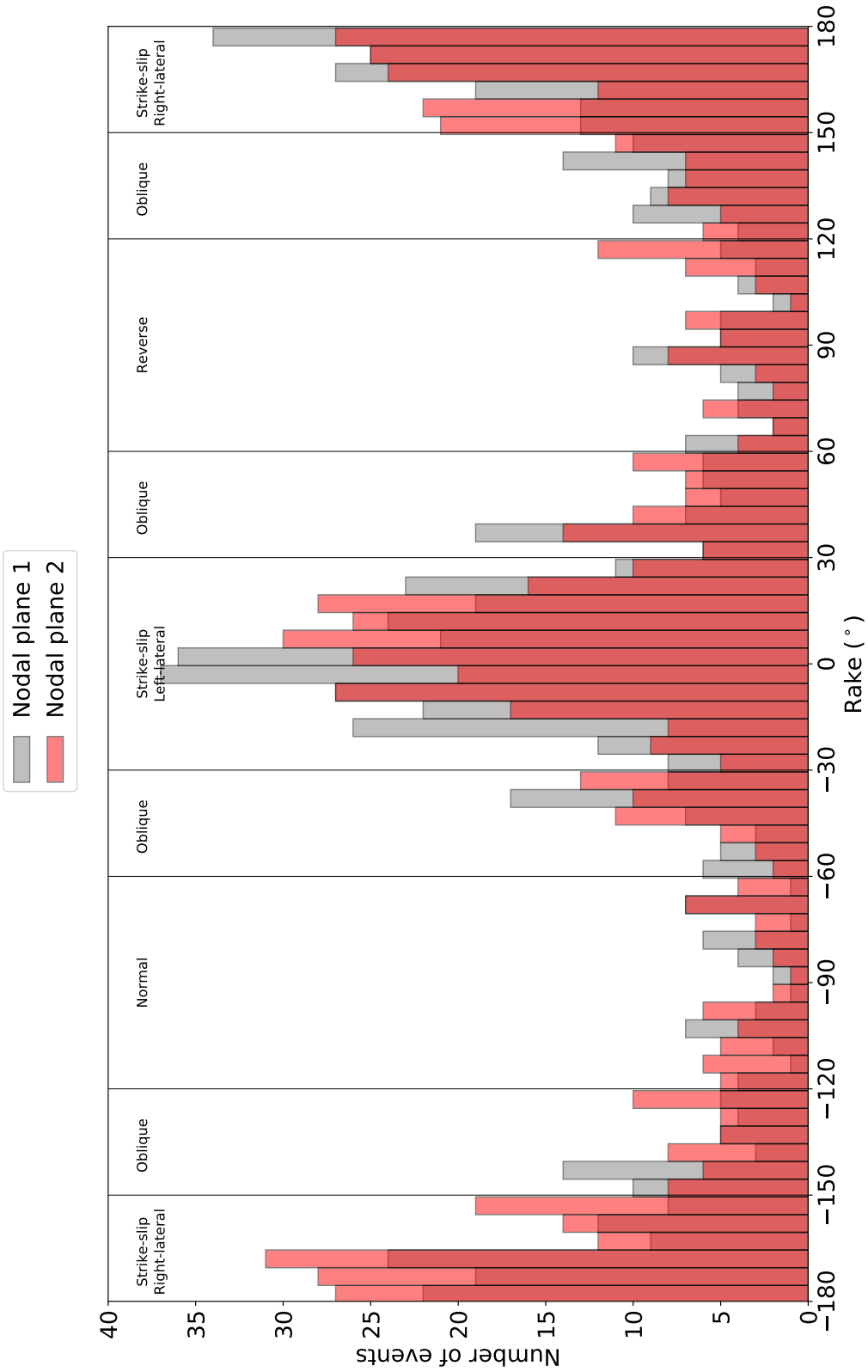

Figure C2: Histogram showing the distribution of the rake values for both nodal planes of all the focal mechanisms.

Figure C3.

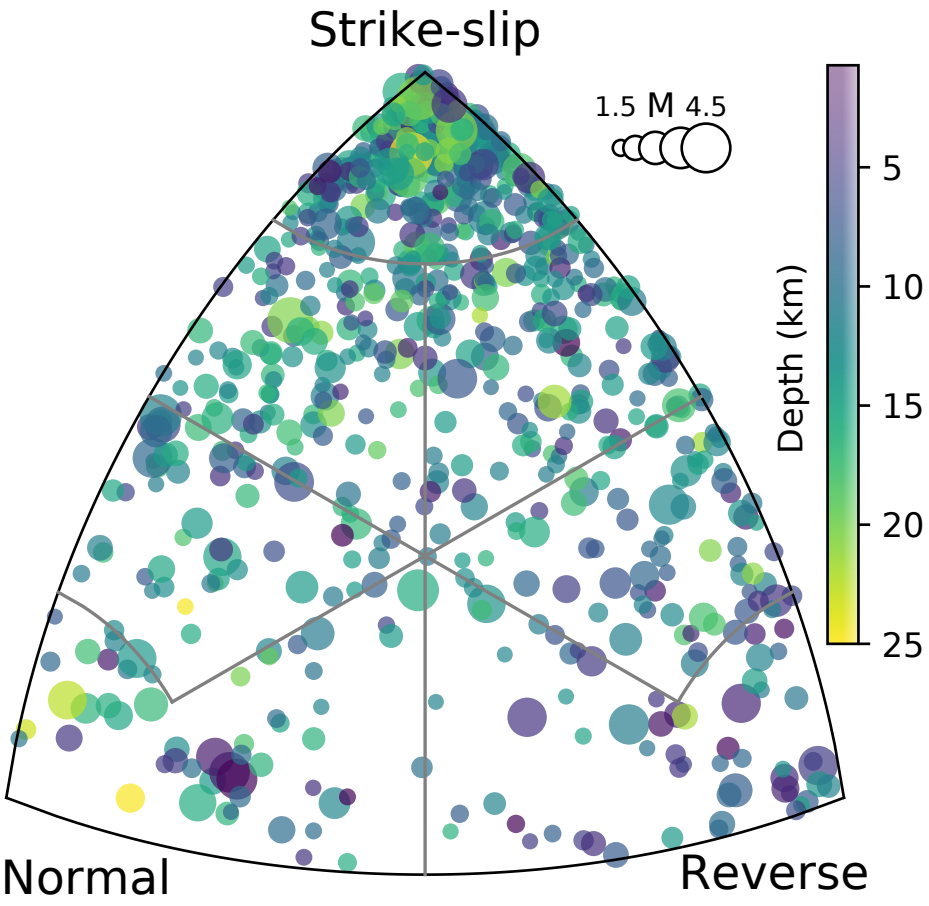

Figure C3: Focal mechanism classification diagram of the distribution of B, T and P principal axes for all focal mechanisms. Circle size is proportional to their magnitudes and colors represent the earthquake's hypocentral depths (see color scale on the right).

Figure C4.

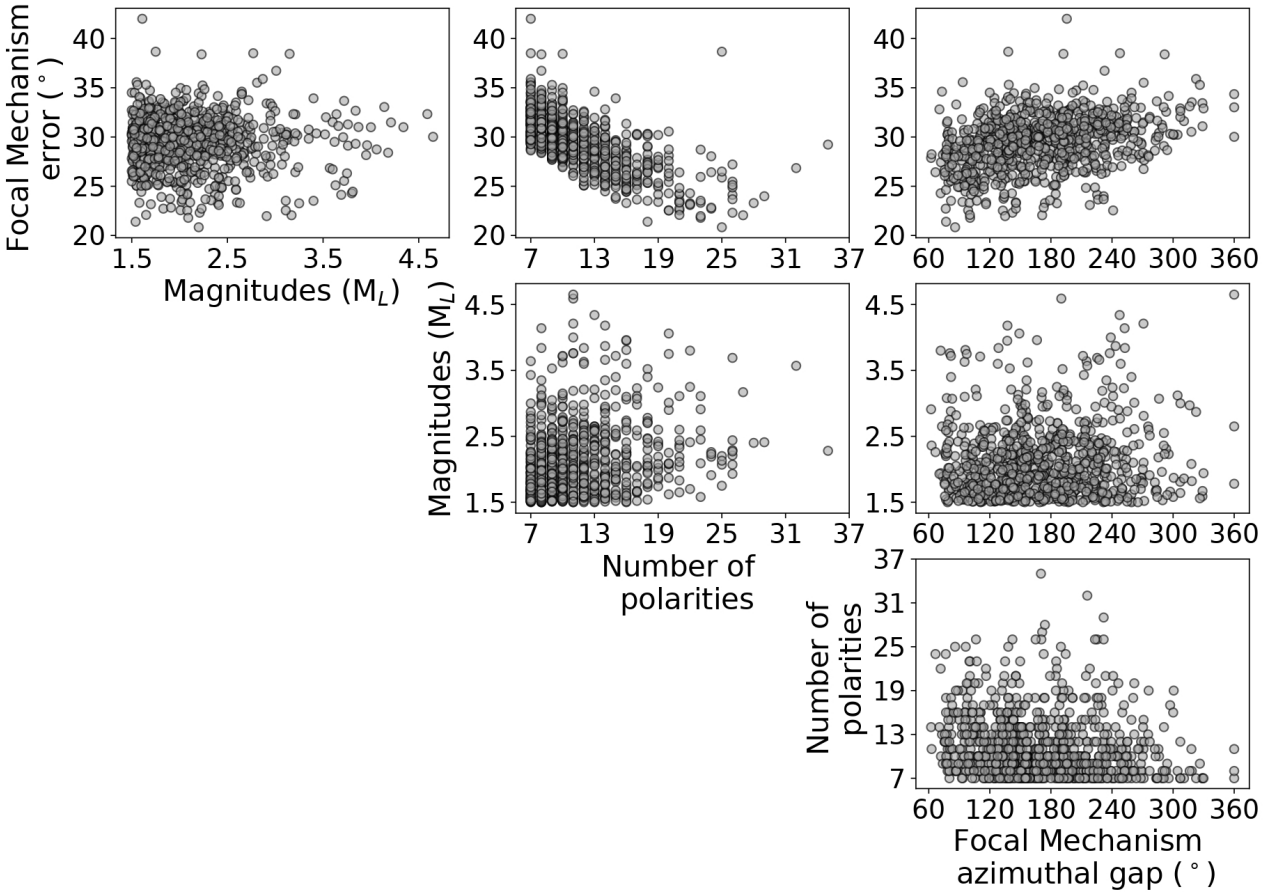

Figure C4: Focal mechanism details. Subplots examine the relations between a number of focal mechanism parameters (i.e. focal mechanism error, magnitude, number of polarities and azimuthal gap).

Figure C5.

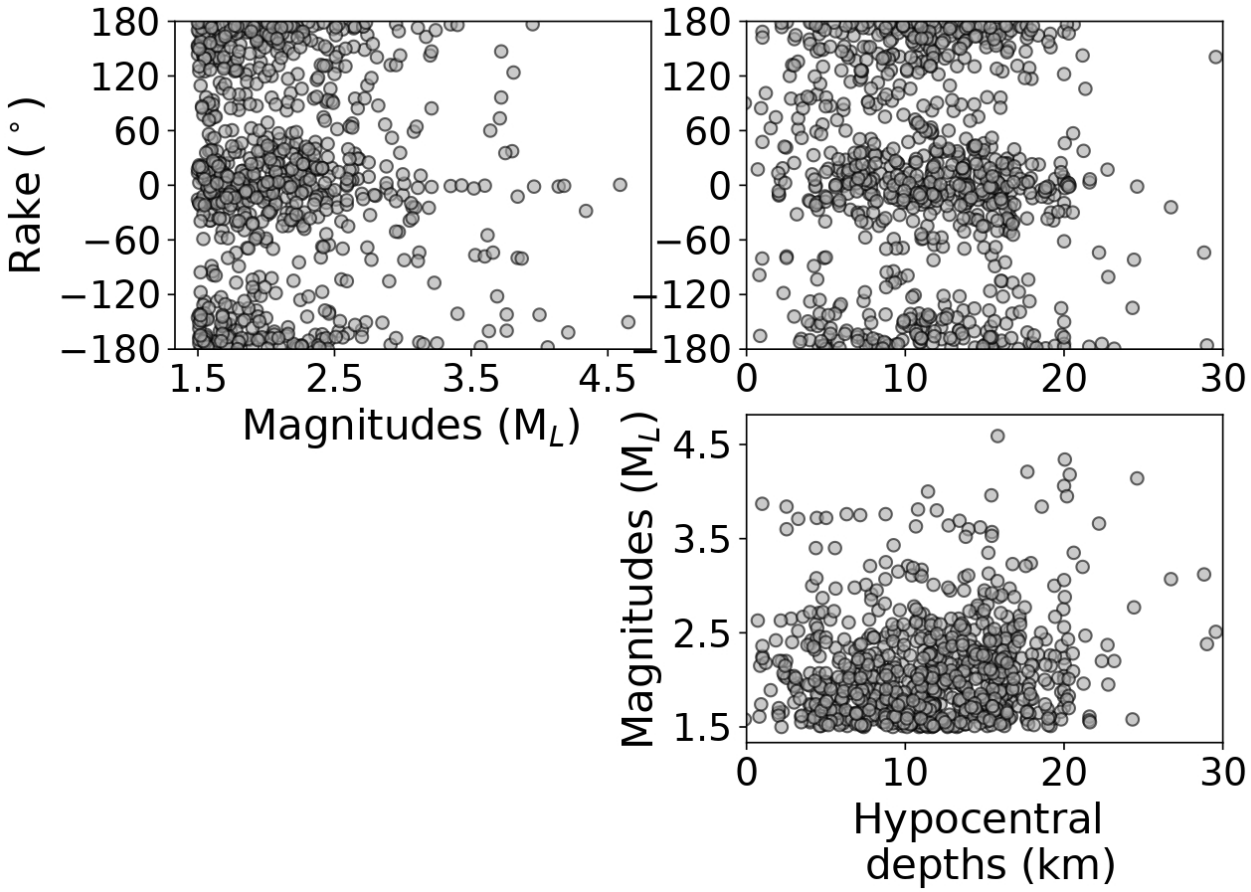

Figure C5: Focal mechanism rakes plotted against their magnitudes and hypocentral depths.

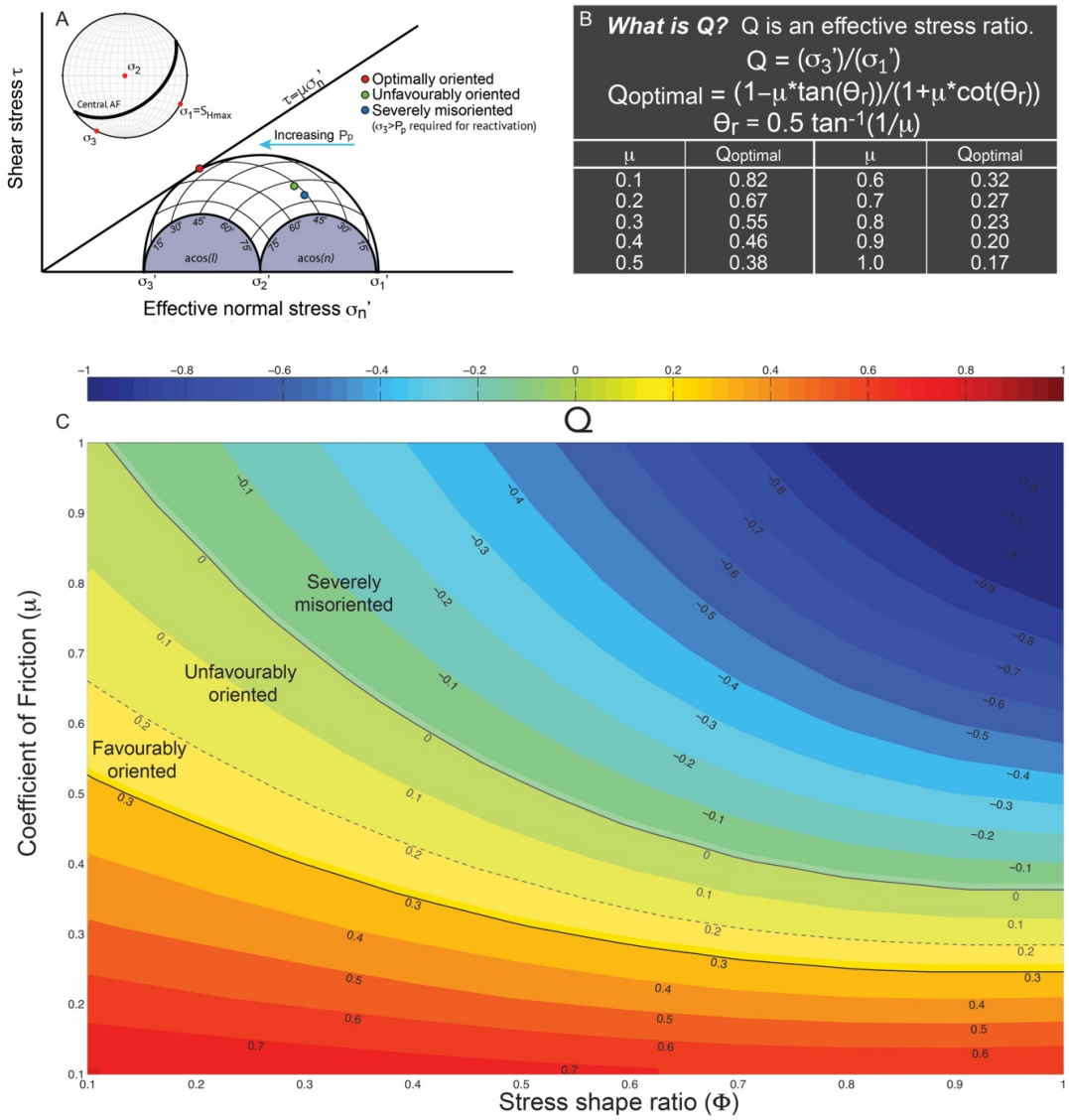

Figure C6: Three dimensional stress analysis calculations for the central Alpine Fault. Figure adopted from *Boulton et al.* (2018). A) Three dimensional Mohr circle for stress shape ratio Φ=0.5. B) Definitions of stress shape ratio, Q, and $Q_{optimal}$ for varying friction coefficient values. C) Contour plot for Q values for a fault plane oriented 055°/45° SE and principal stress orientations S_1=S_{Hmax}=0/117°, S_2=S_v, and S_3=0/207° calculated by *Boese et al.* (2012).

Text C1: Polarity tests

Prior to calculating the focal mechanisms using P wave polarities, the seismic instruments were meticulously tested for any systematic polarity errors or inconsistencies. To do this, we use the first arrivals of three teleseismic events recorded by our composite network and a number of explosions from a quarry located near Whataroa (Appendix E).

First motion polarities are critical for an accurate determination of focal mechanisms determined using P wave polarities. To check the polarities of the SAMBA, GeoNet and ALFA-08 network seismic sites we use the first onsets from a number of strong teleseismic events. In particular, we use the Mindanao region (Philippines) earthquake on October 4, 2009 with a magnitude of M = 6.6 M_w and the Banda Sea region (Indonesia) on December 10, 2012 with a magnitude of M = 7.1 M_w. We found that all DFDP-10, half of the WIZARD instruments and the four southern SAMBA sites at Copland Valley, Mt. Baird, Solution Ranges and Lansborough (COVA, MTBA, SOLU, LARB) show reversed polarities on the vertical components. We also observed that some sites (e.g. MTFE, REYN, WHAT, POCR) had noisy conditions and the polarity recordings were emergent and in some cases inconsistent. Thus we did not use polarity picks from these four seismic sites.

Text C2: Spatial variation of S_{Hmax} using k-means

The k-means algorithm, looks for similarities within a given data set of earthquake locations without using any labels. The only attribute defined beforehand is the number of clusters that the data set will be divided to. First, the cluster centroids are randomly decided. Then, the algorithm goes through each of the earthquake locations (longitude, latitude and depth) and depending on the distance from the previously defined centroids assigns them to one of the clusters. At the same time, the cluster centroids are moved to the mean value of locations of the clusters. This process is repeated until there is no change in the clusters centroids.

Fig. C7 illustrates the orientation of the maximum horizontal compressive stress S_{Hmax} with 80% confidence intervals using the k-means clustering algorithm for focal mechanisms with hypocentral depths smaller than 25 km. Bowties showing the S_{Hmax} orientations are colored according to the clusters median hypocentral depth. S_{Hmax} has an average value of 121 $\pm$ 10°, which is in general agreement with previous studies (*Boese et al.*, 2012; *Warren-Smith et al.*, 2017; *Townend et al.*, 2012). There is no significant variation of the S_{Hmax} relative to the Alpine Fault or the hypocentral depth. Table C1 summarizes the cluster and stress inversion details using the k-means clustering algorithm.

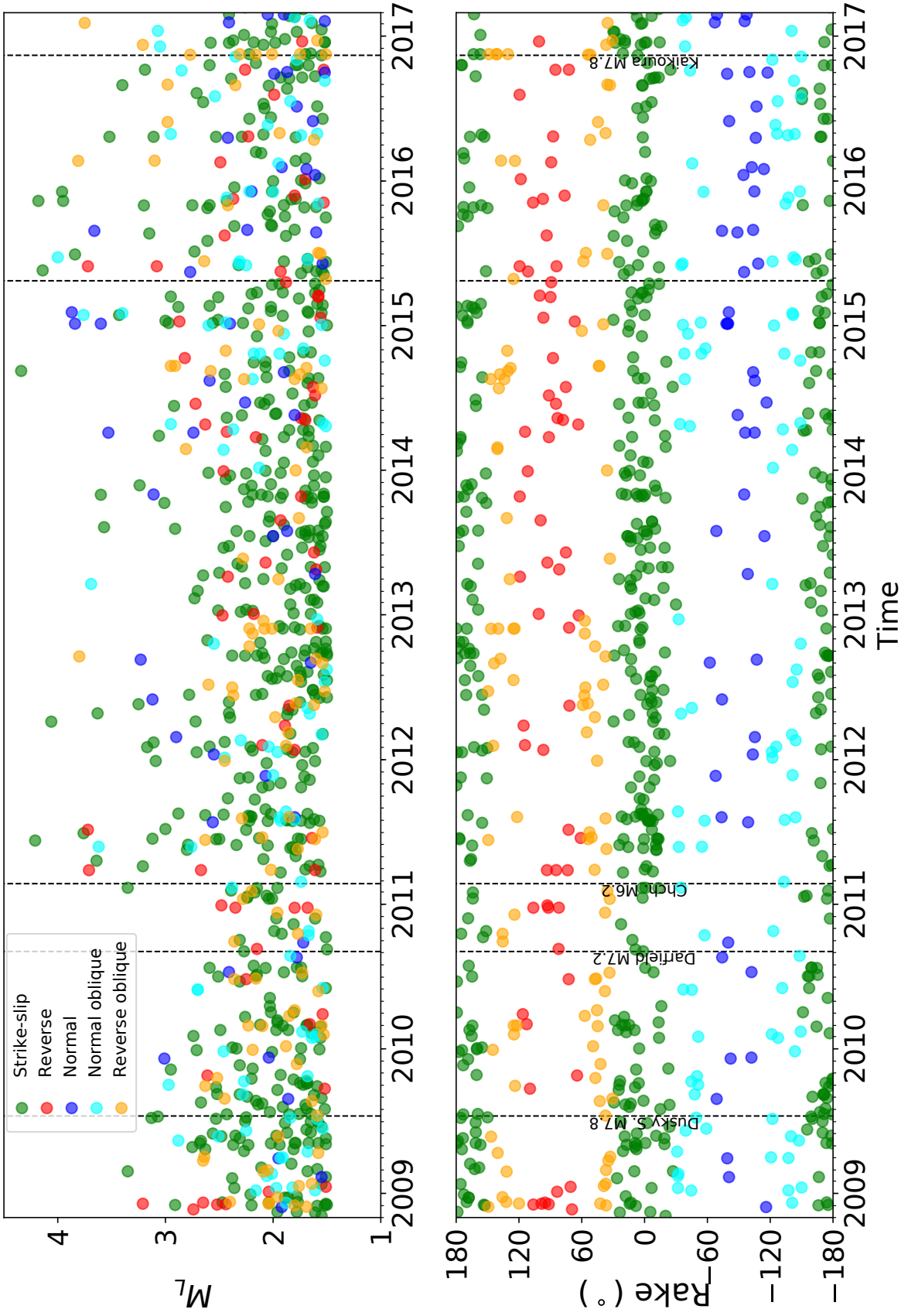

Figure C7: Distribution of earthquake magnitudes and focal mechanisms rake values versus time. The color of the circles indicates the type of faulting (Blue stands for normal, green for strike-slip, red for reverse, cyan for oblique-normal and orange for oblique-reverse faulting.

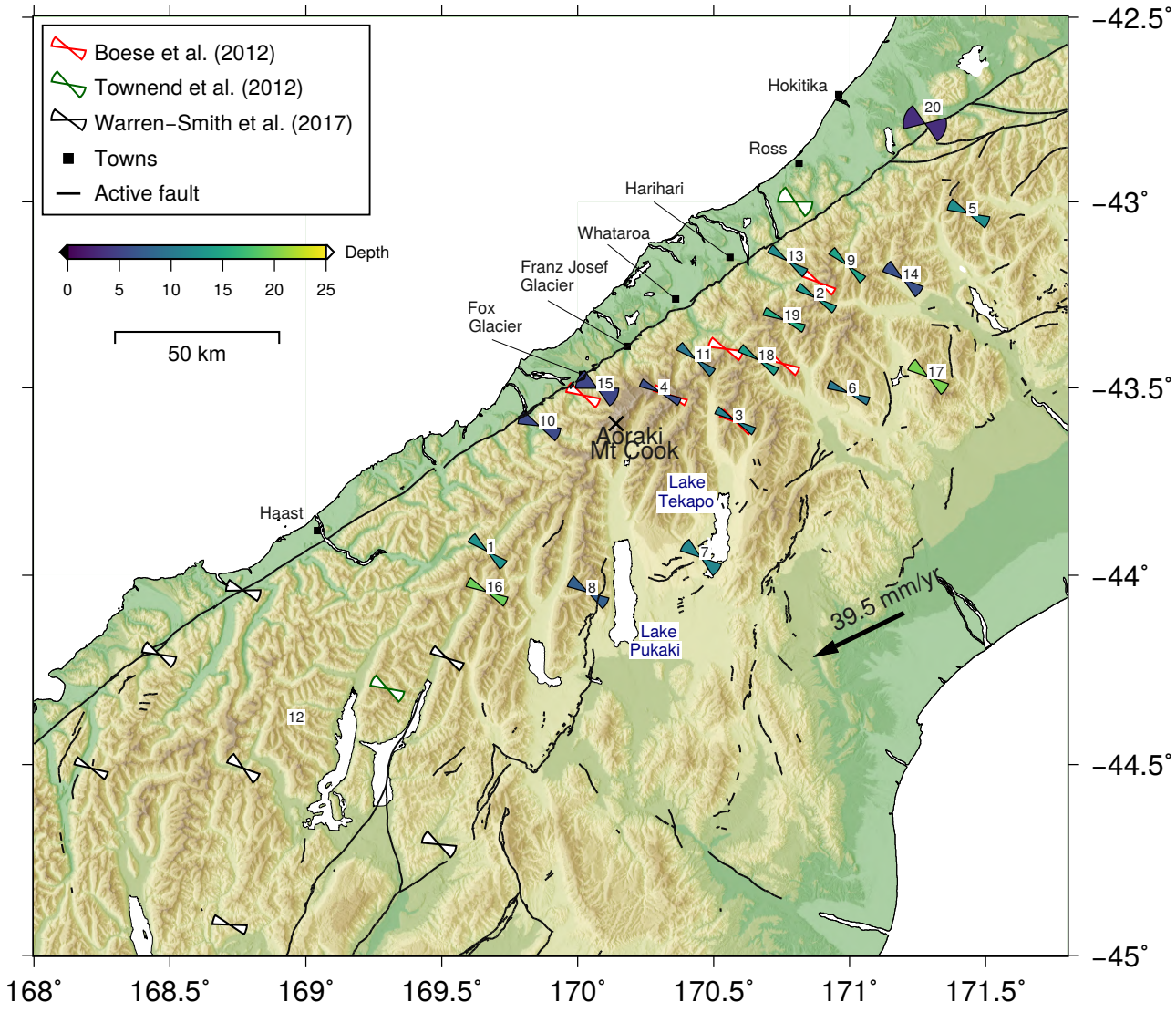

Figure C8: Distribution of stress directions along the central and southern Alpine Fault. Focal mechanisms are clustered in three dimensions (latitude, longitude and depth) using k-means algorithm. Bowties indicate the direction and 90th percentile error for the direction of the maximum horizontal compressive stress (S_{Hmax}) and are colored according to the median value of the cluster's hypocentral depths (see color scale). Numbers indicate the number of the bin details of which are presented in Table C1. Results from previous studies are also shown. White bowties with red, green, and black outlines show the stress directions calculated by *Boese et al.* (2012), *Townend et al.* (2012), and *Warren-Smith et al.* (2017a), respectively. Arrow indicates the local velocity of Pacific Plate relative to Australia [∼39.5 mm/yr in Fox Glacier;](*DeMets et al.*, 2010).

Table C1: Mean S_{Hmax} orientations from inversions of focal mechanisms using the kmeans clustering algorithm with 10% and 90% percentiles. N is the number of focal mechanisms that each cluster contains. ν is the mean stress ratio $(S_1–S_2)/(S_1\text{-}S_3)$ for each cluster that has values between 0 and 1.

Bin	Latitude (°)	Longitude (°)	Depth (km)	N	S_1 (Trend/Plunge)	S_2 (Trend/Plunge)	S_3 (Trend/Plunge)	R	S_{Hmax}
1	-43.94	169.67	12.7	25	134.1/76	82.3/22	39.9/74	0.1 (-0.2/+0.2)	130.8 (-14.7/+14.2)
2	-43.26	170.88	13.4	89	122.4/80	107.0/10	32.0/87	0.8 (-0.1/+0.1)	122.3 (-11.2/+10.7)
3	-43.59	170.58	11.1	105	119.8/89	33.9/7	29.7/83	1.0 (-0.1/+0.0)	120.0 (-10.9/+10.5)
4	-43.51	170.3	5.8	77	116.6/87	7.7/9	27.0/82	0.7 (-0.1/+0.1)	116.7 (-11.2/+10.7)
5	-43.03	171.44	12.3	17	116.7/72	93.4/20	24.3/83	0.6 (-0.4/+0.3)	115.7 (-16.6/+16.2)
6	-43.51	171.0	10.0	66	113.2/87	30.2/21	22.1/69	0.8 (-0.2/+0.1)	113.1 (-11.4/+11.1)
7	-43.95	170.45	11.4	12	128.5/83	70.7/14	37.0/79	0.7 (-0.4/+0.3)	127.9 (-19.9/+19.2)
8	-44.05	170.04	7.6	16	122.1/90	50.4/2	32.1/89	0.8 (-0.2/+0.1)	122.1 (-16.6/+16.5)
9	-43.17	170.99	14.4	70	133.1/84	134.8/6	43.1/90	0.4 (-0.2/+0.2)	133.2 (-11.8/+11.4)
10	-43.6	169.86	5.7	28	114.8/85	18.1/39	29.0/52	0.6 (-0.3/+0.3)	115.2 (-19.2/+18.5)
11	-43.42	170.43	9.9	33	130.5/73	107.8/18	38.5/83	0.3 (-0.2/+0.2)	129.0 (-12.9/+12.5)
12	-44.38	168.93	24.4	3	-	-	-	-	-
13	-43.16	170.77	12.1	50	125.3/76	124.0/14	35.2/90	0.5 (-0.2/+0.2)	125.2 (-12.7/+12.3)
14	-43.21	171.2	6.1	17	127.9/90	27.1/3	37.9/87	0.4 (-0.3/+0.4)	128.1 (-17.7/+17.2)
15	-43.5	170.07	5.3	30	110.2/73	16.1/77	69.1/22	0.5 (-0.3/+0.3)	116.0 (-26.0/+28.6)
16	-44.04	169.67	19.4	29	118.3/81	94.0/10	27.7/86	0.5 (-0.3/+0.3)	118.0 (-13.6/+13.2)
17	-43.47	171.29	20.0	9	126.8/88	47.1/11	36.4/79	0.8 (-0.3/+0.2)	126.6 (-17.5/+17.3)
18	-43.43	170.66	13.9	50	123.9/89	107.9/1	33.9/90	0.5 (-0.2/+0.2)	123.9 (-11.7/+11.1)
19	-43.32	170.76	15.3	96	113.4/79	126.3/12	23.9/87	0.4 (-0.2/+0.2)	113.8 (-11.1/+10.8)
20	-42.79	171.28	3.2	11	109.9/84	18.3/75	41.4/16	0.5 (-0.4/+0.4)	111.2 (-35.7/+34.1)

Text C3: Normal and shear stress component calculations along the Alpine Fault

We wish to compute the components of shear and normal stress acting on the Alpine Fault at various locations, and make use of three right–handed coordinate systems defined as follows:

1. Principal stress coordinates (**S**), with axes ($\hat{s}_1$, $\hat{s}_2$, $\hat{s}_3$) corresponding to the maximum, intermediate, and minimum compressive stresses, respectively;
2. Fault coordinates (**F**), with axes ($\hat{f}_1$,$\hat{f}_2$,$\hat{f}_3$) = ($\hat{f}_\theta$,$\hat{f}_\delta$,$\hat{f}_\theta \times \hat{f}_\delta$) corresponding to the strike vector, down–dip vector, and downward–pointing fault normal $\hat{n} = \hat{f}_\theta \times \hat{f}_\delta$, respectively.
3. Geographic coordinates (**G**), with axes ($\hat{g}_1$,$\hat{g}_2$,$\hat{g}_3$) = ($\hat{N}$,$\hat{E}$,$\hat{D}$) corresponding to the north, east, and down directions, respectively.

Focal mechanism stress inversions, obtained using the Bayesian approach of *Arnold and Townend* (2007), yield a reduced form of the stress tensor $\mathbf{S} = 1/(\mathrm{S}_1 - \mathrm{S}_3)[\mathbf{S} - \mathrm{S}_3\ \mathbf{I}]$ that depends only on the stress ratio $R = (\mathrm{S}_1 - \mathrm{S}_2)/(\mathrm{S}_1 - \mathrm{S}_3)$ and the three angles specifying the orientations of the principal stress axes. With respect to principal stress coordinates, the reduced stress tensor is:

$$\mathbf{S}_S = \begin{pmatrix} 1 & 0 & 0 \\ 0 & 1-R & 0 \\ 0 & 0 & 0 \end{pmatrix}$$

For simplicity, we omit reference to the word "reduced" and refer to $\mathbf{S}_S$ as the stress tensor.

The stress tensor is expressed in the principal stress axes (**S**) coordinate system and specifically by the orientations of the three principal stress axes $\hat{s}_1$, $\hat{s}_2$ and $\hat{s}_3$.

We construct two transformation matrices that relate geographic and principal stress coordinates ($\mathbf{R}_{GS}$) and geographic and fault coordinates ($\mathbf{R}_{GF}$) to transform the stress tensor into the fault coordinates defined above, via geographic coordinates. These matrices are defined so that, for example, a vector specified with respect to principal stress coordinates, $\mathbf{x}_S$ is represented with respect to geographic coordinates as $\mathbf{x}_G = \mathbf{R}_{GS}\ \mathbf{x}_S$. The transformation matrix $\mathbf{R}_{GS}$ between **S** and **G** is an orthogonal matrix with columns that are the representations of $\hat{s}_1$, $\hat{s}_2$, and $\hat{s}_3$ with respect to **G**. Similarly, the transformation matrix $\mathbf{R}_{GF}$ between **F** and **G** is the orthogonal matrix with columns that are representations of $\hat{f}_1$, $\hat{f}_2$, and $\hat{f}_3$ with respect to **G**. Accordingly,

$$\mathbf{R}_{GS} = \begin{pmatrix} \hat{s}_1 & \hat{s}_2 & \hat{s}_3 \end{pmatrix}_G = \begin{pmatrix} \cos t_1 \cos p_1 & \cos t_2 \cos p_2 & \cos t_3 \cos p_3 \\ \sin t_1 \cos p_1 & \sin t_2 \cos p_2 & \sin t_3 \cos p_3 \\ \sin p_1 & \sin p_2 & \sin p_3 \end{pmatrix}$$

where t_i and p_i are the trend and plunge of the ith principal stress, and

$$\mathbf{R}_{GF} = \begin{pmatrix} \hat{f}_1 & \hat{f}_2 & \hat{f}_3 \end{pmatrix}_G = \begin{pmatrix} \cos\theta & -\sin\theta\cos\delta & \sin\theta\sin\delta \\ \sin\theta & \cos\theta\cos\delta & -\cos\theta\cos\delta \\ 0 & \sin\delta & \cos\delta \end{pmatrix}$$

where θ and δ are the strike and dip of the fault.

Using these rotation matrices, we can express $\mathbf{S}$ with respect to fault coordinates via successive rotations:

$$\begin{aligned} \mathbf{S}_F &= \mathbf{R}_{FG}\mathbf{S}_G\mathbf{R}_{FG}^T \\ &= \mathbf{R}_{GF}^T\mathbf{S}_G\mathbf{R}_{GF} \\ &= \mathbf{R}_{GF}^T\mathbf{R}_{GS}\mathbf{S}_G\mathbf{R}_{GS}^T\mathbf{R}_{GF} \end{aligned}$$

We assume an average strike of θ=55° and a dip of δ=50° proposed by *Guo et al.* (2017) based on the presence of velocity contrasts and the alignment of Fault Zone Guided Wave earthquakes. The normal unit vector on the inferred plane of the fault is defined by the following:

$$\hat{n}_G = \mathbf{R}_{GF} \cdot \hat{n}_F = \begin{pmatrix} \cos\theta & -\sin\theta\cos\delta & \sin\theta\sin\delta \\ \sin\theta & \cos\theta\cos\delta & -\cos\theta\cos\delta \\ 0 & \sin\delta & \cos\delta \end{pmatrix} \begin{pmatrix} 0 \\ 0 \\ 1 \end{pmatrix}$$

That gives the normal vector, $\hat{n}_G$, of the inferred plane for the Alpine Fault in respect to the geographic coordinate system that is in the following formula.

$$\hat{n}_G = (n_N, n_E, n_D) = \begin{pmatrix} \sin\theta\sin\delta \\ -\cos\theta\sin\delta \\ \cos\delta \end{pmatrix}$$

Using Cauchy's formula we then compute the traction vector on the normal unit vector $\hat{n}_G$ of the inferred Alpine Fault plane.

$$T = \hat{n}_G \cdot \mathbf{S}_S$$

We can now compute the normal stress component, σ_n, on the inferred fault plane using the following equation:

$$\sigma_n = \sqrt{T \cdot \hat{n}_G}$$

The shear stress component vector, τ_n, on the inferred fault plane can be calculated using

the following:

$$\begin{aligned}\hat{\tau}_i &= T - \sigma_n \cdot \hat{n}_G \\ &= T - T \cdot \hat{n}_G \hat{n}_G\end{aligned}$$

The magnitude of the shear stress component can be given by:

$$\tau_n = \sqrt{(\tau_1^2 + \tau_2^2 + \tau_3^2)}$$

Data Set C1.

Dataset C1. Dataset C1 of the electronic appendices contains the focal mechanism information of the relocated earthquake locations, constructed using the methods described in the main article.

1. YYYY – Year
2. MM – Month
3. DD – Day
4. HH – Hours (UTC time)
5. MM – Minutes (UTC time)
6. SS – Seconds (UTC time)
7. Lat – Latitude in degrees
8. Lon – Longitude in degrees
9. Depth – Hypocentral depth in kilometers
10. Mag – Local magnitude calculated
11. Str – Strike of the first nodal plane of the focal mechanism in degrees
12. Dip – Dip of the first nodal plane of the focal mechanism in degrees
13. Rak – Rake of the first nodal plane of the focal mechanism in degrees
14. Fme – Error estimation of the focal mechanism
15. Hor unc – Horizontal uncertainty obtained by 200 bootstraps
16. Ver unc – Vertical uncertainty obtained by 200 bootstraps

D Supporting Information for Chapter 5: "Crustal thermal structure and exhumation rates near the central Alpine Fault"

Introduction

The section here contains five figures and a table that summarise initial processing steps that are described with detail in Chapter 5. The analytical solution of the 1-D thermal profile is also provided here.

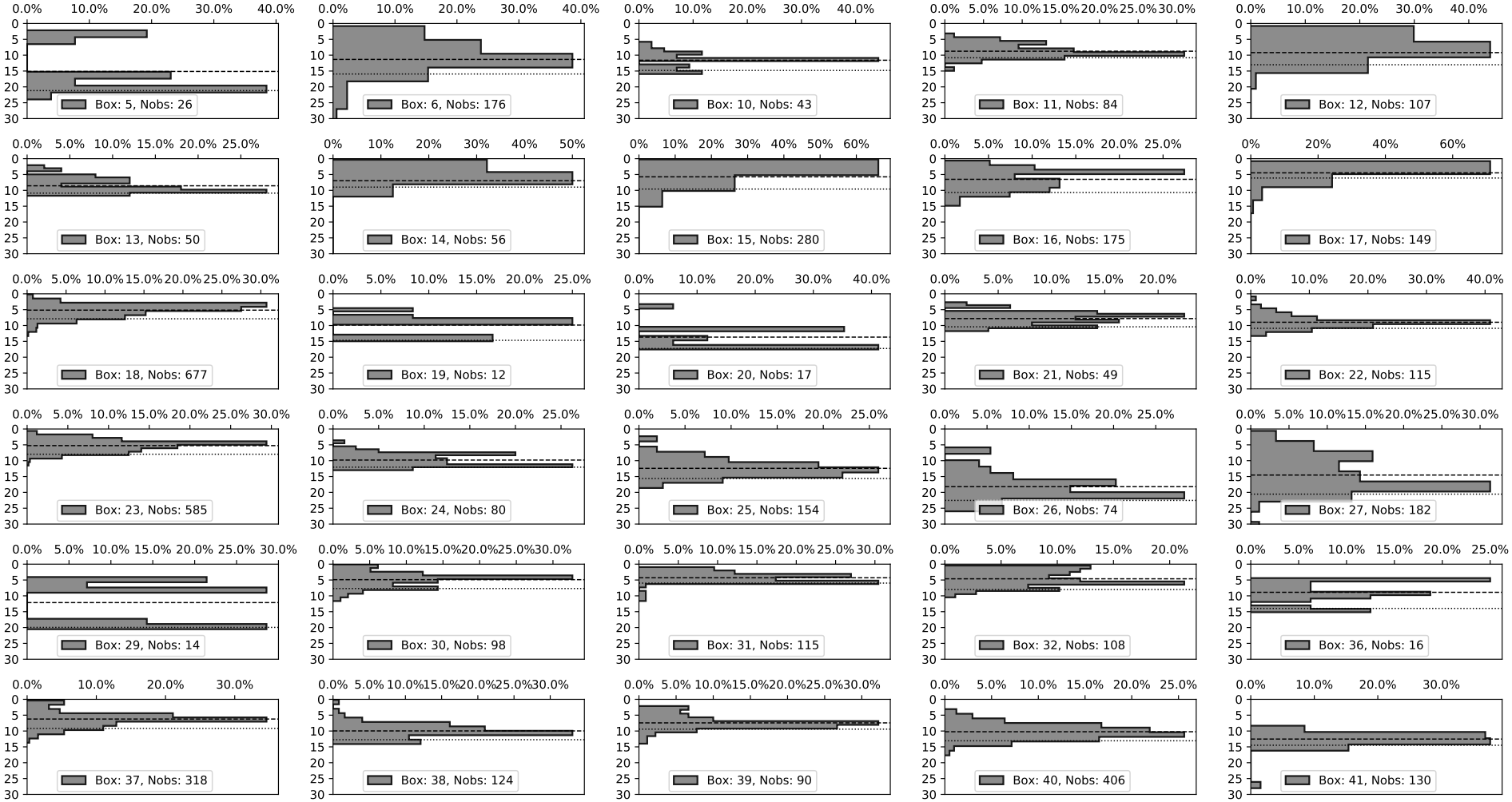

Figure D1: Earthquake hypocentral depth histograms I

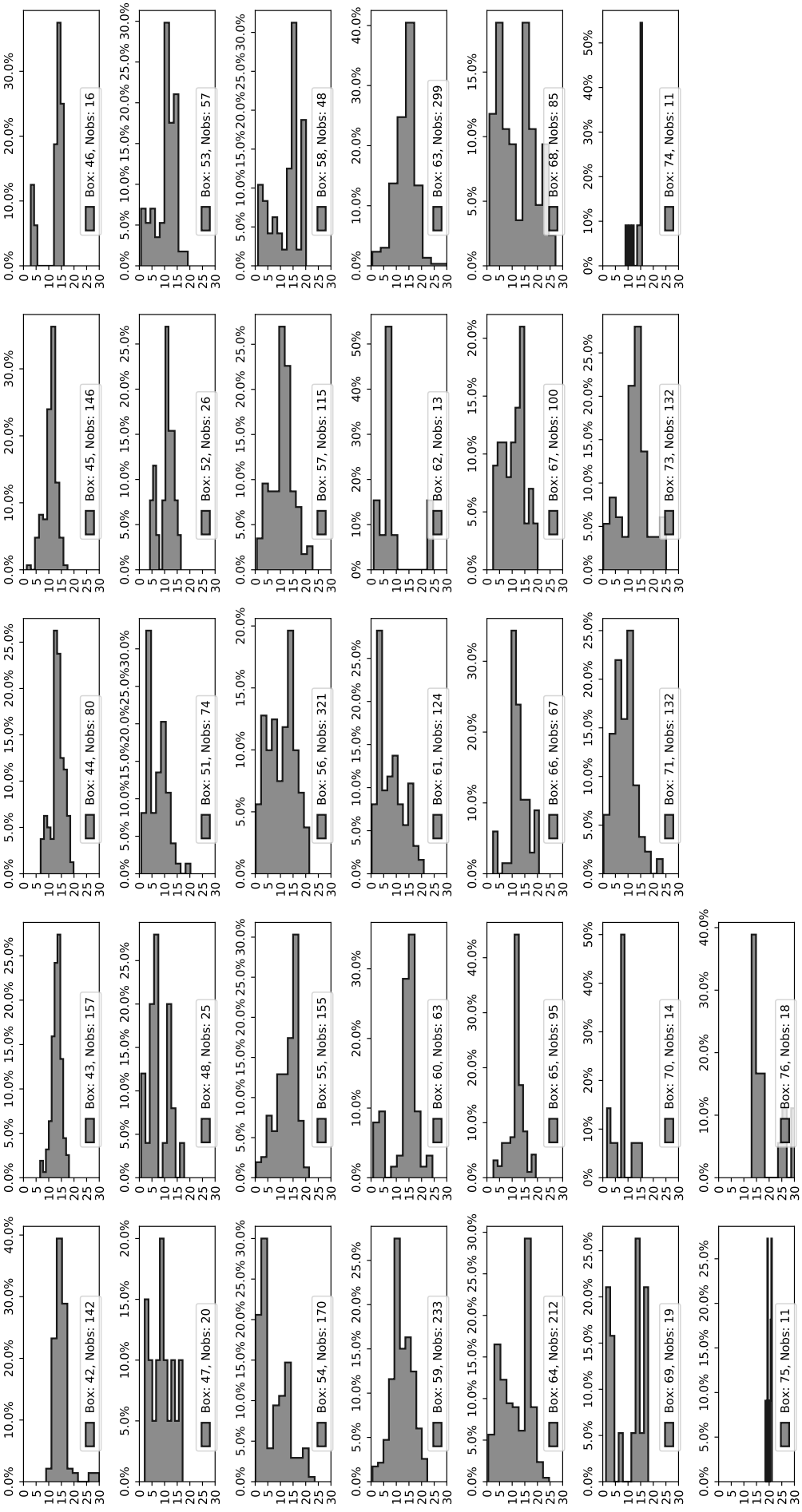

Figure D2: Earthquake hypocentral depth histograms II

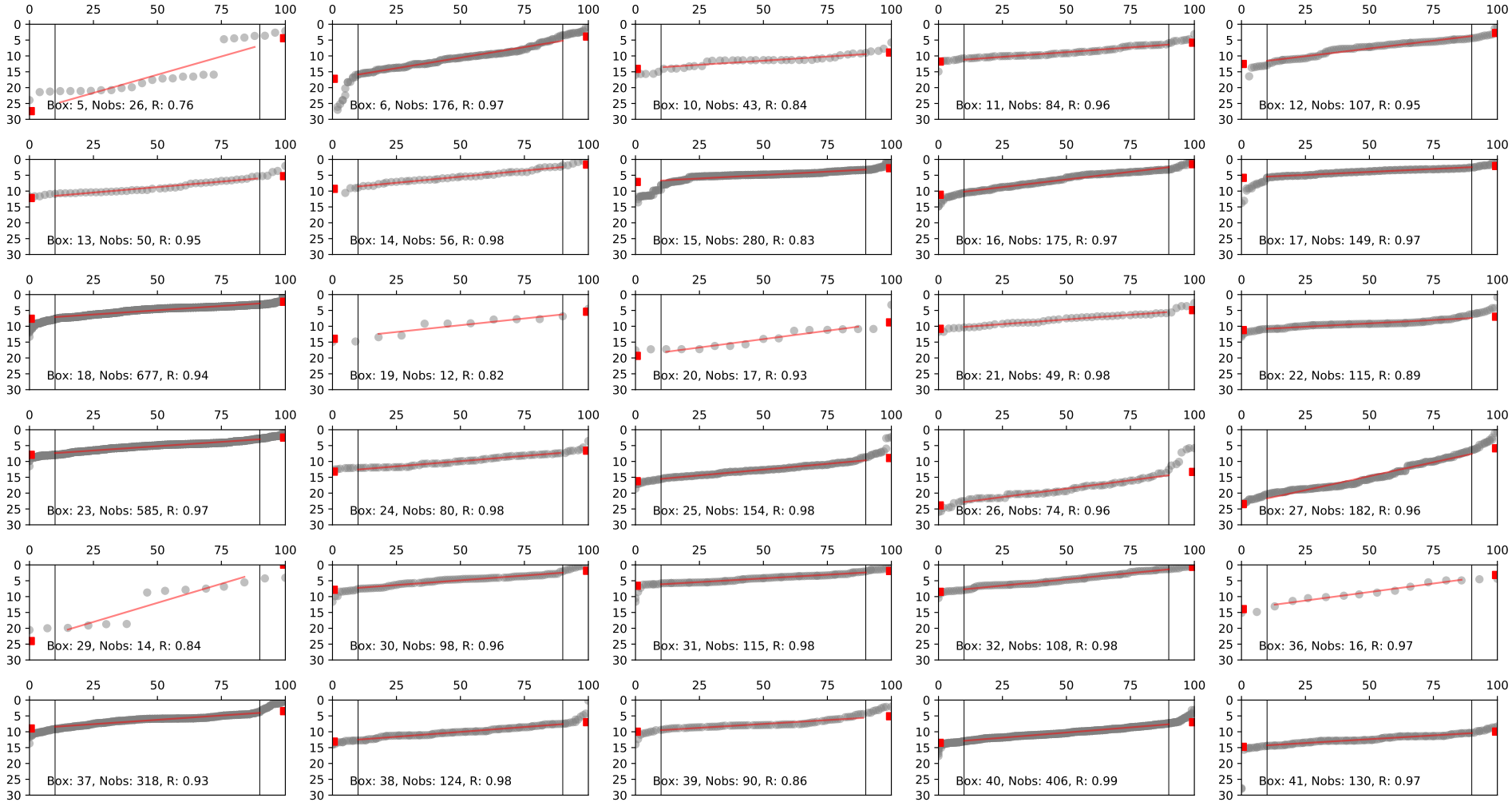

Figure D3: Cumulative distribution function of hypocentral depths that have at least 10 observations (boxes 1-30). Red line depicts a linear regression line that fits the 10 to 90 % interval of the data. Red squares show the z0 and z100 predicted values from the linear regression lines.

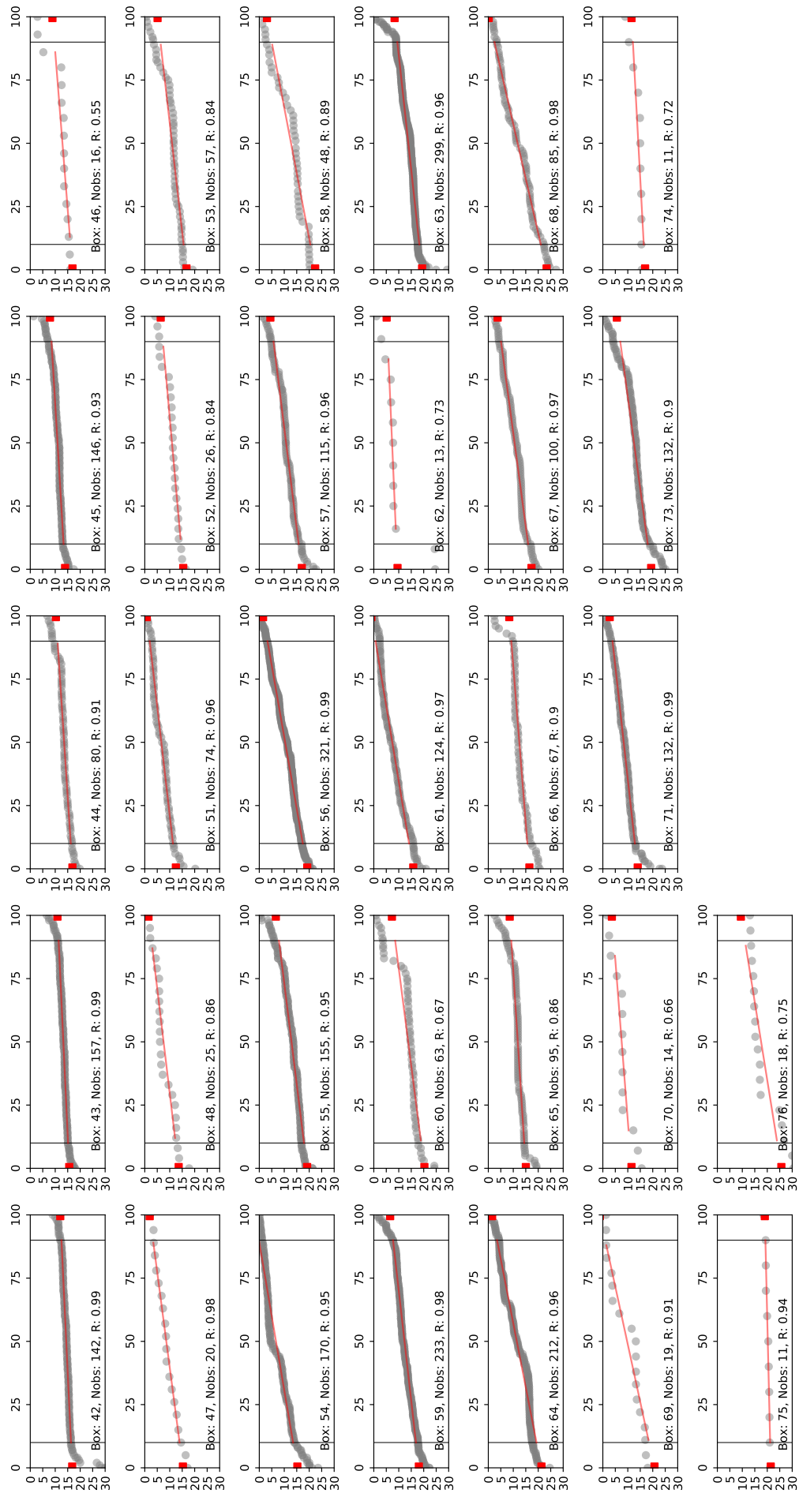

Figure D4: Cumulative distribution function of hypocentral depths that have at least 10 observations (boxes 31-61). Red line depicts a linear regression line that fits the 10 to 90 % interval of the data. Red squares show the z0 and z100 predicted values from the linear regression lines.

Text D1: Temperature profile with depth calculations

The 1-D thermal structure used in the present thesis (Chapter 5) is described by the following second-order differential equation:

$$\kappa\frac{d^2T}{dz^2} + Cv\frac{dT}{dz} + H = C\frac{dT}{dt} \tag{D.1}$$

where T is the temperature, z is the vertical distance, t is the time, κ is the thermal conductivity, C is the volumetric heat capacity, H is the volumetric heat productivity, and v is the exhumation rate. Assuming steady state, a solution has the following form:

$$\kappa\frac{d^2T}{dz^2} - Cv\frac{dT}{dz} = -H \tag{D.2}$$

Trying a solution of the form $T = Ae^{rz}$ yields the auxilary equation

$$\kappa r^2 - Cvr = 0 \tag{D.3}$$

which has the two roots $r = 0, \frac{Cv}{\kappa}$ and hence the complementary function is determined to have the following form:

$$T_c = A_1 + A_2 e^{\frac{Cv}{\kappa}z} \tag{D.4}$$

Substitution in Equation D.2 yields the general solution:

$$T = A_1 + A_2 e^{\frac{Cv}{\kappa}z} + \frac{H}{Cv}z \tag{D.5}$$

This can be verified in the following way:

$$\begin{aligned} \frac{dT}{dz} &= A_2\frac{Cv}{\kappa}e^{\frac{Cv}{\kappa}z} + \frac{H}{Cv} \\ \frac{d^2T}{dz^2} &= A_2\frac{C^2v^2}{\kappa^2}e^{\frac{Cv}{\kappa}z} \\ \kappa\frac{d^2T}{dz^2} - Ckv\frac{dT}{dz} &= A_2\frac{C^2v^2}{\kappa}e^{\frac{Cv}{\kappa}z} - Cv(A_2\frac{Cv}{\kappa}e^{\frac{Cv}{\kappa}z} + \frac{H}{Cv}) = -H \end{aligned} \tag{D.6}$$

Applying the boundary conditions $z = z_0$ and $T = T_0$ yields:

$$T_0 = A_1 + A_2 e^{\frac{Cv}{\kappa}z_0} + \frac{H}{Cv}z_0 \tag{D.7}$$

and $z = z_1$ and $T = T_1$ yields:

$$T_1 = A_1 + A_2 e^{\frac{Cv}{\kappa} z_1} + \frac{H}{Cv} z_1 \tag{D.8}$$

Subtracting Equation D.7 from D.8 we obtain the following:

$$T_1 - T_0 = A_2 (e^{\frac{Cv}{\kappa} z_1} - e^{\frac{Cv}{\kappa} z_0}) + \frac{H}{Cv} (z_1 - z_0) \tag{D.9}$$

$$A_2 = \frac{(T_1 - T_0) - \frac{H}{Cv}(z_1 - z_0)}{e^{\frac{Cv}{\kappa} z_1} - e^{(\frac{Cv}{\kappa} z_0)}} \tag{D.10}$$

and from Equation D.7

$$A_1 = T_0 - A_2 e^{(\frac{Cv}{\kappa} z_0)} - \frac{H}{Cv} z_0 \tag{D.11}$$

Figure D5.

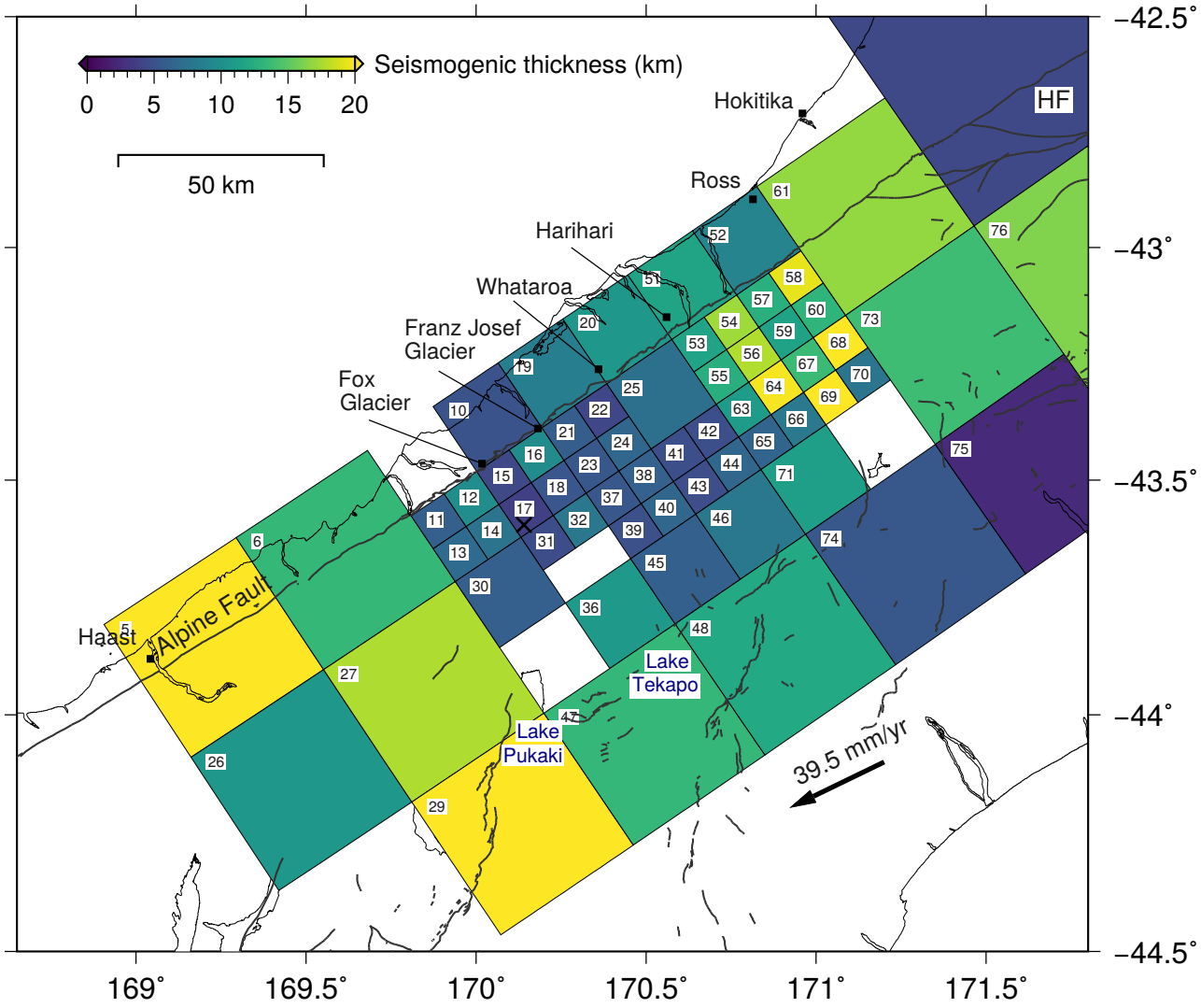

Figure D5: Map showing the spatial distribution of the difference between the lower cut-off depths and the upper cut-off depths of the seismicity, which represents the thickness of the seismogenic part of the crust near the central Alpine Fault.

Table D1.

Table D.1: Details of the linear regression lines parameters obtained for boxes with enough observations. Parameter bin is the number of the bin obtained using the quadtree gridding algorithm. N is the number of the observations within each box. z_0 and z_{100} are respectively the predicted lower and upper cutoff hypocentral depths for each box. The line of the slopes gives an indication of the thickness of the seismogenic part of the crust within each box.

Bin	N	Upper	Lower	Line slope	Uplift
6	176	3.88	17.21	-0.13	3.03
11	84	5.83	11.79	-0.06	4.23

12	107	2.76	12.54	-0.1	3.83
13	50	5.28	12.19	-0.07	3.93
14	56	1.64	9.29	-0.08	5.95
15	280	2.77	7.11	-0.04	8.36
16	175	1.51	11.16	-0.1	4.54
17	149	2.07	5.82	-0.04	10.78
18	677	2.27	7.63	-0.05	7.66
21	49	4.91	10.8	-0.06	4.74
22	115	6.99	11.2	-0.04	4.54
23	585	2.47	7.91	-0.05	7.26
24	80	6.6	13.22	-0.07	3.43
25	154	8.93	16.23	-0.07	2.32
26	74	13.31	23.88	-0.11	1.11
27	182	5.86	23.47	-0.18	1.21
30	98	1.86	7.85	-0.06	7.36
31	115	1.92	6.58	-0.05	9.17
32	108	0.61	8.49	-0.08	6.65
37	318	3.49	8.96	-0.05	6.15
38	124	6.97	13.1	-0.06	3.53
39	90	5.1	9.97	-0.05	5.34
40	406	6.99	13.5	-0.07	3.33
41	130	9.94	14.75	-0.05	2.82
42	142	12.02	16.8	-0.05	2.12
43	157	10.89	15.61	-0.05	2.52
44	80	10.27	16.88	-0.07	2.12
45	146	7.9	13.95	-0.06	3.13
53	57	5.13	16.71	-0.12	2.12
54	170	-1.87	15.25	-0.17	2.62
55	155	6.64	19.17	-0.13	1.41
56	321	1.52	19.21	-0.18	1.41
57	115	4.44	17.04	-0.13	2.02
58	48	3.06	22.38	-0.19	0.51
59	233	6.55	18.05	-0.11	1.72
60	63	7.26	20.28	-0.13	1.11
61	124	-0.99	15.8	-0.17	2.42
63	299	8.33	19.34	-0.11	1.31
64	212	1.52	21.3	-0.2	0.81
65	95	8.57	15.04	-0.06	2.72
66	67	8.4	16.46	-0.08	2.22
67	100	3.73	17.3	-0.14	1.92
68	85	0.14	23.36	-0.23	0.21

71	132	2.76	13.97	-0.11	3.13
73	132	5.62	19.36	-0.14	1.31

E Polarity tests

First motion polarities are critical for an accurate determination of fault plane solutions. Hence, we need to be very careful and check that the polarities recorded by all instruments are correct (not reversed). As some instruments may have been wrongly plugged, resulting in systematically wrong polarities.

The composite seismic network used in the present study comprises of 74 seismic sites from five different temporary arrays (SAMBA, ALFA-08, DFDP-10, DFDP-13 and WIZARD) and five GeoNet seismic sites. These temporary arrays operated in different time periods from late 2008 to early 2017. Information about the instrument's orientations is available in their dataless seed files obtained from IRIS–DMC (Incorporated Research Institutions for Seismology Data Management Center). We found a number of sites with reversed polarities. All DFDP10 sensors were found with reversed polarities in addition to four SAMBA sites (southern sites; COVA, MTBA, SOLU, LARB). Also, the ten short period instruments from WIZARD are also reversed.

We have an initial estimation of whether a seismometer is reversed or not. To make sure that these information are correct we also compare the first onsets at all seismic sites from teleseismic events. We looked through a number of teleseismic events that occurred from late 2008 to early 2017 had a minimum magnitude of 6.5 and lied within the following coordinates (Latitude from -50 to 20 and longitude from 110 to 180; Fig. E.1).

Polarity tests for DFDP10 and all SAMBA sites (apart from MTBA, SOLU and LARB) have already been tested by the previous PhD study of Carolin Boese. Consequently, we know that the DFDP-10 array sensors (short-period Mark Products L22-3D), deployed from January to May 2010, had reversed vertical-component polarities. The surface SAMBA seismic sensors (Mark Products L4-3D) temporary installed at Whataroa and Potters Creek (WHAT, POCR) were also found to have reversed vertical components. One of these senors was later deployed at Copland Valley seismic site (COVA), so this site has reversed polarities compared to the rest of the SAMBA sites.

To check the polarities of the ALFA network seismic sites we use the first onsets from the Mindanao region (Philippines) earthquake on October 4, 2009 with a magnitude of M = 6.6 M_w (Fig. E.2). All polarities at the ALFA-08 sites are consistent with the ones from the SAMBA and GeoNet sites (Fig. E.3). We next use another teleseismic earthquake, that occurred in the Banda Sea region (Indonesia) on December 10, 2012 with a magnitude of M = 7.1 M_w, to examine the polarity recordings from the WIZARD seismic sites (Fig. E.4). Broadband WIZARD seismic sites are consistent with the SAMBA seismic sites (Fig. E.5)

while the short-period seismic sites either show ambiguous first onsets or are reversed.

Finally to test the consistency of the DFDP-10 and DFDP-13 seismic sites polarity recordings we use the first onsets from a number of blasts from the Whataroa quarry (Fig. E.6 and E.7) due to their proximity to the quarry. All four DFDP-13 seismic sites show consistent polarities when compared to the SAMBA sites, while a number of DFDP-10 seismic sites are found to give reversed polarities.

Polarity recordings could not be picked reliably due to noisy conditions from the following sites: REYN, MTFE, ROTO and NOLA.

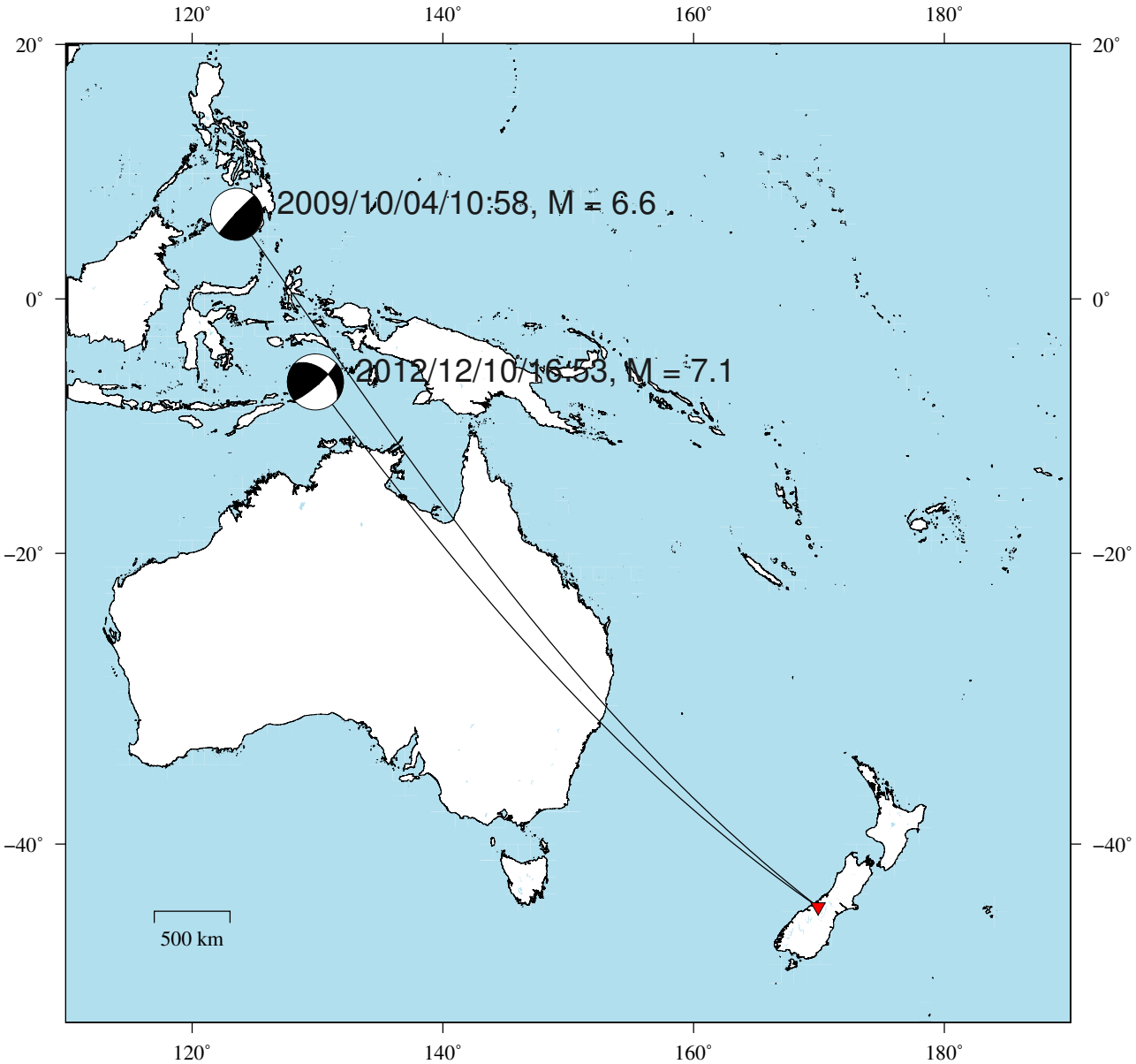

Figure E.1: Earthquake locations and focal mechanism solutions for teleseismic events used for polarity tests.

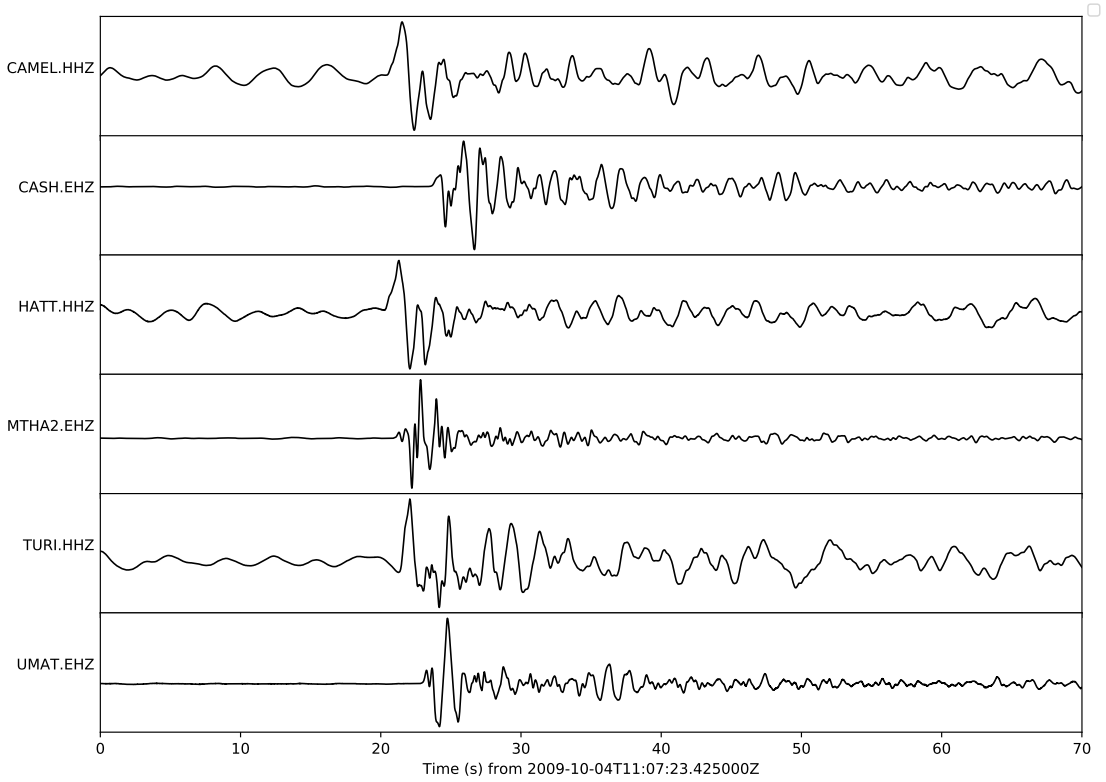

Figure E.2: Unfiltered waveforms from ALFA-08 seismic sites showing the first arrivals of the teleseismic event that occurred in the Mindanao region (Philippines), at 10:58 (UTC) on October 4, 2009, with a moment magnitude of 6.6 M_w.

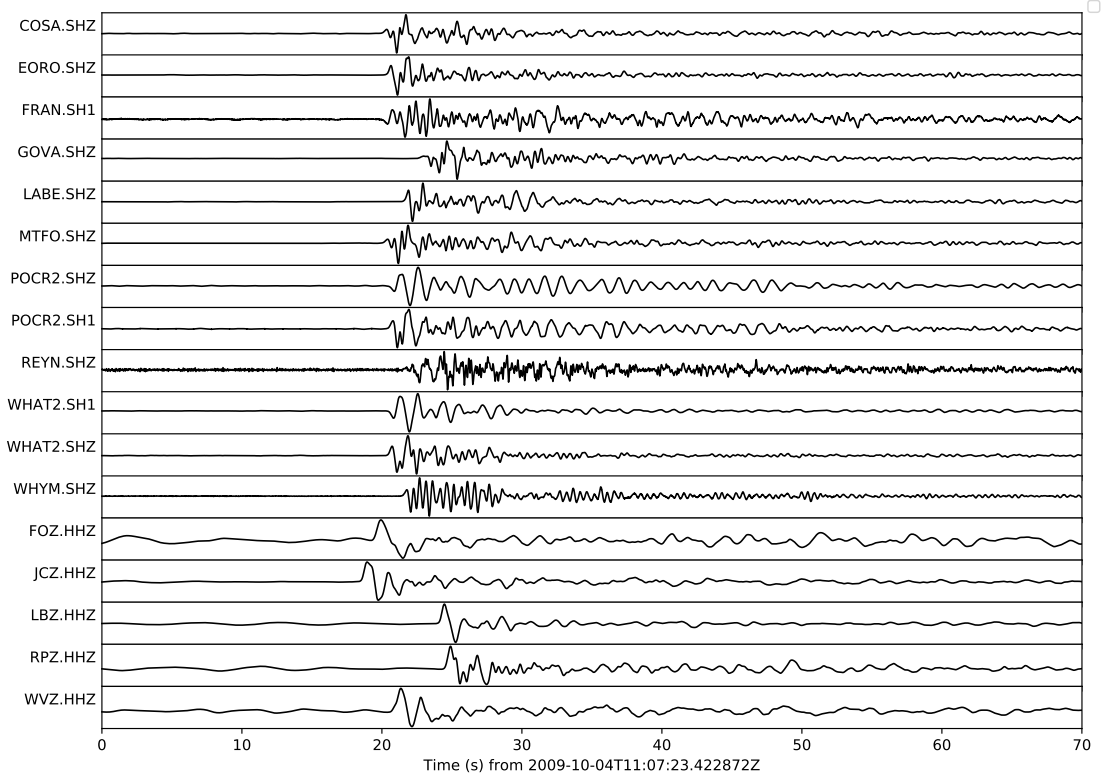

Figure E.3: Unfiltered waveforms from SAMBA and GeoNet seismic sites showing the first arrivals of the teleseismic event that occurred in the Mindanao region (Philippines), at 10:58 (UTC) on October 4, 2009, with a moment magnitude of 6.6 M_w.

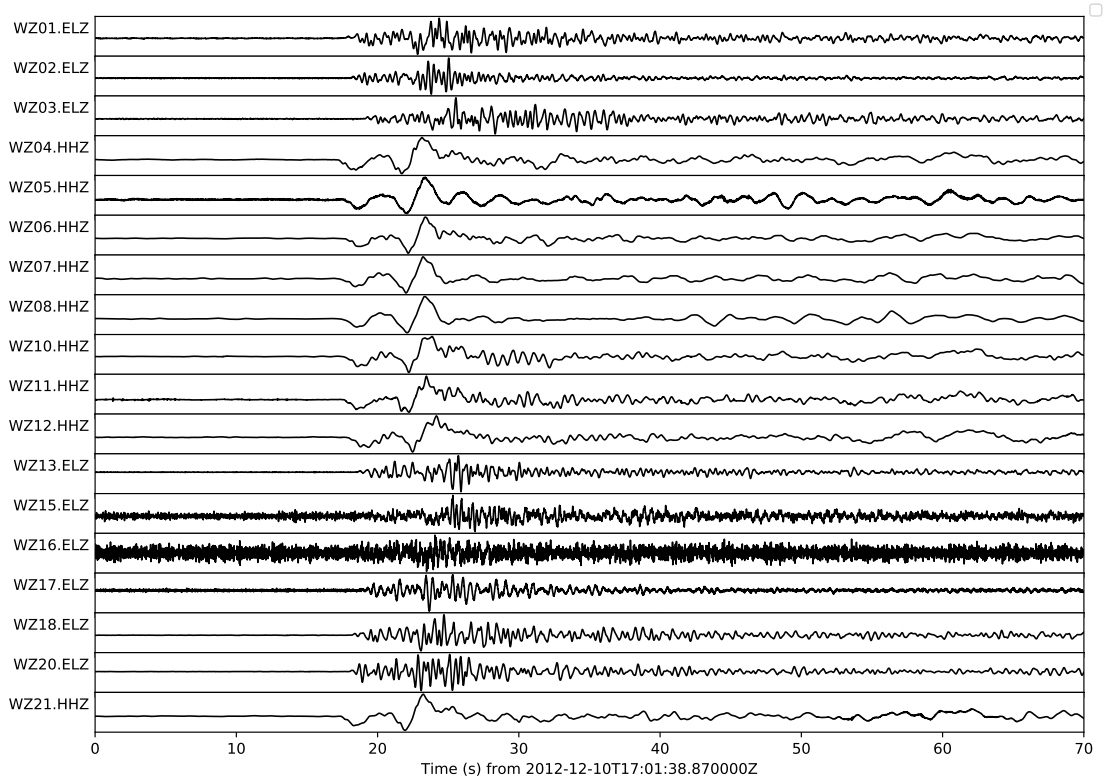

Figure E.4: Unfiltered waveforms from WIZARD seismic sites showing the first arrivals of the teleseismic event that occurred in the Banda Sea region (Indonesia), at 16:53 (UTC) on December 10, 2012, with a moment magnitude of 7.1 M_w.

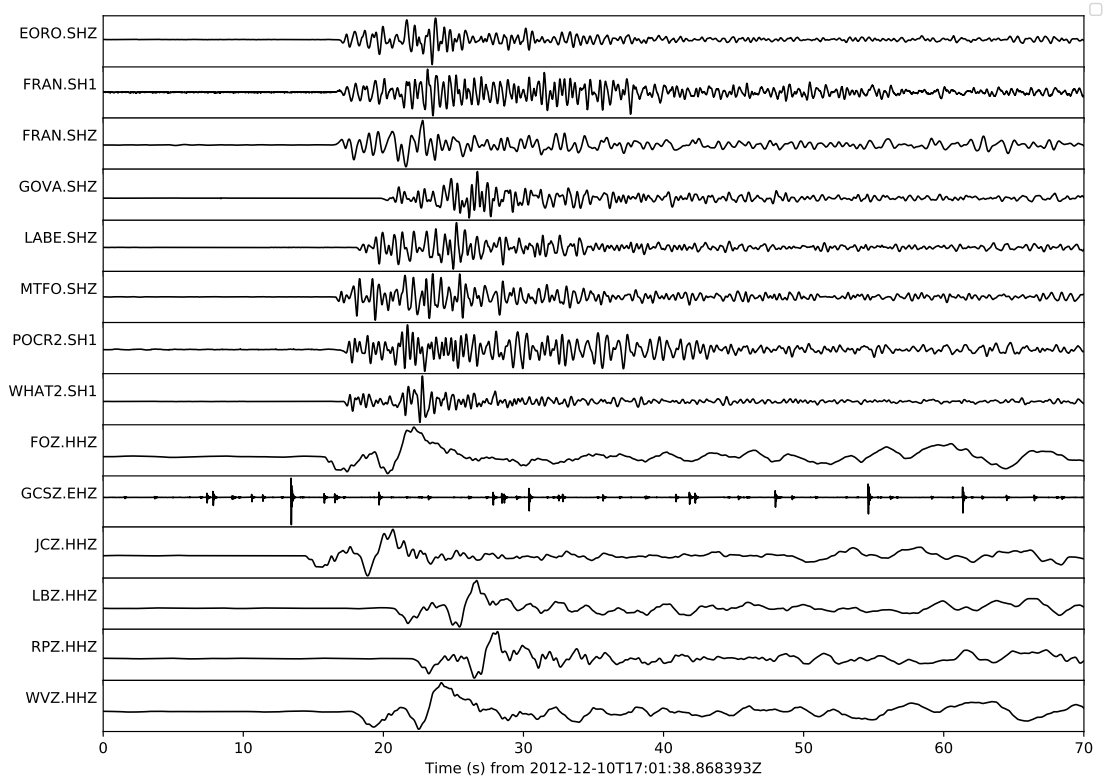

Figure E.5: Unfiltered waveforms from SAMBA and GeoNet seismic sites showing the first arrivals of the teleseismic event that occurred in the Banda Sea region (Indonesia), at 16:53 (UTC) on December 10, 2012, with a moment magnitude of 7.1 M_w.

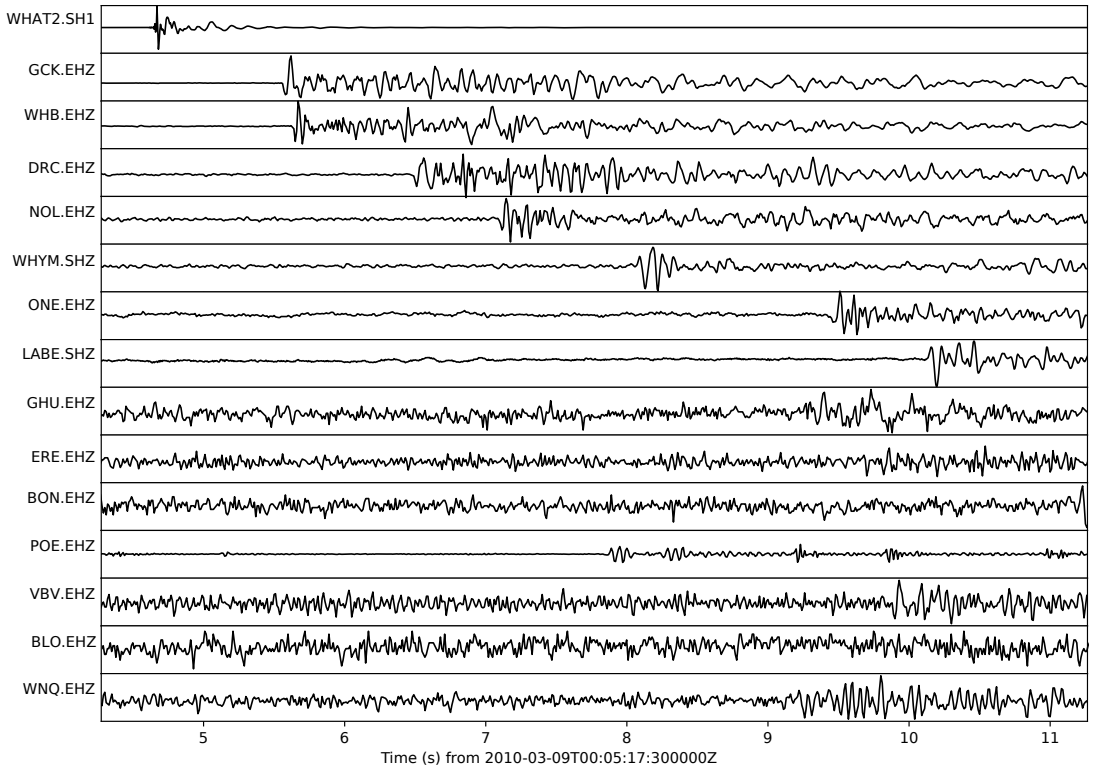

Figure E.6: First arrivals from blast in Whataroa quarry I

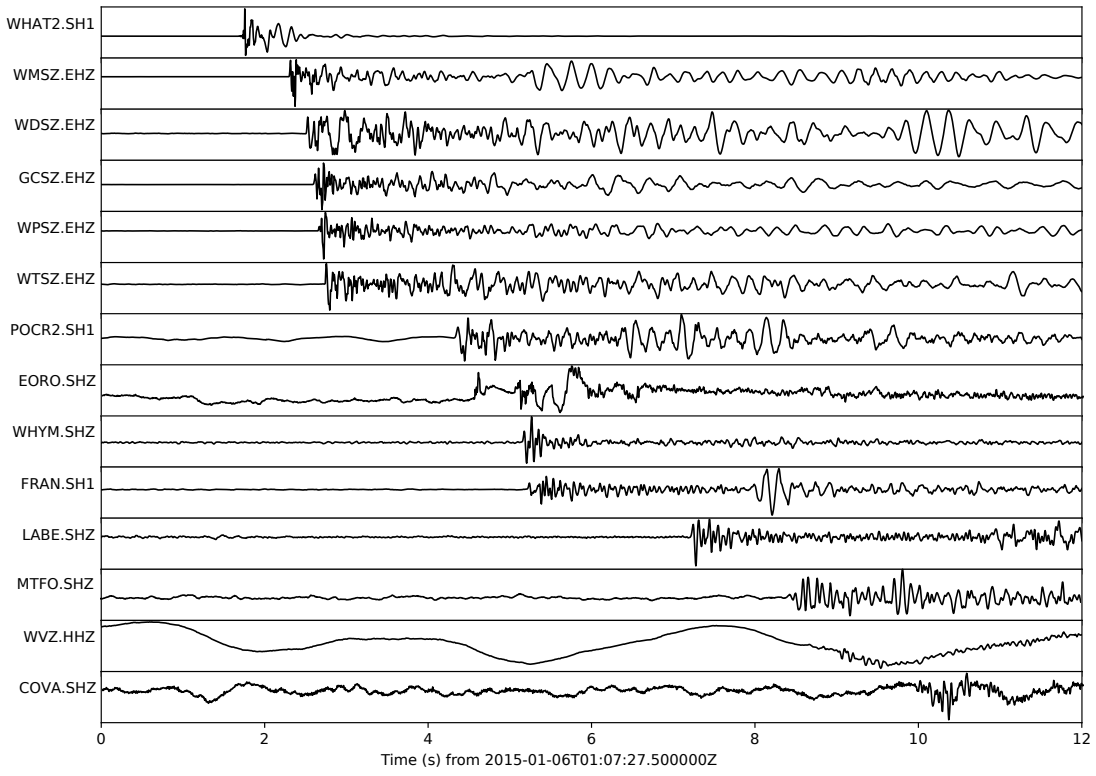

Figure E.7: First arrivals from blast in Whataroa quarry II

Bibliography

Adams, C. J., Uplift rates and thermal structure in the Alpine Fault Zone and Alpine Schists, Southern Alps, New Zealand, *Geological Society Special Publication*, *9*, 211–222, doi:10.1144/GSL.SP.1981.009.01.19, 1981.

Adams, J., Paleoseismicity of the Alpine Fault seismic gap, *Geology*, *8*, 72–76, 1980.

Aki, K., and P. G. Richards, *Quantitative seismology*, 2002.

Albaric, J., J. Déverchère, C. Petit, J. Perrot, and B. Le Gall, Crustal rheology and depth distribution of earthquakes: Insights from the central and southern East African Rift System, *Tectonophysics*, *468*(1-4), 28–41, doi:10.1016/j.tecto.2008.05.021, 2009.

Allen, R. V., Automatic earthquake recognition and timing from single traces, *Bulletin of the Seismological Society of America*, *68*(5), 1521–1532, 1978.

Allis, R. G., and Y. Shi, New insights to temperature and pressure beneath the central Southern Alps, New Zealand, *New Zealand Journal of Geology and Geophysics*, *38*(4), 585–592, doi:10.1080/00288306.1995.9514687, 1995.

Allis, R. G., R. Henley, and A. Carman, *The thermal regime beneath the Southern Alps*, 79–85 pp., Royal Society of New Zealand, Wellington, 1979.

Anderson, H., and T. Webb, New Zealand seismicity: Patterns revealed by the upgraded National Seismograph Network, *New Zealand Journal of Geology and Geophysics*, *37*(4), 477–493, doi:10.1080/00288306.1994.9514633, 1994.

Anderson, H., T. Webb, and J. Jackson, Focal mechanisms of large earthquakes in the South Island of New Zealand, *Geophysical Journal International*, *115*, 1032–1054, 1993.

Angelier, J., Determination of the mean principal directions of stresses for a given fault population, *Tectonophysics*, *56*(3-4), doi:10.1016/0040-1951(79)90081-7, 1979.

Arabasz, W. J., and R. Robinson, Microseismicity and geologic structure in the northern south island, new zealand, *New Zealand Journal of Geology and Geophysics*, *19*(5), 569–601, doi:10.1080/00288306.1976.10426309, 1976.

Arnold, R., and J. Townend, A Bayesian approach to estimating tectonic stress from seismological data, *Geophys. J. Int., 170*, *1336-1256,*, 2007.

Baillard, C., W. C. Crawford, V. Ballu, C. Hibert, and A. Mangeney, An automatic kurtosis-based P- and S- phase picker designed for local seismic networks, *Bulletin of the Seismological Society of America*, *104*, 394–409, doi:10.1785/0120120347An, 2014.

Bakun, W. H., and A. G. Lindh, Local magnitudes, seismic moments, and coda durations for earthquakes near Oroville, California, *Bulletin of the Seismological Society of America*, *67*(3), 615–629, 1977.

Balfour, N. J., M. K. Savage, and J. Townend, Stress and crustal anisotropy in Marlborough, New Zealand: Evidence for low fault strength and structure-controlled anisotropy, *Geophysical Journal International*, *163*(3), 1073–1086, doi:10.1111/j.1365-246X.2005.02783.x, 2005.

Baratin, L.-M., C. J. Chamberlain, J. Townend, and M. K. Savage, Focal mechanisms and inter-event times of low-frequency earthquakes reveal quasi-continuous deformation and triggered slow slip on the deep Alpine Fault, *Earth and Planetary Science Letters*, *484*, 111–123, doi:10.1016/j.epsl.2017.12.021, 2018.

Barnes, P. M., R. Sutherland, and J. Delteil, Strike-slip structure and sedimentary basins of the southern Alpine Fault, Fiordland, New Zealand, *Bulletin of the Geological Society of America*, *117*(3-4), 411–435, doi:10.1130/B25458.1, 2005.

Barth, N. C., C. Boulton, B. M. Carpenter, G. E. Batt, and V. G. Toy, Slip localization on the southern Alpine Fault New Zealand, *Tectonics*, *32*(3), 620–640, doi:10.1002/tect.20041, 2013.

Barth, N. C., D. K. Kulhanek, A. G. Beu, C. V. Murray-Wallace, B. W. Hayward, D. C. Mildenhall, and D. E. Lee, New c. 270kyr strike-slip and uplift rates for the southern Alpine Fault and implications for the New Zealand plate boundary, *Journal of Structural Geology*, *64*, 39–52, doi:10.1016/j.jsg.2013.08.009, 2014.

Batt, G. E., and J. Braun, The tectonic evolution of the Southern Alps, New Zealand: Insights from fully thermally coupled dynamical modelling, *Geophysical Journal International*, *136*(2), 403–420, doi:10.1046/j.1365-246X.1999.00730.x, 1999.

Batt, G. E., J. Braun, B. Kohn, and I. McDougall, Thermochronological analysis of the dynamics of the Southern Alps, New Zealand, *Bulletin of the Geological Society of America*, *112*(2), 250–266, 2000.

Beaucé, E., W. B. Frank, and A. Romanenko, Fast Matched Filter (FMF): An Efficient Seismic Matched-Filter Search for Both CPU and GPU Architectures, *Seismological Research Letters*, *89*(1), 165–172, doi:10.1785/0220170181, 2017.

Beavan, J., M. Moore, C. Pearson, M. Henderson, B. Parsons, S. Bourne, P. England, D. Walcott, G. Blick, D. Darby, and K. Hodgkinson, Crustal deformation during 1994-1998 due to oblique continental collision in the central Southern Alps, New Zealand, and implications for seismic potential of the Alpine fault, *Journal of Geophysical Research: Solid Earth*, *104*(B11), 25,233–25,255, doi:10.1029/1999JB900198, 1999.

Beavan, J., D. Matheson, and P. Denys, A vertical deformation profile across the Southern Alps, New Zealand, from 3.5 years of continuous GPS data, *Proceedings of the Cahiers du Centre Européen de Géodynamique et de Séismologie workshop: The State of GPS Vertical Positioning Precision: Separation of Earth Processes by Space Geodesy, Luxembourg*, *23*, 111–123, 2004.

Beavan, J., P. Denys, M. Denham, B. Hager, T. Herring, and P. Molnar, Distribution of present-day vertical deformation across the Southern Alps, New Zealand, from 10 years of GPS data, *Geophysical Research Letters*, *37*(16), 7–11, doi:10.1029/2010GL044165, 2010.

Beeler, N. M., G. Hirth, T. E. Tullis, and C. H. Webb, On the depth extent of coseismic rupture, *Bulletin of the Seismological Society of America*, *108*(2), 761–780, doi:10.1785/0120160295, 2018.

Benson, W. N., Meeting of the Geological Division of the Pacific Science Congress in New Zealand, February, 1949, *International Proceedings of the Geological Society of America*, *11*, 11–13, 1952.

Berryman, K. R., S. Beanland, A. F. Cooper, H. N. Cutten, R. J. Norris, and P. R. Wood, The Alpine fault, New Zealand: Variation in Quaternary structural style and geomorphic expression., *Annales Tectonicae*, *VI*, 126–163, 1992.

Berryman, K. R., U. A. Cochran, K. J. Clark, G. P. Biasi, R. M. Langridge, and P. Villamor, Major Earthquakes Occur Regularly on an Isolated Plate Boundary Fault, *Science*, *336*(6089), 1690–1693, doi:10.1126/science.1218959, 2012.

Beyreuther, M., R. Barsch, L. Krischer, T. Megies, Y. Behr, and J. Wassermann, ObsPy: A Python Toolbox for Seismology, *Seismological Research Letters*, *81*(3), 530–533, doi:10.1785/gssrl.81.3.530, 2010.

Biasi, G. P., R. M. Langridge, K. R. Berryman, K. J. Clark, and U. A. Cochran, Maximum-likelihood recurrence parameters and conditional probability of a ground-rupturing earthquake on the southern Alpine fault, South Island, New Zealand,

Bulletin of the Seismological Society of America, *105*(1), 94–106, doi:10.1785/0120130259, 2015.

Boese, C. M., Microseismicity in the central Southern Alps, Westland, New Zealand., Ph.D. thesis, Victoria University of Wellington, 2012.

Boese, C. M., J. Townend, E. Smith, and T. Stern, Microseismicity and stress in the vicinity of the Alpine Fault, central Southern Alps, New Zealand, *Journal of Geophysical Research: Solid Earth*, *117*(2), 1–20, doi:10.1029/2011JB008460, 2012.

Boese, C. M., T. A. Stern, J. Townend, S. Bourguignon, A. Sheehan, and E. G. C. Smith, Sub-crustal earthquakes within the Australia-Pacific plate boundary zone beneath the Southern Alps, New Zealand, *Earth and Planetary Science Letters*, *376*, 212–219, doi:10.1016/j.epsl.2013.06.030, 2013.

Boese, C. M., K. M. Jacobs, E. G. C. Smith, T. A. Stern, and J. Townend, Background and delayed-triggered swarms in the central Southern Alps, South Island, New Zealand, *Geochemistry, Geophysics, Geosystems*, *15*(April 2014), 945–964, doi:10.1002/2013GC005171.Received, 2014.

Boese, C. M., T. A. Stern, K. Michailos, J. Townend, C. M. Boese, T. A. Stern, K. Michailos, J. Townend, and J. Townend, Implications of upper-mantle seismicity for deformation in the continental collision zone beneath the Alpine Fault , South Island , New Zealand, *New Zealand Journal of Geology and Geophysics*, *0*(0), 1–26, doi:10.1080/00288306.2018.1509357, 2018.

Bohnhoff, M., C. Wollin, D. Domigall, L. Küperkoch, P. Martínez-Garzón, G. Kwiatek, G. Dresen, and P. E. Malin, Repeating Marmara Sea earthquakes: indication for fault creep, *Geophysical Journal International*, *210*(1), 332–339, doi:10.1093/gji/ggx169, 2017.

Bonner, J. L., D. D. Blackwell, and E. T. Herrin, Thermal constraints on earthquake depths in California, *Bulletin of the Seismological Society of America*, *93*(6), 2333–2354, doi:10.1785/0120030041, 2003.

Boulton, C., D. E. Moore, D. A. Lockner, V. G. Toy, J. Townend, and R. Sutherland, Frictional properties of exhumed fault gouges in DFDP-1 cores, Alpine Fault, New Zealand, *Geophysical Research Letters*, *41*, 356–362, doi:doi:10.1002/2013GL058236, 2014.

Boulton, C., N. C. Barth, D. E. Moore, D. A. Lockner, J. Townend, and D. R. Faulkner, Frictional properties and 3-D stress analysis of the southern Alpine Fault, New Zealand, *Journal of Structural Geology*, *114*(February), 43–54, doi:10.1016/j.jsg.2018.06.003, 2018.

Bourguignon, S., T. A. Stern, and M. K. Savage, Crust and mantle thickening beneath the southern portion of the Southern Alps, New Zealand, *Geophysical Journal International*, *168*(2), 681–690, doi:10.1111/j.1365-246X.2006.03208.x, 2007.

Bourguignon, S., S. Bannister, C. M. Henderson, J. Townend, and H. Zhang, Structural heterogeneity of the midcrust adjacent to the central Alpine Fault, New Zealand: Inferences from seismic tomography and seismicity between Harihari and Ross, *Geochemistry, Geophysics, Geosystems*, *16*, 1017–1043, doi:10.1002/2014GC005702, 2015.

Bradley, B. A., S. E. Bae, V. Polak, R. L. Lee, E. M. Thomson, and K. Tarbali, Ground motion simulations of great earthquakes on the Alpine Fault: effect of hypocentre location and comparison with empirical modelling, *New Zealand Journal of Geology and Geophysics*, *60*(3), 188–198, doi:10.1080/00288306.2017.1297313, 2017.

Byerlee, J. D., Brittle-ductile transition in rocks, *Journal of Geophysical Research*, *73*(14), 4741–4750, doi:10.1029/jb073i014p04741, 1968.

Caldwell, J. G., and C. Frohlich, Microearthquake study of the Alpine fault zone near Haast, South Island, New Zealand, *Bull. Seismol. Soc. Am.*, *65*(5), 1097–1104, 1975.

Chamberlain, C. J., Improved earthquake detection as a probe for active fault structures in New Zealand's central Southern Alps, Ph.D. thesis, Victoria University of Wellington, 2016.

Chamberlain, C. J., D. R. Shelly, J. Townend, and T. A. Stern, Low-frequency earthquakes reveal punctuated slow slip on the deep extent of the Alpine Fault, New Zealand, *Geochemistry, Geophysics, Geosystems*, *15*(7), 2984–2999, doi:10.1002/2014GC005436, 2014.

Chamberlain, C. J., C. M. Boese, J. D. Eccles, M. K. Savage, L. Baratin, J. Townend, A. K. Gulley, K. M. Jacobs, A. Benson, S. Taylor-Offord, C. Thurber, B. Guo, T. Okada, R. Takagi, K. Yoshida, R. Sutherland, and V. G. Toy, Real-Time Earthquake Monitoring during the Second Phase of the Deep Fault Drilling Project, Alpine Fault, New Zealand, *Seismological Research Letters*, *88*(6), 1443–1454, doi:10.1785/0220170095, 2017a.

Chamberlain, C. J., C. M. Boese, and J. Townend, Cross-correlation-based detection and characterisation of microseismicity adjacent to the locked, late-interseismic Alpine Fault, South Westland, New Zealand, *Earth and Planetary Science Letters*, *457*, 63–72, doi:10.1016/j.epsl.2016.09.061, 2017b.

Chamberlain, C. J., C. J. Hopp, C. M. Boese, E. Warren-Smith, D. Chambers, S. X. Chu, K. Michailos, and J. Townend, EQcorrscan: Repeating and Near-Repeating

Earthquake Detection and Analysis in Python, *Seismological Research Letters*, *89*(1), 173–181, doi:10.1785/0220170151, 2017c.

Chen, W.-P., and P. Molnar, Focal Depths of intracontinental and intraplate earthquakes and their implications for the thermal and mechanical properties of the lithosphere, *Journal of Geophysical Research*, *88*, 4183–4214, 1983.

Cichowicz, A., An automatic S-phase picker, *Bulletin of the Geological Society of America*, *83*, 180–189, 1993.

Cochran, U. A., K. J. Clark, J. D. Howarth, G. P. Biasi, R. M. Langridge, P. Villamor, K. R. Berryman, and M. J. Vandergoes, A plate boundary earthquake record from a wetland adjacent to the Alpine fault in New Zealand refines hazard estimates, *Earth and Planetary Science Letters*, *464*, 175–188, doi:10.1016/j.epsl.2017.02.026, 2017.

Cox, S. C., and D. J. Barrell, Geology of the Aoraki area, *Lower Hutt: GNS Science. Institute of Geological & Nuclear Sciences 1:250,000 geological map 15. 71 p. + 1 folded map.*, 2007.

Cox, S. C., and R. Sutherland, Regional Geological Framework of South Island, New Zealand, and its Significance for Understanding the Active Plate Boundary, *A Continental Plate Boundary: Tectonics at South Island, New Zealand*, pp. 19–46, doi:10.1029/175GM03, 2007.

Cox, S. C., M. W. Stirling, F. Herman, M. Gerstenberger, and J. Ristau, Potentially active faults in the rapidly eroding landscape adjacent to the Alpine Fault, central Southern Alps, New Zealand, *Tectonics*, *31*(2), 1–24, doi:10.1029/2011TC003038, 2012.

Cox, S. C., C. D. Menzies, R. Sutherland, P. H. Denys, C. Chamberlain, and D. A. H. Teagle, Changes in hot spring temperature and hydrogeology of the Alpine Fault hanging wall, New Zealand, induced by distal South Island earthquakes, *Geofluids*, *15*, 216–239, doi:10.1111/gfl.1209, 2015.

Cross, A. J., S. Kidder, and D. J. Prior, Using microstructures and TitaniQ thermobarometry of quartz sheared around garnet porphyroclasts to evaluate microstructural evolution and constrain an Alpine Fault Zone geotherm, *Journal of Structural Geology*, *75*, 17–31, doi:10.1016/j.jsg.2015.02.012, 2015.

Davey, F. J., T. Henyey, S. Kleffman, A. Melhuish, D. Okaya, T. A. Stern, and S. I. G. T. S. w. Group, Crustal reflections from the Alpine Fault Zone, South Island, New Zealand, *New Zealand Journal of Geology and Geophysics*, *38*(4), 601–604, doi:10.1080/00288306.1995.9514689, 1995.

Davey, F. J., T. Henyey, W. S. Holbrook, D. Okaya, T. A. Stern, A. Melhuish, S. Henrys, H. Anderson, D. Eberhart-Phillips, and T. McEvilly, Preliminary results from a geophysical study across a modern, continent-continent collisional plate boundary—the Southern Alps, New Zealand, *Tectonophysics*, *288*(1), 221–235, doi: 10.1016/S0040-1951(97)00297-7, 1998.

Davey, F. J., D. Eberhart-Phillips, M. D. Kohler, S. Bannister, G. Caldwell, S. Henrys, M. Scherwath, T. Stern, and H. Van Avendonk, Geophysical Structure of the Southern Alps Orogen, South Island, New Zealand, *A Continental Plate Boundary: Tectonics at South Island, New Zealand*, pp. 47–72, doi:10.1029/175GM04, 2007.

Deichmann, N., and M. Garcia-Fernandez, Rupture geometry from high-precision relative hypocentre locations of microearthquake clusters, *Geophysical Journal International*, *110*(3), 501–517, doi:10.1111/j.1365-246X.1992.tb02088.x, 1992.

DeMets, C., R. G. Gordon, and D. F. Argus, Geologically current plate motions, *Geophysical Journal International*, *181*(1), 1–80, doi:10.1111/j.1365-246X.2009.04491.x, 2010.

Diehl, T., E. Kissling, S. Husen, and F. Aldersons, Consistent phase picking for regional tomography models: Application to the greater Alpine region, *Geophys. J. Int.*, *176*, 542–554, doi:10.1111/j.1365-246X.2008.03985.x, 2009.

Dodson, H. M., Closure Temperature in Cooling Geochronological and Petrological Systems, *Contrib. Mineral. Petrol.*, *40*, 259–274, doi:10.1007/BF00373790, 1973.

Doser, D. I., and H. Kanamori, Depth of seismicity in the Imperial Valley region (1977-1983) and its relationship to heat flow, *J. Geophys. Res.*, *91*(5), 675–688, 1986.

Douglas, A., Bandpass filtering to reduce noise on seismo- grams: is there a better way?, *Bull. Seismol. Soc. Am.*, *87*(4), 770–777, 1997.

Eberhart-Phillips, D., and S. Bannister, Three-dimensional crustal structure in the Southern Alps region of New Zealand from inversion of local earthquake and active source data, *Journal of Geophysical Research: Solid Earth*, *107*(B10), 2262, doi: 10.1029/2001jb000567, 2002.

Eberhart-Phillips, D., M. Chadwick, and S. Bannister, Three-dimensional attenuation structure of central and southern South Island, New Zealand, from local earthquakes, *Journal of Geophysical Research*, *113*(B5), B05,308, doi:10.1029/2007JB005359, 2008.

Eccles, J. D., a. K. Gulley, P. E. Malin, C. M. Boese, J. Townend, and R. Sutherland, Fault Zone Guided Wave generation on the locked, late interseismic Alpine Fault, New Zealand, pp. 1–8, doi:10.1002/2015GL064208.Received, 2015.

Efron, B., and G. Gong, A leisurely look at the bootstrap, the jackknife, and cross-validation, *The American Statistician*, *37*, 36–48, doi:10.1080/00031305.1983.10483087, 1983.

Eiby, G. A., Sesmic regions of New Zealand, *New Zealand Department of Scientific and Industrial Research, Geophysics Division*, 1971.

Evison, F., Seismicity of the Alpine Fault, New Zealand, *Bull. R. Soc. NZ*, *9*, 161–165, 1971.

Feenstra, J., C. Thurber, J. Townend, S. Roecker, S. Bannister, C. Boese, N. Lord, S. Bourguignon, and D. Eberhart-Phillips, Microseismicity and P–wave tomography of the central Alpine Fault, New Zealand, *New Zealand Journal of Geology and Geophysics*, *59*(4), 483–495, doi:10.1080/00288306.2016.1182561, 2016.

Frank, W. B., N. M. Shapiro, A. L. Husker, V. Kostoglodov, and M. Campillo, Repeating seismicity in the shallow crust modulated by transient stress perturbations, *Tectonophysics*, *687*, 105–110, doi:10.1016/j.tecto.2016.09.003, 2016.

Fuis, G. S., M. D. Kohler, M. Scherwath, U. Brink, H. J. A. V. Avendonk, and J. M. Murphy, a Comparison Between the Transpressional Plate Boundaries of the South Island , New Zealand , and Southern California , Usa, *Victoria*, (419), 2006–2006, 2007.

Geiger, L., Herdbestimmung bei Erdbeben aus den Ankunftszeiten, Nachrichten der K. Gesellschaft der Wissenschaften zu Gottingen, *Math.-Phys. Klasse*, pp. 331–349, 1910.

Gephart, J. W., and D. W. Forsyth, An improved method for determining the regional stress tensor using earthquake focal mechanism data: application to the San Fernando earthquake sequence., *Journal of Geophysical Research*, *89*(B11), 9305–9320, doi:10.1029/JB089iB11p09305, 1984.

Gibbons, S. J., and F. Ringdal, The detection of low magnitude seismic events using array-based waveform correlation, *Geophys. J. Int.*, *165*, 149–166, doi:10.1111/j.1365-246X.2006.02865.x, 2006.

Gleadow, A. J., and I. R. Duddy, A natural long-term track annealing experiment for apatite, *Nuclear Tracks*, *5*(1-2), 169–174, doi:10.1016/0191-278X(81)90039-1, 1981.

Guo, B., C. Thurber, S. Roecker, J. Townend, C. Rawles, C. Chamberlain, C. Boese, S. Bannister, J. Feenstra, and J. Eccles, 3-D P- and S-wave velocity structure along the central Alpine Fault, South Island, New Zealand, *Geophysical Journal International*, *209*(2), 935–947, doi:10.1093/gji/ggx059, 2017.

Hanks, T. C., Estimation of High-Frequency Strong Ground Motion, *Journal of Geophysical Research*, *84*, 2235–2242, doi:10.1029/JB084iB05p02235, 1979.

Hardebeck, J. L., and E. Hauksson, Role of fluids in faulting inferred from stress field signatures, *Science*, *285*(5425), 236–239, doi:10.1126/science.285.5425.236, 1999.

Hardebeck, J. L., and A. J. Michael, Stress orientations at intermediate angles to the San Andreas Fault, California, *Journal of Geophysical Research: Solid Earth*, *109*(11), 1–16, doi:10.1029/2004JB003239, 2004.

Hardebeck, J. L., and A. J. Michael, Damped regional-scale stress inversions: Methodology and examples for southern California and the Coalinga aftershock sequence, *Journal of Geophysical Research: Solid Earth*, *111*(11), 1–11, doi:10.1029/2005JB004144, 2006.

Harrington, R. M., E. S. Cochran, E. M. Griffiths, X. Zeng, and C. H. Thurber, Along-strike variations in fault frictional properties along the san andreas fault near cholame, california, from joint earthquake and low-frequency earthquake relocations, *Bulletin of the Seismological Society of America*, *106*(2), 319–326, doi:10.1785/0120150171, 2016.

Hartigan, J., *Clustering algorithms*, Wiley, 1975.

Hauksson, E., and M.-A. Meier, Applying Depth Distribution of Seismicity to Determine Thermo-Mechanical Properties of the Seismogenic Crust in Southern California: Comparing Lithotectonic Blocks, *Pure and Applied Geophysics*, doi:10.1007/s00024-018-1981-z, 2018.

Havskov, J., and L. Ottemoller, SEISAN: Ther Earthquake Analysis Software for Windows, Solaris, Linux and MACOSX Version 8.2 Manual., doi:10.1785/gssrl.70.5.532, 2008.

Herman, F., J. Braun, and W. J. Dunlap, Tectonomorphic scenarios in the Southern Alps of New Zealand, *Journal of Geophysical Research: Solid Earth*, *112*(4), doi:10.1029/2004JB003472, 2007.

Herman, F., S. C. Cox, and P. J. Kamp, Low-temperature thermochronology and thermokinematic modeling of deformation, exhumation, and development of topography in the central Southern Alps, New Zealand, *Tectonics*, *28*(5), doi:10.1029/2008TC002367, 2009.

Howarth, J. D., S. J. Fitzsimons, R. J. Norris, and G. E. Jacobsen, Lake sediments record high intensity shaking that provides insight into the location and rupture length of large earthquakes on the Alpine Fault, New Zealand, *Earth and Planetary Science Letters*, *403*, 340–351, doi:10.1016/j.epsl.2014.07.008, 2014.

Howarth, J. D., S. J. Fitzsimons, R. J. Norris, R. Langridge, and M. J. Vandergoes, A 2000 yr rupture history for the Alpine fault derived from Lake Ellery, South Island, New Zealand, *Bulletin of the Geological Society of America*, *128*(3-4), 627–643, doi:10.1130/B31300.1, 2016.

Howarth, J. D., U. A. Cochran, R. M. Langridge, K. Clark, S. J. Fitzsimons, K. Berryman, P. Villamor, and D. T. Strong, Past large earthquakes on the Alpine Fault: paleoseismological progress and future directions, *New Zealand Journal of Geology and Geophysics*, *0*(0), 1–20, doi:10.1080/00288306.2018.1464658, 2018.

Ito, K., Seismogenic layer, reflective lower crust, surface heat flow and large inland earthquakes, *Tectonophysics*, *306*(3-4), 423–433, doi:10.1016/S0040-1951(99)00069-4, 1999.

Jackson, J., Strength of the continental lithosphere: time to abandon the jelly sandwich?, *GSA Today*, *12*, 4–10, 2002.

Janku-Čápová, L., Thermal and hydraulic characterization of the hanging-wall of the central Alpine Fault, Ph.D. thesis, Victoria University of Wellington, 2018.

Jiang, J., and N. Lapusta, Deeper penetration of large earthquakes on seismically quiescent faults, *Science*, *352*(6291), 1293–1297, doi:10.1126/science.aaf1496, 2016.

Kamp, P. J. J., N. Zealand, and P. F. Green, Department of Geology, The University of, *Earth*, *8*(2), 169–195, 1989.

Khattri, K., Earthquake focal mechanism studies-A review, *Earth Science Reviews*, *9*(1), 19–63, doi:10.1016/0012-8252(73)90161-X, 1973.

Kidder, S., V. Toy, D. Prior, T. Little, A. Khan, and C. Macrae, Constraints on Alpine Fault (New Zealand) Mylonitization Temperatures and Geothermal Gradient from Ti-in-quartz Thermobarometry, *Solid Earth*, *9(5)*, 1123–1139, doi:10.5194/se-9-1123-2018, 2018.

Kisslinger, C., R. Bowman, and K. Koch, Procedures for computing focal mechanisms from local (SV/P) data, *71*(6), 1719–1729, 1981.

Kohler, M. D., and D. Eberhart-Phillips, Intermediate-depth earthquakes in a region of continental convergence: South Island, New Zealand, *Bulletin of the Seismological Society of America*, *93*(1), 85–93, doi:10.1785/0120020043, 2003.

Koons, P., Some thermal and mechanical consequences of rapid uplift: an example from the Southern Alps, New Zealand, *Earth and Planetary Science Letters*, *86*(2-4), 307–319, doi:10.1016/0012-821X(87)90228-7, 1987.

Koons, P. O., Two-sided orogen: collision and erosion from the sandbox to the Southern Alps, New Zealand, *Geology*, *18*(8), 679–682, 1990.

Koons, P. O., R. J. Norris, D. Craw, and A. F. Cooper, Influence of exhumation on the structural evolution of transpressional plate boundaries: An exmaple from the Southern Alps, New Zealand, *Geology*, *31*(1), 3–6, 2003.

Kostrov, V. V., Seismic moment and energy of earthquakes, and seismic flow of rock, *Earth Physics*, *1*, 23–40, 1974.

Krischer, L., T. Megies, R. Barsch, M. Beyreuther, T. Lecocq, C. Caudron, and J. Wassermann, ObsPy: A bridge for seismology into the scientific Python ecosystem, *Computational Science and Discovery*, *8*(1), 0–17, doi:10.1088/1749-4699/8/1/014003, 2015.

Lamb, S., and E. Smith, The nature of the plate interface and driving force of interseismic deformation in the New Zealand plate-boundary zone, revealed by the continuous GPS velocity field, *Journal of Geophysical Research: Solid Earth*, *118*(6), 3160–3189, doi:10.1002/jgrb.50221, 2013.

Lamb, S., N. Mortimer, E. Smith, and G. Turner, Focusing of relative plate motion at a continental transform fault: Cenozoic dextral displacement 700 km on New Zealand's Alpine Fault, reversing 225 km of Late Cretaceous sinistral motion, *Geochem. Geophys. Geosyst.*, pp. 1197–1213, doi:10.1002/2015GC006225.Received, 2016.

Lamb, S., R. Arnold, and J. D. P. Moore, Locking on a megathrust as a cause of distributed faulting and fault-jumping earthquakes, *Nature Geoscience*, doi:10.1038/s41561-018-0230-5, 2018.

Lay, V., S. Buske, A. Lukács, A. R. Gorman, S. Bannister, and D. R. Schmitt, Advanced seismic imaging techniques characterize the Alpine Fault at Whataroa (New Zealand), *Journal of Geophysical Research: Solid Earth*, *121*(12), 8792–8812, doi:10.1002/2016JB013534, 2016.

Lee, W. H. K., and J. C. Lahr, HYPO71: a computer program for determining hypocenter, magnitude, and first motion pattern of local earthquakes, *Tech. rep.*, US Geological Survey, 1972.

Leitner, B., and D. Eberhart-Phillips, A focused look at the Alpine fault, New Zealand: Seismicity, focal mechanisms, and stress observations, *Journal of Geophysical Research*, *106*(2000), 2193–2220, 2001.

Leonard, M., and B. L. N. Kennett, Multi-component autoregressive techniques for the analysis of seismograms, *Physics of the Earth and Planetary Interiors*, *113*, 247–263, 1999.

Lienert, B. R., E. Berg, and L. N. Frazer, HYPOCENTER: An earthquake location method using centered, scaled, and adaptively damped least squares, *Bulletin of the Seismological Society of America*, *76*(3), 771–783, 1986.

Little, T. A., S. Cox, J. K. Vry, and G. Batt, Variations in exhumation level and uplift rate along the oblique-slip Alpine fault, central Southern Alps, New Zealand, *Bulletin of the Geological Society of America*, *117*(5-6), 707–723, doi:10.1130/B25500.1, 2005.

Lomax, A., J. Virieux, P. Volant, and C. Berge-thierry, Probabilistic earthquake location in 3D and layered models, in *Advances in Seismic Event Location*, pp. 101–134, Springer, 2000.

Lomax, A., A. Michelini, and A. Curtis, Earthquake Location, Direct, Global-Search Methods, in *Encyclopedia of Complexity and Systems Science*, edited by R. A. Meyers, pp. 1–33, Springer New York, New York, NY, doi:10.1007/978-3-642-27737-5{_}150-2, 2009.

Lund, B., and R. Slunga, Stress tensor inversion using detailed microearthquake information and stability constraints: Application to Ölfus in southwest Iceland, *Journal of Geophysical Research: Solid Earth*, *104*(B7), 14,947–14,964, doi:10.1029/1999JB900111, 1999.

Lund, B., and J. Townend, Calculating horizontal stress orientations with full or partial knowledge of the tectonic stress tensor, *Geophysical Journal International*, *170*(3), 1328–1335, doi:10.1111/j.1365-246X.2007.03468.x, 2007.

Magistrale, H., and H.-w. Zhou, Lithologic Control of the Depth of Earthquakes in Southern California, *Science*, *273*(5275), 639–642, doi:10.1126/science.273.5275.639, 1996.

Martínez-Garzón, P., M. Bohnhoff, G. Kwiatek, and G. Dresen, Stress tensor changes related to fluid injection at the Geysers geothermal field, California, *Geophysical Research Letters*, *40*(11), 2596–2601, doi:10.1002/grl.50438, 2013.

Martinez-Garzon, P., G. Kwiatek, M. Ickrath, and M. Bohnhoff, MSATSI: A MATLAB Package for Stress Inversion Combining Solid Classic Methodology, a New Simplified User-Handling, and a Visualization Tool, *Seismological Research Letters*, *85*(4), 896–904, doi:10.1785/0220130189, 2014.

McKenzie, D., The Relation Between Fault Plane Solutions for Earthquakes and the Directions of the Principal Stresses, *Bulletin of the Seismological Society of America*, *59*(2), 591–601, 1969.

Menke, W., and D. Schaff, Absolute earthquake locations with differential data, *Bulletin of the Seismological Society of America*, *94*(6), 2254–2264, doi:10.1785/0120040033, 2004.

Mesimeri, M., V. Karakostas, E. Papadimitriou, G. Tsaklidis, and K. Jacobs, Relocation of recent seismicity and seismotectonic properties in the Gulf of Corinth (Greece), *Geophysical Journal International*, (December 2017), 1123–1142, doi:10.1093/gji/ggx450, 2017.

Michael, A. J., Determination of Stress from Slip Data: Faults and Folds, *Journal of Geophysical Research*, *89*(B13), 517–526, doi:10.1029/JB089iB13p11517, 1984.

Michailos, K., E. G. C. Smith, C. J. Chamberlain, M. K. Savage, and J. Townend, Variations in seismogenic thickness along the central Alpine Fault, New Zealand, revealed by a decade's relocated microseismicity, *Geochemistry Geophysics Geosystems*, *20*, doi:https://doi.org/10.1029/2018GC007743, 2019.

Michelini, A., and A. Lomax, The effect of velocity structure errors on double-difference earthquake location, *Geophysical Research Letters*, *31*(9), 1–4, doi:10.1029/2004GL019682, 2004.

Mogi, K., Two kinds of seismic gaps, *Pure and Applied Geophysics PAGEOPH*, *117*(6), 1172–1186, doi:10.1007/BF00876213, 1979.

Mortimer, N., New Zealand's geological foundations, *Gondwana Research*, *7*(1), 261–272, doi:10.1016/S1342-937X(05)70324-5, 2004.

Nadeau, R. M., and L. R. Johnson, Seismological studies at Parkfield VI: moment release rates and estimates of source parameters for small repeating earthquakes, *Bulletin of the Seismological Society of America*, *88*(3), 790–814, 1998.

Nazareth, J. J., and E. Hauksson, The seismogenic thickness of the southern California crust, *Bulletin of the Seismological Society of America*, *94*(3), 940–960, doi:10.1785/0120020129, 2004.

Niemeijer, A. R., C. Boulton, V. G. Toy, Townend J., and Sutherland R., Large-displacement, hydrothermal frictional properties of DFDP-1 fault rocks, Alpine Fault, New Zealand: Implications for deep rupture propagation, *Journal of Geophysical Research: Solid Earth*, *2015*(120), 450–487, doi:10.1002/2014JB011176.Received, 2016.

Nikolov, S., Trend or no trend: a novel nonparametric method of classifying time series, Ph.D. thesis, Massachusetts Institute of Technology, 2012.

Norris, R. J., and A. F. Cooper, Origin of small-scale segmentation and transpressional thrusting along the Alpine Fault, New Zealand, *Geological Society of America Bulletin*, *107*(2), 231–240, doi:10.1130/0016-7606(1995)107⟨0231:OOSSSA⟩2.3.CO;2, 1995.

Norris, R. J., and A. F. Cooper, Erosional control on the structural evolution of a transpressional thrust complex on the Alpine Fault, New Zealand, *Journal of Structural Geology*, *19*(10), 1323–1342, doi:10.1016/S0191-8141(97)00036-9, 1997.

Norris, R. J., and A. F. Cooper, Late Quaternary slip rates and slip partitioning on the Alpine Fault, New Zealand, *Journal of Structural Geology*, *23*(2-3), 507–520, doi:10.1016/S0191-8141(00)00122-X, 2001.

Norris, R. J., and A. F. Cooper, The Alpine Fault, New Zealand: Surface Geology and Field Relationships, *A Continental Plate Boundary: Tectonics at South Island, New Zealand*, pp. 157–175, doi:10.1029/175GM09, 2007.

Norris, R. J., and V. G. Toy, Continental transforms: A view from the Alpine Fault, *Journal of Structural Geology*, *64*, 3–31, doi:10.1016/j.jsg.2014.03.003, 2014.

O'Brien, G. A., S. C. Cox, and J. Townend, Spatially and temporally systematic hydrologic changes within large geoengineered landslides, Cromwell Gorge, New Zealand, induced by multiple regional earthquakes, *Journal of Geophysical Research: Solid Earth*, *121*, 8750–8773, doi:10.1002/2016JB013418, 2016.

Okaya, D., S. Henrys, and T. Stern, Double-sided onshore-offshore seismic imaging of a plate boundary: "super-gathers" across South Island, New Zealand, *Tectonophysics*, *355*(1-4), 247–263, doi:10.1016/S0040-1951(02)00145-2, 2002.

O'Keefe, B. C., Microseismicity of the central Alpine Fault region, New Zealand, Ph.D. thesis, Victoria University of Wellington, 2008.

Omuralieva, A. M., A. Hasegawa, T. Matsuzawa, J. Nakajima, and T. Okada, Lateral variation of the cutoff depth of shallow earthquakes beneath the Japan Islands and its implications for seismogenesis, *Tectonophysics*, *518-521*, 93–105, doi:10.1016/j.tecto.2011.11.013, 2012.

Orchiston, C., T. Davies, R. Langridge, T. Wilson, J. Mitchell, M. Hughes, K. Berryman, S. Fitzsimmons, M. Hicks, J. Ingham, D. Johnston, P. Barnes, and A. Davies, Alpine Fault Magnitude 8 Hazard Scenario, (October), 45, 2016.

Orchiston, C., J. Mitchell, T. Wilson, R. Langridge, T. Davies, B. Bradley, D. Johnston, A. Davies, J. Becker, and A. McKay, Project AF8: developing a coordinated, multi-agency response plan for a future great Alpine Fault earthquake, *New Zealand Jour-*

nal of Geology and Geophysics, *61*(3), 389–402, doi:10.1080/00288306.2018.1455716, 2018.

Petersen, T., K. Gledhill, M. Chadwick, N. H. Gale, and R. John, Comparison of Seismicity Rates in the New Madrid and Wabash Valley Seismic Zones, *Seismological Research Letters*, *82*(6), 951–954, doi:10.1785/gssrl, 2011.

Peyton, S. L., and B. Carrapa, An Introduction to Low-temperature Thermochronologic Techniques, Methodology, and Applications, *Aapg*, pp. 15–36, doi:10.1306/13381688St653578, 2013.

Rawles, C. J., and C. H. Thurber, A non-parametric method for automatic determination of P-wave and S-wave arrival times: application to local micro earthquakes, *Geophysical Journal International*, *202*, 1164–1179, doi:10.1093/gji/ggv218, 2015.

Reiners, P. W., and M. T. Brandon, Using Thermochronology To Understand Orogenic Erosion, *Annual Review of Earth and Planetary Sciences*, *34*(1), 419–466, doi:10.1146/annurev.earth.34.031405.125202, 2006.

Reiners, P. W., T. L. Spell, S. Nicolescu, and K. A. Zanetti, Zircon (U-Th)/He thermochronometry: He diffusion and comparisons with 40Ar/39Ar dating, *Geochimica et Cosmochimica Acta*, *68*(8), 1857–1887, doi:10.1016/j.gca.2003.10.021, 2004.

Reyners, M., Subcrustal earthquakes in the central South Island, New Zealand, and the roof of the Southern Alps, *Geology*, *15*(December), 1168–1171, 1987.

Richter, C. F., An instrumental earthquake magnitude scale, *Bulletin of the Seismological Society of Americal*, *25*(1), 1–32, 1935.

Richter, C. F., *Elementary Seismology*, Freeman and Co, San Francisco 1958, 1958.

Ring, U., and M. Bernet, Fission-track analysis unravels the denudation history of the Bonar Range in the footwall of the Alpine Fault, South Island, New Zealand, *Geological Magazine*, *147*(6), 801–813, doi:10.1017/S0016756810000208, 2010.

Ristau, J., Update of regional moment tensor analysis for earthquakes in New Zealand and adjacent offshore regions, *Bulletin of the Seismological Society of America*, *103*(4), 2520–2533, doi:10.1785/0120120339, 2013.

Robinson, R., Temporal variations in coda duration of local earthquakes in the Wellington region, New Zealand, *Pure and Applied Geophysics PAGEOPH*, *125*(4), 579–596, doi:10.1007/BF00879573, 1987.

Rolandone, F., R. Bürgmann, and R. M. Nadeau, The evolution of the seismic-aseismic transition during the earthquake cycle: Constraints from the time-dependent depth

distribution of aftershocks, *Geophysical Research Letters*, *31*(23), 1–4, doi:10.1029/2004GL021379, 2004.

Ross, Z. E., and Y. Ben-Zion, Automatic picking of direct P, S seismic phases and fault zone head waves, *Geophysical Journal International*, *199*(1), 368–381, doi:10.1093/gji/ggu267, 2014.

Schaff, D. P., and P. G. Richards, On finding and using repeating seismic events in and near China, *Journal of Geophysical Research: Solid Earth*, *116*(3), 1–20, doi:10.1029/2010JB007895, 2011.

Scherbaum, F., *Of poles and zeros: Fundamentals of digital seismology*, Springer Science & Business Media, 2013.

Scherwath, M., T. Stern, F. Davey, D. Okaya, W. S. Holbrook, R. Davies, and S. Kleffmann, Lithospheric structure across oblique continental collision in New Zealand from wide-angle P wave modeling, *Journal of Geophysical Research*, *108*(B12), 2566, doi:10.1029/2002JB002286, 2003.

Scholz, C., The brittle-plastic transition and the depth of seismic faulting, *Geologische Rundschau*, *77/1*, 319–328, 1988.

Scholz, C., J. Rynn, R. Weed, and C. Frohlich, Detailed seismicity of the Alpine Fault Zone and Fiordland, South Island, New Zealand, *Geoexploration*, *84*, 3297–3316, doi:10.1016/0016-7142(74)90043-x, 1973.

Scholz, C. H., *The mechanics of earthquakes and faulting.*, Cambridge university press, 1990.

Scholz, C. H., Earthquakes and friction laws, *Nature*, *391*(6662), 37–42, doi:10.1038/34097, 1998.

Seward, D., Cenozoic basin histories determined by fission-track dating of basement granites, South Island, New Zealand, *Chemical Geology: Isotope Geoscience Section*, *79*(1), 31–48, doi:10.1016/0168-9622(89)90005-5, 1989.

Shaw, B. E., and S. G. Wesnousky, Slip-length scaling in large earthquakes: The role of deep-penetrating slip below the seismogenic layer, *Bulletin of the Seismological Society of America*, *98*(4), 1633–1641, doi:10.1785/0120070191, 2008.

Shelly, D. R., A 15 year catalog of more than 1 million low-frequency earthquakes: Tracking tremor and slip along the deep San Andreas Fault, *Journal of Geophysical Research: Solid Earth*, *122*(5), 3739–3753, doi:10.1002/2017JB014047, 2017.

Shelly, D. R., W. L. Ellsworth, and D. P. Hill, Fluid-faulting evolution in high definition: Connecting fault structure and frequency-magnitude variations during the 2014 Long Valley Caldera, California, earthquake swarm, *Journal of Geophysical Research : Solid Earth*, *121*, 1776–1795, doi:10.1002/2015JB012719, 2016a.

Shelly, D. R., J. L. Hardebeck, W. L. Ellsworth, and D. P. Hill, A new strategy for earthquake focal mechanisms using waveform-correlation-derived relative polarities and cluster analysis: Application to the 2014 Long Valley Caldera earthquake swarm, *Journal of Geophysical Research: Solid Earth*, *121*(12), 8622–8641, doi:10.1002/2016JB013437, 2016b.

Shi, Y., R. Allis, and F. Davey, Thermal modeling of the Southern Alps, New Zealand, *Pure and Applied Geophysics PAGEOPH*, *146*(3/4), doi:10.1007/bf00874730, 1996.

Sibson, R. H., Fault zone models, heat flow, and the depth distribution of earthquakes in the continental crust of the united states, *Bulletin of the Seismological Society of America*, *72*(1), 151–163, 1982.

Sibson, R. H., Roughness at the base of the seismogenic zone: contributing factors., *Journal of Geophysical Research*, *89*(B7), 5791–5799, doi:10.1029/JB089iB07p05791, 1984.

Sleeman, R., and T. V. Eck, Robust automatic P-phase picking: an on-line implementation in the analysis of broadband seismogram recordings, *Phys. Earth planet. Inter., 113*, pp. 265–275, 1999.

Smith-Konter, B. R., D. T. Sandwell, and P. Shearer, Locking depths estimated from geodesy and seismology along the San Andreas Fault System: Implications for seismic moment release, *Journal of Geophysical Research: Solid Earth*, *116*(6), 1–12, doi:10.1029/2010JB008117, 2011.

Stein, S., and M. Wysession, *An introduction to seismology, earthquakes, and earth structure*, John Wiley & Sons, 2009.

Stern, T., P. Molnar, D. Okaya, and D. Eberhart-Phillips, Teleseismic P wave delays and modes of shortening the mantle lithosphere beneath South Island , New Zealand, *Journal of Geophysical Research*, *105*(B9), 21,615–21,631, doi:10.1029/2000JB900166, 2000.

Stern, T., S. Kleffmann, M. Scherwath, D. Okaya, and S. Bannister, Low seismic wave speeds and enhanced fluid pressures beneath the Southern Alps of New Zealand, *Geology*, *29*, 679–682, 2001.

Stern, T., D. Okaya, S. Kleffmann, M. Scherwath, S. Henrys, and F. Davey, *Geophysical exploration and dynamics of the Alpine fault zone*, 207–233 pp., Wiley Online Library, 2007.

Stirling, M., G. McVerry, M. Gerstenberger, N. Litchfield, R. Van Dissen, K. Berryman, P. Barnes, L. Wallace, P. Villamor, R. Langridge, G. Lamarche, S. Nodder, M. Reyners, B. Bradley, D. Rhoades, W. Smith, A. Nicol, J. Pettinga, K. Clark, and K. Jacobs, National seismic hazard model for New Zealand: 2010 update, *Bulletin of the Seismological Society of America*, *102*(4), 1514–1542, doi:10.1785/0120110170, 2012.

Sutherland, R., Cenozoic bending of New Zealand basement terranes and Alpine Fault displacement: A brief review, *New Zealand Journal of Geology and Geophysics*, *42*(2), 295–301, doi:10.1080/00288306.1999.9514846, 1999.

Sutherland, R., K. Berryman, and R. Norris, Quaternary slip rate and geomorphology of the Alpine fault: Implications for kinematics and seismic hazard in southwest New Zealand, *Bulletin of the Geological Society of America*, *118*(3-4), 464–474, doi:10.1130/B25627.1, 2006.

Sutherland, R., D. Eberhart-Phillips, R. Harris, T. A. Stern, R. J. Beavan, S. Ellis, S. Henrys, S. Cox, R. Norris, K. Berryman, J. Townend, S. Bannister, J. Pettinga, B. Leitner, L. Wallace, T. Little, A. Cooper, M. Yetton, and M. Stirling, Do Great Earthquakes Occur on the Alpine Fault in Central South Island, New Zealand?, *A Continental Plate Boundary: Tectonics at South Island, New Zealand*, *175*, 235–251, doi:10.1029/175GM12, 2007.

Sutherland, R., M. Gurnis, P. J. Kamp, and M. A. House, Regional exhumation history of brittle crust during subduction initiation, Fiordland, southwest New Zealand, and implications for thermochronologic sampling and analysis strategies, *Geosphere*, *5*(5), 409–425, doi:10.1130/GES00225.SA2, 2009.

Sutherland, R., V. G. Toy, J. Townend, S. C. Cox, J. D. Eccles, D. R. Faulkner, D. J. Prior, R. J. Norris, E. Mariani, C. Boulton, B. M. Carpenter, C. D. Menzies, T. A. Little, M. Hasting, G. P. De Pascale, R. M. Langridge, H. R. Scott, Z. Reid Lindroos, B. Fleming, and J. Kopf, Drilling reveals fluid control on architecture and rupture of the Alpine fault, New Zealand, *Geology*, *40*(12), 1143–1146, doi:10.1130/G33614.1, 2012.

Sutherland, R., J. Townend, and V. Toy, DFDP-2 Science Team. 2015. Deep Fault Drilling Project (DFDP), Alpine Fault Boreholes DFDP-2A and DFDP-2B Technical Completion Report, GNS Science Report 2015/50, *Tech. rep.*, 2015.

Sutherland, R., J. Townend, V. G. Toy, P. Upton, J. Coussens, and S. T. DFDP2, Extreme hydrothermal conditions at an active plate-bounding fault, *Nature*, *546*(7656), 137–140, doi:10.1038/nature22355, 2017.

Tagami, T., Zircon Fission-Track Thermochronology and Applications to Fault Studies, *Reviews in Mineralogy and Geochemistry*, *58*(1), 95–122, doi:10.2138/rmg.2005.58.4, 2005.

Tarantola, A., *Inverse problem theory: Methods for data fitting and model parameter estimation*, 613p pp., Elsevier, Amsterdam, 1987.

Tarantola, A., and B. Valette, Modern equipment for narrow fabric weaving and braiding, *Reviews of Geophysics and Space Physics*, *20*(2), 219–232, 1982.

Thurber, C., S. Roecker, J. Feenstra, N. Lord, G. O'Brien, J. D. Pesicek, S. C. Bannister, and J. Townend, Seismic site characterization for the Deep Fault Drilling Project (DFDP), Alpine Fault, New Zealand: Preliminary results from the WIZARD array, in *AGU Fall Meeting Abstract*, 2012.

Thurber, C. H., Nonlinear Earthquake Location: Theory and Examples, *Bulletin of the Seismological Society of America*, *75*(3), 779–790, 1985.

Tippet, J., and P. Kamp, Fission track analysis of the late Cenozoic vertical 184 JR Waldbauer and CP Chamberlain kinematics of continental Pacific crust, South Island, New Zealand, *Journal of Geophysical Research*, *98*, 16–119, 1993.

Townend, J., and M. D. Zoback, Implications of earthquake focal mechanisms for the frictional strength of the San Andreas fault system, *Geological Society, London, Special Publications*, *186*(1), 13–21, doi:10.1144/GSL.SP.2001.186.01.02, 2001.

Townend, J., and M. D. Zoback, Regional tectonic stress near the San Andreas fault in central and southern California, *Geophysical Research Letters*, *31*(15), 1–5, doi:10.1029/2003GL018918, 2004.

Townend, J., and M. D. Zoback, Stress, strain, and mountain building in central Japan, *Journal of Geophysical Research: Solid Earth*, *111*(3), 1–11, doi:10.1029/2005JB003759, 2006.

Townend, J., R. Sutherland, and V. Toy, Deep fault drilling project-alpine fault, New Zealand, *Scientific Drilling*, (8), 75–82, doi:10.2204/iodp.sd.8.12.2009, 2009.

Townend, J., S. Sherburn, R. Arnold, C. Boese, and L. Woods, Three-dimensional variations in present-day tectonic stress along the Australia-Pacific plate boundary in New Zealand, *Earth and Planetary Science Letters*, *353-354*, 47–59, doi:10.1016/j.epsl.2012.08.003, 2012.

Townend, J., R. Sutherland, V. G. Toy, J. D. Eccles, C. Boulton, S. C. Cox, and D. McNamara, Late-interseismic state of a continental plate-bounding fault: Petrophysical results from DFDP-1 wireline logging and core analysis, Alpine Fault, New Zealand, *Geochemistry, Geophysics, Geosystems*, *14*(9), 3801–3820, doi:10.1002/ggge.20236, 2013.

Townend, J., R. Sutherland, V. G. Toy, M. L. Doan, B. Célérier, C. Massiot, J. Coussens, T. Jeppson, L. Janku-Capova, L. Remaud, P. Upton, D. R. Schmitt, P. Pezard, J. Williams, M. J. Allen, L. M. Baratin, N. Barth, L. Becroft, C. M. Boese, C. Boulton, N. Broderick, B. Carpenter, C. J. Chamberlain, A. Cooper, A. Coutts, S. C. Cox, L. Craw, J. D. Eccles, D. Faulkner, J. Grieve, J. Grochowski, A. Gulley, A. Hartog, G. Henry, J. Howarth, K. Jacobs, N. Kato, S. Keys, M. Kirilova, Y. Kometani, R. Langridge, W. Lin, T. Little, A. Lukacs, D. Mallyon, E. Mariani, L. Mathewson, B. Melosh, C. Menzies, J. Moore, L. Morales, H. Mori, A. Niemeijer, O. Nishikawa, O. Nitsch, J. Paris, D. J. Prior, K. Sauer, M. K. Savage, A. Schleicher, N. Shigematsu, S. Taylor-Offord, D. Teagle, H. Tobin, R. Valdez, K. Weaver, T. Wiersberg, and M. Zimmer, Petrophysical, Geochemical, and Hydrological Evidence for Extensive Fracture-Mediated Fluid and Heat Transport in the Alpine Fault's Hanging-Wall Damage Zone, *Geochemistry, Geophysics, Geosystems*, *18*(12), 4709–4732, doi:10.1002/2017GC007202, 2017.

Toy, V. G., D. J. Prior, and R. J. Norris, Quartz fabrics in the Alpine Fault mylonites: Influence of pre-existing preferred orientations on fabric development during progressive uplift, *Journal of Structural Geology*, *30*(5), 602–621, doi:10.1016/j.jsg.2008.01.001, 2008.

Toy, V. G., D. Craw, A. F. Cooper, and R. J. Norris, Thermal regime in the central Alpine Fault zone, New Zealand: Constraints from microstructures, biotite chemistry and fluid inclusion data, *Tectonophysics*, *485*(1-4), 178–192, doi:10.1016/j.tecto.2009.12.013, 2010.

Toy, V. G., C. J. Boulton, R. Sutherland, J. Townend, R. J. Norris, T. A. Little, D. J. Prior, E. Mariani, D. Faulkner, C. D. Menzies, H. Scott, and B. M. Carpenter, Fault rock lithologies and architecture of the central Alpine fault, New Zealand, revealed by DFDP-1 drilling, *Lithosphere*, *7*(2), 155–173, doi:10.1130/L395.1, 2015.

Upton, P., and D. Craw, Extension and gold mineralisation in the hanging walls of active convergent continental shear zones, *Journal of Structural Geology*, *64*, 135–148, doi:10.1016/j.jsg.2013.08.004, 2014.

Upton, P., and R. Sutherland, High permeability and low temperature correlates with proximity to brittle failure within mountains at an active tectonic boundary, Man-

apouri tunnel, Fiordland, New Zealand, *Earth and Planetary Science Letters*, *389*, 176–187, doi:10.1016/j.epsl.2013.12.032, 2014.

Upton, P., P. O. Koons, and C. P. Chamberlain, Penetration of deformation-driven meteoric water into ductile rocks: Isotopic and model observations from the Southern Alps, New Zealand, *New Zealand Journal of Geology and Geophysics*, *38*(4), 535–543, doi:10.1080/00288306.1995.9514680, 1995.

Upton, P., D. Craw, B. Yu, and Y.-G. Chen, Controls on fluid flow in transpressive orogens, Taiwan and New Zealand, *Geological Society, London, Special Publications*, *359*(1), 249–265, doi:10.1144/SP359.14, 2011.

Van Avendonk, H. J. A., W. S. Holbrook, D. Okaya, J. K. Austin, F. Davey, and T. Stern, Continental crust under compression: A seismic refraction study of South Island Geophysical Transect I, South Island, New Zealand, *Journal of Geophysical Research B: Solid Earth*, *109*(6), 1–17, doi:10.1029/2003JB002790, 2004.

Vassallo, M., C. Satriano, and A. Lomax, Automatic Picker Developments and Optimization: A Strategy for Improving the Performances of Automatic Phase Pickers, *Seismological Research Letters*, *83*(3), 541–554, doi:10.1785/gssrl.83.3.541, 2012.

Vavryčuk, V., Iterative joint inversion for stress and fault orientations from focal mechanisms, *Geophysical Journal International*, *199*(1), 69–77, doi:10.1093/gji/ggu224, 2014.

Vry, J. K., J. Baker, R. Maas, T. A. Little, R. Grapes, and M. Dixon, Zoned (Cretaceous and Cenozoic) garnet and the timing of high grade metamorphism, Southern Alps, New Zealand, *Journal of Metamorphic Geology*, *22*(3), 137–157, doi:10.1111/j.1525-1314.2004.00504.x, 2004.

Walcott, R. I., Modes of oblique compression: Late Cenozoic tectonics of the south island of New Zealand, *Reviews of Geophysics*, *36*(1), 1, doi:10.1029/97RG03084, 1998.

Waldhauser, F., HypoDD - A Program to Compute Double-Difference Hypocenter Locations, *USGS Open File Report*, *01-113*, 1–25, doi:http://geopubs.wr.usgs.gov/open-file/of01-113/, 2001.

Waldhauser, F., and W. L. Ellsworth, A Double-difference Earthquake location algorithm: Method and application to the Northern Hayward Fault, California, *Bulletin of the Seismological Society of America*, *90*(6), 1353–1368, doi:10.1785/0120000006, 2000.

Wallace, L. M., J. Beavan, R. McCaffrey, K. Berryman, and P. Denys, Balancing the plate motion budget in the South Island, New Zealand using GPS, geological and seismological datas, *Geophysical Journal International*, *168*(1), 332–352, doi: 10.1111/j.1365-246X.2006.03183.x, 2007.

Walsh, D., R. Arnold, and J. Townend, A Bayesian approach to determining and parametrizing earthquake focal mechanisms, *Geophysical Journal International*, *176*(1), 235–255, doi:10.1111/j.1365-246X.2008.03979.x, 2009.

Wang, C.-Y., Liquefaction beyond the Near Field, *Seismological Research Letters*, *78*(5), 512–517, doi:10.1785/gssrl.78.5.512, 2007.

Wannamaker, P. E., G. R. Jiracek, J. A. Stodt, T. G. Caldwell, V. M. Gonzalez, J. D. McKnight, and A. D. Porter, Fluid generation and pathways beneath an active compressional orogen, the New Zealand Southern Alps, inferred from magnetotelluric data, *Journal of Geophysical Research*, *107*(B6), 1–21, doi:10.1029/2001JB000186, 2002.

Warren-Smith, E., S. Lamb, and T. A. Stern, Stress field and kinematics for diffuse microseismicity in a zone of continental transpression, South Island, New Zealand, *Journal of Geophysical Research: Solid Earth*, *122*(4), 2798–2811, doi: 10.1002/2017JB013942, 2017a.

Warren-Smith, E., S. Lamb, T. A. Stern, and E. Smith, Microseismicity in Southern South Island, New Zealand: Implications for the Mechanism of Crustal Deformation Adjacent to a Major Continental Transform, *Journal of Geophysical Research: Solid Earth*, *122*(11), 9208–9227, doi:10.1002/2017JB014732, 2017b.

Warren-Smith, E., B. Fry, L. M. Wallace, E. R. Chon, S. A. Henrys, A. F. Sheehan, K. Mochizuki, S. Y. Schwartz, S. C. Webb, and S. Lebedev, Episodic stress and fluid pressure cycling in subducting oceanic crust during slow slip, *Nature Geoscience*, doi:10.1038/s41561-019-0367-x, 2019.

Warren-Smith, E., C. J. Chamberlain, S. Lamb, and J. Townend, High-Precision Analysis of an Aftershock Sequence Using Matched-Filter Detection: The 4 May 2015 M L 6 Wanaka Earthquake, Southern Alps, New Zealand, *Seismological Research Letters*, *88*(4), 1065–1077, doi:10.1785/0220170016, 2017.

Wech, A. G., C. M. Boese, T. A. Stern, and J. Townend, Tectonic tremor and deep slow slip on the Alpine Fault, *Geophys. Res. Lett., 39*, *39*(L10303), doi:10.1029/2012GL051751, 2012.

Wech, A. G., A. F. Sheehan, C. M. Boese, J. Townend, T. A. Stern, and J. A. Collins, Tectonic Tremor Recorded by Ocean Bottom Seismometers, *Seismological Research Letters*, *84*(5), 752–758, doi:10.1785/0220120184, 2013.

Wellman, H., and R. Willet, The Geology of the West Coast from Abut Head to Milford Sound – Part 1, 1942.

Wellman, H. W., An uplift map for the South Island of New Zealand, and a model for uplift of the Southern Alps, in The Origin ofthe Southern Alps, *Royal Society of New Zealand Bulletin*, *in Walcott*(18), 13–20, 1979.

Wells, A., M. D. Yetton, R. P. Duncan, and G. H. Stewart, Prehistoric dates of the most recent Alpine fault earthquakes, New Zealand, *Geology*, *27*(11), 995–998, 1999.

Wiemer, S., and M. Wyss, Minimum magnitude of completeness in earthquake catalogs: Examples from Alaska, the Western United States, and Japan, *Bulletin of the Seismological Society of America*, *90*(4), 859–869, doi:10.1785/0119990114, 2000.

Williams, C. F., Observations from the 1992 Landers earthquake, *23*(16), 2029–2032, 1996.

Woessner, J., J. L. Hardebeck, and E. Hauksson, What is an instrumental seismicity catalog, *Community Online Resource for Statistical Seismicity Analysis*, (September), 1–14, doi:10.5078/corssa-38784307., 2010.

Wolfe, C. J., On the mathematics of using difference operators to relocate earthquakes, *Bulletin of the Seismological Society of America*, *92*(8), 2879–2892, doi:10.1785/0120010189, 2002.

Yano, T. E., T. Takeda, M. Matsubara, and K. Shiomi, Japan unified hIgh-resolution relocated catalog for earthquakes (JUICE): Crustal seismicity beneath the Japanese Islands, *Tectonophysics*, *702*, 19–28, doi:10.1016/j.tecto.2017.02.017, 2017.

Yao, D., J. I. Walter, X. Meng, T. E. Hobbs, Z. Peng, A. V. Newman, S. Y. Schwartz, and M. Protti, Detailed spatiotemporal evolution of microseismicity and repeating earthquakes following the 2012 Mw 7.6 Nicoya earthquake, *Journal of Geophysical Research: Solid Earth*, doi:10.1002/2016JB013632, 2017.

Zachariasen, J., K. Berryman, R. Langridge, C. Prentice, M. Rymer, M. Stirling, and P. Villamor, Timing of late holocene surface rupture of the wairau fault, Marlborough, New Zealand, *New Zealand Journal of Geology and Geophysics*, *49*(1), 159–174, doi:10.1080/00288306.2006.9515156, 2006.

Zeitler, P. K., A. S. Meltzer, P. O. Koons, D. Craw, B. Hallet, C. P. Chamberlain, W. S. Kidd, S. K. Park, L. Seeber, M. Bishop, and J. Shroder, Erosion, Himalayan geodynamics, and the geomorphology of metamorphism, *GSA Today*, *11*(1), 4–9, 2001.